Loughborough University

Viability and Characterization of the Laser Surface Treatment of Engineering Ceramics

by

Pratik Shukla **(BEng (Hons), DIS, MScR.)**

A doctorate Thesis

Submitted in partial fulfilment of the requirement for the award of

Doctorate of Philosophy

of Loughborough University

Dec 2007 – Jan 2011

Wolfson School of Mechanical and Manufacturing Engineering,

Loughborough University

Abstract

Laser surface treatment of engineering ceramics offers various advantages in comparison with conventional processing techniques and much research has been conducted to develop applications. Even so, there still remains a considerable gap in knowledge that needs to be filled to establish the process. By employing a fibre laser for the first time to process silicon nitride (Si_3N_4) and zirconia (ZrO_2) engineering ceramics, a comparison with the CO_2 and a Nd:YAG lasers was conducted to provide fundamental understanding of various aspects of the laser beam-material interaction. Changes in the morphology, microstructure, surface finish, fracture toughness parameter (K_{1c}) were investigated, followed by thermal finite element modelling (FEM) of the laser surface treatment and the phase transformation of the two ceramics, as well as the effects of the fibre laser beam parameter - brightness (radiance).

Fibre and CO_2 laser surface treatment of both Si_3N_4 and ZrO_2 engineering ceramics was performed by using various processing gases. Changes in the surface roughness, material removal, surface morphology and microstructure were observed. But the effect was particularly more remarkable when applying the reactive gases with both lasers and less significant when using the inert gases. Microcracking was also observed when the reactive gases were applied. This was due to an exothermic reaction produced during the laser-ceramic interaction which would have resulted to an increased surface temperature leading to thermal shocks. Moreover, the composition of the ceramics was modified with both laser irradiated surfaces as the ZrO_2 transformed to zirconia carbides (ZrC) and Si_3N_4 to silicon dioxide (SiO_2) respectively.

The most appropriate equation identified for the determination of the fracture toughness parameter K_{1c} of the as-received, CO_2 and the fibre laser surface treated Si_3N_4 and ZrO_2 was $K_{1c}=0.016\ (E/Hv)^{1/2}\ (P/c^{3/2})$. Surfaces of both ceramics treated with CO_2 and the fibre laser irradiation produced an increased K_{1c} under the measured conditions, but with different effects. The CO_2 laser surface treatment produced a thicker and softer layer whereas the fibre laser surface treatment increased the hardness by only 4%. This is inconsiderable but a reduction in the crack lengths increased the K_{1c} value under the applied conditions. This was through a possible transformation hardening which occurred within both engineering ceramics.

Experimental findings validated the generated thermal FEM of the CO_2 and the fibre laser surface treatment and showed good agreement. However, a temperature difference was found between the CO_2 and fibre laser surface treatment due to the difference in absorption of the near infra-red (NIR) wavelength of the fibre laser being higher than the mid infra-red (MIR) wavelength of the CO_2 laser. This in turn, generated a larger interaction zone on the surface that was not induced further into the bulk, as was the case with the fibre laser irradiation. The MIR wavelength is therefore suitable for

the surface processing of mainly oxide ceramics and surface treatments which do not require deep penetration. Phase transformation of the two ceramics occurred at various stages during the fibre laser surface treatment. The ZrO_2 was transformed from the monoclinic (M) state to a mixture of tetragonal + cubic (T+C) during fibre laser irradiation and from T+C to T and then a partially liquid (L) phase followed by a possible reverse transformation to the M state during solidification. The Si_3N_4 transformed to a mixture of α-phase and β-phase ($\alpha \rightarrow \alpha+\beta$) followed by $\alpha+\beta$ and fully transforms from $\alpha+\beta \rightarrow \beta$-phase. What is more, is a comparison of the fibre laser-beam brightness parameter with that of the Nd:YAG laser. In particular, physical and microstructural changes due to the difference in the laser-beam brightness were observed.

This research has identified the broader effects of various laser processing conditions, as well as characterization techniques, assessment and identification of a method to determine the K_{1c} and the thermal FEM of laser surface treated engineering ceramics. Also, the contributions of laser-beam brightness as a parameter of laser processing and the influence thereof on the engineering ceramics have been identified from a fundamental viewpoint. The findings of this research can now be adopted to develop ceramic fuel cell joining techniques and applications where laser beam surface modification and characterization of engineering ceramics are necessary.

Dedicated to my Parents...

Acknowledgements

First of all, I take this opportunity to thank my parents for the unconditional love, support, encouragement which they have provided for me in every way possible. I will always be indebted to this. Without it, the journey before and during my PhD would have been completely impossible. Words can be rather small for such acknowledgements! A special thank you also goes to my good friend and fiancé Kshamta for always being there particularly when times were hard. Her endless support, patience and encouragement gave me the strength and the determination to achieve my goal.

I would also like to thank my school friend Sid (Syeed) for being there at all times, whenever it was required, as well as giving valuable contributions to my mission in terms of moral support and encouragement throughout the whole duration of my PhD and many other ventures before that.

During the course of this work, I was given valuable advice, ideas and technical guidance by Dr Houzheng Wu (Department of Materials) on several occasions which helped me to shape my work better and allowed me to produce inter-disciplinary research. A special thank you also goes to Mr Jagpal Singh from the metrology lab as he was always ready to help when operating equipment, sample analysis and technical support. I would also to like acknowledge Mr Andy Sandevar for helping me to cut, grind, polish and prepare my ceramic samples and Enzo Liotti for his kind assistance in conducting the TG-DSC thermal analysis. Thanks to my colleagues David Waugh and Colin Dowding for helping me in many ways with my research in general and the various members of the Optical Engineering group who has contributed. Herewith, I also send my gratitude to Anish Paul who provided some good technical assistance with conducting FEGSEM analysis and technical guidance with the latter part of my thesis. I would also thank Michelle Grant for assisting me with conducting the three-point bending strength study.

I would also like to acknowledge the contributions of Mr Steve Allitt and Dr Phillip Swanson from the Advanced Joining Centre, Coventry University for their valuable advice and providing the facility for me to conduct some of my experiments. Also, thanking Elliot and David Gatward from Microkerf Ltd. for their time and for providing the equipment to conduct the remainder of my experiments.

Above all, I would like to express my sincere gratitude to my supervisor Dr Jonathan Lawrence for first of all giving me the opportunity to conduct this PhD. I have seen myself grow and develop as a person and a researcher throughout the duration of my PhD that has largely been due to his influence, which I am greatly indebted to. It would have been impossible for me to undergo the whole venture without his contributions, valuable advice, guidance, time and the support as well as keeping a track of my work throughout the complete duration of the research. Finally, I would like to thank all those who directly and indirectly helped me in achieving my goal.

List of Publications

Book Chapter

1. **Shukla P.P.**, Lawrence J. (2011) Chapter 6 – Assessment of a Suitable Method for the Evaluation of Fracture Toughness Parameter (K_{1c}) of Laser Surface Treated Engineering Ceramics**,** In: D.S. Yilbas (ED.) Laser Machining and Surface Treatment, London: Elsevier.
   To be submitted in 2011

Journal Papers

1. **Shukla, P.P.**, Lawrence, J., Wu, H. (2009) **'**On the fracture toughness of a zirconia engineering ceramic and the effects thereon of surface processing with fibre laser radiation'. *Proceedings of the Institution of Mechanical Engineers, Part B, Journal of Engineering Manufacture* **224**, (B10), 1555-1570. DOI: 10.1243/09544054JEM1777

2. **Shukla, P.P**., Lawrence, J. (2010) 'Surface characterization and compositional evaluation of a fibre laser processed silicon nitride (Si_3N_4) engineering ceramic'. *Lasers in Engineering* **20 (5-6)**, 359 – 370.

3. **Shukla, P.P.**, Lawrence, J. (2010) 'Fracture toughness modification by using a fibre laser surface treatment of a silicon nitride engineering ceramic'. *Journal of Materials Science* **45 (23)**, 6540-6555. DOI: 10.1007/s10753-010-4743-6

4. **Shukla, P.P.**, Lawrence, J. (2011) 'Evaluation of fracture toughness of ZrO_2 and Si_3N_4 engineering ceramics following CO_2 and fibre laser surface treatment'. *Optics and Lasers in Engineering* **49**, 229 - 239. DOI:10.1016/j.optlaseng.2010.09.010.

5. **Shukla, P.P.**, Lawrence, J. (2011) 'Mathematical modelling of the fibre laser Surface processing of a Zirconia engineering ceramic by means of three-dimensional finite element analysis'. *Proceedings of the Institution of Mechanical Engineers, Part C, Journal of Mechanical Engineering Science*, **225(4)**, 949 – 964. DOI: 10.1243/09544062JMES2434.

6. **Shukla, P.P.**, Lawrence, J. (2011) 'Examination of temperature distribution on silicon nitride engineering ceramics during fibre laser surface treatment'. *Optics and Lasers in Engineering*. **(Published Online)** Accepted on the 15th January 2011. DOI: 10.1016/j.optlaseng.2011.01.014.

7. **Shukla, P.P.**, Lawrence, J., Paul A. (2011) 'Influence of laser beam brightness during laser surface treatment of ZrO_2 engineering ceramics'. *Lasers in Engineering.* **Accepted** on 6th December 2010 (in press).

8. **Shukla, P.P**., Lawrence, J. (2011) 'Distribution of temperature during fibre laser radiation and the effects on the phase transformation of ZrO_2 engineering ceramic'. *Surface Engineering*, (in press). **Accepted** on the 3rd January 2011.

9. **Shukla, P.P.**, Lawrence, J. (2011) 'Modification of fracture toughness parameter (K_{1c}) following CO_2 laser surface treatment of a Si_3N_4 engineering ceramic'. *Surface Engineering*, (in press) **Accepted** on the 7th January 2011.

10. **Shukla, P.P.**, Lawrence, J. (2011) 'Characterization and compositional study of a zirconia engineering ceramic irradiated with a fibre laser beam'. *Optics & Laser Technology*, (in press). **Accepted** on the 2nd February 201.

11. **Shukla, P.P.**, Lawrence, J. (2011) 'On the Establishment of an Appropriate Method for Evaluating the Residual Stresses after Laser Surface Treatment of ZrO_2 and Si_3N_4 Engineering Ceramics'. *Far East Journal of Mechanical Engineering and Physics*. *(in press)*. **Accepted on 15** on the 22nd December 2010.

12. **Shukla, P.P**., Lawrence, J. 'A Comparative Study on the Processing Parameters during Fibre and CO_2 laser Surface Treatments of Silicon Nitride Engineering Ceramic'. *International Journal of Advanced Manufacturing Technology*. **Accepted** on 6th March 2011.

13. **Shukla, P.P**., Lawrence, J. 'A comparison of fibre and Nd:YAG laser beam brightness influences after surface processing of a Si_3N_4 engineering ceramic'. *Journal of Laser Applications.* **Under consideration**, Submitted on 4th March 2011.

14. **Shukla, P.P**., Lawrence, J. 'Investigation of temperature distribution during CO_2 and Fibre laser processing of Si_3N_4 engineering ceramic by means of computational and experimental approach'. *Journal of Manufacturing Processes.* **Under consideration**, Submitted on 8th March 2011.

15. **Shukla, P.P**., Lawrence, J. 'Establishment of processing parameters during CO_2 and fibre laser surface treatment of ZrO_2 engineering ceramic'. *Proceedings of the Institution of Mechanical Engineers, Part B, Journal of Engineering Manufacture.* **Under Consideration**, Submitted on the 12th March 2011.

Conference Papers

1. **Shukla, P.P.**, Lawrence, J. (2009), "Laser surface treatment of engineering ceramics and the effects thereof on fracture toughness", *The 27th International Congress on Applications of Lasers and Electro-Optics (ICALEO 2009): Laser Materials Processing*, 2 - 5 November 2009, Orlando, FL., USA, **102**, 109-115. Orlando: Laser Institute of America (2009).

2. **Shukla, P.P.**, Lawrence, J. (2009), "Characterization and compositional evaluation of laser processed engineering ceramics", *The 27th International Congress on Applications of Lasers and Electro-Optics (ICALEO 2009): Laser Materials Processing*, 2 - 5 November 2009, Orlando, FL., USA, **102**, 122-.132. Orlando: Laser Institute of America (2009).

3. **Shukla, P.P.**, Lawrence, J. (2010), "Fracture Toughness modification by means of CO_2 Laser Processing of a Silicon Nitride Engineering Ceramic", *The 36th International Manufacturing Automated Systems Technology Applications Design Organization and Management Research (MATADOR) Conference*, 14 – 16 July 2010, Manchester, UK, **16**, 519-522.

4. **Shukla, P.P.**, Lawrence, J. (2010), "Thermal analysis of fibre laser treated zirconia engineering ceramic", *The 36th International Manufacturing Automated Systems Technology Applications Design Organization and Management Research (MATADOR) Conferenc*e, 14 – 16 July 2010, Manchester, UK, **16**, 539-542.

Table of Content

VIABILITY AND CHARACTERIZATION OF THE LASER SURFACE TREATMENT OF ENGINEERING CERAMICS

Part 1

ENGINEERING CERAMICS, INDUSTRIAL LASERS AND PREVIOUS RESEARCH

PART 2

TOPOGRAPGHICAL, MORPHOLOGICAL, COMPOSITIONAL AND MICROSTRUCTURAL ASPECTS

PART 4

NEW PERSPECTIVES ON LASER BEAM-MATERIAL INTERACTION

Glossary of Terms

B.

BSI……British Standards Institute

C.

CAD……Computer Aided Design

CD……Compact Disk

CMM……Co-ordinate Measuring Machine

CIP……Cold Isostatic Pressing

CNB……Chevron Notched Beam

CVD……Chemical Vapour Deposition

CW……Continuous Wave

D.

DCB……Double Cantilever Beam

DOE……Diffractive Optical Element

DT……Double Torsion

DTA……Differential Thermal Analysis

DSC……Differential Scanning Calometry

DOI……Digital Object Identification

E.

FIR……Far Infra-Red

EDX……Energy Dispersive X-ray

F.

FEA……Finite Element Analysis

FEM……Finite Element Modelling

FEGSEM……Field Emission Gun Scanning Electron Microscope

H.

HAZ……Heat Affected Zone

HP……Hot Pressed

HIP……Hot Isostatic Pressing

HPDL……High Power Diode Laser

HPSN……Hot Pressed Silicon Nitride

HDOE……Holographic Diffractive Optical Element

J.

JIT…….....……Just In Time

I.

IF……..……..Infinite Focus

ISO……..…International Organization for Standardization

L.

LASER…….……..…Light Amplification Stimulated Emission Radiation

LSM……Laser Surface Melting

LIM……Laser Interaction with Materials

M.

MIR……..……..Mid Infra-Red

N.

NC……..…….……Numerical Control

NIR…….……Near Infra-Red

Nd:YAG…….….Neodymium Yttrium Aluminium Garnet

Nd:YLF……Neodymium, Yttrium, Lithium Fluoride

P.

PSZ…….…..…Partially Stabilized Zirconia

R.

RB……..……...Reaction Bonded

RBSN…….……..Reaction Bonded Silicon Nitride

RSSN…….……..…Reaction Sintered Silicon Nitride

S.

S…….…….……Sintered

SENB…….……..Single Edge Notched Beam

SSN…….……....Sintered Silicon Nitride

SEM…….…..Scanning Electron Microscope

SIALON……..……..…Silicon, Aluminium, Oxygen, Nitrogen

STDEV……..……...…….……Standard Deviation

T.

TEM……..Transverse Electromagnetic Mode

TG……...Thermo gravimetric (Analysis)

U.

UV……..…….…..…….....Ultraviolet

W.

WLI…….……..White Light Interferometer

WW……..……...World War

X.

XRD……...…….……...X-Ray Diffraction (analysis)

Y.

YSiALON…….……...Yttria, Silicon, Aluminium, Oxygen, Nitrogen

YSZ…….……....Yttria Stabilized Zirconia

Nomenclature

A	Amps
A	Radiation Constant (in Chapter 7)
a	Two times the average flaw size (2c)
Al	Aluminium
Al_2O_3	Alumina
Ar	Argon
AΩ	Solid Angle of Divergence
b	Breadth
B_4C	Boron Carbide
Bi	Butyl rubber filled supper conductive ceramic
BN	Boron nitride
Br	Brightness
c	Average flaw size
C	Carbon
C	Cubic Phase (in Chapter 7)
CaO	Calcia
c-BN	Boron Nitride
cm^2	Centi-meters Squared
CO_2	Carbon Dioxide
c_p	Specific Heat (See Equation 7.1, Chapter 7)
CW	Continuous Wave
D	Average diagonal size
d	Depth
E	Young's modulus
F	Force
G	Centre of the axis of whole section
g	grams
G_1	Centre of area where the forces is taken from
GPa	Giga Pascal
He	Helium
HeNe	Helium Neon
HV	Hardness (Vickers)
Hz	Hertz
Ic	Interior cracks
Ixx	Second moment of area

J	Joules
K_{1c}	Fracture Toughness Property
Kc	Plane stress fracture toughness
kg	Kilo gram
k_{ij}	Conductivity Co-efficient
kw	Kilo Watts
L	Latent heat per unit mass of the material undergoing phase change
L	Liquid (Phase)
l	Litres
m	Meters
m/min	metres per minute
M	Monoclinic Phase
M^2	Laser beam quality factor
m^3	metre cubed
MgO	Magnesia Oxide
Mm	Millimetres
MPa	Mega Pascal
ms	milliseconds
mW	mili Watts
N	Newtons
N_2	Nitrogen
Nm	nano-metres
O_2	oxygen
P	load (kg)
Pc	load impact
P_{out}	Output Power
q	Heat energy across the surface
q_b	Rate of heat generation per unit volume
R	Radius
Ra	Surface Roughness
rad	Radians
s	Seconds
Si	Silicon
Si_3N_4	Silicon Nitride
SiC	Silicon Carbide
SiO_2	Silicon Oxide
sr^{-1}	Steradians

T	Tetragonal (Phase)
TiB_2	Titanium boride
TiO_2	Titanium dioxide
V	Volts
V	Volume
W	Watts
wt	Weight
Y	Yttria (Yttrium)
Y_2O_3	Yttria
Zr	Zirconium
ZrB_2	Zirconia Boride
ZrC	Zirconia Carbide
ZrO_2	Zirconia Oxide
α	Alpha (representation of a phase)
β	beta (representation of a phase)
γ	Cubic (representation of a phase)
δ	Delta
δA	Area of Rectangle
δy	Dimension of rectangle
ε	Epsilon
θ	Theta (temperature at this point on surface (see Equations 7.2 and 7.3)).
θ^0	Reference Temperature
θ_f	Phase change temperature
θ^Z	Absolute zero on the temperature scale
λ	Wavelength
π	Pi
ρ	Mass Density (see Equation 7.1, Chapter 7)
σ	Sigma (Resultant Stresses)
%	Percentage
+ve	Positive
-ve	Negative
$\sum$	Sum (of)
$^{\circ}C$	Degree Celsius
µm	micro-metre
3-D	Three Dimensional

List of Figures

Chapter 1: Background and State-of-the-Art Engineering Ceramics

Chapter 2: Background of Industrial Lasers

Chapter 4: On the Establishment of Laser Surface Treatment Parameters

Chapter 5: Characterization and Compositional Evaluation of Laser Surface Treated Engineering Ceramics

Chapter 6: Assessment of a Suitable Method for the Evaluation of Fracture Toughness Parameter (K_{1c}) of Laser Surface Treated Engineering Ceramics

Chapter 7: Thermal Analysis of Laser Surface Treated Engineering Ceramics

Figure 7.26 Parameters obtained from the FEM of the CO_2 laser surface treated ZrO_2, showing the correlation of various factors with one another: (a) power density *versus* temperature, (b) depth *versus* power density, (c) power density *versus* traverse speed, (d) power density *versus* time, (e) traverse speed *versus* temperature and (f) depth *versus* temperature.

Figure 7.27 Schematic of the surface temperature reading in (a), and (b) the bulk temperature of the Si_3N_4 engineering ceramic.

Figure 7.28 Experimental temperature distribution over the surface length in (a) and (b) the temperature distribution through the bulk of the fibre laser processed Si_3N_4 engineering ceramic.

Figure 7.29 FEM of the heat distribution of the fibre laser focused at 0mm from the edge (position 1) of the Si_3N_4 engineering ceramic work-piece (start of the laser treatment) in (a) and (b) the cross-sectional view.

Figure 7.30 Temperature curves from the FEM of the initial stage at 0mm from the edge (position 1) of the fibre laser irradiation of the Si_3N_4 engineering ceramic for (a) the heat distributed over the length of the sample, and (b) the heat distribution through the depth of the sample.

Figure 7.31 FEM of the heat distribution of the fibre laser focused at 12.5mm from the edge (position 2) of the Si_3N_4 engineering ceramic in (a), and the cross-sectional view in (b) and (c).

Figure 7.32 Temperature curves from the FEM of the fibre laser irradiation at 25mm from the edge (position 3) of the Si_3N_4 engineering ceramic for (a) the heat distributed over the length of the sample, and (b) the heat distribution through the depth of the sample.

Figure 7.33 FEM of the heat distribution of the fibre laser beam focused in the centre (position 3) of the Si_3N_4 engineering ceramic in (a), and in the cross-section in (b) and (c).

Figure 7.34 Temperature curves from the FEM of the fibre laser irradiation at 25mm from the edge (position 3) of the Si_3N_4 engineering ceramic for (a) the heat distributed over the length of the sample and (b) the heat distribution through the depth of the sample.

Figure 7.35 Parameters obtained from the FEM showing the correlation of various parameters with one another; (a) power density *versus* temperature; (b) depth *versus* power density; (c) power density *versus* traverse speed; (d) power density *versus* time; (e) traverse speed *versus* temperature; (f) depth *versus* temperature and (g) depth *versus* time for fibre laser surface treatment of the Si_3N_4 engineering ceramic.

Figure 7.36 Heating and cooling curve from the TG-DSC analysis for the as-received surface of the Si_3N_4 engineering ceramic.

Chapter 8: Influence of Laser-Beam Brightness During Surface Treatment of ZrO_2 Engineering Ceramic

List of Tables

Chapter 5: Characterization and Compositional Evaluation of Laser Surface Treated Engineering Ceramics

Chapter 6: Assessment of a Suitable Method for the Evaluation of Fracture Toughness Parameter (K_{1c}) of Laser Surface Treated Engineering Ceramics

List of Equations

$K_{1c} = 0.0101\ P/(ac^{1/2})$	[167]	(6.1)
$K_{1c} = 0.0724\ P/c^{3/2}$	[171]	(6.2)
$K_{1c} = 0.0515\ P/c^{3/2}$	[153]	(6.3)
$K_{1c} = 0.0134\ (E/Hv)^{1/2}\ (P/c^{3/2})$	[154]	(6.4)
$K_{1c} = 0.0330\ (E/Hv)^{2/5}\ (P/c^{3/2})$	[157]	(6.5)
$K_{1c} = 0.0363\ (E/Hv)^{2/5} (P/a^{1.5})\ (a/c)^{1.56}$	[172]	(6.6)
$K_{1c} = 0.095\ (E/Hv)^{2/3}\ (P/c^{3/2})$	[173]	(6.7)
$K_{1c} = 0.022\ (E/Hv)^{2/3}\ (P/c^{3/2})$	[173]	(6.7)
$K_{1c} = 0.035\ (E/Hv)^{1/4}\ (P/c^{3/2)})$	[174]	(6.9)
$K_{1c} = 0.016\ (E/Hv)^{1/2}\ (P/c^{3/2})$	[166]	(6.10)
$K_{1c} = 0.079\ (P/a^{3/2}) \log (4.5\ a/c)$ for $0.5 \leq c/a < 4.5$	[175]	(6.11)
$K_{1c} = 0.4636\ (P/a^{3/2})\ (E/Hv)^{2/5}\ (10^{F})$	[175]	(6.12)
$K_{1c} = 0.0141\ (P/a^{3/2})\ (E/Hv)2/5 \log (7.4^{a}/c)$	[173]	(6.13)
$K_{1c} = 0.0232\ [f\ (E/Hv)]\ P/(ac^{1/2})$ † for $c/a \leq \approx 2.7$	[173]	(6.14)
$K_{1c} = 0.417\ [f\ (E/Hv)]\ P/(a^{0.42} c^{1.07})$ † for $c/a \geq \approx 2.$	[174]	(6.15)
$HV = 2P \sin [\theta/2]/ D^2 = 1.7544P / D^2$		(6.16)
$\partial^2 (k\theta)/\partial x^2 + \partial^2 (k\theta)/\partial y^2 + \partial^2 (k\theta)/\partial z^2 + qb = \rho c_p \partial\theta/\partial t$		(7.1)
$q = - h\ (\theta - \theta^0),$		(7.2)
$q = A\ [(\theta - \theta^Z)^4 - (\theta^0 - \theta^Z)^4],$		(7.3)
$A = \varepsilon\sigma,$		(7.4)
$\theta = \theta_f,$		(7.5)
$\Delta\ q_s\ dS = -\rho L\ dV/dt$		(7.6)
$Br = \frac{P_{out}}{A\Omega}$		(8.1)

$$\Omega = \pi \theta^2 = \lambda^2 / \pi w^2_0 \quad (8.2)$$

$$M^4 = M^2_y . M^2_x \quad (8.3)$$

$$Br = \frac{P_{out}}{M^4 \times \lambda^2} \quad (8.4)$$

Introduction

1. Lasers in Material Processing

Laser aided material processing has developed tremendously since the first invention of the laser in the 1960's. Since then, the applications of lasers have continuously increased in the manufacturing/engineering sectors and more in recent years in the product packaging, medical, entertainment and in the military sectors. This is because of the advantages that are generally offered by laser systems. Industrial laser systems offer high speeds, accuracy, and shorter process times, high power density focused on a localized area, deep penetrating treatment and aesthetics, which allow laser systems to hold a commercial advantage in comparison with conventional manufacturing methods. Industrial lasers can cut, join, remove material, mark and conduct surface treatments which could modify various properties of engineering and non-engineering materials depending on the application and its end use.

Various types of lasers to this date operate with different power outputs, wavelengths, beam profile and delivery systems to process various materials. Those are namely: CO_2, neodymium, yttrium aluminium garnet (Nd:YAG), high powered diode (HPDL), excimer, and the fibre lasers. The selection of a particular laser system is dependent on the suitability of wavelength, power output, material threshold and the requirements for the application for which it is used for. The interaction of a particular laser source with a material is a phenomenon. This is because the effects and the end results are dependent on the material's characteristics and the mechanical properties which also determine its feasibility for laser processing. Application of the CO_2 and the Nd:YAG laser has dominated in the material processing industry over the last few decades, but diode and excimer lasers and in the recent years fibre lasers have also gained popularity. Figure 1 illustrates the application of different industrial lasers in the material processing and their suitability to process different materials.

Fibre lasers have been around since 2004 and have rapidly established a place in the laser aided material processing sector [1]. Fibre lasers hold an advantage over the conventional laser sources as they provide high power with better absorption, high beam quality, focused on a small spot size, low maintenance, energy efficiency (low cost per wattage), high accuracy and repeatability, high brightness (power per unit area) and the suitability of using fibre optics to transport the beam. Such aspects increase the potential for new opportunities (applications) in comparison to other counterparts [2]. Current application of fibre lasers are expanding in the industrial scene with processing metals, plastics and some ceramics (scribing and marking). Nevertheless, from a laser material interaction view point, the effects of the fibre laser interaction on engineering ceramics is not fully discovered or understood as it is still new in the market.

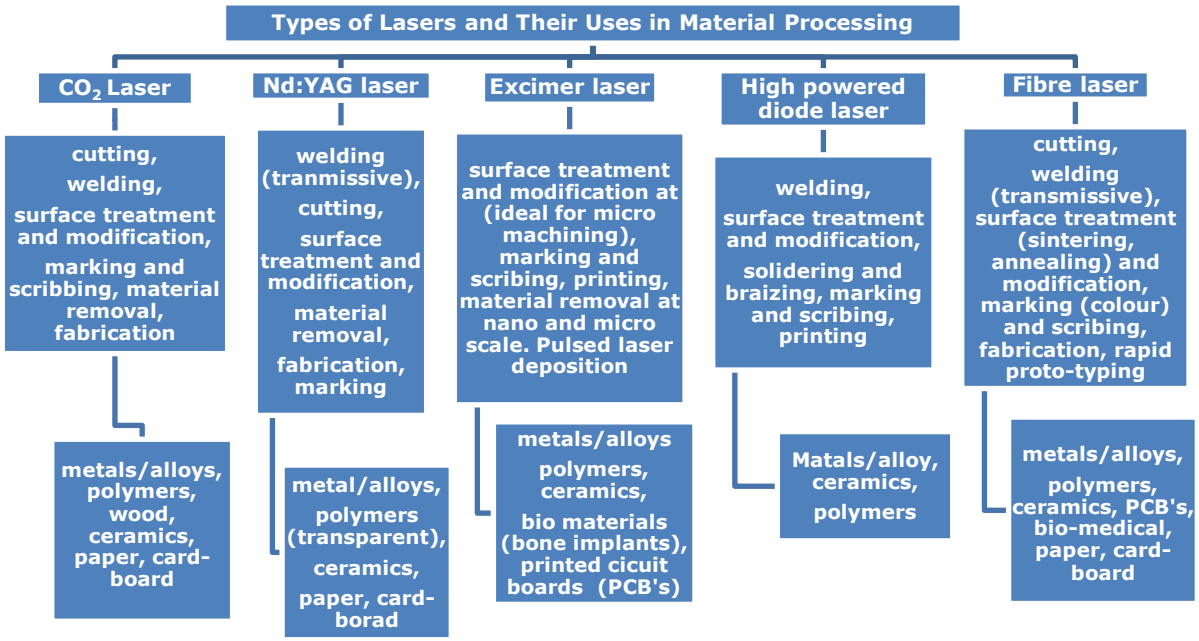

Figure 1 A chart illustrating the application of variety of industrials lasers for processing various engineering and non-engineering materials [3 - 5].

2. Research Rationale

Lack of resource and environmental issues have encouraged reduction in carbon emissions and the need to generate energy cleanly. This has generated much interest for research in this area, particularly for the technology of fuel cells to generate electricity from a continuously supplied stream of fuel and oxidant. These provide a means of converting the chemical energy directly to electrical energy. The technology of fuel cells for the generation of electricity could meet the current demands for a clean and renewable energy source. The fuel cells are made by screen-printing the active cell material into a flat ceramic tube. This results in flat ceramic tube with 15 fuel cells on each side. When the tubes are combined into bundles, then into strips and ultimately into fuel cell stacks, the amount of electricity generated is not inconsiderable. When the stacks are combined then multi-megawatt power plant can be created. To meet current market requirement for electricity, not to mention potential future growth, scaling-up the fuel cell stack combinations, and thus scaling-up of the fuel cell manufacturing process, is essential for large-scale generation capacity. However, the current manufacturing methods available for making the fuel cell tubes are time-consuming. In particular, the firing procedures that are necessary to vitrify the surface of the fuel cell tubes in order to seal them mean that each fuel cell tube can take at least four-days to make [6]. Such long cycle times give rise to manufacturing process that instead of being based on mass production, are based on batch production. This results in high production costs that consequently prevent large economies of scale being realized. One method that could reduce the manufacturing time for the fuel cell by replacing the firing processes would be to employ lasers to vitrify the surface of the fuel cells

because lasers would offer faster processing times and avoids a lengthy preparation to undergo the firing process. In addition, laser systems are also flexible since a laser can be mounted on a multi-axial robotic system or a large gantry machine for processing complex and large shaped parts. This can accommodate the joining of the fuel cell assembly. Research has advanced in the field of laser machining of ceramics [7-11], surface treatment [12-22] and laser cutting [23-33] and drilling of ceramics [34-37]. But the effects of laser processing of engineering ceramics are still unknown and not fully reported in most of the published literatures. The unknown aspects in particular are the effects during the laser interaction with oxide and nitride ceramics. Also, a comparative study by using a near infra-red (NIR) and mid infra-red (MIR) wavelengths by observing the differences in the laser modified surface layer from a compositional, microstructural, thermal shocking, internal phase changes, and fracture toughness as well as influence on the ceramics by using a high brightness laser beams. This research firstly attempts to elucidate the physical aspects and the mechanisms of the laser material interaction in particular. Laser processing of engineering ceramics through this would be better understood for future applications such as laser assisted joining of engineering ceramics. Joining of engineering ceramics would be useful as an alternative process when manufacturing ceramic fuel cell as considerable amount of lead time, tooling, labour cost and man hours would be saved. This in turn would also be profitable for the fuel cell manufacturers. Joining of the fuel cell was however, abandoned after the initial stages of this research. This was due to a likely industrial collaborator pulling away from the proposal. This meant that resource such as experimental material was not freely available to fully complete the required investigations. Hence, laser-ceramic interactions were investigated in order to achieve the end objective of joining the fuel cells. In doing so, will allow one to thoroughly understand the wider effects on the oxide and the nitride engineering ceramics. In particular the microstructure, surface topography, change in composition, laser modified surface characteristics such as thermal shocking, fracture toughness of the laser induced surface layer, as well as internal changes in phase so that a potential laser assisted fuel cell joining technology can be developed.

Laser surface treatment is essentially important because it has the potential to enhance surface strength, improve mechanical properties of the material such as hardness which is ideal for applications where wear rate is high due to shearing stresses. Laser surface treatment is also useful for improving the surface roughness, which in turn, could enhance the co-efficient of friction and reduce the shear stress acting on the material. Moreover, laser surface treatment could also be used to cover microcracks over ceramic surfaces. This inherently, provides a mean of maintaining the component life and elongates the functional life. In addition, aesthetics can also be improved by means of laser surface treatment (for ceramics in particular) by creating a modified glassy layer. This research is the first step towards attempting to join engineering ceramics by firstly understanding the science behind the laser material interaction by means of surface treatment. This in its own way would also fill the gap in knowledge. Moreover, the thesis elaborates the physical effects that take

place particularly during the fibre laser-interaction with the engineering ceramics which demonstrate the topography, compositional and the microstructural changes.

In addition, a gap in knowledge is also filled by investigating the fracture toughness parameter (K_{1c}), of the engineering ceramics after the laser surface processing. This is because metals and alloys in comparison to ceramics comprise of higher facture toughness. Therefore, it would prove to be beneficial if the K_{1c} of ceramics can be improved by means of laser processing. Improvement in the ceramics K_{1c} would also increase the possibility of the ceramics usage for the demanding applications since they would perform better in comparison to metals due to their high hardness, low thermal conductivity (particularly ZrO_2), low co-efficient of friction and wear rate. A change in the K_{1c} has an influence on the materials functionality or diversity to its applications. By improving the K_{1c} of materials can increase its functional capabilities such as longer functional life, improved performance under higher cyclic and mechanical loading. This research also demonstrates a technique to calculate the K_{1c} by employing Vickers indentation test for laser surface treated cold isostatic pressed (CIP) silicon nitride (Si_3N_4) and zirconia (ZrO_2) engineering ceramics.

The final aspect being investigated is the influence of the fibre laser-beam brightness thereof on the engineering ceramics. This is also unreported in any of the published literatures. Fibre lasers are known to comprise of high brightness in comparison with other lasers. This would significantly influence aspects such as penetration depth, hardness, laser-beam footprint and the microstructure as well the ceramics surface characteristics in comparison to those produced by another laser with lower brightness. This is because high brightness laser beam would result to high power per unit area. This in comparison to the identical power delivered by another laser with lower brightness would produce different effects. Therefore, the influence of the fibre laser beam brightness in comparison to the Nd:YAG laser beam is also presented in this thesis. This was due to the fact that the wavelengths of the two lasers are in the same region, which would allow one to understand the influence of the laser-beam brightness parameter with similar wavelength, power density and traverse speed as input parameters.

Both the ZrO_2 and the Si_3N_4 engineering ceramics were selected as they both have different mechanical and thermal properties. This in turn will create different effects to the laser surface treatments. Furthermore, both the ZrO_2 and Si_3N_4 engineering ceramics are more frequently used for many applications within the engineering, medical and power generation sectors so undertaking this research would contribute to achieving more diversity with current and future applications of the two ceramics.

3. Research Background and Approach

Experiments were conducted by employing a CO_2 (10.06 µm), Nd:YAG (1.064 µm) laser and is compared to the more recent fibre (1.075 µm) laser. This is the first time a surface treatment of the

engineering ceramics has been performed hitherto by employing the fibre laser. The CIPed ZrO_2 and Si_3N_4 engineering ceramics were investigated for their physical interaction during laser processing. Laser material interaction was evaluated by studying the surface integrity, morphology and the microstructure by using scanning electron microscopy (SEM), field emission gun scanning electron microscopy (FEGSEM) and focus variation technique. The chemical changes were investigated by using the energy dispersive x-ray analysis (EDX). Mechanical effects such as change in hardness were investigated by using the Vickers indentation method which was followed by determination of the fracture toughness parameter (K_{1c}) by using imperical equations from the literature. Increasing the K_{1c} of the ceramics is ideal as it can open up new avenues for demanding applications if the material could be made to develop further resistance to fracture induced by means of a laser surface treatment. If a crack is to propagate on the material surface, then the applied or existing tensile stress must first overcome and increase the compressive stress. This could be potentially induced by the laser treatment.

Thermal effects were investigated by using the thermogravimetry/differential thermal scanning calometry (TG/DSC). This was by analysing the physical changes in the ceramics occurring during the thermal exposure. This was complimented by conducting a prior investigation of the temperature distribution during the laser surface treatment. Then the process was modelled by using a finite element model (FEM) which would show the distribution of temperatures during the laser-material interaction. This helped to determine the concurrent phase transformation which the engineering ceramics would generally undergo. The laser-beam brightness (radiance) as a parameter is generally ignored in most investigations and in published work. The effects of the brightness of the fibre laser in comparison to the Nd:YAG laser was therefore studied with respect to change in hardness, dimensional size and the microstructure.

4. Aims and Objectives

A comparison is made throughout the thesis between the CO_2 and the fibre laser followed by the Nd:YAG and the fibre laser to examine and discuss the topographical, morphological, compositional, micro-structural, mechanical and thermal events resulting from laser-ceramic interactions. The objectives of this research are as follows:

(i) To obtain suitable parameter window in respect to achieving a defect-free surface by conducting experiments on the ZrO_2 and the Si_3N_4 engineering ceramics in particular by using the CO_2 and the fibre laser surface treatments.

(ii) To investigate the laser-material interaction by conducting a microstructural, topographical and a compositional analysis of the ZrO_2 and Si_3N_4 engineering ceramics.

(iii) To asses and identify the analytical technique for determination of fracture toughness property (K_{1c}) and to further determine the K_{1c} of the as-received and laser irradiated surfaces of the ZrO_2 and the Si_3N_4 engineering ceramics.

(iv) To study the thermal effects of the laser-material interaction by conducting an experimental and a computational analysis of the laser surface treatment of the ZrO_2 and Si_3N_4 engineering ceramics.

(v) To investigate the effect of the laser beam parameter brightness during laser processing of the engineering ceramics.

5. Thesis Structure

The structure of the thesis is presented in the schematic in Figure 2 which illustrates the construction of the thesis divided in four parts:

Part 1 - Background of ceramics, industrial lasers used and a review of previous research with respect to laser-material interaction is covered in this part.

Part 2 - Physical and scientific aspects namely: composition, microstructure and characterization are discussed herein.

Part 3 - Mechanical and thermal aspects, those are: measurement of surface hardness, determination of fracture toughness and the residual stress, followed by experimental and computational investigation of thermal effects.

Part 4 – New perspectives on laser beam-material interaction (study of the laser beam parameter: brightness)

Part 1 presents the first three Chapters of the thesis which demonstrates the background of the engineering ceramics in Chapter 1. Introduction to lasers is presented in Chapter 2 and a review of prior work, particularly within the field of laser-material processing of various ceramics in Chapter 3.

Part 2 includes Chapter 4 and Chapter 5 which justifies the laser parameters chosen for the investigation in Chapter 4. Characterization of the CO_2 and fibre laser irradiated ceramics with respect to compositional, microstructural and topographical changes is demonstrated in Chapter 5.

Part 3 demonstrates the mechanical and the thermal aspects where the fracture toughness parameter (K_{1c}) was investigated in Chapter 6. Furthermore, Chapter 7 discusses the thermal effects of the laser surface treatment where an experimental and a computational model (FEM) are presented. This is further complimented by work on phase transformation of the ZrO_2 and Si_3N_4 engineering ceramics.
Part 4 presents Chapter 8 which investigated the influence of laser-beam parameter - brightness. This is a comparative study between the fibre and the Nd:YAG laser surface treatment.

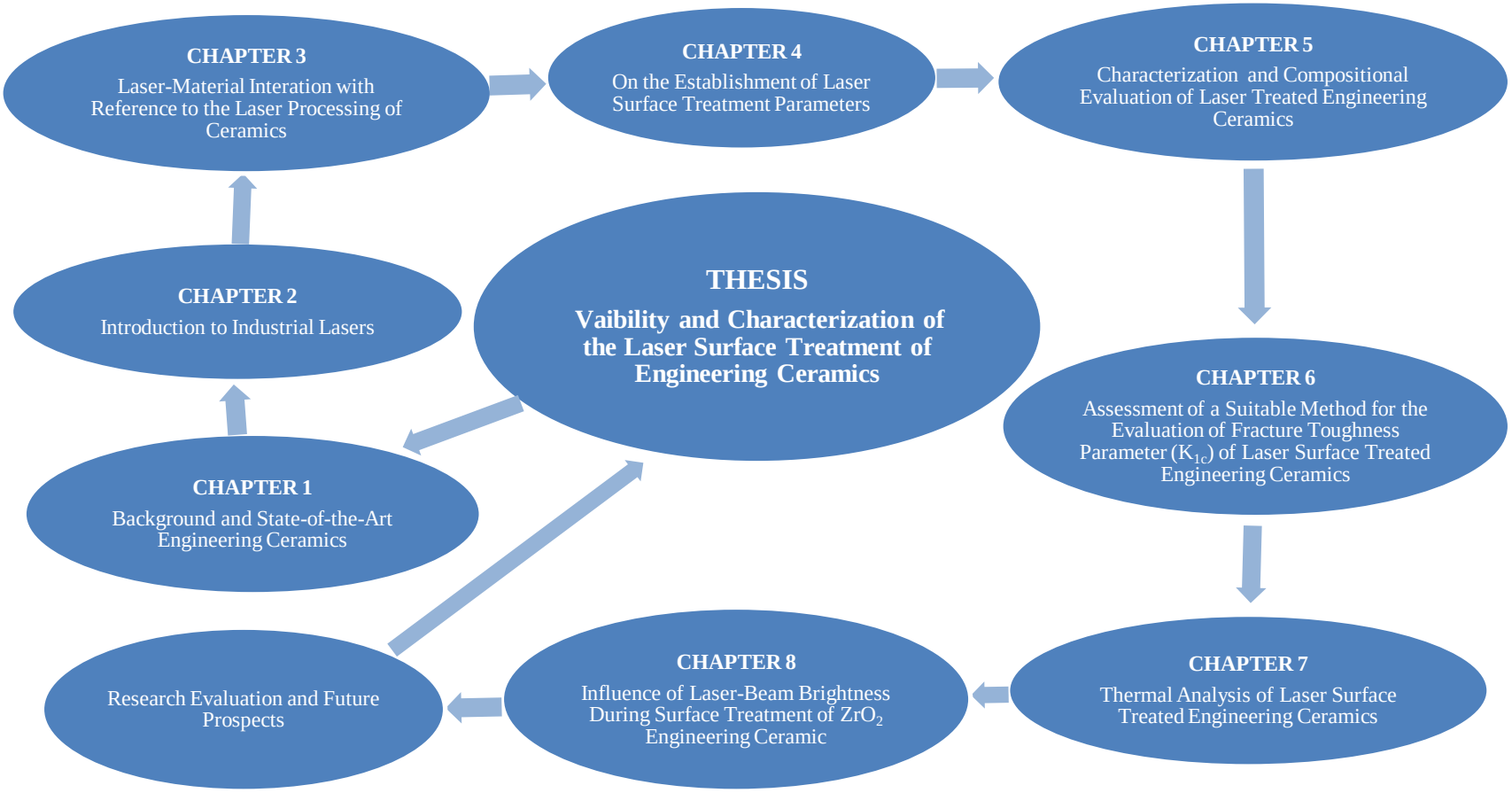

Figure 2 A schematic of the thesis structure and the project cycle.

PART 1

ENGINEERING CERAMICS, INDUSTRIAL LASERS AND PREVIOUS RESEARCH

CHAPTER 1
Background and State-of-the-Art Engineering Ceramics

This Chapter introduces the ceramics used within the selected engineering and non-engineering sectors. Manufacturing of the ceramics along with its physical properties, characteristics and its crystal structures are explained. Benefits of using ceramics over metallic materials are further justified along with a short summary of the cost issues. Justification of the failures of conventional parts made from metallic materials is addressed and how the existing problems with such metallic components can be overcome by using the engineering ceramics such as Si_3N_4, SiC, $Zr0_2$ and Al_2O_3. The main industries in focus are aerospace and automotive, although, applications within bio-medical and military sectors are also mentioned.

1.1 Engineering Ceramics and Their History

The word ceramic originates from the Greek word called *keramicos* (κεραμικός) meaning pottery [37]. *Keramicos* as a word has roots from the ancient Indian language called Sanskrit meaning "to burn". The Greeks refer to pottery as things made from the burnt earth. The history of ceramics dates back 10,000 years and is inorganic, non-metallic material, traditionally applicable to make pottery and chinaware for hundreds of years [37]. Traditional ceramics were made from inorganic materials such as clay minerals, dissolved rocks under the effect of water, and particles of sand mixed together to form products of white-wares, bricks, cements and tiles.

Modern ceramics otherwise known as technical or engineering ceramics are typically metal oxides, carbides, nitrides and borides (such as Si_3N_4, SiC, B_4C, and TiB_2). Complex ceramics are often mixture of several species, comprising of controlled composition in order to comply with a specific demand.

Advancements were made in late 1960s and 70s in the field of material technology to develop engineering ceramics that can be utilised for many demanding, ostensibly impossible and challenging applications. These ceramics have minimum similarity with their origins and are now capable of performing in the most vigorous conditions. Moreover, they are economically competitive than metallic materials in the long run due to the longer functional life of a product [37 -41].

Components made from ceramics tend to cost high due to their processing difficulties and high tooling and wear cost. Si_3N_4 ceramics cost between £20 - £30 per kg in comparison with metallic components (carbon steels). The cost of metals, however, is up to £0.50 - £0.70 per kg [42]. But the cost of ceramic parts may be considered economical if life cycle costs of the components are taken into consideration.

Ceramic parts provide longer durability and better performance at high operating speed without failing under high pressure and applied cyclic stresses which could be compromised with the cost of metal parts in comparison such as performance bearings used for both of the motor-sports and aerospace applications. The typical engineering ceramics are Al_2O_3, ZrO_2, Si_3N_4, SiC, BN and BC. There are many more which are used for various industrial applications and the reasons for their use in comparison with other materials are further justified:

1.2 Physical Properties of Engineering Ceramics

- Very high temperature strength - when exposed to elevated temperatures.
- Creep resistance - resistance of deformation at high temperature under certain stressing condition and when exposed to high stressing condition for fatigue.
- Low density - which allows the bulk of the ceramic to be light weight, in comparison to the metallic materials.
- Fracture toughness parameter (K_{1c}) - is low in comparison to metals/alloys. However, ceramics have a reasonable K_{1c} for the various applications that it is used for.
- Hardness and wear resistance - which makes the ceramics comprise of low friction co-efficient when under exposed to shearing stress (in contact with another component (metals in particular)).
- Electrical resistance - ideal for electrical insulation.
- Good chemical resistance – during its exposure to vigorous chemical environments.
- High melting temperature - ideal for high temperature applications.
- Brittle - in comparison with metallic materials due to its high hardness.
- Good thermal insulator - ideal for high temperature applications.
- Good electrical insulator - in comparison with metallic materials.
- Corrosion resistant - when exposed to water, oxygen and salt.

1.3 Rationale for the Use of Engineering Ceramics

Engineering ceramics offer wide range of mechanical and thermal properties such as high melting point; corrosion and wear; bending strength; hardness; heat resistance under extreme conditions; physical stability; chemical inertness; very good electrical conductivity combined with their suitability for mass production. These properties are typically superior to conventionally used metals, plastics and glass type materials. Ceramics are 60% lighter in comparison with conventional metals and alloys. A Si_3N_4 roller bearing for example would therefore, operate at much higher speeds and proves to be more efficient in comparison with the conventional bearings. Ceramic bearings for example are able to run dry and no lubrication is required. Hence, the use of engineering ceramics tends to make life easy for engineers to produce oil free engines and component systems.

1.4 Ceramic Manufacture

Utilization of ceramics to manufacture complex engineering parts with intricate shapes, size and geometry has become common in the recent years [44]. The conventional machining methods such as drilling, milling and diamond cutting can be used to process ceramics; however, it is time consuming and expensive due to excessive tool wear and processing times. Other method use powder processing, moulding and compaction [44, 45]. Typical method of ceramic processing is conducted in various stages that create a final engineering component from powder of raw materials. The powder is then mixed with additives and pressed to bond the material into a particular shape aided by high temperature furnaces to heat the ceramic so densification and strength are induced. The schematic in Figure 1.2 illustrates the conventional processing method of engineering ceramics.

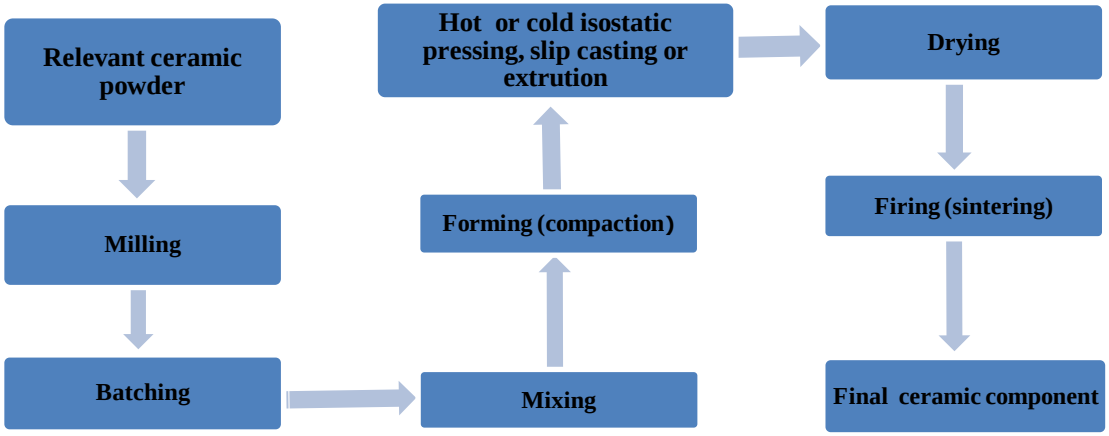

Figure 1.1 A schematic diagram showing the steps involved in processing engineering ceramics [46].

Loose earth-wares such as sand, stones, clay, concrete and granite are prepared and milled which involve crushing of the elements by mechanical means to form a partially dense ceramic powder. The crushed ceramic powder is then batched which means that the powder is weighed and is prepared for mixing of the additives and stabilizers to form the green body which is further mixed to forms the thick slurry of the ceramic. The ceramic slurry is then placed into a rubber mould and compacted at high pressure during CIPing [46]. Thereafter, the rubber mould is placed in a high pressure chamber for further compression by using the dry-bag isostatic pressing technique (see Section 1.3.3). The drying process involved removal of binders and or water by controlled heating. This is where the ceramic part gains a significant amount of brittleness. The next stage generally involves sintering the ceramic up to 1600°C which helps to increase its density to the maximum value that is close to the theoretical or the desired values. This also decreases the level of porosity and enhances the strength level of the component.

1.4.1 Reaction Bonding

Si_3N_4 ceramics are usually made by using this method and are classified as reaction bonded Si_3N_4 (RBSN). The reaction of the silicon powder with the nitrogen atmosphere starts at 1200°C. The

nitriding of the ceramic then occurs at 1450°C which takes around 150 to 200 hours. Nitrogen – hydrogen or nitrogen-hydrogen-helium, gas mixtures are used to enhance the strength of the ceramic and to give a faster and well controlled reaction. This process allows production of near to net shape components with complex profiles. The silicon has the tendency to expand to about 20% during the conversion to the nitride. However, there is a minimum change in the overall volume of the component which allows accurate shapes to be produced without undergoing an expensive and timely finishing process. Mechanical properties of RB Si_3N_4 (Young's modulus, hardness and strength) are therefore lower than that of the HP Si_3N_4 and S Si_3N_4 (sintered) [42, 43].

1.4.2 Hot Isostatic Pressing (HIP)

The hot isostatic pressing of a Si_3N_4 (HP Si_3N_4) is generally formed by placing the Si_3N_4 powder into a graphite die and pressed at elevated temperatures which assist in increasing the densification. Mixture of graphite is added as the system is held at external temperature of 2000°C with equal distribution of applied pressure (see Figure 1.3). The advantage of the process is that high density and high strength parts are produced. However, the process has a short die life with feasibility of producing only simple shaped billets. The components are also required to be ground after the hot pressing is conducted. This however, adds further expenses to the cost of manufacturing the component [42, 43].

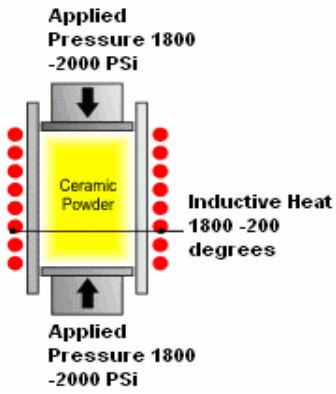

Figure 1.2 A schematic diagram of the compression of ceramic powder as reaction bonded and hot pressed in a pressurized chamber [42].

1.4.3 Cold Isostatic Pressing (CIP)

The mixture of ceramic powder containing the respective bonding agent is called the green body and is placed into a flexible polyurethane mould of certain shaped, size and according to the specification of the desired product or component part. The CIP is conducted at room temperature. The flexible mould containing the green body is then compressed at high pressure of up to 455 bar (6600 Psi, depending on product size shape and required densification), from all directions (see Figure 1.4). This is because compaction of the components of uniform shape and of high quality can be produced. Cold isostatic parts are generally made from two methods: wet-bag isostatic pressing and dry-bag isostatic pressing as mentioned previously. Components made from the wet-bag isostatic

pressing are immersed into a liquid (generally water or oil) which transmits uniform pressure to the green body. The dry-bag isostatic pressing rather contains the water or oil within the mould as opposed to the wet-bag isostatic pressing and is supplied (pumped) at high pressure by channel into the mould which provides assistance in transmitting uniform pressure to the green body. However, the dry-bag isostatic pressing is costly due to high tooling cost so wet-bag isostatic pressing is more frequently used [47].

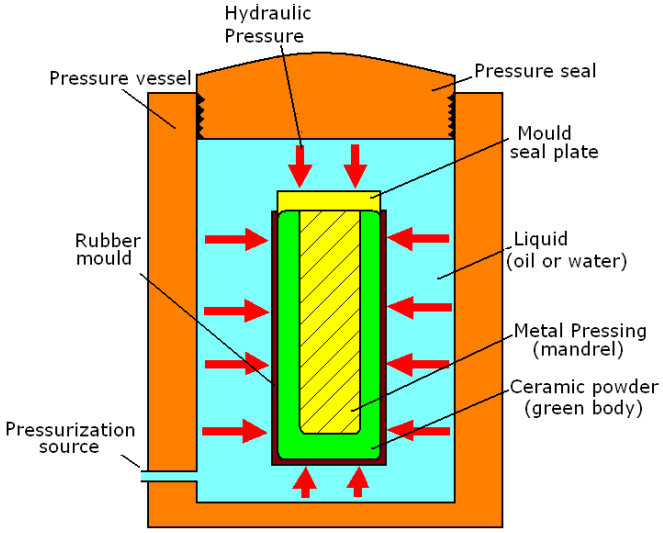

Figure 1.3 A schematic diagram of the CIP (wet-bag pressing) technique [47].

1.4.4 Sintered (Firing)

A sintered Si_3N_4 for example is made by compacting the Si_3N_4 powder which is heated to just under the melting point of the sintering additives. Diffusion and grain growth would occur with the sintering process and is presented in Figure 1.5 where the three stages of bonding occurs with increase of the temperature and bonding of the additives with the Si_3N_4 powder. The Si_3N_4 powder is combined with additives such as magnesium oxide (MgO) and yttrium oxide (Y_2O_3) combined with alumina oxide (Al_2O_3). These additives assist the liquid phase sintering process. However, protection must be given to the process to avoid evaporation of the Si_3N_4 powder and the additives. This is done by providing a high pressure gas atmosphere (1 to 7 MPa). The sintering process is conducted in a pool of Silicon powder at temperatures of up to 2070°C, for 5 hours in order to produce HP Si_3N_4. For demanding applications, hot pressed and sintered Si_3N_4 are used since the ceramic has stable high temperature mechanical and physical properties. The cost of the sintering process is also lower than reaction bonding or hot pressing. The sintering process is also used in powder metallurgy where many metals such as bronze, tungsten are also sintered.

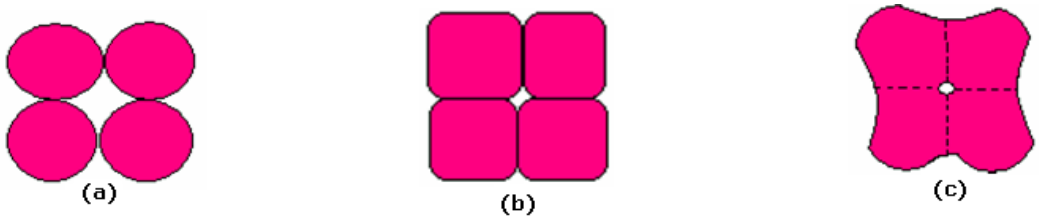

Figure 1.4 Bonding of the ceramic particles with increasing heat showing; (a) circular particles loosely in contact, (b) the shape changes as the temperature increases (heat brings the particles closer and forms a tighter bond) and (c) the gap between each particle vanishes and forms a rigid bond which is closely packed together.

1.5 Crystal Structures

Crystal structures with different ceramics vary as the processing conditions additives and raw materials differ. Figure 1.6 and Figure 1.7 presents an example of the three phases of the crystal structure for a Si_3N_4 ceramic. Direct contact between silicon and nitrogen at high temperatures form a solid substance which is known as Si_3N_4. Si_3N_4 is the main component in the Si_3N_4 ceramic as about 99% of the material is a commercial Si_3N_4. The material has three crystal structures which are designated α, β, and γ. The designated letters represent the phases of crystals known as α being tetragonal, β being hexagonal close packed and γ being cubic (c), which is a (modification to boron nitride, c-BN). The most common phases of Si_3N_4 are α and β (Figure 1.6) that can be formed in normal pressure conditions [47]. In order to produce γ-phase; synthesis under extreme pressure conditions must be carried out. The γ-phase has a spinal type structure illustrated in Figure 1.7, where the silicon atoms organise six nitrogen atoms octahedrally as well as one other silicon atom organising four nitrogen atoms tetrahedrally [47]. All three phases (α, β, γ) have hexagonal structures that are constructed by corner sharing Si_3N_4 tetrahedra. In sequence of "ABAB" or "ABCDABCD"; they are considered to obtain silicon and nitrogen atoms [47]. Si_3N_4 exhibits polymorphism, which means that it can exist as different crystal structures under different conditions such as temperature and pressure during processing.

ZrO_2 ceramic is usually added with magnesia, yttria or calcia for stabilization. However, the main crystal phases present within the ceramic are usually: monoclinic (M), tetragonal (T) and cubic (C) depending on the applied temperature and or pressure to the ceramic during its processing stage [37]. The three major phases available for a ZrO_2 ceramic which are usually transformed to C, (γ)-ZrO_2 at 2300°C above 1100°C to T, β-ZrO_2 and below 1100°C to M, α-ZrO_2 as further presented in Chapter 7 from the experimental TG-DSC analysis.

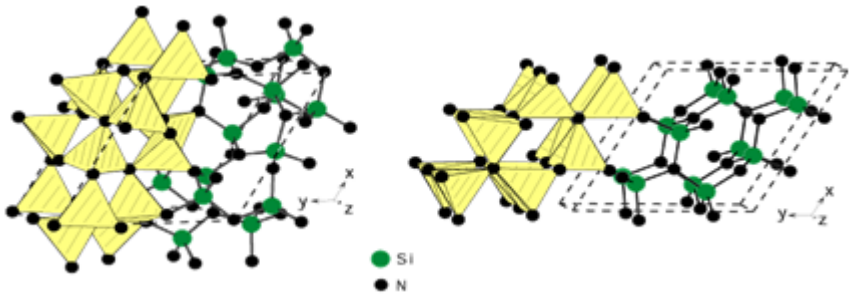

α – Si_3N_4 β - Si_3N_4

Figure 1.5 Crystal structures of triagonal α-Si_3N_4 and hexagonal β-Si_3N_4, emphasizing the corner-sharing Si_3N_4 tetrahedra [47].

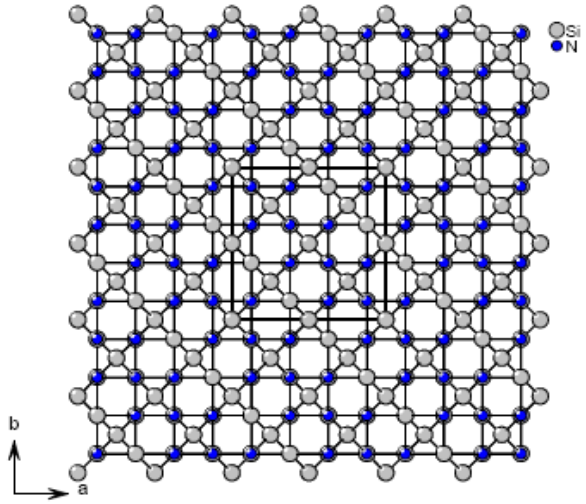

Figure 1.6 Spinal structure of γ (cubic) phase Si_3N_4 [47].

1.6 Selected Applications of Engineering Ceramics

Technical ceramics are widely used within the engineering sector, particularly for the most demanding and the environmentally prominent applications. This Section comprises of the main areas where ceramics are widely applicable (aerospace, automotive and the medical industry) as presented in Table 1.1. The reasons why they have been selected in particular are because of the advancing usage of the material within the various industrial sectors and for the future demands that the ceramics will have particularly in the aerospace and the bio-medical industry.

Table 1.1 Typical Application of ceramics in various industrial sectors.

Engineering Ceramics	Applications				
	Medical	**Industrial**	**Automotive**	**Aerospace**	**Military**
Al_2O_3	Cementing devices with the human bone "morphological fixation", bone implants,	Thread guides, electrical components (resistors, capacitors), armours, industrial magnets, grinding media, welding nozzles	Seals rings, bushings, cylinder liner valves, bearings	Gas turbine engine components (bearings, seals, valves).	Bullet proof vests
SiC	N/A	Abrasives, refectory, furnaces, cutting tool insert, wear plates	Heat exchangers, seals, valves	Heat exchangers, gas turbine combustion liners,	
ZrO_2	Thumb, hip, knee joint replacement, dental posts, brackets and inlays.	Power generation applications (fuel cells), electrical components (resistors, capacitors)	Combustion liners, bearings catalytic converters (honeycomb).	Transition sections in gas turbine engines, rotor blades and their coatings, nozzle guide vanes, bearing,	Knives
Si_3N_4	Bone Growth	Shields for defence industry, cutting tools, resistors, capacitors, industrial magnets, cutting tools, welding jigs fixture	Pistons, exhaust manifold, bushings, seals, turbo charger	Valves, bearings, turbine blades, rocket nozzles, rotors	Armour platings, bullet proof vests, body and vehicle armours
BN/BC	N/A	Nuclear reactors, radiation shields, armours, golf cleats and in other sports applications	Bearing liners, seals, gaskets	Nozzles	Unknown

1.6.1 Aerospace

Ceramics such as Si_3N_4 and SiC have a wide usage for both industrial and aerospace gas turbine engines (turbine blades in particular). For example a gas turbine engine maybe required to operate in freezing conditions from a cold start at ambient temperature (possibly less than $0^{\circ}C$) to instant temperature change of up to $1000^{\circ}C$. This would send a shock to the turbine parts that operate in the hot area of the engine. Therefore, the material of the turbine components requires strength; high temperature resistance; stability in combustible atmosphere; response to high frequency and vibration and a good response of thermal expansion as well as thermal conductivity. During these conditions, ceramics have the tendency to perform well in comparison with conventional metal alloys. Since 1975, turbine parts such as blades, nozzle guide vanes, jet engine igniters, and rotors have been made from Si_3N_4 and SiC ceramics [37] due to their adhering qualities such as high temperature strength, hardness and wear resistance and low density. Si_3N_4 is also applied in space applications to make radomes for missiles used for the air defence systems. It is chosen for this application because its mechanical strength and dielectric properties comply with the requirements of the application [49].

1.6.2 Automotive

Typical applications of ceramics in the automotive sector (particularly in the use of diesel engine parts) are pistons, exhaust valves, rocker arm, camshaft, cam lobe, head, port and cylinder liners, turbocharger and exhaust manifolds, seals, spark plug insulators, sensors, thermal barrier coatings, disk brakes in the sports cars [37-41] and more parts are replacing the conventional materials used. The use of ceramic components in the automotive diesel engine is now common and figures from a leading ceramic manufacturer (Ceradyne Ceramics Ltd.) [49 -50] illustrate over 2.5 million components being manufactured for the use of diesel engines during 1999-2001 [50]. Laser surface treatment can prove to be highly effect in improving the co-efficient of friction as well as induce compressive residual stresses within the surface and sub-surface of the component as upon success would lead engineering ceramics to operate for longer period of time. This would minimize the repair and/or replacement cost which in the end would reduce maintenance costs.

1.6.3 Biomedical Applications

For ease of physical movement and better quality of human life it is often required that many important body parts are to be replaced or repaired before a complete failure occurs. For such a need, certain qualities by the replaceable material have to comply. Those requirements are namely: high wear resistance; strength; low coefficient of friction; corrosion resistance along with a very good bio-compatibility. Ceramics such as Al_2O_3 and ZrO_2 have proven to comply with the specific mechanical needs for many biomedical applications [37, 47, 51]. Replaceable human body parts such as hip implants, teeth, knee and thumb joints can be replaced or repaired by using such ceramic materials (see Table 1.1 for further details). The areas where ceramics are applied within the medical industry

are: a) replacements and repairs, b) diagnosis and c) treatment and therapy [37]. Depending on the ceramics composition, there are some that are identical to human bones and are acceptable by the human body. Al_2O_3 and ZrO_2 do not operate in the same way. However, they are inert and have a limited effect to the defences of the human body [37].

The uses of Si_3N_4 ceramics have also been successfully tested for a potential bone growth application around its surface so that the Si_3N_4 serves as a bulk of the bone-ceramic implant [52]. The work of Guedes *et al.* [52] has shown that Si_3N_4 is a suitable material for biomedical applications such as artificial knee-joint, hip-balls, acetabulae and dental implants bone as bone growth can form around the Si_3N_4 ceramic which would then be able to transform into a functional implants. This was due to the ceramic being a non-cytotoxic material with sufficient fracture toughness, high wear resistance and low friction coefficient. In addition, laser surface treatment is highly beneficial for this type of application since creating a desirable surface topography by means of laser surface treatment would assist in increased formation of bone growth around the outer skin of the ceramic.

1.6.4 Military Application

Ceramics were introduced in the military sector since 1960 as the demands for better performance and superior materials had increased after the WW II [37]. Many applications in the military sector are now using engineering ceramics. This is due to their desirable physical properties such as high strength to weight ratio, ability to withstand high temperatures, high hardness and corrosion resistance. These are all necessary for making parts as used in the military sectors namely: armoured platings, bullet proof vests, armoured seats and as sharp weaponery [37]. Variety of ceramics such as ZrO_2, Si_3N_4, SiC, Al_2O_3, and B_4C ceramics are now being put to use and perform with better efficiency, endurance and protection in comparison to the conventional materials previously used [53]. Laser surface treatment can be somewhat useful for this application; upon success of achieving a high hardness by transformation toughness would in turn, increase the usage of engineering ceramics for making sharp weaponery with durability and longer functional life.

1.7 Summary

The uses of ceramic components within various engineering sectors are now common, particularly, where high performance, reliability and maintenance cost in the long run are important. This Chapter addresses the constraints and benefits of using engineering ceramics for selected applications. Justifications are given for the reasons why the conventional parts made from metallic materials fail and how the existing problems with such metallic components can be overcome by using the engineering ceramics. There are still concerns for the use of engineering ceramics. Those are the cost of the raw materials; processing techniques; timely processing methods; machineability (due to their high hardness, brittle nature) and expensive tooling costs. However, such aspects should not be taken

in account if high product performance, efficiency, reliability, endurance and longer functional life of the products in general are required. The following areas were reviewed in this Chapter:

- History of engineering ceramics and typical costs were briefly discussed;
- Physical properties of the engineering ceramics and the reasons why they are ideal for various applications were also presented;
- Reasons for the use of engineering ceramics for selected applications was also discussed;
- Various manufacturing methods used to process the engineering ceramics has also been covered;
- Applications within the automotive, aerospace, military and biomedical sectors were addressed.

CHAPTER 2
Background of Industrial Lasers

This Chapter introduces the typical industrial laser systems that are used within laser aided material processing. Application of laser systems in material processing and are presented along with reasons for implementations. Technical aspects are mentioned along with laser beam characteristics and optics issues as well as some of the major laser parameters that are used for the experimentation are also described.

2.1 Introduction to Lasers

The term LASER is a definition for Light Amplification by Stimulated Emission of Radiation. A laser is a highly concentrated source of coherent light which provides a high input of energy into a small dimensional surface area [54-61]. Laser light is differentiated by three important features from a conventional light.

Monochromatic - this light can be focused at a discrete wavelength. The beam is one colour and one wavelength unlike the conventional ray of light which is incoherent radiated in all directions and contains different wavelengths which cannot be focused to a discrete point [5].

Coherent - it is important for the laser beam to be of the same frequency and amplitude in a phase, in order to contain the level of concentration in material processing or communication [5].

Uni-directional - It is the parallel beam of light which has a minimum spread. It can be focused on to a small area to give high power density [5].

To generate a laser light, it is required that excitation energy by stimulated emission of a suitable medium is supplied. During stimulated emission, organized photons (coherent) are released which contain a discrete certain energy and a wavelength that is dependent on the energy difference between excited state and the ground state. Excitation is usually generated with electrical discharge such as high voltage. The photons have certain energy and a phase. The emitted photon is in a phase with the one that collides with the excited atoms. When this photon encounters another atom, it tends to revert back to the ground state. However, in doing so, it will generate an identical photon. The properties of these two photons are uni-directional and coherent [5].

The two photons will collide with two exited atom and revert back to the ground state and in doing so will release further identical photons. This is the amplification stage. The photons are generated in the optical resonator and travel in the longitudinal and the transverse direction. There are two mirrors which are partially reflective inside the optical resonator. The photons which are travelling in the path of the mirror (longitudinal direction) pass through [5]. The premature laser beam is a result of the photons that pass through the partially reflective mirror also known as the “leaky mirror”. The

Nd:YAG laser uses xenon flash lamps for excitation and the CO_2 lasers use radio wave excitation. Within a laser system there are several parts which aid the generation of a laser beam. This is summed up in Figure 2.1 which represents the parts required to produce the laser beam.

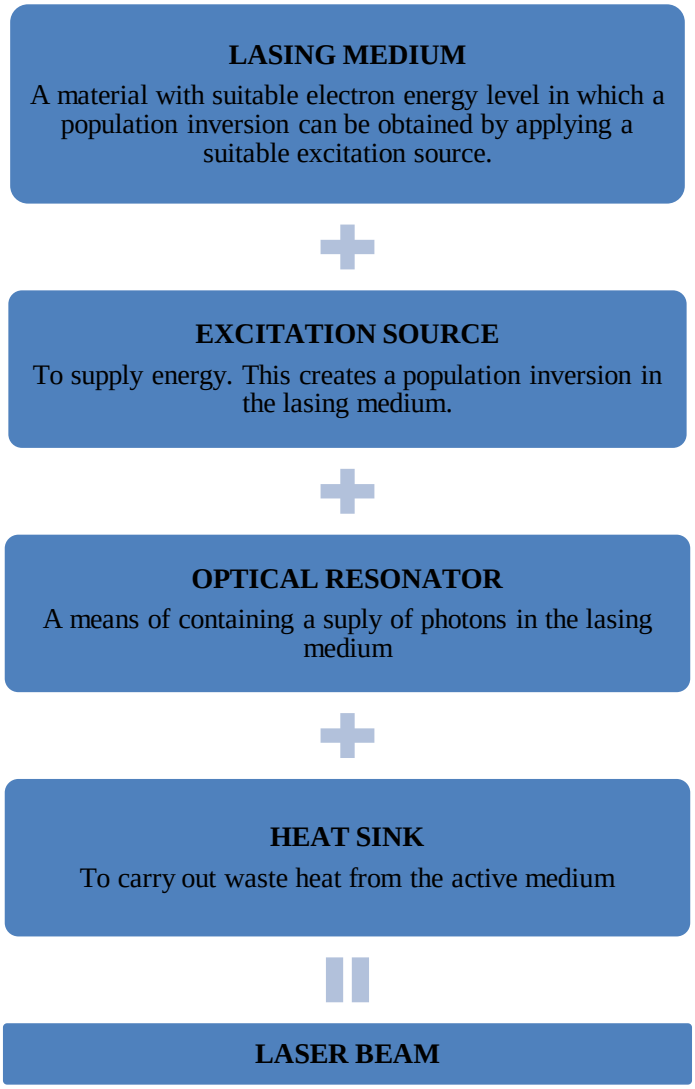

Figure 2.1 A schematic diagram demonstrating the stages in making of the laser beam [5].

2.2 Laser Classification

There are different classes of lasers which perform in the various industrial sectors. Lasers are classified according to their power outputs. Class 1 laser are used for CD players and measuring distances and bar code reader applications. Class 2 lasers are used for the medical application and class 3 A and often B are used for laser printers as well as light shows and entertainment systems. Table 2.1 presents the different types of lasers as applicable in the various industrial sectors.

Table 2.1 Classification of lasers with various applications in different industrial sectors [5].

Class & Description	Industrial Sectors	Application
CLASS 1 - SAFE	Entertainment	CD Players
	Surveying	Measuring distance and straightness
	Supermarkets	Bar Code Readers
CLASS 2 - LOW POWER(visible CW)	Medical	Medical lasers
CLASS 3A - LOW MEDIUM POWER LASERS **CLASS 3B**	Laser scanners	Laser Printers,
	Spectrometry, stereo lithography, & entertainment	Light Show & Entertainment
CLASS 3B** - MEDIUM POWER LASERS	Marking	Dates, stamps, barcodes scribing
	Paint Removal	Paint removal from motor vehicle bumpers.
	Pattern Marking	Pattern marking on plastic materials.
CLASS 4 - HIGH POWER LASERS	Cutting	Various steels, aluminium, zinc, copper, plastics, cast iron
	Welding	Various steels, Aluminium, copper, brass, plastics, cast iron
	Heat Treatment / Sintering	Change in materials property.

2.3 Engineering Applications of Industrial Lasers

2.3.1. Laser Machining

Demmer *et al.* [62] investigated the prospect of laser assisted machining, where the laser beam and a milling/turning tool was utilised to process ceramic parts (Si_3N_4 bearings in particular). Demmer *et al.* conducted experiments by using a 1 kw diode laser with a focal spot size of 9mm x 3mm rectangular beam. This was positioned at 90°C to the work-piece by using various sizes of the milling or turning cutters available. The concept behind the technique is to pre-heat the processing material prior to machining. This would avoid excessive tool wear during machining the ceramics and allow softening of the material so there is an increase in the material removal rate. Adverse effects such as loss of hardness due to softening of the material are avoided as the heated material is removed. Laser assisted machining of ceramics offer economical and efficient machining especially with difficult to machine parts [62]. The technology has already been implemented for industrial applications to process ceramic parts such as Si_3N_4 [62].

2.3.2. Laser Cutting

Laser cutting is the most popular and commonly used process from all laser material processing applications. Laser cutting is applied to many materials within and outside of the engineering sector. Table 2.2 illustrates the laser cutting applications with various materials as used within different engineering sectors [5]:

Table 2.2 Applications of industrial lasers in material processing.

	Industrial Sectors		
	Automotive	**Aerospace**	**Other Industry**
Materials and Applications	Cutting of steels for sun roofs	Hard Brittle ceramics Si_3N_4	Garment Cutting
	Ignition coils	Titanium Alloys used for air frame structures	Cutting of kevlar for armour plates
	Wipers (steel)	Aluminium alloys	Fibre glass
	Door locks (steels)	Aluminium honey comb	Various type of wood for the furniture industry
	Dash boards (polymers)	Boron Epoxy	Cutting of cigarette paper
	Auto roof liners (PVC)	Three dimensional profile cutting (robotically) of stainless steel	Many electronic application such as Printed Circuit boards (PCB's)

2.3.3 Laser Welding

Laser welding requires induction of lower power densities than laser cutting. In most cases, if the laser beam can cut a material, then it is most likely that it can weld. However, there are other issues involved such as the material's ability to melt flow and solidify. Application of laser welding is very popular in the motor vehicle industry to join steels (tailored blanks in particular) [6, 63]. Numerous parts are joined by using laser aided robotic systems. The schematic diagram in Figure 2.2 presents some parts of a car that are welded by using an industrial laser as illustrated in Figure 2.2. Laser welding is also utilised for other applications such as joining plastics by transmissive welding for packaging application as well as high speed laser welding for joining of spacer bars used in double glazed window separation [63, 64]. High speed welding also has a potential to be applicable in the can manufacturing industry to seam weld tin plated steel food cans as shown by Page *et al.* [63], Blundell *et al.* [64] and Shukla *et al.* [73].

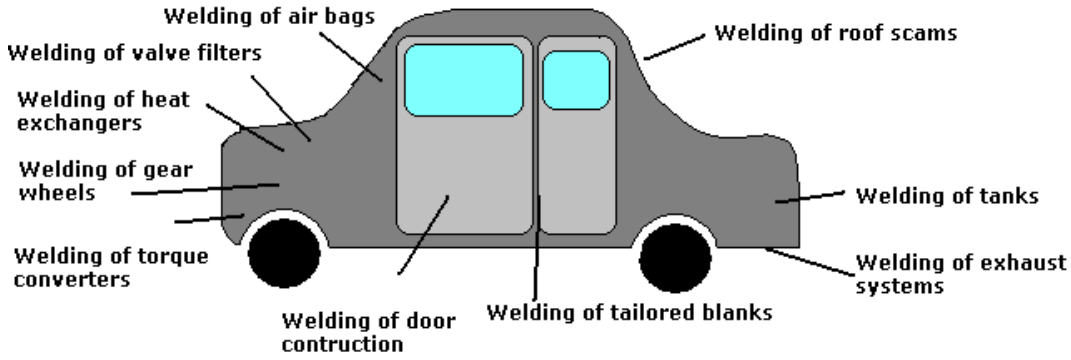

Figure 2.2 A schematic diagram showing the application of laser welding within a motor vehicle [5].

2.3.4 Laser Drilling

There are two ways in which a hole can be drilled with a laser beam. First, is by running the laser around the edge of the profile of the hole to be cut (specifically large holes). The second is by drilling small holes by using a pulsed laser beam, assisted by a high pressured gas to blast out a desired hole or a circular area. This is ideal for smaller diameter holes in particular and is popular for processing coolant holes within gas turbine blades [65].

2.3.5 Laser Surface Treatment

Laser surface treatment of a material is conducted to induce and/or enhance certain material properties. A prime example of this process is laser peening of metallic materials such as gear teeth's, springs, valves and particularly where deep level of residual stress is required. This is a recent development in the area of laser surface treatment of engineering components. The process employs a Nd: YLF (Neodymium, aluminium, yttrium, lithium fluoride) laser and generates a pulsed beam into the material which produces a shock-wave (thermal expansion) through the surface. The laser pulse can be fired on the work-piece several times to induce compressive residual stress depending on the required depth of the stress as seen in Figure 2.3. The input of the compressive residual stress is as much as four times larger than that of the conventional mechanical shot peening technique [66-67]. The deep residual stresses induced into the material would assist in combating fatigue and corrosion failures. Component life and hardness of the material is enhanced in the same way as it would be with that of the conventional shot peening technique. However, the depth of the residual stresses with laser peening can be four times deeper than that of the mechanical shot peening technique [66-67].

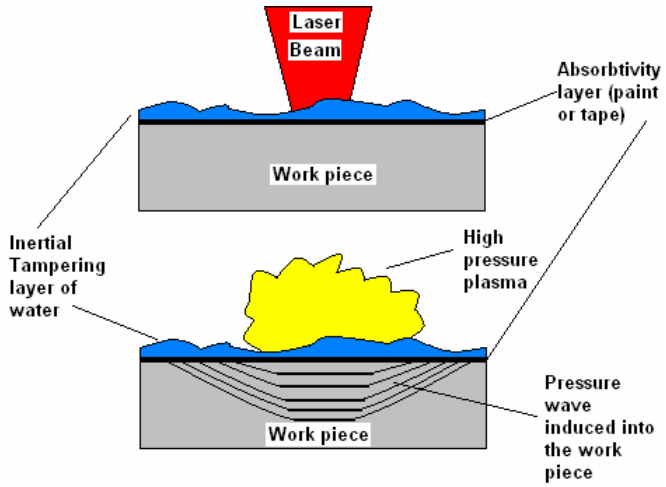

Figure 2.3 A schematic diagram to show the process of laser shock peening and the way in which residual stress is induced by the high pressure plasma [13].

2.3.6 Laser Marking

Laser marking is used for numerous application within the automotive; medical; product packaging and identifications; creation of pattern; logos; printing; labelling; making patterns on cloths and many other applications which required presentation of either information or for aesthetics. Laser marking is conducted on materials such as metals, polymers, wood, for logos bar codes and to present images or in-graving. Ceramics are usually scribed prior to cutting so the cutting depth becomes smaller after the laser scribing. Marking patterns on garments and cloths has also become popular with controlled laser parameters to ablate the surface at microscopic level and to produce a distinct pattern on garments such as denim jeans and T-shirts. Printed circuit boards are also laser marked with tracks prior to the assembly and soldering of components.

2.4 Rationale for the Use of Lasers

Lasers have now existed for over 50 years and have became one of the important tools within the manufacturing industry for cutting; drilling; welding; marking; machining; surface treatment and many other useful applications that aid and suit the manufacturing of engineering component. The following points address why laser systems are much superior over other systems and processes [6, 13]:

- Deep penetrating treatment in comparison with other processes;
- Shorter process time which in turn gives faster throughputs and just in time (JIT) delivery;
- High speeds and accuracy in processing intricate components and shapes;
- Good dynamic response along with superior motion systems and freedom of movement which enhances the programming capabilities of processing complex shapes and geometries;
- Aesthetically pleasing cuts, welds and marking of products;
- Improvement with surface roughness;
- No tool change required;

- Feasibility of cooling the work-piece, which is not always available with many other machinery and systems.

These features in comparison with conventional processing systems are much more attractive and desirable to invest in for many manufacturers' by tailoring the laser systems to suite their unique application and product specification.

2.5 CO_2 Lasers

The carbon dioxide (CO_2) lasers produce a beam in the far IR region of 10.6 µm wavelength. High laser power within the rages of kW's can be focussed to a spot size of approximately 0.10 to 0.6mm in diameter. The beam is most likely accompanied by an in process assist gas and would be coaxially fed. A high electrical voltage discharge excites the lasing medium as shown in Figure 2.4. This enables the photon amplification mechanism to generate the stored optical energy that is steadily released *via* the output mirror. Cavity walls absorbed the heat generated by off axis photons which are cooled by continuous flow of liquid coolant that is itself cooled in a heat exchanger otherwise known as a chiller [69].

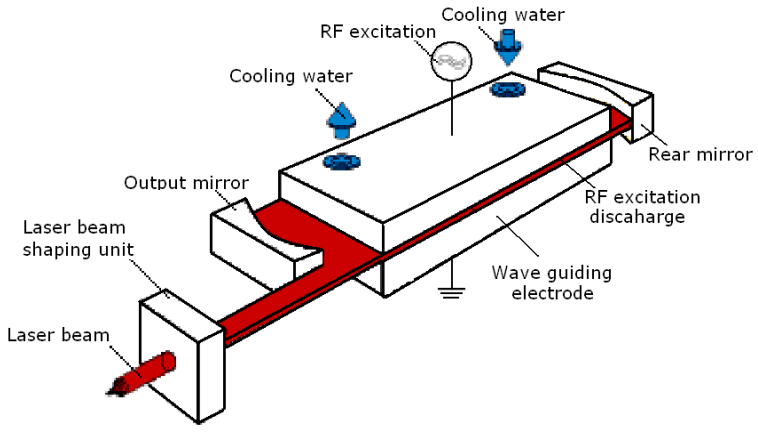

Figure 2.4 CO_2 laser beam generation unit [69].

2.6 Excimer Lasers

The excimer laser has a repetitively pulsed beam and operates in the ultraviolet range. This means that the wavelength of the excimer laser is shorter than the wavelength of a natural light. The energy produced by the excimer laser is well absorbed by various materials (polymers in particular) and is ideally used for less severe processing applications rather than cutting or melting of materials. The energy produced by this type of laser removes a fine layer of the treated surface avoiding major surface heating and burning which rather results to localized surface modification as opposed to the surface melting and material removal. This makes it ideal for surface treatment and modification applications especially within the medical industry for refractive eye surgery [56, 70]. Excimer lasers have a minimum beam size of 0.25µm and are capable of drilling fine holes in a human hair. Its input power range is between 10 A to 370 V, generating over 100 W at the material surface by high

and low powered systems. Figure 2.5 illustrates the basic construction of an excimer laser [5]. The excitation occurs by flooding the cavity with ultraviolet light generated by spark discharge of electrons. Together with the high photon energy of the ultraviolet light capable of producing high peak powers densities to generate the excimer laser beam.

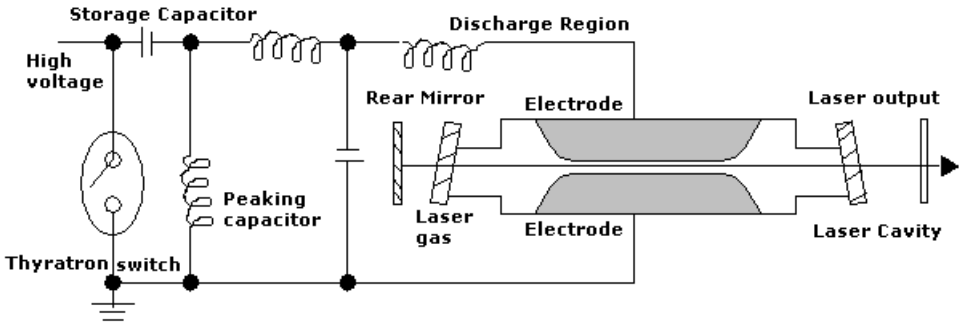

Figure 2.5 Construction of an excimer laser [5].

2.7 Fibre Lasers

The fibre laser is delivered by a fibre cable of a very fine diameter. This would allow minimum use of complex optics and produces a stable beam. The fibre laser can operate in CW or pulse mode. The operating wavelength of a fibre laser is 1.075 µm with a Gaussian beam profile of TEM_{00}. The quality of a modern fibre laser is high. The fibre laser also has a high brightness laser-beam. Hence, it would produce higher power per unit area, which in turn, would produces low cost per wattage as mentioned previously in the introduction. The fibre laser beam is produced in the laser medium and is delivered through a fibre optics cable. The excitation occurs in the doped fibre cable which is the cavity as illustrated in Figure 2.6. The "Brag Gratings" are attached at the two ends of the fibre to enhance the efficiency. The diode pump helps the population inversion by using Erbium atoms within the cavity. Power density of the fibre laser ranges from 1 W to 1 kW which allows them to be applicable for intense applications such as drilling, cutting and welding to less demanding applications (in relation to laser power output) such as marking, and macro-machining [71].

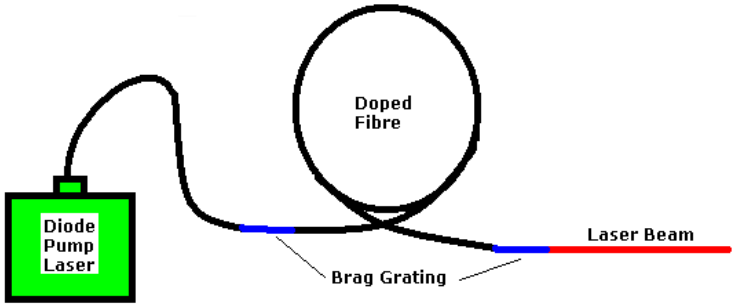

Figure 2.6 A schematic diagram of a fibre laser system.

2.8 Nd:YAG Lasers

A Nd:YAG laser comprises of a crystal rod which produces the lasing medium. The crystal rod is composed of a neodymium, yttrium aluminium garnet. Nd:YAG laser is pumped by using a flash

lamp to generate the laser beam. The emitting wavelength of the Nd:YAG laser is 1.064 µm in the IR region. The operating mode of the laser can be in the pulsed or a CW mode. The pulsed laser operates with a Q switch which is an inserted switch in the laser cavity and opens when there is a maximum population of inversion in the neodymium ions. The light then travels through the cavity, depopulating the excited laser medium at maximum population inversion. Power of 20 mW, at a pulsed duration of 10 ns is achieved. The output to a CW beam is lower than that of the pulsed beam which can be distinguished as it changes colour from a pulse mode pink or purple to almost white light mode. The excitation is created by a flash-lamp or laser diode molecules which are arranged around the Nd:YAG rod as shown in the diagram below. The resonator located co-axially to the rod contains high reflective mirrors as well as partially reflective output coupler. Figure 2.7 illustrates a simple diagram of a Nd:YAG laser beam delivery systems and arrangement.

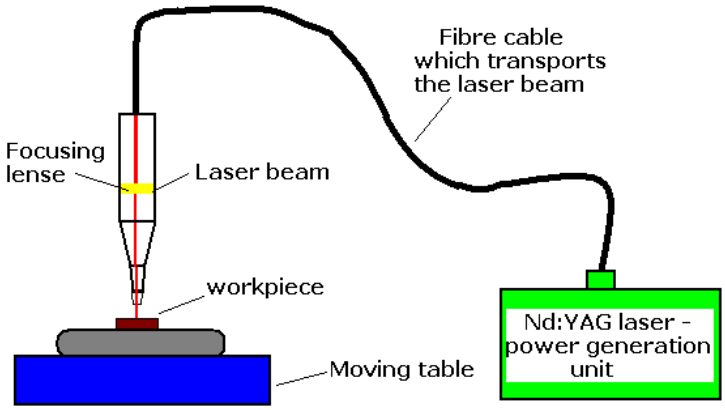

Figure 2.7 A schematic diagram showing the beam delivery of a Nd:YAG laser.

2.9 Laser beam Characteristics

2.9.1 Wavelengths

The laser beam is either absorbed, reflected or transmitted during the laser-material interface. If there is reflection, then there is no change made to the surface of the work-piece. If it is absorbed into the material, then the material will be heated, allowing cutting, welding or surface treatment to take place depending on the applied laser parameters. Various materials absorb different wavelengths better than other materials. For example aluminium has a reflectivity of 95% of the laser light at room temperatures. However, if it is heated to 700^{o}C it will absorb up to 70% of the laser light. Non-metals such as polymers absorb CO_2 laser wavelengths better than the Nd:YAG wavelength. So which type of laser to use, is dependent on the processing material. Table 2.3 shows the wavelengths of various types of lasers with different wavelengths. The highlighted area in represents the lasers wavelength utilised for this research.

Table 2.3 Wavelengths for different types of lasers [5].

Laser Type	Wavelength (μm)
Carbon dioxide (MIR)	10.60
Nd: YAG (NIR)	1.064
Fibre (NIR)	1.075
Excimer	0.249
Ruby ($CrAlO_3$) (red)	0.694
Rhodamine 6G dye (tunable)	0.570 - 0. 650
Helium neon (red)	0.633
Helium neon (green)	0.543
Argon (green)	0.514
Argon (blue)	0.477
Nitrogen (UV)	0.337
Xenon chloride (UV)	0.307
Krypton fluoride (UV)	0.247
Argon fluoride (UV)	0.193

2.9.2 Beam Modes

Variation in the beam mode has a large influence on the material being processed. In recent years, it has been found that holographic resonators can be used to change the Gaussian beam profiles of various types of lasers [5]. The beam can be of many different variants of Gaussian configuration, which means that each type of beam has a unique end shape and profile. The power density (footprint) of each beam therefore varies. Hence, the interaction with the material will also differ as the beam mode changes and produces a change in the distribution of energy over the material. Figure 2.8 represents a profile of common beam modes [5].

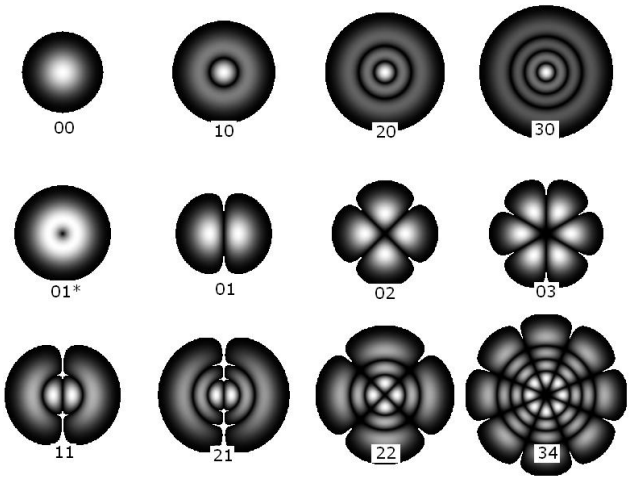

Figure 2.8 A schematic diagram showing the footprint of various Gaussian beam modes [5].

2.9.3 Beam Quality

The CO_2 laser has a highest quality beam profile (TEM_{00}). This type of beam contains a small spot size, highest power density, longer focal range and low divergence. Figure 2.9 shows the graphical profile of a high quality beam which has the maximum heat intensity being concentrated in the centre. For such a beam, the M^2 quality factor is usually close to M^2=1. The beam quality factor increase with decreasing beam quality for lower order Gaussian beam.

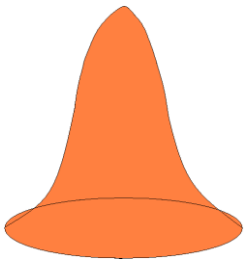

Figure 2.9 A schematic diagram of a Gaussian beam mode TEM_{00} for a CO_2 Laser.

Nd:YAG lasers have a medium quality beams in the region of TEM_{01}* (see Figure 2.10) which can be of a doughnut shape or a "top hat" beam which (often travels down a fibre optic) with larger spot size, wider width, which in turn, is ideal for thick metal cutting applications. Other poor quality beams have multimode larger spot size, wider width which is ideal for welding rather than cutting or drilling applications [69].

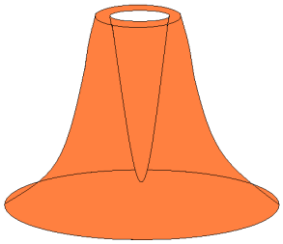

Figure 2.10 A schematic diagram of a Gaussian beam mode TEM_{01}* for the Nd: YAG laser generally known as "central null".

2.10 Laser Optics

2.10.1 Conventional Laser Optics

Conventional optics within a laser system would comprise of copper or gold coated mirrors and concave and/or convex lenses to focus or defocus the laser beam. The lenses come in various thicknesses and are replaceable after certain hours of processing or if there is a change in the processing material thickness.

2.10.2 Holographic Diffractive Optical Element (HDOE)

HDOE are computer generated holographic optical elements which replace the conventional lenses and congregate with the beam delivery system in order to control the shape, size and the end profile of the active laser beam [72]. HDOE could be made to transform into a "top hat" "ruby post" or a

"peaked edge line" as presented in Figure 2.11. The difference between a Gaussian beam and a HDOE beam is the controllability to a desired shape and still keeping the same area of the beam distribution. This is useful for surface processing ceramics as the energy distribution can be controlled to effect thermal shock that generally results during laser-ceramic interaction.

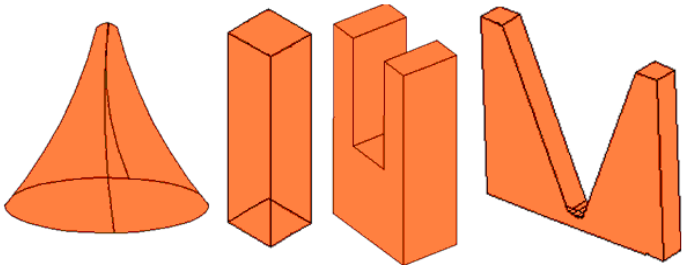

Figure 2.11 A schematic diagram of the distribution of various laser beam profiles (a) Gaussian beam, (b) "top hat", (c) "Rugby post" (DOE), (d) peak edge line (DOE) [72].

A diffractive optical element (DOE) is a small mirror which consists of thousands of 6µm squares that are set below the surface at various submicron depths [72]. As the raw beam of 20mm diameter is fired at the DOE, the mirrors execute a particular wave. The waves then combine and interfere with each other to generate a premeditated beam shape. HDOE are put to use by being mounted within the laser beam delivery system of a CO_2 laser (see Figure 2.12). HDOE offer advantages such as large focal depth in comparison with the conventional lenses. Hence, the working distance automatically becomes less critical. Conventional lenses require regular maintenance. This is not required with HDOE if it is well protected from fumes and dust. HDOE also reduces the amount of moving parts required such as galvanometers within the CO_2 laser systems as well as the flexibility to shape the beam. It is ideal for the surface treatment applications since it allows the motion system to traverse around the part at high speed, flexibility and a sufficient depth of penetration. The more surface area that is covered by the laser pulse would reduce the cost of the operation as the process time of the treatment is reduced. This is more beneficial especially when processing larger parts [72].

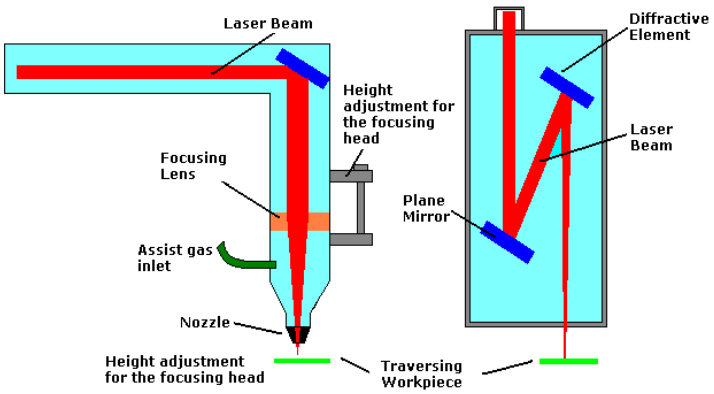

Figure 2.12 The beam delivery system for Gaussian beam in (a) and (b) the holographic diffractive optical elements [72].

2.11 Laser Parameters

2.11.1 Spot Diameter and Focal Position

The optimum focused spot size results to the maximum power density applied at the surface (see Figure 2.13). Focal position and spot sizes vary for every material being processed and are different for every process, such as welding - larger spot size is desired. For cutting, a fine spot size is desirable. For surface treatment, a larger spot size, which has a distribution of laser energy over large surface area, would be ideal. The focal position can be changed to vary the diameter of the beam. It is one of the major parameters of the laser material processing. Adjustment of focusing conditions enables a wide range of processes to be performed by changing the power density for a given application. In general, a raw laser beam is delivered from the lasing unit and it is focused into a smaller spot size by passing through a lens. This means that the operator can control the focal spot size by changing the focal length or focusing above or below the material. This in turn controls the effective power density. The diameter of the beam will change as the focal length is varied. If an application requires lower power density, then the focal position can be changed in the positive or the negative direction (above or into) the material. Figure 2.13 represents the variation in the spot diameter as the length of the beam is varied. The focal position at 0mm (optimum) contains the finest beam spot diameter; ± the optimum beam diameter of the focal length would produce the same spot diameter of the beam.

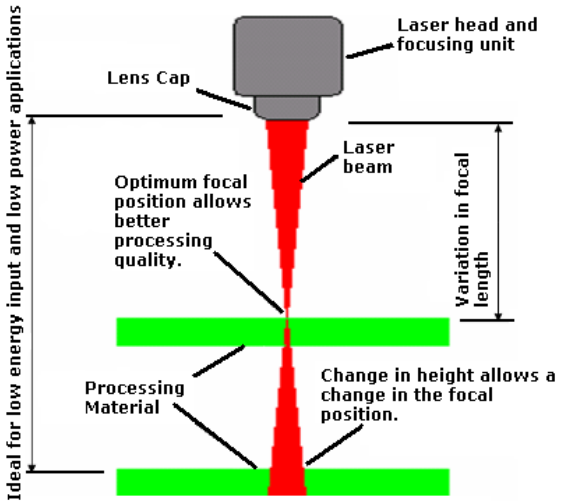

Figure 2.13 A schematic diagram showing the change in the spot diameter as the focal length is adjusted.

2.11.2 Assist Gases

Assist gases also have a very important role to play in laser material processing as it controls factors such as material removal, input temperature, generation of the plasma plume and the effective change in the composition. It is usually required that shield gases are used in order to protect the material in the region of the laser processing zone from a atmospheric contamination such as oxidation [13]. Often ionised vapour in the form of plasma (high temperature ionised gas) is generated from the material at high incident power. The plasma plume is likely to induce ionisation in the shielding gas creating a cloud of plasma in the path of the laser beam [63, 64]. Gases such as helium have a higher ionisation potentials compared to other gases such as argon and nitrogen. Hence they are more resistant to plasma formation. Argon, helium and nitrogen are used when it is required to cool the processing material or the system components. Argon tends to be the most common shield gas, since it's overall cost and suitability towards material processing is appropriate. However, helium tends to be used when high quality processing is required. In other cases, a mixture of helium with argon may be used [5]. Figure 2.14 shows an auxiliary (side gas) supply used to dissipate the plasma cloud from the laser-material interaction zone. The mixed plasma cloud can serve to effectively block part of the incident laser beam. The incident laser photons can be absorbed or scattered by this plasma, depending on the conditions. Nd:YAG laser wavelength is less absorbed by metal and gas plasmas than the CO_2 laser. Therefore, a side gas is more often used on CO_2 lasers than the Nd:YAG lasers.

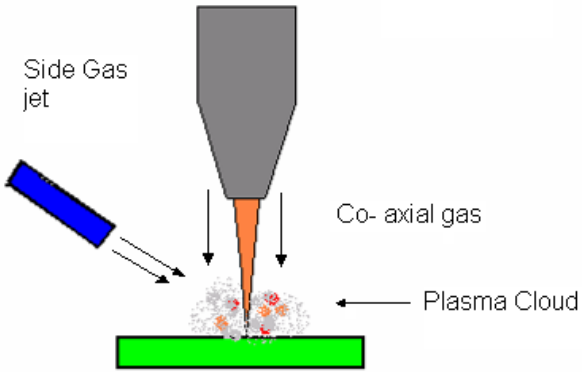

Figure 2.14 A schematic diagram of the coaxial gas with generation of a plasma plume.

2.11.3 Laser Power

Laser power is the most common parameter and has the tendency to influence the major events that take place during the laser-material interaction. Laser power is controlled by either increasing the input laser power function within a laser system or by defocusing the laser beam. High power densities are required with cutting and sufficient power density is required for welding. For example, defocusing the laser beam is useful for a butt weld application so that the power density is spread across both plates to ensure uniform melting. The power output could be either CW or pulse as mentioned previously. There could also be an increase in the power density from the nominal CW if the laser is pulsed. However, this can only be performed for a certain period of time. For example CW, 2 kW, Nd:YAG laser can be pulsed to 5 kW within a limited range of frequencies and duty cycle [62]. The major parameters for the output beam are pulsing frequency (cycles per second), maximum pulse intensity and duty cycle. The reason why these parameters are important is because they control the input of energy into the material which inherently affects the depth of penetration, porosity and crack initiation, particularly with the engineering ceramics.

2.11.4 Traverse Speed

Traverse speed is also known to be one of the important and most common parameters in laser material processing. Change in the traverse speed with a constant laser power and spot size applied would result to remarkable effects on the material. As well as the laser power, the traverse speed of the laser beam would also dictate the power density being induced within the material. This is because increasing the traverse speed at constant power would reduce the laser-material interface time and decreasing the traverse speed leads to increase in the time which the laser beam interacts with the material.

2.12 Pulse and Continuous (CW) Modes

Laser beam can be commonly delivered in two ways. Either by using the pulse or by using the CW mode. This is purely dependant on the laser system, processing material and the specific requirement of the processing component and or the material composition. Some lasers such as Nd:YAG (diode pump in particular) are best operated by using the pulsed mode. This is due to its construction and

beam delivery system as well as its operating wavelength. CO_2 laser systems function better by using the CW mode as it operates with a higher wavelength (10.6 µm) and a right angle delivery system by using (optics and mirror assembly). However, CO_2 lasers can be pulsed but are not efficient and effective in comparison with the naturally pulse operating lasers. The vice versa also applies to the Nd:YAG laser as it can operate in a CW mode. However, it is more efficient when it functions with the pulsed mode.

2.13 Motion system and Control

Motion could be created between the laser beam and the material by either moving the optics at a stationery work-piece or by moving the work-piece beneath a stationary laser beam. Optics can be moved by the aid of X-Y table or by using a multi-axis industrial robot where the laser beam can be transmitted through a fibre optics cable such as the Nd:YAG or a fibre laser system. Other systems consist of complete moving parts where the optics is moving along with the moving work-piece.

2.14 Summary

This Chapter has reviewed the laser systems and various aspects of laser-material processing namely:

- Laser beam delivery systems and how the laser beam is produced;
- Laser beam classification are differed with respect to their applications;
- Various laser-material processing methods are also reviewed such as laser machining; drilling; cutting; marking and surface treatment.
- Reasons for the uses of lasers processing are also stated;
- Beam characteristics, associated laser beam parameters, options in optics, as well as assist gases were also discussed.

Experiments conducted in this thesis will be based on the parameters discussed in this Chapter. Parameters mentioned in this Chapter were explored on the ZrO_2 and the Si_3N_4 engineering ceramics so a threshold can be found. This is further illustrated in Chapter 4.

CHAPTER 3
Laser Beam-Material Interaction with Reference to the Laser Processing of Ceramics

This Chapter focuses on the review of literature in relation with the interaction of the laser beams with predominantly ceramic based materials. Laser surface treatment of ceramics has slowly gained popularity but is still unknown in many areas such as laser welding in particular and ceramic-to-ceramic joining. Due to lack of understanding and feasibility has hindered its use for many applications as the physical effects of the process are not clearly understood. This Chapter summarizes the effects of the laser beam interface with ceramics not only during, but after the material interaction with respect to major processing techniques such as laser surface treatment, drilling, cutting, welding, machining. Also, attempt to address the gap in knowledge is further investigated in this research.

3.1 The Laser Beam-Engineering Ceramic-Interaction

Laser-material interaction is considered to be a very complex phenomenon because it involves multi-factors which control and significantly influence the effects which occur on the material being processed. Laser-material interaction was reported by Wang *et al.* [74] to comprise of a thermal, physics, dynamic and many other scientific aspects. Wang *et al*. stated that the factors influencing laser-material interaction are laser output energy, the composition of the material, the specimen thickness and temperature distributions. Interaction of the laser beam with metals in particular have been thoroughly investigated by many other authors; namely: Prat *et al.* [75, 76], Lim [77] and Illyefalvi [77], who discussed the issues of diffusion in material transport caused by laser processing of thin films. Issue of laser coupling with materials, effects of plasma with increasing intensity [75, 79], formation of a shock wave and impulse are also addressed [76]. Materials such as C5790 graphite and aluminium alloy AU4G were used for the experimentation [75, 76]. One of the major dependencies of the outcome of the laser material interaction is the particular material being processed. Laser beam interaction with metals would produce a different effect to that of the ceramics due to the difference in their structure. Metals absorb the thermal energy better than materials such as ceramics and the thermals shock results in placing the material under compressive stress as the heat attempts to escape. This does not occur with ceramics as the thermal shock induced would expand the porous surface and provoke the microcracks and porosity to expand which in the end causes failures.

Wong *et al.* [70] examined the excimer laser interaction with a partially stabilized ZrO_2 (PSZ) and suggested that lasers with shorter wavelength than 307 nm are ideal to produce the desired chemical reaction and material removal. The results showed severe surface melting and the formation of columnar structures. This was dependent on the amount of laser fluence and was influenced by the direction of the plasma plume expansion. In this case, the plasma plume expanded away from the normal and led to formation of short columinar structure.

Work of Vlasova *et al.* [71] presented the effects of Nd:YAG laser interaction with a sheet of Silicon (upper layer) and Al_2O_3 (lower layer) which first demonstrated the composition of the ablated element exhibited from the laser-ceramic interaction. The ablated mixture comprised of silicon, oxygen and nitrogen. The Al_2O_3 layer also fractured after the laser material interaction, with evidence of oxidation occurring with the top layer of silicon. The interaction of Al_2O_3 with SiO_2 produced the simultaneous nitriding of the melt and decomposition of SIALONs with the formation of mullite and the ejection of mullite drops also occurred at the thickness off 270-1040 nm.

3.2 Laser Welding

Joining of ceramic-to-ceramic is an important aspect as it could produce more complex structures and also create opportunities for the ceramics to be used in areas where conventional materials would fail. This is particularly so for laser welding of ceramics but to this date; laser welding of ceramic-to-ceramic is not a fully developed area. This is because the mechanism of joining ceramic-to-ceramic by using a heat source is different to that of the metal. Metals have the tendency to melt and reflow with higher viscosity compared to the ceramics when exposed to the thermal energy whereas the ceramics are less viscous and do not melt and reflow easily compared to metals. Moreover, the thermal conductivity is low for the ceramics which means the dissipation of heat through the material is faster in comparison to metals which in turn would allow rapid cooling to take place (super cooling), after the event of instantaneous heating by the laser beam. This would minimize the chance of the ceramic to melt and re-flow. The effect of super cooling is also a contributor of the cracks which occur within the ceramic during the laser interaction. This is why laser assisted ceramic-to-ceramic joining has been proven to be successful by a very few workers [72-73]. Riviere *at al.* [72] presented a paper demonstraiting the technique of laser welding of ceramics. This was performed by pre-heating the SiO_2-Al_2O_3 by the Nd:YAG laser and then butt welding it by using the CO_2 laser. The results showed porosities within the microstructure of the weld bead, but higher bend strength was reported for the laser welded material as opposed to the parent material. Hirsch *et al.* [73] modelled a laser spot welding process by using a FEM and compared the data with an experimental model to show that both models were successful in predicting the depth and the diameter of the ceramic weld pool. Mikhailova *et al.* [74] employed a double-step method for welding two strips of Bi (2223) high temperature superconducting ceramics. This was by initially performing the laser melting and subsequent short-term thermal annealing technique. The results showed that fluid flow must be

considered in order to accurately model the molten pool characteristics of the ceramics, since the coupling of the fluid flow to heat flow is more important for ceramics than for metals. Melting of the laser irradiated zone was found, after cooling the reliable mechanical and electrical contact was also seen. The microstructure of the laser welded ceramic also differed as phase and chemical changes were found.

3.3 Surface Treatment

Surface treatments by using a laser beam can lead to remarkable effects such as the change in the materials property through induction of thermal energy into the substrate by means of a shock or a gentle treatment. Surface treatment can be conducted either by using a pulsed or CW laser beam. For the pulsed treatment, an intense laser beam can be focused to a small spot which is made to traverse over the material surface by creating a tailored thermal shock wave [6, 75, 76]. The thermal shock wave travels deep into the material and induces residual stresses which can be controlled to the requirement and only on the selected areas of the surface of the material. The local region being treated does not introduce any detrimental levels of heat into the bulk material [75, 76]. This process is called laser peening or "laser shock peening". Hackle *et al.* [75] and Steen [5] stated that laser peening technology offers a greater degree of process control. This allows much deeper level of compressive stress to be inhibited and it maintains the appropriate quality of the surface finish on metals. A pulsed beam of 25 J for 25 ns was produced by an Nd:YLF (neodymium, yttrium, lithium, flouride) [75]. The beam is focused onto the work-piece and the desired area to be peened is covered with material (black coloured adhesive tape) which acts as an ablative and thermal insulating layer. This is a good practice and would be ideal to use for experiments in this work as the black colour is generally absorbent to the heat produced by the laser beam. Water was made to flow over the layer to absorb the laser pulse energy and thermal shocks. Gathering of plasma within the water produces pressure that creates the shock waves and immediately penetrate into the surface of the metal and plastically strains the surface. The plastic strain then induces compressive residual stresses into the material at depth of 1 to 7 mm depending on the power density of the focused beam and other system parameters [75]. The benefit of laser peening has only showed with metal alloys. It is feasible to induce deep residual stresses into a ceramic surface but the same effect has only been successful by the work of Kazuma *et al.* [77] who demonstrated plastic strain into the surface layer of a Si_3N_4 ceramic by inducing a compressive residual stress layer on the surface. The residual stress in compression was said to have become larger with increasing peak power density of the irradiated laser pulses. Up to 100 µm of residual compressive stress was introduced particularly in the centre of the laser induced shot. A four-point bending test results also showed an increase of the bending strength and Weibull modulus by laser peening. The reason for the lack of interest by researchers in this area is due to the fact that ceramics are brittle. By firing a pulse of laser at a material is equivalent to throwing a sharp hot rod at the material surface. This increases the potential for the

material to crack as it is already brittle and has a porous structure [77]. Metals in comparison are much ductile and comprise of higher fracture strength and ductility. Hence, the energy of the laser shock does not lead to formation of severe cracking. Metal improvement company Ltd. [67] stated that laser peening of ceramics has not been performed due to lack of industrial demand. If there was a demand for such applications which require laser peening then it would be surely considered for research.

Lawrence and Li conducted an experimental investigation for the differences between beam interaction characteristics of SiO_2/Al_2O_3 ceramic by employing a CW CO_2, Nd: YAG, Excimer and HPDL [16, 22]. Laser absorption, fluence threshold, thermal loading and the beam interaction at the melt-pool was investigated by using the Beer - Lambert's Law [77] and Stefan solution [79, 90]. Absorption length, thermal loading and melt-pool characteristics were determined by using the values from the experimental work presented by Lawrence and Li [91]. It was concluded that an evidence of re-solidification was found on the SiO_2/Al_2O_3 ceramics when applying the CO_2, Nd: YAG, and HPDL's. The ceramic had undergone some melting but not much influence of the excimer laser was found on the SiO_2/Al_2O_3. This was because of the lower wavelength of the excimer laser. Excimer laser was said to have no effect to the melting of the SiO_2/Al_2O_3 ceramic [91].

Furthermore, Lawrence and Hao [92] used ceramics for biomedical applications which involved improvement of surface properties of ceramics by using industrial lasers on the Al_2O_3 and ZrO_2 ceramics. Other work by Lawrence and Li showed improvement in the surface properties of the same ceramics [93]. A 60 W high powered diode laser was used to investigate the adhesion characteristics of Al_2O_3, SiO_2-TiO_2, clay tiles and other ceramic tiles. The main property investigated was the contact angle which was proven to be enhanced. The laser beam was fired with adding four types of different liquids to the ceramic for wetting the material surface. Those were human blood, human blood plasma, glycerol and 4-Octanol. The results showed that due to the improvement in the material surface roughness the contact angle was reduced which resulted in the material exhibiting better adhesion characteristics. Evidence of some oxidation was found and formation of glass element was also seen. This indicated that the composition of the ceramic was changed. Hence, it resulted into the material comprising of better adhesion characteristics [93]. It can be gathered from reviewing the literature that the experimentation for this work can be conducted by using inert gas to protect the ceramic material from oxidation and exposure to the ambient atmosphere. However, on the other hand it may be desirable to oxidise the material and attempt to change its composition in order to gain any benefits. In particular, fracture toughness parameter K_{1c}, as the work in [13] demonstrated some enhancement with the fracture property of Si_3N_4.

Sun *et al.* [14, 15] investigated the effects of CO_2 laser surface processing on the Si_3N_4 and eliminated imperfections within the ceramic by applying a CO_2 laser beam. The researchers found

that the fracture behaviour was considerably affected by surface treating of the Si_3N_4 by means of using the CO_2 laser. Fracture origins from the machining process and bending strength were improved. A four point bending test, fractographic analysis and SEM micrographs were used to analyse the materials surface integrity. Sun *et al.* used a CO_2 laser to minimise the detrimental effects caused by grinding as the heat from the sliding motion created friction. Laser surface treatment was done after severe grinding of the ceramic in order to remove the mechanically induced cracks. Both high and low powered CW CO_2 lasers were used to treat the Si_3N_4 surface. It was found that the condition of grinding has a big influence on the fracture strength of the Si_3N_4. Longitudinal direction grinding in comparison with transverse directional grinding demonstrated much more resistance to fracture [14, 15]. The laser used in the work of Sun *et al.* was a square shaped beam. This type of beam usually has a "top hat" end profile which means that the power distribution during its focus would be uniform. But this was not clearly defined Sun *et al.* since the CO_2 laser beams are conventionally of TEM_{00} Gaussian beam mode. The Gaussian configuration of TEM_{00} (comprised of a ring shaped end profile laser beam). So the distribution of power for this type of beam would not be uniform throughout its surface area and this is desirable in order to obtain a uniform effect on the surface during the treatment. Results from the fractographic analysis showed that there were two types of cracks found. Machine induced cracks and inherent flaws from the material (porosity). This should, however, be the case with Si_3N_4 due to its characteristic and material structure. The depth of the machining cracks was between 25 to 50 µm. Sun *et al*. also stated that due to the viscous flow of the glassy phase, the surface region of the material has undergone reorganization and relaxation during the CO_2 laser processing. Compressive stresses were induced, as residual strain from machining process was released by the CO_2 laser processing. With longer laser processing time and higher power density, more relaxation of residual strain occurred. The important factor was the difference between the residual stresses in the treated samples to the samples which were untreated (as-machined). The difference was found within the material's surface morphology, microstructure and uniformity which were not further mentioned in any detail [14]. It was assumed that the surface integrity was changed and improved by the secondary glassy phase (YSiA1ON), which underwent a reflowing and rebinding process [14, 15]. This was because the temperature during the CO_2 laser processing was measured to be higher than the stable equilibrium upper temperature of the secondary glassy phase. It was found that softening (possibly melting) of the secondary glassy phase caused infiltration in the surface defects. As the laser power density increased, the ability of the secondary glassy phase to rebind and flow.

Morita *et al.* [20] worked with Si_3N_4 to produce a crack-free surface by using a Nd:YAG pulsed laser processing of ceramics. The increase in peak output power caused the crack propagation and generation of a thick re-cast layer. The peak power was said to be kept low as possible and the pulse duration to be as short as possible for a crack-free processing of ceramics [20]. This also allows

reduction in the thermal stress induced and into the material which justifies the elimination of crack generation during the process. The strength of the laser treated samples was also compared with the strength of ground polished surface by a diamond wheel [20]. The strength of the laser treated samples was reported to be 10 to 20% reduced in comparison with the diamond polished sample due to the residual compressive stress layer being removed by the laser process [20].

3.4 Laser Drilling

Laser drilling of the ceramics has recently developed over the last few years. A feasibility study by Coherent group of lasers Ltd. [94], have shown some success with processing Al_2O_3 and PSZ. However, only 30 to 45% penetration was found with laser treated samples [94]. Murray *et al.* [34, 35] prior to that compared the laser drilling and cutting of ceramic substrates by using a Nd:YAG and a CO_2 laser to process PSZ. A 7.3mm thick sample was used to drill 679µm diameter hole. The test material was heated prior to and after the laser processing and resulted in reduction of microcracks. The cooling process was carried out at 10°C per min. The optimum parameter window for the drilling process was found to be 200Hz, a pulse length of 0.6ms at 3.2 J and a drilling time of 0.75s was achieved. A full penetration cut was also achieved at a speed of 100 mm/min with 170Hz with a pulse length of 0.4ms at 4J. The drilling and cutting process was conducted at ambient temperatures, 1000°C, 1300°C and 1600°C. A co-axial assist gas caused the material to fail beyond 1600°C. Laser drilling caused less damage at the entry region of the hole and was much higher than the damage at the exit due to the effect of the oxygen assist gas [34, 35]. The CO_2 laser parameters were 300Hz, 200W of laser power operating with an oxygen assist gas at 2.5 bar producing a drilled hole less than 1s. Microcracks were also found when employing the CO_2 laser and produced two times the size of microcracking in comparison with the Nd:YAG laser. This was reported due to the higher wavelength operating with the CO_2 laser causing less absorption efficiency and photon energy decreasing with higher wavelength. Due to these two aspects, it was reported that the melting ejection was difficult to obtain. This led to a built up of excessive heat due to high thermal shear during the laser-material interaction stage [34, 35]. Further work by Murray *et al.* [36] showed that at 1100°C to 1300°C a change in the microstructure of the PSZ could have led to a phase transformation from tetragonal (T) to monoclinic (M) phase. At 2300°C the T-phase of the ZrO_2 changes to cubic (C) due to the material having a transition temperature around 2300°C. Due to this change in the microstructure; the materials emissivity is also increased. This improves the coupling of the Nd:YAG laser irradiation, leading to and increasing in temperature and improves the material penetration, especially during the laser drilling process [36].

3.5 Laser Cutting

Laser cutting is the most common process from all the laser assisted processing techniques. Various materials (metal in particular) are conventionally cut by using different laser systems. Earlier

research reported by Naeem *et al.* [26] and Tonshoff *et al*. [23] have conducted experimental work on cutting of ceramics such as Al_2O_3, ZrO_2 and Si_3N_4 and have shown promising results. The authors in [26] state that from observing the laser material interaction, it was found that thicker materials have the tendency to crack sooner in comparison with thin samples (particularly with Al_2O_3). This was said to have occurred due to the material comprising poor thermal shock resistance. Both authors, however, did not produce a complete cutting profile, free from any kind of microcracks or surface flaw resulting from the thermal shock. Trials were conducted by various passes of cuts which produced a final cut profile [26]. The first cut produced a groove into the materials surface, the second cut induced further depth to form a groove and the final cut produced a fully cut profile. This approach can be used for surface treatment also by using lighter power densities and repetitive treatment in intervals which would avoid excessive thermal shocking and build up of heat for the investigations in this research.

Lingfei *et al.* [25] conducted an experimental investigation on laser cutting of ceramics by using a combination of CO_2 and a Nd:YAG laser. The Nd:YAG laser was used to scribe a groove-crack followed by a defocused CO_2 laser which was applied to drive a crack. Al_2O_3 ceramics with the thickness of 1, 4, 6 and 10mm were used for the experiments. It was stated in the literature that laser cutting produced a thermal shock which damages the material to some degree [25]. The thermal shock is produced from the high heat energy generated for the cutting process. Cracking is a common problem with ceramics during any laser processing especially with thin material substrates. However, it was reported by Lingfei *et al.* that a crack-free surface was obtained for curved and linear cutting paths [25]. It was found that 1mm sample of Al_2O_3 ceramic was cut. The parameters used for this process were 700 W, at 2 bar gas pressure by using nitrogen. As the material thickness increased, the surface finish also became rougher (4mm = Ra 5.39, 6 mm = Ra 17.71 and 10 mm = Ra 31.74 µm).

Lei and Lijun [24] worked with Si_3N_4 ceramics and a Q switched CO_2 pulsed laser to produce a crack-free cut surface. The process was similar to the research conducted by Naeem *et al.* [26] as multi passes of the beam were made on the same cut area in order to produce a cutting profile. The experimental results illustrated that as the cutting speed increased. At the same time the length of the cracks decreased. This was because the input of the thermal energy decreased with increasing speed. Hence, the reduction in the crack lengths had appeared. Lei and Lijun *et al.* reported that, a crack-free surface was found as the cutting speed exceeds 220 mm/s with the diameter of the spot size being 100 µm [24]. These parameters can be used for experimentation for this research for the initial experimental study. However, the input of the laser power must be less for a surface treatment in comparison to the laser cutting process.

Voisey *et al.* [27] worked with laser processing of ceramics which involved cutting, drilling, macro-machining as well as surface treatment. Voisey *et al.* found that laser surface treatment of ceramics have several benefits over a conventional process, those are namely:

- Sealing of porosity which occurs due to the laser surface melting;
- Hence, the microcracks are improved which also enhances the corrosion resistance;
- Improvement with the mechanical performance resulting from minimising the pre-existing surface flaws;
- Tribological properties and surface roughness are also improved;
- The aerodynamics of components is also increased specifically with the ceramic coated turbine blades components when the surface roughness was improved;

Moreover, Voisey *et al.* also found that thermal stress induced into the material during the laser process has the tendency to generate cracks [27]. The crack generation can be avoided or reduced by applying two beam techniques which eliminates the cracks created during the first stage of the laser beam. This can be done by adding ceramic powder and heat to the re-melted surface during the second beam interaction. Voisey *et al.* also mentions that processing with an excimer laser produced smaller melt depths and showed improvements in the surface roughness of a SiC [27, 29]. Smaller melt depth indicates that there is less amount of material removal. This is more desirable for laser treating real components if the process was used to minimise existing cracks on a material such as a Si_3N_4 turbine blade.

Solomah *et al.* [30] conducted research on the HP Si_3N_4 by employing a CO_2 laser. Comparative study was conducted by laser machining of a Si_3N_4 with the conventional diamond machining, cutting and drilling processes. Solomah *et al.* suggested that laser machining could be a cost effective technique to reduce the cost of ceramic machining during applications such as drilling, profile and line cutting. A high power CO_2 laser beam was fired as a CW and in a pulsed mode with varying power levels (50 to 500W) by using argon, oxygen, nitrogen as assist gases. The focused spot size of the beam was 100µm. The test samples were traversed by using an x-y table and a programmable motion controller. Samples were then ground and polished by using a diamond wheel. However, this is not considered for this research as it would not be ideal to grind and polish the surface after the laser treatment has been performed. This is because there is a risk of wearing away the laser irradiated layer. It would not do any justice if the laser irradiated layer was removed since further analysis would be required. Also, with a spot size of 100µm, it is not possible to treat a large surface area of the component part. Therefore, the beam is required to be directed multiple times in order to obtain certain coverage of the treated surface with no gaps remaining in between the treated areas.

The results of Solomah *et al.* showed that the laser cut samples of the Si_3N_4 contained surface flaws and porosity and stated that laser cutting of such ceramics cannot be conducted alone. However, it

can be a complimentary process to the conventional diamond grinding. It was also found by Solomah *et al.* that during laser cutting, oxygen is the most suitable gas despite the laser beam being in a CW or a pulsed mode. Use of oxygen as an assist gas for processing ceramics in particular may not be ideal since the atmospheric effect by oxygen could change the composition of the top surface of the ceramic as found by Shukla [13]. Also the change is the material composition during CW treatment is large in comparison with the pulsed mode due to the fact that the laser beam is firing at the material surface for a longer period of time which allows the processing area to be affected by the oxygen assist gas. The pulsed beam has a lower duty cycle so the effect of oxygen is minimal in comparison. Microcracking was also found during laser drilling with molten material splatter gathering around the hole. It was also said in [30] that it is difficult to laser drill a hole in comparison with producing a cut since the molten material splatter is difficult to flush than a cut front during the laser cutting process. Voisey *et al.* also mentioned that the laser beam operating in the pulse mode can reduce cracking in comparison with a laser beam operating in a CW mode. Nonetheless, according to the work of Shukla [13]; a pulsed beam is described to be more effective in generating cracks in comparison to the CW beam. This is due to the thermal shock being introduced in a short interval time. The pulse beam would create rapid heating, followed by the rapid cooling. This in turn produces contraction and expansion within the ceramic as the thermal energy is escapes.

3.6 Summary

This Chapter has addressed various aspects of laser-material interaction. Several features were extracted from the literature to assist with the experimental work conducted in this thesis. Those features are as follows:

- The guidelines for applying a range of parameters were gathered but the parameters window suggested in the literature will differ for the engineering ceramics used in this research. This is because of the unique composition within the ceramics and the different laser systems used herein.
- The use of larger spot size. This is because the laser energy density would be distributed over a larger surface area. This is particularly useful for laser surface treatment.
- Low gas flow rate would allow easy flow of assist gas to absorb into the surface of the ceramics. This would avoid excessive material removal from the ceramics during the laser-material interaction.
- The use of black ink coating can be adopted from the work of Hackle *et al.* [75]. This would assist in reducing the reflection of the laser beam and would improve the absorption, particularly for the white ZrO_2 engineering ceramic;

- To conduct experiments by using various processing conditions, created by using reactive and non-reactive assist gases. This would prove to be fruitful for investigating the laser- material interaction.

PART 2

TOPOGRAPHICAL, MORPHOLOGICAL, COMPOSITIONAL AND MICROSTRUCTURAL ASPECTS

CHAPTER 4
On the Establishment of Laser Surface Treatment Parameters

This Chapter demonstrates the development of the laser processing parameters that were used to perform the laser surface treatment of both the ZrO_2 and the Si_3N_4 engineering ceramics by means of a CO_2 and a fibre laser surface treatment. The main objective was to produce a laser surface treatment free from major surface cracking without using any of the pre or post heating techniques, as this would increase the cost of the process and add more expense to the product when considering a bigger point of view. From this a platform was formed which was then used to conduct further investigations as presented in the future Chapters.

4.1 Introduction

Determination of laser parameters is an important aspect to study prior to any laser processing. This is because it allows one to understand the materials behaviour and the capacity of the material to withstand the thermal energy which is being induced by the laser beam. This is specifically important for ceramics as they are prone to cracking when exposed to thermal shock which is generally introduced during the laser-ceramic interaction. To date, limited investigations have been performed with respect to achieving a ideal surface treatment of various ceramics with respect to the ceramic being crack-pore- and defect-free [95-100]. Murray *et al.* [34-37] performed several investigations by using the a CO_2 laser to cut ceramics which used a pre-heating method of the ceramic substrate to temperature up to 1500°C in a furnace and then performed the laser cutting process. Ester *et al.* [95] conducted an investigation on Al_2O_3 and ZrO_2 based oxide ceramics by employing a HPDL. Laser irradiated area of 50mm x 7mm was said to have a crack-free surface. This was performed by controlling the laser power, traverse speed, and the sample temperature by pre-heating the surface of the ceramic. Triantafyllidis *et al.* [96-100] performed several investigations on laser surface treatment of mainly Al_2O_3 based refractory ceramics by employing the HPDL. Earlier work of Triantafyllidis *et al.* identified solidification cracking due to the generation of very large temperature gradients that occurred within the ceramics. Triantafyllidis *et al.* further showed that the refractory Al_2O_3 ceramic can be treated with a combination of laser source (HPDL beam trailed by a CO_2 laser or vice versa), to eliminate the crack propagation by temperature control [96-97]. However, such methods were not always repeatable with ease and efficiency, since it required timely set-up and arrangement to take place. Further investigation showed that crack free-surfaces improved the properties of the ceramic surface. Those properties were corrosion resistance; contact characteristics and surface morphology; contact angle; wetting and water permeability [97, 99]. Another investigation by Triantafyllidis *et al.* [100] stands out from the others as it used the

HPDL to process refractory Al_2O_3 ceramic by using none of the post of pre-heating methods which are conventional ideas in processing ceramics by using a laser beam. Triantafyllidis *et al.* reported that a crack-free surface treatment was possible with the parameter window speed being 0.4mm/sec and a power density of 6×102 W/cm^2 which led to a crack-free surface treatment for the Al_2O_3 refractory ceramics. However, these parameters are unique for the refractory Al_2O_3 only with the particular composition. Other ceramics such as the ZrO_2 and Si_3N_4 are somewhat different due to their chemical composition which also changes the mechanical and thermal properties and has an effect during laser processing.

Although, ceramics have a low thermal conductivity and high resistance to withstand heat or thermal energy, there is still a limit or a threshold which it can resist before it fails. This failure occur either by shattering *via* producing brittle fractures or propagation of sharp cracks. In general, failure of ceramics under thermal loading occurs due to the introduction of the thermal shock, particularly during intense energy beam such as a laser. This is further justified in this Chapter but the most important aspect is to induce just enough energy into the ceramic so that it does not crack. For this to be successful, it is required that correct use of laser power, traverse speed, spot size and the gas flow rate are used. Although, the literature review provided some guidelines towards a range of parameters which are applicable for laser processing of various ceramics, but it is still unclear with respect to the threshold of the ceramics used for this research. This because all ceramics are different due to their processing history since the material composition (additives) and processing methods used to process the ceramics (used in this work) are somewhat different in comparison to that of the previous investigations. Therefore, a systematic method was used and is presented in this Chapter which demonstrates the approach of changing one factor (parameter) at a time to obtain the optimum parameter window for the ZrO_2 and the Si_3N_4 engineering ceramics by employing the fibre and the CO_2 lasers. Laser power; traverse speed; spot size and the appropriate power density were investigated since both since both ceramics have a different threshold for laser processing.

4.2 Background of the Experimental Materials: ZrO_2 and Si_3N_4 Engineering Ceramics

The first ceramic material used for the experimentation was a cold isostatic pressed (CIP) ZrO_2 with 95 wt% ZrO_2 and 5 wt% yttria (Tensky International Company, Ltd). The second ceramic material used for the experimentation was a cold isostatic pressed (CIP) Si_3N_4 with 90 wt% Si_3N_4, 6 wt% yttria and 4 wt% other, unspecified content. This initially contained a high content of α-phase as specified by the manufacturer. Furthermore, the microscopic image of the as-received Si_3N_4 with a similar composition was compared to the work of previous researchers (see Chapter 7) to confirm that the Si_3N_4 ceramic was in the α-phase state. Each of the samples were obtained in a bulk of 10 x 10 x 50mm^3 (see Figure 4.1) made from a specific rubber mould, to a specified dimension, from which all ceramics were CIPed. This was because the dimensions shown in Figure 4.1 were best suited for the laser processing experiments. The surface roughness was 1.57μm for the ZrO_2 and

1.56µm for the Si_3N_4 ceramics (as-received from the manufacturer). A smoother surface than specified for both ceramics would have much lower surface flaws and microcracks. This in turn, would lead to higher surface strength and wear resistance but initial experiments showed that polished shinier surfaces (below 1.57µm for the ZrO_2 and 1.56µm for the Si_3N_4), would reflect the beam and would therefore, reduced beam absorption into the surface and sub-surface of the ceramics. Thus, the surfaces were not ground and polished to achieve a better surface finish. The experiments were conducted in ambient condition at a known atmospheric temperature (20°C).

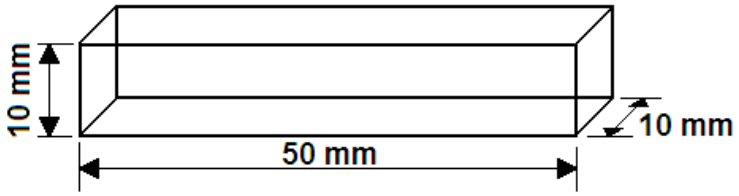

Figure 4.1 A schematic diagram of the experimental work-piece of the ZrO_2 and Si_3N_4 engineering ceramics as used in this research.

4.3 Fibre Laser Surface Treatment of the Si_3N_4 and the ZrO_2 Engineering Ceramics

A 200 W fibre laser (SPI-200c-002; SPI, Ltd.) emitting a CW mode beam at a wavelength of 1.075µm was used in this work. The fibre laser comprised of a Gaussian beam configuration of TEM_{00} with a beam quality factor of M^2 = 1.2. Experiments were conducted by varying one parameter at a time and by keeping the other parameters constant. Therefore, the laser power was varied from 25 to 200 W (max laser power) and simultaneously, the traverse speed was varied from 25 to 500 mm/min by keeping the focal position constant for both the engineering ceramics. From initial experiments, it was found that laser power of 143.25 W, traverse speed of 100 mm/min for the Si_3N_4 engineering ceramic and the power of 137.5 W at the traverse speed of 100 mm/min for the ZrO_2 engineering ceramic with a spot size of 3mm used for both the engineering ceramics was found to be an ideal constant to use in order to conduct the surface treatment (see Section 4.5.1 and Section 4.5.2). From this, identification of the range of laser power and power density required to reach the material threshold was achieved and are represented by graphical means. The processing gas used for this set of experiment was compressed air which was supplied at a flow rate of 25 l/min. Initial experiments showed that the flow rate in excess of 25 l/min was blowing off excessive material during the laser-ceramic interaction. This was significant during surface cracking of the ceramic as the cracked surfaces were eventually blown away and produced a large crater. Lower gas pressure would result to lower interaction between the laser beam and the ceramic. Hence, 25 l/min was found to be appropriate for this study. This prevented the ceramic debris from travelling upwards into the lens and protected the optics. Programming of the laser was conducted by using an SPI software which integrated with the laser system. A 50mm line was programmed by using numerical control (NC) programming as a potential beam path which was transferred by a .dxf file. The nozzle

indicated in Figure 4.2 was removed for all experiments. This was to obtain a larger spot size, based on the fact that laser welding in general is conducted with a larger spot size. This distributed the power on a bigger surface area, which is ideal for conducting the surface treatment. A larger laser beam was applied as it is more suitable for performing the laser surface treatment as opposed to laser cutting or drilling where high power density is required in the smaller surface area to penetrate through the material. In this case, a defocused beam allows the energy to distribute over a larger surface area which prevent thermal shocks and sever cracking of the ceramics. In any case, the defocused beam yet remained Gaussian.

All surfaces of both the Si_3N_4 and ZrO_2 engineering ceramics to be treated were marked with a black ink coating prior to the laser surface treatment. This was to enhance the absorption and allow the laser beam to further penetrate into the ceramic surface. Initial experiments reviewed that the black ink coating helped the beam to absorb better into the material. This was particularly the case with the white ZrO_2 engineering ceramic since it reflected the beam without the black ink coating. Furthermore, it was necessary to conduct like by like experiments with both laser types by using identical material surface conditions so a true comparison of the effects of the two lasers can then be further performed. The back ink coating was generally removed by the CO_2 or the fibre laser surface treatment and was not found to have any further effect on the ceramics after the laser surface interaction had taken place.

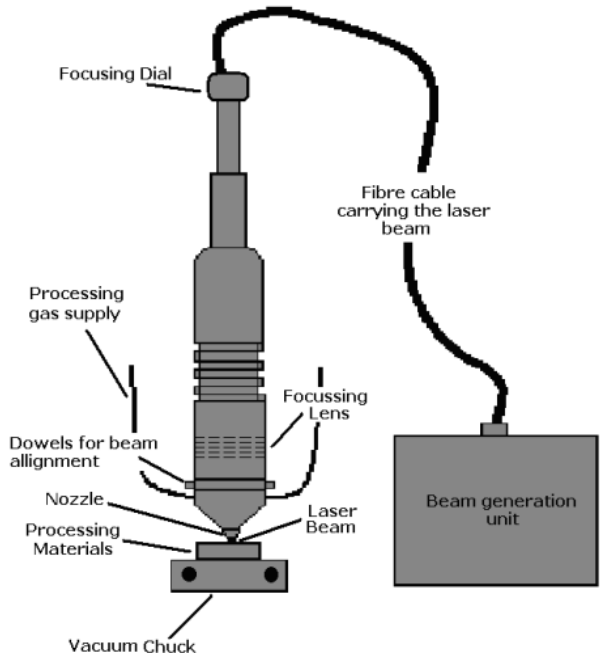

Figure 4.2 A schematics diagram of the experimental set-up of the fibre laser surface treatment of ZrO_2 and Si_3N_4 engineering ceramics.

4.4 CO_2 Laser Treatment of ZrO_2 and Si_3N_4 Engineering Ceramics

A 1.5 kW, Everlase S47, Coherent, CO_2 laser was employed to conduct experiments on both the ZrO_2 and the Si_3N_4 engineering ceramics (see Figure 4.3). The CO_2 laser comprised of a Gaussian beam configuration of TEM_{01} with a beam quality factor of $M^2 = 1.3$. One parameter was changed at any one time in order to determine the ultimate parameter window. The trials ranged from 50 to 200 W of laser power with a CW beam applied with a 10.6µm wavelength, while the beam spot size was kept constant at 3mm with a gas flow rate of 25 l/min by using compressed air assist gas. The traverse speed ranged from 25 to 700 mm/min to determine the ultimate speed required to process both engineering ceramics. Programming of the laser was conducted by using a independent software which integrated with the laser machine. A 50mm line was programmed by using NC programming as a potential beam path transferred by a .dxf file. Stand-off distance between the nozzle and the work-piece was kept to 16mm in order to obtain a focal spot size of 3mm. Parameters used for the CO_2 laser surface treatment were not directly comparable to those of the fibre laser surface treatment. This was due to the difference in the wavelength and the nozzle shape and diameter as well as the high power laser not being able to execute stably when operating at lower laser powers.

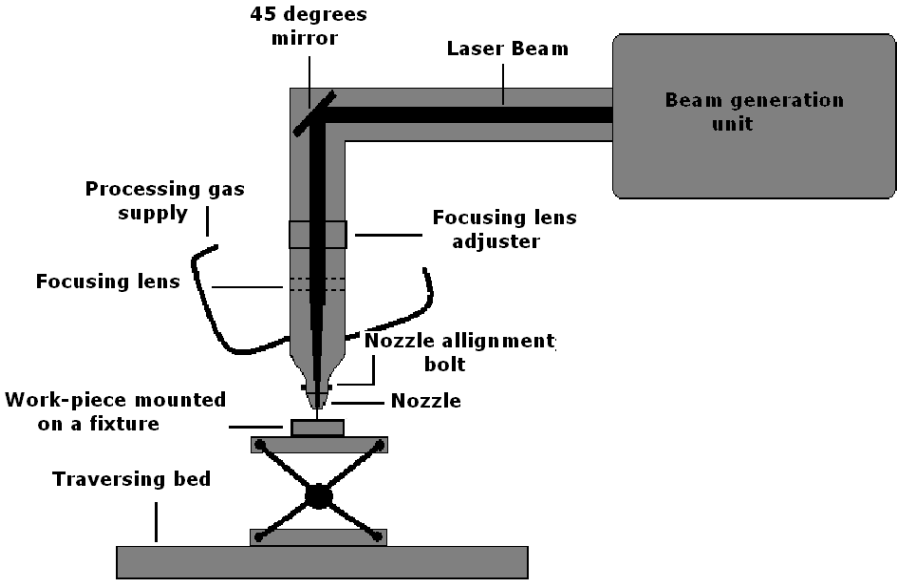

Figure 4.3 A schematic diagram of the experimental set-up of the CO_2 laser surface treatment of the ZrO_2 and the Si_3N_4 engineering ceramics.

4.5 Results and Discussion

4.5.1 Fibre Laser Surface Treatment of the Si_3N_4 Engineering Ceramic

In order to find the threshold of the Si_3N_4 engineering ceramic, a systematic approach was used. This is where the laser power was changed whilst other parameters such as the spot size of 3mm, traverse speed of 100 mm/min and gas flow rate of 25 l/min were kept constant during the fibre laser surface treatment. Table 4.1 show the range of powers used from 25 to 200 W and from 694 to 4761 W/mm^2

along with other associated parameters. During each stage, the effects of the laser-ceramic interaction were recorded. This is where it was found that 143.25 W or 3979 W/mm^2 was ideal for producing a surface treatment that comprised of very few cracks on the surface of the Si_3N_4 engineering ceramic. As more laser power was introduced at a constant speed, the surface of the Si_3N_4 began to show some effects. Those were a change in colour, appearance of few surface cracks to medium and then produced high cracking profile. Colour key used to show the effects in Table 4.1 to 4.3 are also shown in Figure 4.4 to 4.7.

Table 4.1 Effects of varying of laser power by using a 3mm constant size spot at the traverse speed of 100 mm/min and a gas flow rate of 25 l/min after fibre laser surface treatment of the Si_3N_4 engineering ceramic.

Experiments	1	2	3	4	5	6	7	8	9	10
Laser Power (W)	25	50	75	100	125	137.5	143.25	150	175	200
Power Density (W/mm^2)	694	1379	2073	2277	3472	3719	3979	4167	4556	4761
Speed (mm/min)	100	100	100	100	100	100	100	100	100	100
Effects										

From investigating the laser power, it was found that 143.25 W at a speed of 100 mm/min was the most ideal and produced the lowest cracks during the fibre laser surface treatment. Furthermore, the traverse speed was then investigated which varied from 25 to 500 mm/min. At the same time, laser power of 143.25 W and a spot size of 3mm were kept constant. The effects were then observed in terms of the surface cracks generated as result of the fibre laser-Si_3N_4 interaction. As one can see from Table 4.2, that lower traverse speeds resulted to more laser-material interaction time. This inherently produced high surface cracking. As the traverse speed increased, the laser-ceramic interaction time also increased. This in turn resulted to inducing lower thermal energy into the ceramic and therefore, reduced the cracks propagation. At a speed of 25 mm/min, evidence of high cracking was found as opposed to 500 mm/min. This is where there were no effects on the Si_3N_4 engineering ceramic. The most ideal speed as shown in Table 4.2 was 100 mm/min and generated very few cracks during the fibre laser surface treatment.

Table 4.2 Effects of varying the traverse speed by using 143.25 W of constant laser power, a 3mm spot size and a gas flow rate of 25 l/min after fibre laser surface treatment of the Si_3N_4 engineering ceramic.

Experiments	1	2	3	4	5	6	7	8	9	10	11	12
Laser Power (W)	143.25	143.25	143.25	143.25	143.25	143.25	143.25	143.25	143.25	143.25	143.25	143.25
Power Density (W/mm^2)	3979	3979	3979	3979	3979	3979	3979	3979	3979	3979	3979	3979
Speed (mm/min)	25	50	75	100	150	200	250	300	350	400	450	500
Effects												

It was found that the most ideal power for the fibre laser surface treatment of Si_3N_4 ceramic was 143.25W applied at a traverse speed of 100 mm/min. Therefore, the effects produced by varying the spot size needed exploration. Hence, the beam diameter of the fibre laser was varied from 0.5 to 4.5mm, whilst keeping a constant laser power, traverse speed and gas flow rate as presented in Table 4.3. In general, the smallest spot size produces high power density in comparison to a larger spot size, which would affect the laser processing in a detrimental way. This is also true for the results in this study as the smallest spot size used (0.5mm) resulted to producing the highest surface cracks and the largest spot size used (4.5mm) barely changed the colour of the Si_3N_4. Spot size of 3mm used with a laser power of 143.25 W had produced 3979 W/mm^2 of laser power density with a traverse speed of 100 mm/min generated the most desired fibre laser surface treated zone in terms of producing a lowest cracked surface.

Table 4.3 Effects of varying the spot size by using 143.25 W of constant laser power, traverse speed of 100 mm/min and a gas flow rate of 25 l/min after fibre laser surface treatment of the Si_3N_4 engineering ceramic.

Experiments	1	2	3	4	5	6	7	7	9
Spot Size (mm)	0.5	1	1.5	2	2.5	3	3.5	4	4.5
Power (W)	143.25	143.25	143.25	143.25	143.25	143.25	143.25	143.25	143.25
Power Density (W/mm^2)	143250	35713	15917	7953	5730	3979	2923	2237	1769
Speed (mm/min)	100	100	100	100	100	100	100	100	100
Effects									

The effects of the laser parameters can be further presented with respect to the crack propagation of the Si_3N_4 during the fibre laser surface treatment. Figure 4.4 shows that the increase in travese speed results to the laser beam having less effect. Evidance of high crack propagation can be found with traverse speed under 100 mm/min and with increasing travese speed the laser induced cracks had began to reduce untill there was no physical effect found on the surface of the Si_3N_4 beyond 450 to 500 mm/min. Figure 4.5 showed the effects of the laser power and the power density on the fibre

laser irradiated Si_3N_4 surface. The laser power and the power density has a close relationship, as the power density is dependant on the laser power and the diameter of the laser spot used. It can be seen that with increasing laser power and increasing power density, the propagation of cracks and the effects on the ceramic would increase due to high energy being induced into the ceramic. Therefore, it would increase the temeprature at the laser-ceramic interface. This in turn would also increase the thermal shock which characteristically leads to propagation of a crack.

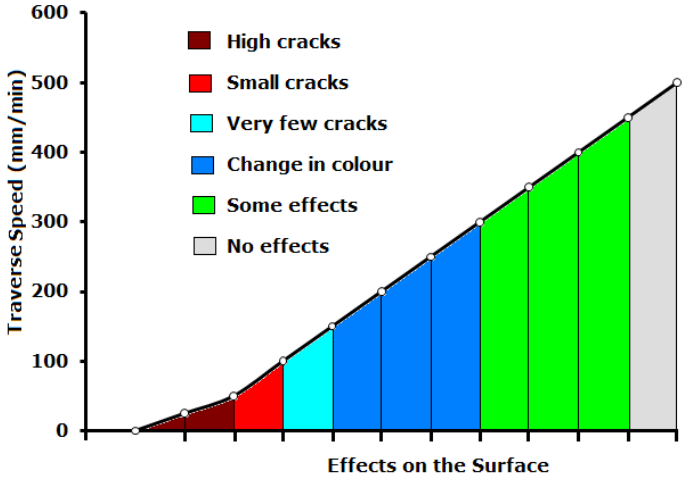

Figure 4.4 Effects of the traverse speed on the surface of the Si_3N_4 engineering ceramic after fibre laser surface treatment.

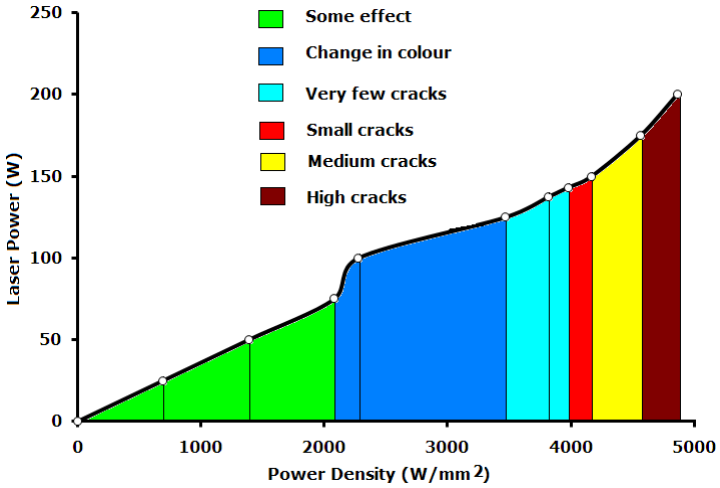

Figure 4.5 Relationship between laser power and power density which shows the effects of the fibre laser surface treatment of the Si_3N_4 engineering ceramic by keeping a constant traverse speed of 100 mm/min, 3mm spot size and 25 l/min gas flow rate.

Figure 4.6 presents the effects of the laser power and the travese speed with respect to cracking on the fibre laser irradiated surface of the Si_3N_4 and demosnstrates that with increasing speed and increasing power the effects also become distict. However, high surface cracking begins to appear when applying high laser power and low travese speed. Therefore, a combination of the power and speed was important to apply. It was found that 100 mm/min at about 143.25W was ideal to use in

terms of generating a fibre laser treated surface which comprised of the lowest surface cracks. Figure 4.7 illustrates the the effect of power density and the travese speed. As the power density is incresed and the traverse speed is decreased, the propagation of the surface cracks are also increased. Travese speed of 100 mm/min and the power density of 3979 W/mm^2 was found to be appropriate to generate the lowest surface cracks on the Si_3N_4.

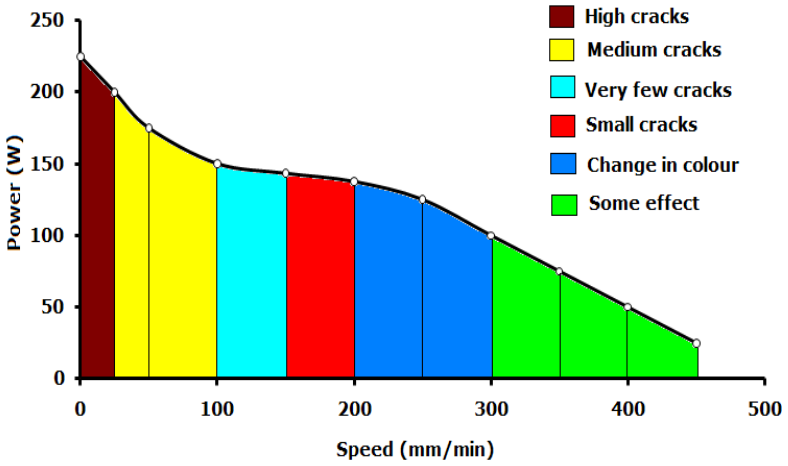

Figure 4.6 Relationship between laser power and traverse speed showing the effects of the fibre laser surface treatment of the Si_3N_4 engineering ceramic, by keeping a constant spot size of 3mm and 25 l/min gas flow rate.

Figure 4.7 illustrates the relationship of power density and spot size of the fibre laser upon the Si_3N_4 engineering ceramic. The graph showed that with lower spot size produced high power input and larger power density would be generated. This would consequently propagate high surface cracks on the Si_3N_4 engineering ceramic. It was found that at cosntant laser power, and travese speed, the spot size below 3mm generated high surface cracks as the fibre laser beam diameter was altered from being large to small.

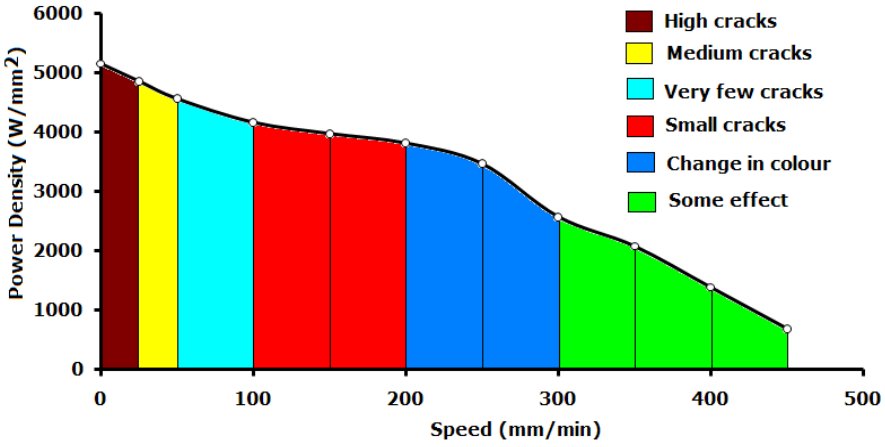

Figure 4.7 Relationship between power density and traverse speed showing the effects of the fibre laser surface treatment of the Si_3N_4 engineering ceramic by keeping a constant spot size of 3mm and 25 l/min gas flow rate.

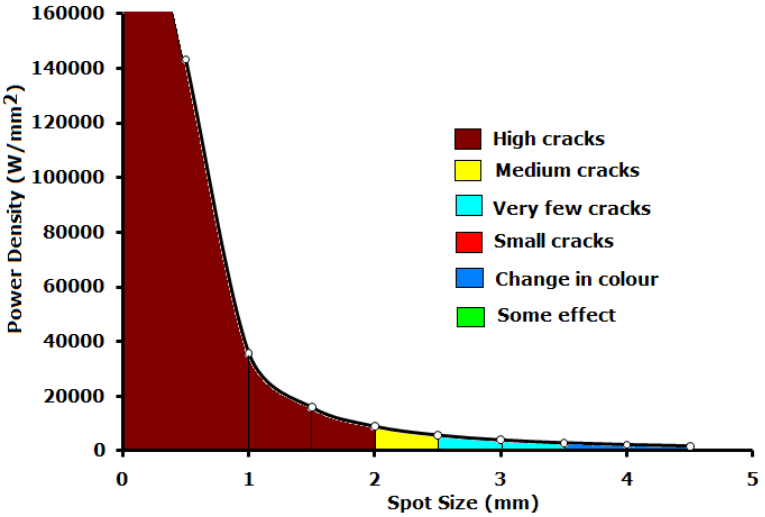

Figure 4.7 Relationship between power density and spot size showing the effects of the fibre laser surface treatment of the Si_3N_4 engineering ceramic, by keeping a traverse speed of 100 mm/min, gas flow rate of 25 l/min and laser power of 143.5W.

4.5.2 Fibre Laser Surface Treatment of the ZrO_2 Engineering Ceramics

Parameters used for the fibre laser surface treatment of the ZrO_2 were fairly similar to that of the Si_3N_4 except that the ZrO_2 had a different threshold to that of the Si_3N_4. This was because the ZrO_2 ceramic comprised of higher thermal conductivity than the Si_3N_4. This meant that the heat was easily transferred to the ZrO_2 than the Si_3N_4 and it was easy and quicker to heat the ZrO_2. This intrinsically would produce higher thermal shock as well as surface cracking. The approach to find the threshold of the ZrO_2 engineering ceramic was the same to that of the Si_3N_4 as presented in Table 4.4 to 4.6 and in Figure 4.9 to 4.13. The power was varied from 25 to 200W and the traverse speed was initially kept constant to 100 mm/min by using a constant spot size of 3mm. The fibre laser had began to affect the surface of the ZrO_2 from changing its colour at 75W to producing a very few to high cracks at various power intervals and eventually cracked at 200W of laser power. It was established that the ideal laser power was 137.5W in order to generate the lowest surface cracks so the traverse speed was investigated and is presented in Table 4.5. This is where the laser power, focal spot size, power density and the gas flow rate were kept constant and the traverse speed was varied from 25 to 500W. This is how it was confirmed that 100 to 150 mm/min produced the lowest cracks and beyond the speed of 150 mm/min produced colour changes up to 350 mm/min and had no further visual effects on the surface of the ZrO_2. Lower speeds of 50 to 70 mm/min generated high cracking and further shattered the ceramic when the traverse speed was reduced to 25 mm/min. This was obvious as the laser beam was spending more time on the ZrO_2 surface which increased the thermal energy input and generated the surface cracks. Figure 4.12 shows the effects of varying the spot size on the ZrO_2 as the spot size was varied from small to large. It was found that the ZrO_2 had shattered below 2mm spot diameter. Above 2mm of spot diameter, the laser beam produced high level of cracking and then generated the lowest cracks at a beam diameter of 3 to 3.5mm. Fibre laser

beam diameter larger than 3.5mm showed some influence on the ceramic. However, beyond 4.5mm had showed no visual effects. Colour key used to show the effects in Table 4.4 to 4.6 are also shown in Figure 4.9 to 4.13.

Table 4.4 Effects of varying of the laser power by using a 3mm constant size spot at the traverse speed of 100 mm/min and gas flow rate of 25 l/min, after fibre laser surface treatment of the ZrO_2 engineering ceramic.

Experiments	1	2	3	4	5	6	7	8	9	10
Laser Power (W)	25	50	75	100	125	137.5	143.25	150	175	200
Power Density (W/mm^2)	94	1379	2073	2277	3472	3719	3979	4167	4556	4761
Speed (mm/min)	100	100	100	100	100	100	100	100	100	100
Effects										

Table 4.5 Effects of varying of the traverse speed by using a 3mm constant size spot with the laser power of 137.5 W, 3719 W/mm^2 power density and gas flow rate of 25 l/min, after fibre laser surface treatment of the ZrO_2 engineering ceramic.

Experiments	1	2	3	4	5	6	7	7	9	10	11	12
Laser Power (W)	137.5	137.5	137.5	137.5	137.5	137.5	137.5	137.5	137.5	137.5	137.5	137.5
Power Density (W/mm^2)	3719	3719	3719	3719	3719	3719	3719	3719	3719	3719	3719	3719
Speed (mm/min)	25	50	75	100	150	200	250	300	350	400	450	500
Effects												

Table 4.6 Effects of varying the spot size by using 137.25 W of constant laser power, traverse speed of 100 mm/min and a gas flow rate of 25 l/min, after fibre laser surface treatment of the ZrO_2 engineering ceramic.

Experiments	1	2	3	4	5	6	7	7	9
Spot Size (mm)	0.5	1	1.5	2	2.5	3	3.5	4	4.5
Power (W)	137.5	137.5	137.5	137.5	137.5	137.5	137.5	137.5	137.5
Power Density (W/mm^2)	137500	34775	15277	7594	5500	3919	2706	2147	1697
Speed (mm/min)	100	100	100	100	100	100	100	100	100
Effects									

Figure 4.9 represents the appearance of the surface cracks with increasing laser power densities and traverse speed. As one can see that the graph shows that with high power density and low traverse speed, the ZrO_2 ceramic had shattered, but as the power density decreases and the traverse speed

increases, the cracking of the ceramic begins to reduce until there is no significant effect on the material beyond 450 mm/min. This is also shown the Figure 4.10.

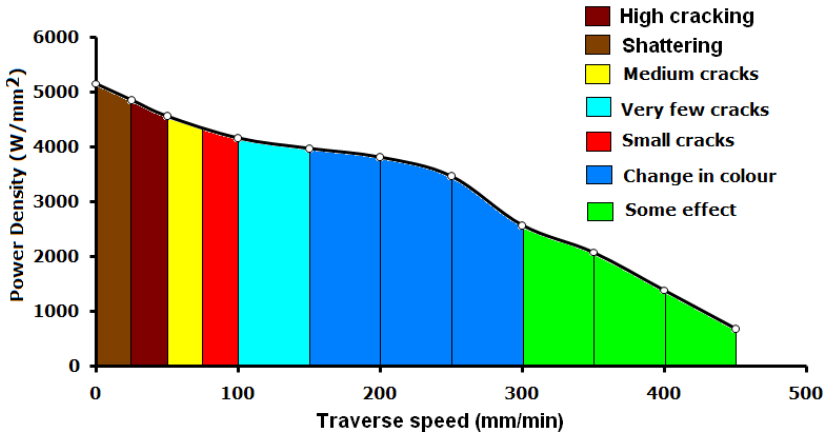

Figure 4.9 Relationship between power density and traverse speed which shows the effects of the fibre laser surface treatment of the ZrO_2 engineering ceramic by keeping a constant spot size of 3mm and 25 l/min gas flow rate.

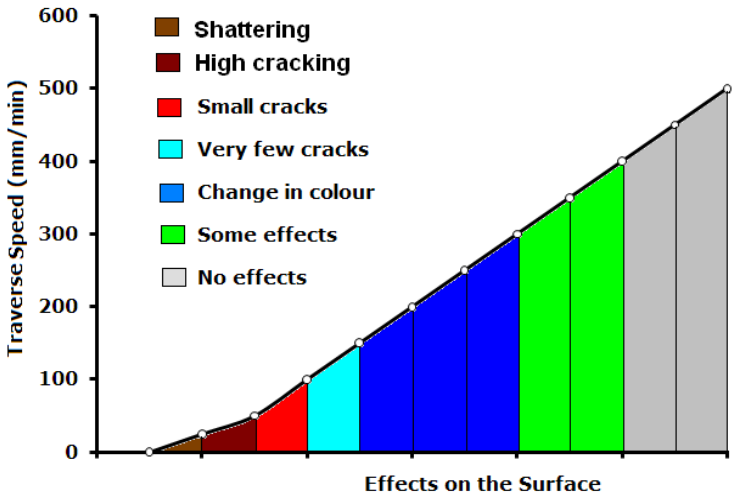

Figure 4.10 Effects of the traverse speed on the surface of the ZrO_2 engineering ceramic after fibre laser surface treatment.

The effects are also similar with the graph illustrating the relationship between the laser power and traverse speed (see Figure 4.11). Increase in the laser power at low traverse speed had produced shattering and high cracking within the ZrO_2 engineering ceramic. Further reduction in the crack propagation occurred with high traverse speed and lower laser power. This reduced the effect of the thermal shock on the surface of the ZrO_2 engineering ceramic.

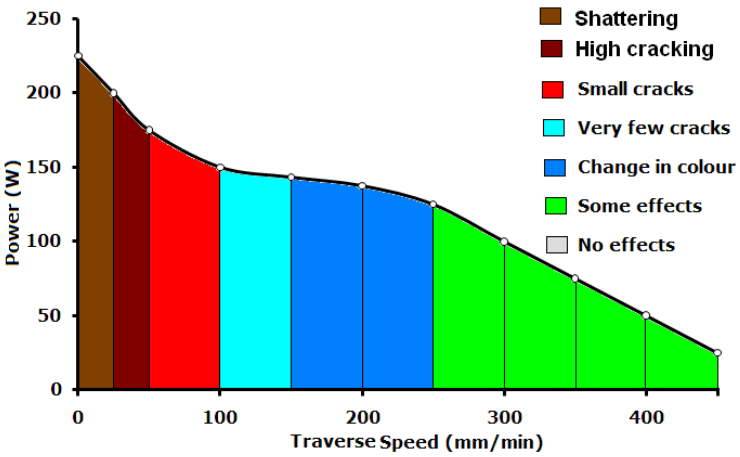

Figure 4.11 Relationship between laser power and traverse speed showing the effects of the fibre laser surface treatment of the ZrO_2 engineering ceramic by keeping a constant spot size of 3mm and 25 l/min gas flow rate.

Figure 4.12 presents the effect of the spot size *versus* the power density show that the laser beam diameter at 3mm produces a power density of 3719 W/mm^2 at a constant traverse speed of 100 mm/min and laser power of 137.5W. This generated the lowest cracking on the fibre laser irradiated layer. Increase in the spot size had resulted to having no effect and decrease in the spot diameter had resulted to significant cracking and shattering of the engineering ceramic. In Figure 4.13, one can see that the smallest cracks only appeared at sufficient power density of 3719 W/mm^2 and a laser power of 137.5W. Until then, the effects were minimal on the surface of the ZrO_2 engineering ceramic.

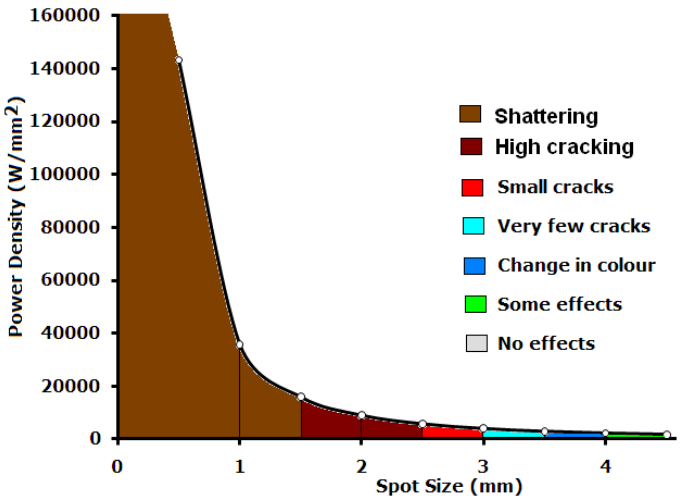

Figure 4.12 Relationship between power density and spot size showing the effects of the fibre laser surface treatment of the ZrO_2 engineering ceramic by keeping a traverse speed of 100 mm/min, gas flow rate of 25 l/min and laser power of 137.25 mm/min.

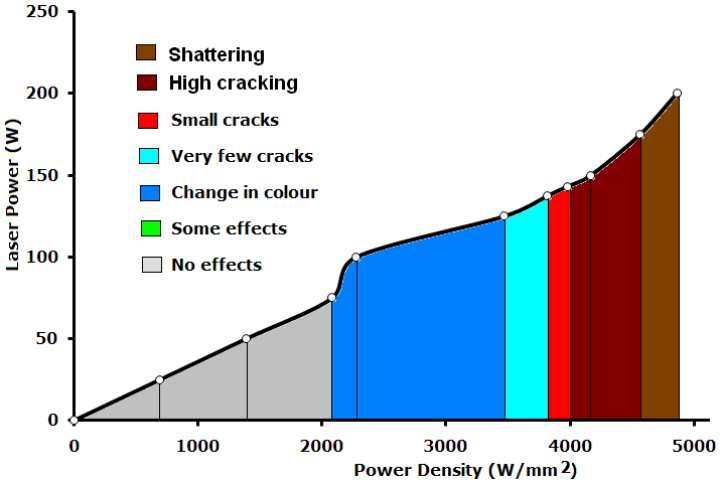

Figure 4.13 Relationship between power density and traverse speed showing the effects of the fibre laser surface treatment of the ZrO_2 engineering ceramic by keeping a constant spot size of 3mm, traverse speed of 100 mm/min and 25 l/min gas flow rate.

4.5.3 CO_2 Laser Surface Treatment of the Si_3N_4 Engineering Ceramic

The effects of the CO_2 laser was different to that of the fibre laser as it was found that the Si_3N_4 ceramic was able to resist higher CO_2 laser power in comparison. Similar approach was used to obtain the most ideal parameters for the CO_2 laser in comparison to the fibre laser. Table 4.7 shows that the traverse speed was initially selected at constant parameter of 100 mm/min to determine the most ideal laser power. Along with that, the supply of the processing gas was kept as a constant to 25 l/min. The power density was changed characteristically, as the laser power was changed. At 25W, no significant effects were found. As the power was raised, the CO_2 laser had began to create some effect by producing discolouration of the Si_3N_4. Moreover, small cracking had then began to occur beyond 200W. Colour key used to show the effects in Table 4.7 to 4.9 are also shown in Figure 4.14 to 4.17.

Table 4.7 Effects of varying of laser power by using a 3mm constant spot size at the traverse speed of 100 mm/min and gas flow rate of 25 l/min after the CO_2 laser surface treatment of the Si_3N_4 engineering ceramic.

Experiments	1	2	3	4	5	6	7	8	9
Laser Power (W)	25	50	75	100	125	150	175	200	225
Power Density (W/mm^2)	694	1379	2073	2777	3472	4167	4761	5556	6250
Speed (mm/min)	100	100	100	100	100	100	100	100	100
Effects									

Table 4.7 shows the use of constant laser power (200W), power density of 5556 W/mm^2, whilst the traverse speed was varied from 25 to 400 mm/min. The effects here were similar in comparison to the fibre laser as the traverse speed below 100 mm/min showed evidence of high cracking. Between the traverse speeds of 100 to 125 mm/min, cracking was reduced to very few cracks. Discolouration

was found with further increase in the traverse speed. This was until 350 mm/min, where only some effects can be seen of the CO_2 laser. Beyond 250 mm/min, no effect was to be seen on the Si_3N_4 engineering ceramic. Table 4.9 shows the variation in spot size by keeping other parameters constant.

Table 4.7 Effects of varying of the traverse speed by using a 3mm constant size spot with the laser power of 200W, 3719 W/mm^2 power density and gas flow rate of 25 l/min after the CO_2 laser surface treatment of the Si_3N_4 engineering ceramic.

Experiments	1	2	3	4	5	6	7	8	9	10	11	12
Laser Power (W)	200	200	200	200	200	200	200	200	200	200	200	200
Power Density (W/mm^2)	5556	5556	5556	5556	5556	5556	5556	5556	5556	5556	5556	5556
Speed (mm/min)	25	50	75	100	125	150	175	200	250	300	350	400
Effects												

Table 4.9 Effects of varying the spot size by using 200W of constant laser power, traverse speed of 100 mm/min and a gas flow rate of 25 l/min after the CO_2 laser processing of Si_3N_4 engineering ceramic.

Experiments	1	2	3	4	5	6	7	8	9
Spot Size (mm)	0.5	1	1.5	2	2.5	3	3.5	4	4.5
Power (W)	200	200	200	200	200	200	200	200	200
Power Density (W/mm^2)	5556	5556	5556	5556	5556	5556	5556	5556	5556
Speed (mm/min)	100	100	100	100	100	100	100	100	100
Effects									

The relationship of power density and laser power with the crack propagation during the CO_2 laser surface interaction is presented in Figure 4.14. This shows that the smallest cracks occurred above 175W to 200W. Below 175W, there is only some influence on the Si_3N_4 ceramic as there was some discoloration. Evidence of high cracking was found beyond 200W. Surface treatment comprising of the smallest surface cracks was found at the traverse speed of 100 and 150 mm/min as shown in Figure 4.15.

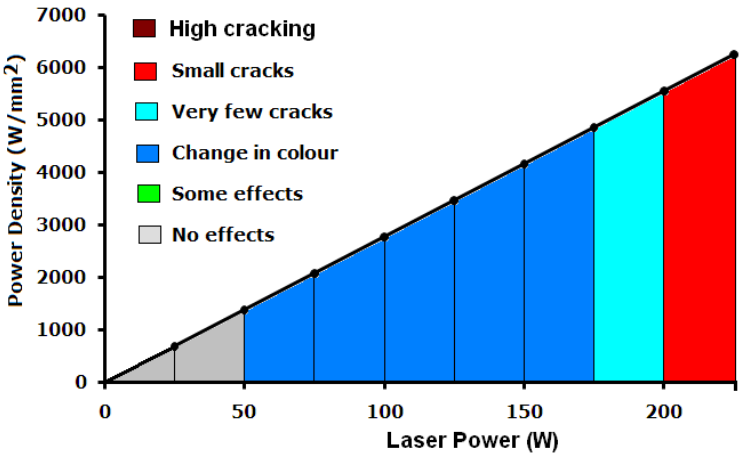

Figure 4.14 Relationship between laser power and power density showing the effects of the CO_2 laser surface treatment of the Si_3N_4 engineering ceramic by keeping a constant traverse speed of 100 mm/min, 3mm spot size and 25 l/min gas flow rate.

High level of cracking was seen under the traverse speed of 50 mm/min as shown in Figure 4.16. As the traverse speed increased, the cracks began to reduce. The smallest cracks were seen at 100 mm/min. Beyond 100 mm/min showed only discolouration and small effects on the surface of the ZrO_2 engineering ceramic.

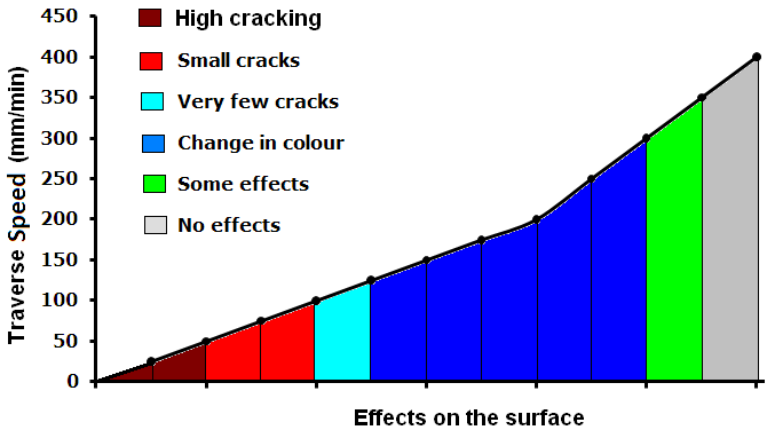

Figure 4.15 Effects of the traverse speed on the surface of the Si_3N_4 engineering ceramic after CO_2 laser surface treatment.

Figure 4.17 shows the relationship between the laser power and the traverse speed. This is where it can be seen that high cracking was to be seen with traverse speed below 100 mm/min and beyond were few cracks were found during the CO_2 laser interaction of the Si_3N_4 ceramic. The cracking effect became less as the traverse speed was increased. This behaviour is also identical in Figure 4.17. This illustrates the relationship of power density and the traverse speed where cracking behaviour of the Si_3N_4 during the CO_2 laser surface treatment is presented. Figure 4.17 presents the variation in spot size during the CO_2 laser treatment of the Si_3N_4 and shows that the surface had began to produce high cracking at spot size of 2mm despite the power density being low. However,

as the spot size began to get larger, the cracking effect had reduced at 3mm and under 4000 W/mm^2. Very few cracks generated by the CO_2 laser were evident from using 3mm to 4.5mm diameter beam, with power density being raised to 6000 W/mm^2. However, beyond 4.5mm of beam diameter, there was only evidence of change in colour despite the laser power density increasing to 7000 W/mm^2. This showed that the spot size had considerable contribution by influencing the surface treatment, as it controlled the thermal energy being induced into the engineering ceramic.

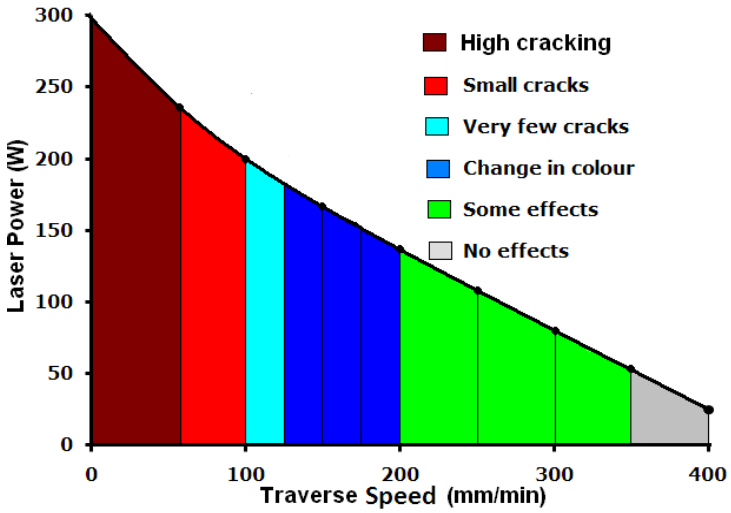

Figure 4.16 Relationship between laser power and traverse speed showing the effects of the CO_2 laser surface treatment of the Si_3N_4 engineering ceramic by keeping a constant spot size of 3mm and 25 l/min gas flow rate.

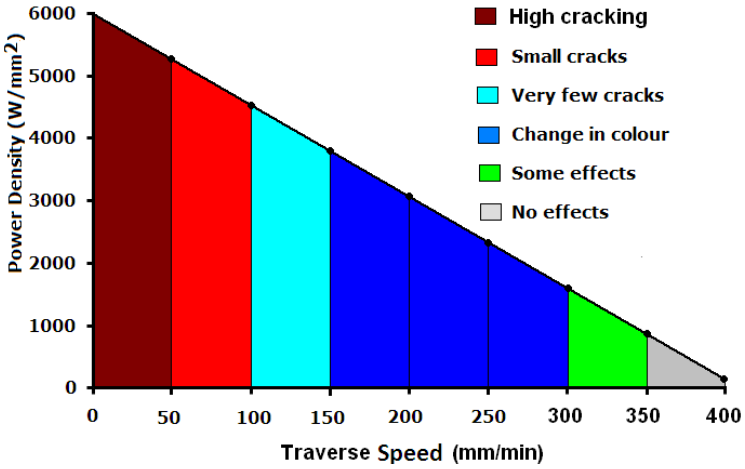

Figure 4.17 Relationship between power density and traverse speed showing the effects of the CO_2 laser surface treatment of the Si_3N_4 engineering ceramic by keeping a constant spot size of 3mm and 25 l/min gas flow rate.

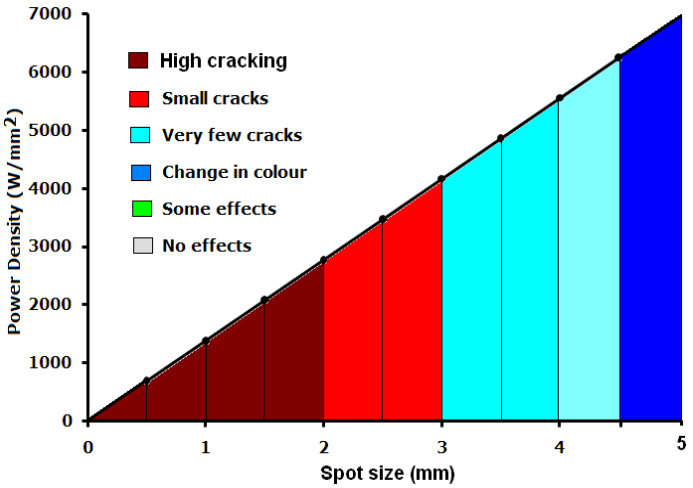

Figure 4.17 Relationship between power density and spot size showing the effects of the CO_2 laser surface treatment of the Si_3N_4 engineering ceramic by keeping a traverse speed of 100 mm/min, gas flow rate of 25 l/min and laser power of 200W.

4.5.4 CO_2 Laser Surface Treatment of the ZrO_2 Engineering Ceramics

Table 4.10 illustrates the effects of the CO_2 laser on the ZrO_2 ceramic as the laser power is changed as well as the power density. It can be seen that at 100 mm/min of constant power produced sufficient amount of cracking followed by shattering of the ZrO_2. This is when the laser power was applied from 25W to 200W. From Table 4.10, it was not clear as to what parameters can be used until experiments with varying the traverse speed was performed. Hence, the laser power was selected at 62.5W. This was in-between the area where there was no effect on the ZrO_2 at 50W and where evidence of small cracking began to appear at 75W. Therefore, 62.5W was selected with the traverse speed being experimented from 25 to 700 mm/min as presented in Table 4.11. Colour key used to show the effects in Table 4.10 to 4.12 are also shown in Figure 4.14 to 4.23.

Table 4.10 Effects of varying of laser power by using a 3mm constant size spot at the traverse speed of 100 mm/min and gas flow rate of 25 l/min after CO_2 laser surface treatment of the ZrO_2 engineering ceramic.

Experiments	1	2	3	4	5	6	7	8
Laser Power (W)	25	50	75	100	125	150	175	200
Power Density (W/mm^2)	694	1379	2073	2777	3472	4167	4761	5556
Speed (mm/min)	100	100	100	100	100	100	100	100
Effects								

Shattering was found until the traverse speed of 100 mm/min was applied at constant laser power of 62.5W and 1736 W/mm^2 power density by using a 3mm diameter CO_2 laser beam. From 200 to 400 mm/min, high cracking was observed. This was reduced to small cracks as the traverse speed increased to 500 mm/min. At 600 mm/min, smallest cracks were to be seen. Beyond 600W, there

were no effects to be observed with traverse speed of up to 700 mm/min. The results at 600 mm/min with an applied laser power of 62.5W and a gas flow rate of 25 l/min showed that the ZrO_2 had shattered or produced high cracking by using a spot size below 3mm. Between 3 to 3.5mm, the CO_2 laser surface treated ZrO_2 comprised of the lowest surface cracks. Beyond 3.5mm, colour change within the ZrO_2 engineering ceramic was to be seen. No significant effect was found with the spot diameter of up to 4.5mm (see Table 4.12).

Table 4.11 Effects of varying the traverse speed by using a 3mm constant size spot with the traverse speed of 600 mm/min, 1736 W/mm^2 power density and gas flow rate of 25 l/min, after CO_2 laser surface treatment of the ZrO_2 engineering ceramic.

Experiments	1	2	3	4	5	6	7	8	9
Laser Power (W)	62.5	62.5	62.5	62.5	62.5	62.5	62.5	62.5	62.5
Power Density (W/mm^2)	1736	1736	1736	1736	1736	1736	1736	1736	1736
Speed (mm/min)	25	50	100	200	300	400	500	600	700
Effects									

Table 4.12 Effects of varying the spot size by using 200W of constant laser power, traverse speed of 600 mm/min and a gas flow rate of 25 l/min after CO_2 laser surface treatment of the ZrO_2 engineering ceramic.

Experiments	1	2	3	4	5	6	7	8	9
Spot Size (mm)	0.5	1	1.5	2	2.5	3	3.5	4	4.5
Power (W)	62.5	62.5	62.5	62.5	62.5	62.5	62.5	62.5	62.5
Power Density (W/mm^2)	62500	15625	20733	3906	2500	1736	1276	977	772
Speed (mm/min)	600	600	600	600	600	600	600	600	600
Effects									

Figure 4.19 shows the relationship between the laser power and the power density during the CO_2 laser treatment of the ZrO_2. The ZrO_2 ceramic up to 50W and 1379 W/mm^2 of power density at the speed of 600 mm/min showed very little affect but began to have some affect on the ZrO_2 surface beyond 50 W and 1379 W/mm^2. Minimal cracking was found at 62.5W with the power density of 1736 W/mm^2 which increased as the laser power and the power density were raised and resulted to high cracking and further shattering. This was different to the effects which the fibre laser had upon the ZrO_2 as higher power density, laser power and low traverse speed were used to obtain the same result.

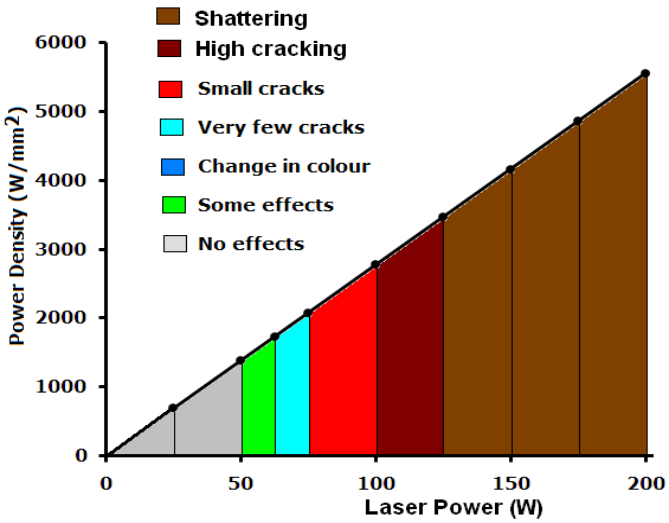

Figure 4.19 Relationship between laser power and power density showing the effects of the CO_2 laser surface treatment of the ZrO_2 engineering ceramic by keeping a constant traverse speed of 600 mm/min, 3mm spot size and 25 l/min gas flow rate.

The effects of the traverse speed as presented in Figure 4.20 and Figure 4.21 showed shattering of the ZrO_2 at lows speed of up to 100 mm/min. High surface cracking was found beyond this and up to 350 mm/min. Thereafter, small cracks were evident until 600 mm/min. Beyond 600 mm/min very few surface cracks were found. The ZrO_2 showed some evidence of laser-material interaction beyond the traverse speed of 650 mm/min. From comparing the effects of laser power density and traverse speed showed that the traverse speed was more contributory in inducing the thermal energy into the ceramic. This is because the ZrO_2 shattered at low power density but the speed was considerably low. With increasing power density and increasing speed showed some reduction in the cracks. However, considerable amount of cracking was prominent until 500 mm/min and was reduced to very small cracks until 650 mm/min (see Figure 4.22).

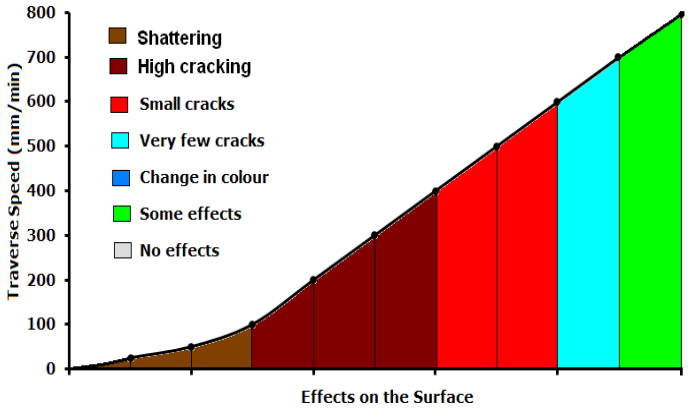

Figure 4.20 Effects of the traverse speed whilst using a constant laser power of 62.5W, a spot size of 3mm and a gas flow rate of 25 l/min on the surface of the ZrO_2 engineering ceramic after the CO_2 laser surface treatment.

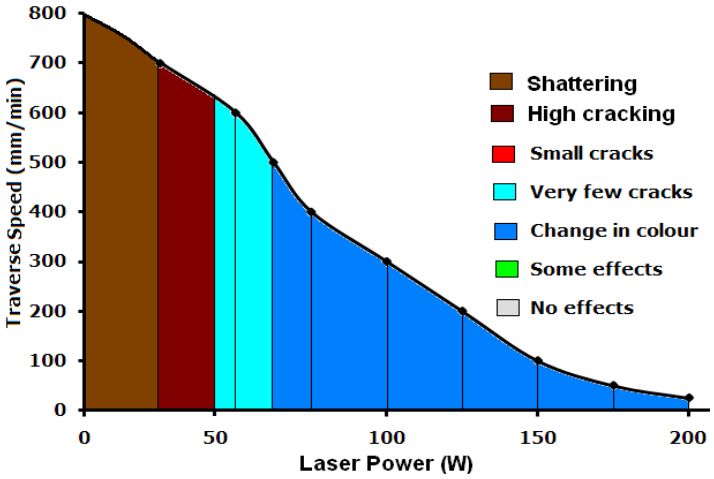

Figure 4.21 Relationship between laser power and traverse speed showing the effects of the CO_2 laser surface treatment of the ZrO_2 engineering ceramic by keeping a constant spot size of 3mm and 25 l/min gas flow rate.

Figure 4.23 showed that the small spot size with increasing power density resulted to generating high cracking on the ZrO_2. The high cracks were found until 2mm of spot diameter and then produced very few cracks at 3mm. Beyond 3.5mm there was some change in colour and visual effect to be seen on the ZrO_2. This continued to occur as the power density was raised despite the increasing spot size and large power distribution on the ZrO_2 ceramic.

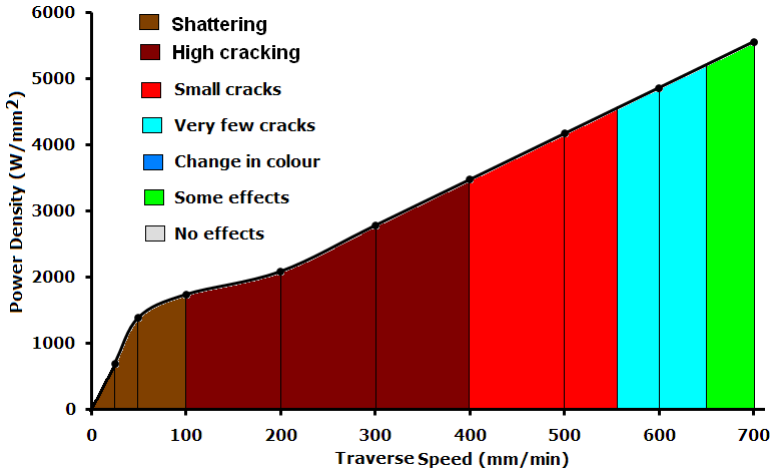

Figure 4.22 Relationship between power density and traverse speed showing the effects of the CO_2 laser surface treatment of the ZrO_2 engineering ceramic by keeping a constant spot size of 3mm and 25 l/min gas flow rate.

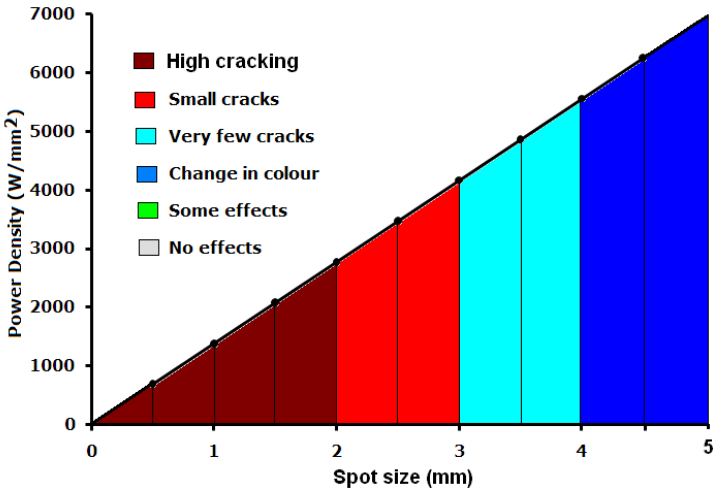

Figure 4.23 Relationship between power density and spot size showing the effects of the CO_2 laser surface treatment of the ZrO_2 engineering ceramic by keeping a traverse speed of 100 mm/min, gas flow rate of 25 l/min and laser power of 600 mm/min.

4.5.5 Mechanism of Crack Propagation

One of the reasons why failure occurs within ceramics is due to the induction of a thermal shock. Thermal shock is a term given for cracking and is also mentioned in the literature [37]. Because ceramics are hard and brittle, it makes them prone to cracking. Low thermal conductivity, high thermal expansion, and low toughness of ceramics generate cracks during exposure to high temperature. Moreover, it is the exposure to difference in the thermal gradient or temperature change which in term makes them fail.

Thermal shock is produced when high temperature is introduced to the ceramic whilst the ceramic is in a state of ambience. This is particularly the case during laser surface treatment as the high power density from laser beam focused on a small surface area interacts with the ceramic which body is at 20 to 25°C temperature. During the laser-ceramic interaction, the processing temperature is almost above 2000°C (depending on the laser parameters and the type of laser used). Most probably, the rise of temperature at the ceramic surface would be from ambient to about 2000°C within a second. Then, it is made to cool as the laser beam moves to another area. In this case, a temperature difference has occurred already. This in turn, would expand the ceramic as it tries to absorb the heat. During this expansion, the areas within the bulk are somewhat cooler in comparison. The cooler areas are working against the induced thermal energy and attempts to contract the ceramic (see Figure 4.24). However, the high thermal energy needs to escape. Hence, the expansion (which is in form of a tensile stress) of the ceramic acts as a force towards contraction (which is in form of a compressive stress) by the bulk (cooler areas). If the tension is sufficient enough and is inhibited to certain level, then it will overcome the compression. This in turn, will cause the ceramic to fail by cracking and often shattering the ceramic into pieces.

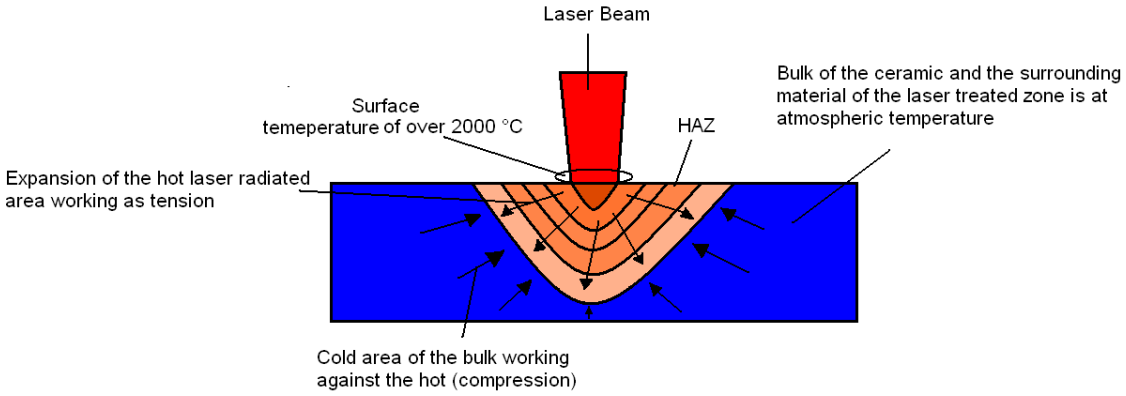

Figure 4.24 Effect of the thermal energy on the surface and within the bulk of the ceramic.

4.5.6 Comparison of the CO_2 Laser Surface Treatment with the Fibre Laser Surface Treatment of the ZrO_2 and the Si_3N_4 Engineering Ceramics

Since cracking occurs due to the difference in the thermal gradient then cracking can be avoided by reducing the thermal gradient. This is by changing the temperature of the ceramic more slowly by means of pre-heating the ceramic before the laser surface treatment or possibly by post-heating if need be. This would be by heating the ceramic after the laser surface treatment (as mentioned earlier in this Chapter). This in turn, would avoid rapid thermal gradient and the clash of hot and cold surfaces occurring at the ceramic surface and within the body. Pre-heating or post heating can be performed as an additional process and could compliment the laser surface treatment. Or the concept of using a combination of dual laser beams to perform the surface treatment can also be adopted to increase the cooling rate by the trailing laser beam. However, from a broader view point, both the dual laser beam processing technique and by using the heating furnace to pre-and post-heat the ceramic are additional processes which add extra value to the total cost of processing rather than the product itself. This includes extra process time, tooling and/or man power. More energy is also required for pre-and post-heating technique to take place as well as doubling the cost of laser processing if two lasers are used as a leading and a trailing heat source. Thus, it was rather economic and less time consuming to use single beam laser source. This was adopted for the investigation in this research and attempts were made to generate the most desirable surface that comprised of minimal cracking, flaws, porosity, and defects so further analysis can be conducted to elucidate the physical effects of laser-ceramic interaction.

Over all, fibre laser surface treatment of both the ZrO_2 and Si_3N_4 engineering ceramic was somewhat different to that of the CO_2 laser. This was because the Gaussian beam modes were for the CO_2 laser was TEM_{01} and the beam quality factor (M^2) was 1.3. In comparison, the fibre laser emitted a beam with a Gaussian profile of TEM_{00} and an M^2 value of 1.1. This indicated a slightly better quality beam. Also, the difference in the wavelength between the two lasers was significant as the fibre laser wavelength was 1.075µm and the CO_2 laser was 10.6 µm. The beam delivery system was also

different since the fibre laser was delivered from a fibre cable and the CO_2 laser being directed by mirrors, and galvano-meters. Consequently, each laser will have different effect on the surface of the two ceramics. It was found that when comparing the two lasers, the wavelength of the CO_2 laser when processing the Si_3N_4 ceramic was being absorbed more than that of the fibre laser as higher power density and same traverse speed was used to reach the threshold for the Si_3N_4 when compared to the fibre laser. When the effects of the two lasers are compared for the ZrO_2 engineering ceramic, it was found that by using the CO_2 laser, low power and high traverse speed were required in comparison to the fibre laser. This was because the ZrO_2 ceramic was shattering when using the identical parameter to the fibre laser. The shattering occurred because the wavelength of the CO_2 laser was being absorbed into the sub-surface of the ceramic. This in turn produced the high thermal energy on the ZrO_2. The NIR of the fibre laser in comparison was more transparent to the oxide ceramic, so the energy of the fibre laser would be absorbed deeper and made it crack less at equivalent laser parameters to the CO_2 laser.

Minimum cracking was observed with using the parameters which is why such parameters were further adopted to conduct experiments for this research as presented in the future Chapters. Table 4.13 shows the ideal parameters found form conducting the laser surface treatments by using the CO_2 and the fibre lasers on both engineering ceramics. These parameter are used for most of the investigations in this thesis except the one in Chapter 8. This utilizes a smaller beam diameter and the lower laser power. This was due to the technical incapability of the Nd:YAG laser used as a comparable source to the fibre (see Chapter 8, Section 8.3.3). By comparing the results herein with those of the previous workers, it can be said that the difference is mainly in the terminology of crack definition as the crack-free surface as described in their research is more realistically described in this research as surface comprising of minimal or very few cracks.

Table 4.13 Selected parameters from initial experiments with a constant spot size of 3mm, gas flow rate of 25 l/min by using compressed air.

Lasers types	**Parameters**					
	Traverse Speed (mm/min)		**Laser Power (W)**		**Power Density (W/mm^2)**	
	Si_3N_4	ZrO_2	Si_3N_4	ZrO_2	Si_3N_4	ZrO_2
CO_2 Laser	100	600	200	62.5	5556	1736
Fibre laser	100	100	143.5	137.5	3979	3719

4.6 Summary

Experimental investigation was conducted on both engineering ceramics by using the CO_2 and the fibre laser. Threshold of the two ceramics were found by using the CO_2 and the fibre laser irradiation. In terms of producing a laser irradiated surface with minimal or no surface cracks, the following parameters were applied and various conclusions were drawn:

- Fibre laser surface treatment of the Si_3N_4 engineering ceramic required 143.25W, at the traverse speed of 100 mm/min. The parameters used for the CO_2 laser surface treatment of the Si_3N_4 engineering ceramic used 200W at the traverse speed of 100 mm/min.

- The best surface with very few cracks on the ZrO_2 engineering ceramic was produced by applying 137.5W at a traverse speed of 100 mm/min when employing the fibre laser surface treatment. The CO_2 laser was required to traverse at 600 mm/min by inducing 62.5W to achieve the desired result on the ZrO_2.

- Both laser surface treatments of the Si_3N_4 and the ZrO_2 engineering ceramic had utilized a beam spot diameter of 3mm and a gas flow rate of 25 l/min.

The fibre laser surface of both the ZrO_2 and the Si_3N_4 engineering ceramic was somewhat different to that of the CO_2 laser due to the difference in the wavelength and the beam delivery system. This was because the fibre laser was delivered from a fibre cable and the CO_2 laser being delivered by mirrors and galvano-meters. Therefore, both lasers produced different results on the surface of the two ceramics. From comparing the two lasers, it was found that the Si_3N_4 engineering ceramic was more resistive towards the wavelength of the CO_2 laser wavelength as opposed to that of the fibre laser. This was due to high power density and same traverse speed was used to reach the threshold.

It was found that low power and high traverse speed was required for the CO_2 laser when surface treating ZrO_2 engineering ceramic in comparison to the fibre laser when the effects of the two lasers are compared. This was because the ZrO_2 shattered when identical parameters to that of the fibre laser were applied. This was because the CO_2 laser wavelength was only being absorbed into the top surface layer of the ceramic. This in turn, produced more interaction to take place at the surface. In comparison, the oxide ceramic is more absorbent to the NIR wavelength of the fibre laser so the energy of the fibre laser would be absorbed deeper and had made it crack less at equivalent laser parameters to the CO_2 laser.

CHAPTER 5
Characterization and Compositional Evaluation of Laser Surface Treated Engineering Ceramics

Surface treatment by means of a CO_2 laser and a fibre laser irradiation was conducted by using various assist gas compositions on CIP Si_3N_4 and ZrO_2 engineering ceramics to observe changes in their surface integrity, microstructure and chemical composition. Vickers indentation method was employed to investigate the change in hardness between the laser treated zone, heat affected zone (HAZ) and the interfaces. Thereafter, scanning electron microscopy (SEM) was used to observe the integrity prior to and after laser surface treatment. The as-received, CO_2 and the fibre laser treated surface topography were measured in 3-D by using a focus variation technique. Energy dispersive X-ray (EDX) analysis was employed to detect surface modifications of the ceramics composition for the as-received and both the CO_2 and fibre laser treatment of the engineering ceramics.

5.1 Introduction

Engineering ceramics have found wide usage in various industrial sectors. In particular, applications in the aerospace and automotive industry comprehensively use engineering ceramics because of their advantageous thermal and mechanical properties when compared to metal and alloys, as well as high wear resistance and low co-efficient of friction which are particularly ideal for high speed bearings, exhaust valves and clevis pins. Turbo charger rotors, pistons, hybrid bearings comprising of a Si_3N_4 casing and ZrO_2 or Si_3N_4 balls and a metallic casing are regularly used due to the ceramics extended functional life, better performance and efficiency in comparison to metallic components. Good thermal insulation and high melting points have enabled engineering ceramics to be readily used for many components within a gas turbine engine. Engineering ceramics also have high acoustic damping capacity to reduce engine noise and are operational in underwater environment due to their corrosive resistance and environmental stability [37, 41, 43, 45]. The die-electric properties of the ceramics also make them applicable for missile radomes.

Laser surface treatment in comparison to the conventional surface processing techniques offers competitive advantages as mentioned previously. Such advantages are an asset to the manufacturers and allow them to achieve better tolerances, reduced production costs, shorter lead times as well as just in times delivery (JIT). Laser surface treatments can be a superior technique for processing of engineering ceramics for a glazing application as an example. This can potentially improve the surface finish as well as the aesthetics of the ceramic component/product. Another example where

laser processing of ceramics can be effective is by applying the laser shock processing technique which is successfully being used for enhancing the wear rate, co-efficient of friction, hardness and to reduce component mass of metals and alloys [66, 101, 102]. This is achieved by forming shockwaves within the metals/alloys and inducing a compressive residual stress layer. Similar effect can also be achieved with ceramics, whereby the functional life of the ceramic components/products can be enhanced if the effects of the laser-ceramic interaction are further understood [103].

Several previous investigations have revealed interesting results when using industrial lasers (high powered) to surface treat refractory ceramics. Previous work by Wang *et al.* [104-106] was conducted by using refractory ZrO_2 and Al_2O_3 ceramics to investigate the microstructural characteristics after melting of the ceramic substrate by using a CO_2 laser. Surface cracking was found in the treated area, but changes to the laser parameters led to modified surface composition and morphology. Further work was conducted by Wang *et al.* [107] by using an Nd:YAG laser to surface treat refractory ceramics by adding nano-particles to modify the surface density and the corresponding microstructure. The laser treatment was conducted prior to and after adding the nano-particles. Results linking to their previous investigations [104-106] showed dendrites that were much finer after the addition of the nano-particles. Triantafyllidis *et al.* [97] performed an investigation by using double laser sources: a CO_2 and a HPDL, to investigate the possibility of generating a crack-free surface on refractory Al_2O_3 ceramics by balancing out the thermal gradient and elongating the solidification rate. The results presented crack-and pore-free surfaces along with deeper penetration in comparison with the single laser processing technique. Further work by Triantafyllidis *et al.* [107] demonstrated laser cladding of thin sheets of Al_2O_3 by employing a high powered CO_2 laser. Substantial grain growth was found on the surface of the treated ceramics along with increase in the grain size.

Variation in employing processing gases has been the subject of several studies. The effect of laser processing of metals by using various shield gases has been investigated extensively [109-113]. Minami *et al.* [114-115] used various processing gases assisted by a HPDL to remove ceramic tile grout. Compressed air, Ar, N_2, and O_2 were used to study their effects on the microstructure, material removal and thermal changes. The findings revealed O_2 to be the most effective gas as it maximized the materials removal rate. Lawrence *et al.* [116] used a HPDL with O_2, Ar, and He assist gasses to study the influence of assist gas on HPDL processed concrete surfaces. The results showed the occurrence of porosities with all of the gases used. Minimal surface cracking and porosity was found from using O_2 in comparison with Ar and He. Better interaction with O_2 was also reported in order to generate sufficient heat and fluidity within the melt pool in comparison to Ar and He. This was due to the faster cooling rate occurring with the Ar and He which resulted in trapping the gas bubble and maximized the possibility to form surface cracking and porosity in contrast with using the O_2 assist gas.

A number of researchers have also worked with laser surface treatment of ceramics to identify the effects of laser beam on material properties, such as the frictional wear [117] and the flexural strength of Si_3N_4 [15]. Sun *et al.* [15] investigated the possibility of eliminating imperfections within the Si_3N_4 ceramics by applying a CO_2 laser. Their results showed improvement in the bend strength by reduced fracture origins and a change in phase as the Si_3N_4 was transformed to YSiAlON. The findings presented in Chapter 6 with regards to changes in the fracture toughness within the ZrO_2 from the fibre laser irradiated surface showed reduced crack lengths. This in turn, increased the fracture toughness of the fibre laser irradiated zone. This reduction in the crack lengths had occurred from the newly formed surface layer with a changed composition.

Despite the wide use of CO_2, Nd:YAG and HPDL to process various technical ceramics, other than the work of this thesis; no work has been done hitherto in which a fibre laser is employed to process the surface of engineering ceramics. This study focuses on the laser-material interaction occurring during the CO_2 and the fibre laser surface treatment of the Si_3N_4 and the ZrO_2 engineering ceramics in various processing gas environments: compressed air; O_2; Ar; N_2 and ambient air (no assist gas). The investigation comprised of observing the surface morphology, changes in the composition, the material removal, the topography, the surface hardness and the HAZ. Even though, the operating wavelength of the fibre laser is in the same region as that of the Nd:YAG laser, the fibre laser was still used due to several inherent advantages. Those advantages are: a better beam quality, smaller spot size, depth of field (longer focal length), depth of penetration, high brightness and better stability. The beam quality of the fibre laser is (M^2 = 1.2) which would execute high power density in a same spot size in comparison to the Nd:YAG laser beam. This in turn, is likely to produce better interaction leading to deep penetration into the ceramic. The longer focal length allows the fibre laser to operate from longer distances. This is ideal to avoid backscatter and beam reflection. Lastly, the high brightness offered by the fibre laser in comparison to that of the Nd:YAG laser is the most advantageous as it induces more photon energy by executing higher power per wattage. This inherently reduces the cost of the surface treatment also and has a real potential to produce better interaction zone in comparison to that of the Nd:YAG laser.

5.2 Experimental Methodology and Analysis

5.2.1 Background of the Experimental Material

The materials used for the experimentation were ZrO_2 and Si_3N_4 engineering ceramics and were described in Chapter 4 (see Section 4.2).

5.2.2 Fibre and CO_2 Laser Surface Treatment Procedure

Both fibre and the CO_2 lasers were employed for the experiments in this Chapter. The details of the two lasers used in this investigation are presented in Chapter 4 (see Section 4.3) where description of both laser parameters applied on both ZrO_2 and Si_3N_4 engineering ceramics are presented as well as

the programming methods used. The processing gases used with both lasers were O_2, N_2, Ar, compressed air as well as ambient air (no gas) supplied at a flow rate of 25 litres/min. Four samples were treated for both ZrO_2 and Si_3N_4 each by employing the two lasers with different processing gas compositions.

5.2.3 Method of Analysis

A Vickers diamond indenter (Vickers (HVTM); Armstrong Engineering, Ltd.) was used to investigate and identify if there are any changes within the surface of the Si_3N_4 and ZrO_2 ceramics after the CO_2 and the fibre laser surface treatments. The hardness measurement was conducted in the standard manner and is described elsewhere [117, 119]. The Vickers indenter was induced five times over the as-received surface (laser unaffected zone), HAZ, and the laser treated surface plane of the Si_3N_4 and ZrO_2 engineering ceramic treated by the CO_2 and the fibre laser by employing the different assist gases. The indentation load applied was 30 kg. From this, an average hardness of each surface plane on each of the samples laser treated by using various conditions was found along with its standard deviation and range as presented in Table 5.1. Indentations were made from approximately on the centre of the laser irradiated track outwards for 4mm in increments of four diamond widths into the laser unaffected region of the sample. Thereafter, the size of the indentions was measured to determine the surface hardness in the prescribed way [117, 119]. The surface topography of the Si_3N_4 and ZrO_2 prior to and after the laser surface treatment was investigated to determine the effect of the laser beams upon the near (top) surface. This was done by using a focus variation technique (Infinite Focus IFM 2.15; Alicona, Ltd.) that performed a three-dimensional (3-D) surface analysis. This analysis produced 3-D surface profiles of the Si_3N_4 and ZrO_2 surfaces under investigation by using around a 2mm diameter beam which travelled to the length of 7mm across the width of the as-received (laser unaffected), HAZ and the laser irradiated surface. The scanning speed used was 30 sec/mm. The as-received, the laser irradiated surfaces and the HAZ of the Si_3N_4 and ZrO_2 ceramics were observed at a microscopic level to examine the surface morphology by using a SEM and the elemental composition to a depth of 1µm by means of EDX analysis (Stereoscan 360; Carl Zeiss Leo, Ltd.). Prior to the SEM and the EDX analysis, the samples were carefully washed in distilled water, and then dried in hot air (150°C) for around 30 seconds. After this, all the samples were Au coated to enhance the surface electrical conductivity.

5.2.4 Observation of the As-received Surface of the Si_3N_4 Engineering Ceramic

Figure 5.1 shows the as-receive sample of the Si_3N_4, with the surface appearing to be somewhat coarse comprising of surface micro-cracks, as one can see specifically in Figure 5.1(a), and closely packed grains being seen in Figure 5.1(b). The grains were measured to be ranging between 1.5 to 2.5µm in size. There was no evidence of the porosity pre-existing on the surface of the as-received Si_3N_4 from observing the SEM images. A compositional study of the as-received surface of the Si_3N_4 showed it to be comprised of 17.5 wt% C, 22 wt% O_2, 35 wt% Si, 4.5 wt% Y. N_2 content of about 22

wt% would also exist in this sample, but the EDX system used was unable to detect any N_2 within the chamber. This is not a problem as the undetected N_2 can be found from substituting the percentage of the other elements that were present.

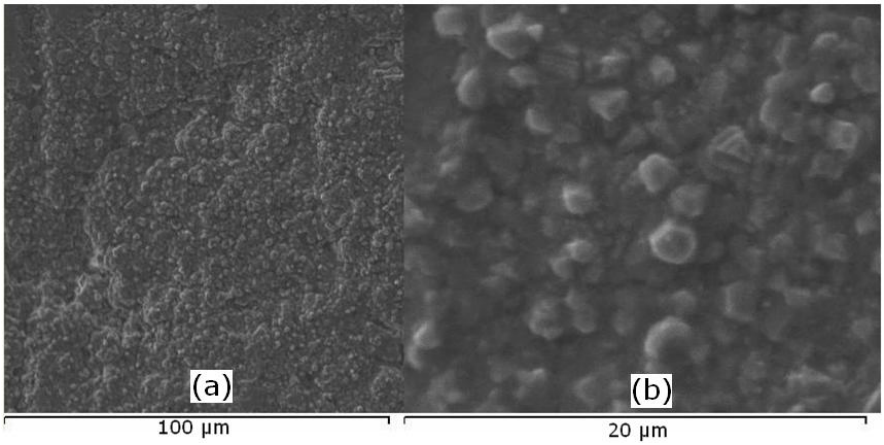

Figure 5.1 SEM images of the as-received surface of the Si_3N_4, (a) at x 500 and (b) x 3000 resolution.

5.2.5 Observation of the As-received Surface of the ZrO_2 Engineering Ceramic

The two micrographs indicated in Figure 5.2(a) and (b) showed the as-received surface of ZrO_2 along with agglomerates (see Section 5.3.4.1) which comprise of the ZrO_2 grains when observed at a higher magnification. The agglomerates ranged between 70µm to 100µm and averaged 95µm. As one can see that the boundaries of the agglomerates are not so closely packed in Figure 5.2. This would have increased the level of pores around the edge of the agglomerate boundaries. However, there was minimal porosity to be seen on the surface of the as-received ZrO_2. The compositions of the top (near) surface layer of the as-received surface were 67.69 wt% Zr, 25.45 wt% O_2, and 5.76 wt% C. The values found were also expected as the main composition of ZrO_2 ceramic comprised of zirconium and oxygen.

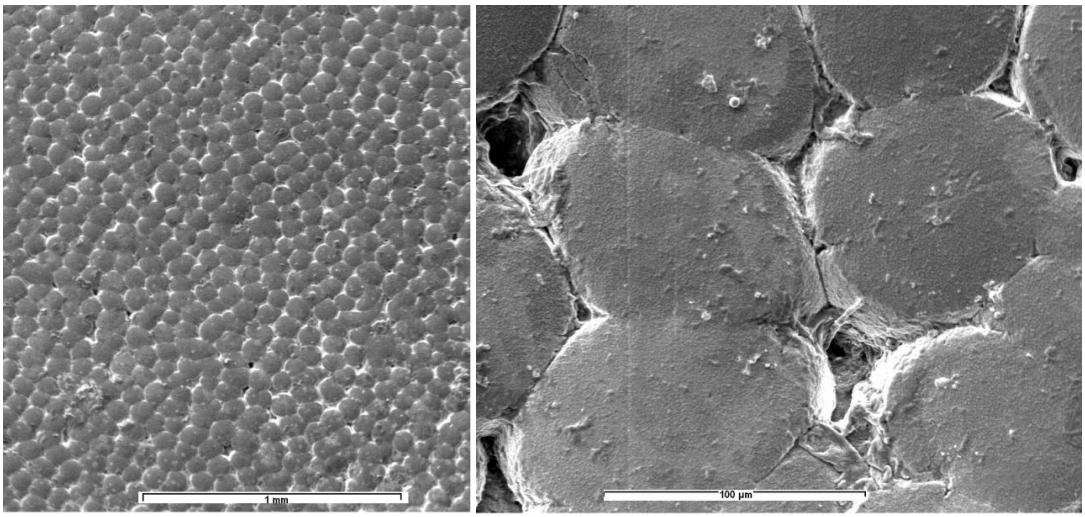

(a) **(b)**

Figure 5.2 SEM images of the as-received surface of the ZrO_2, (a) at x500 and (b) x3000 resolution.

5.3 Results and Discussion

5.3.1 Fibre Laser Surface Treatment of the Si_3N_4 Engineering Ceramic

5.3.1.1 Investigation of the heat affected zone (HAZ) of the Si_3N_4 engineering ceramic

From measuring the surface hardness of the fibre laser irradiated Si_3N_4 ceramic it was found that the fibre laser treatment resulted in a change in the surface hardness on the various zones of the Si_3N_4 engineering ceramic. The hardness changed from within the untreated zone to the HAZ and the fibre laser irradiated zone. An example of the hardness values are given in Figure 5.3 and are further presented in Table 5.1. It was found that the fibre laser irradiated zone comprised of the softest surface layer as the diamond indentation induced into the heat affected region, the interface between each zones and the untreated surface layer (see Figure 5.3). The example shown in Figure 5.3 for the fibre laser irradiated surface by using ambient air showed that the hardness was reduced to 1054 HV on the track and ranged between 960 to 1250 ±10% HV on the outer edges of the laser treated track particularly for the Si_3N_4 surface treated by using the O_2 assist gas. The hardness increased along the edges of the track indicating that the respective surface layer was less influenced. The untreated surface, indicated in Figure 5.3 on both sides of the track, ranged from 1400 to 1600 HV ±10% HV. Variation in the hardness value can be seen with changing indentation loads. If a lower indentation load was used then the penetration of the diamond indenter would be rather low. This is more evident by the work presented in Chapter 6 as much lower indentation loads were applied to determine the K_{1c}. Indentation of 30 kg load was used herein to achieve sufficient depth into the laser treated zones. The penetration depth of the Vickers diamond indentation is presented in Table 5.2. The depth of penetration of the diamond indentation at 30 kg varied as the indenter was induced on different surfaces that were irradiated by the fibre laser from using the various assist gases. This occurred due to the SiO_2 layer being uneven and changing the surface morphology with the different gas compositions used. For instance the diamond indentation penetrated deeper for the surface fibre laser irradiated by using O_2 assist gas. This was due to the formation of the SiO_2 layer being higher as opposed to the one of N_2 or Ar as shown in Table 5.2. This was because the formation of the SiO_2 surface layer by the fibre laser irradiation was lower for the non-reactive assist gases in comparison to the more reactive gases. Hence, the thickness of the SiO_2 layer had changed depending on the assist gases used. The values in Table 5.2 relate to the amount of O_2 content found by each type of treatment as shown later in Figure 5.14. As the O_2 content increases within the fibre laser irradiated sample, the SiO_2 layer became thicker and appears to be considerably softer to the laser unaffected surface (as-received) of the Si_3N_4. This inherently, allowed the diamond indenter to penetrate deeper into the surface of the fibre laser irradiated track.

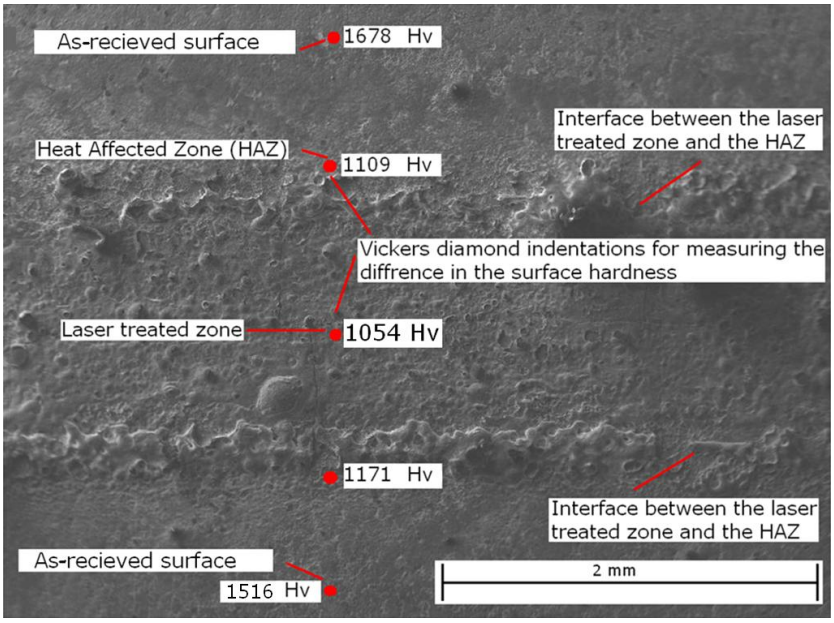

Figure 5.3 SEM image presents an example of the fibre laser irradiated surface of the Si_3N_4 by using ambient air (no gas) showing the fibre laser unaffected surface, fibre laser treated surface and the HAZ.

Table 5.1 Showing the change in the average hardness, STDEV and the range of hardness values found for the fibre laser irradiated zone (track) by using various assist gases, fibre laser unaffected zone and the HAZ of the Si_3N_4 engineering ceramic.

Assist gases	Hardness values in various areas on the surface of the Si_3N_4 engineering ceramic								
	Laser unaffected zone			Fibre laser irradiated track			HAZ		
	Average hardness (HV)	STDEV	Range	Average hardness (HV)	STDEV	Range	Average hardness (HV)	STDEV	Range
O_2	1627	55	1574 - 1710	961	176	712- 1174	1391	155	1264 - 1647
Ar	1694	73	1575 - 1727	1211	103	1103 – 1377	1461	106	1326 - 1574
Compress -ed air	1627	61	1529 - 1670	1202	176	965 - 1463	1576	133	1461 - 1736
N_2	1664	102	1575 - 1727	1243	91	1161 – 1420	1479	114	1330 - 1641
Ambient air	1633	106	1520 - 1757	1203	176	1092 - 1310	1449	99	1305 - 1597

Table 5.2 Depth of penetration by the Vickers diamond indentation at 30 kg load induced on the fibre laser irradiated surfaces of the Si_3N_4 treated by using various assist gases.

Assist gases	Depth of penetration (µm)
O_2	34.04 µm
Ar	30.05 µm
Compressed air	30.31 µm
N_2	29.66 µm
Ambient air	30.14 µm

5.3.1.2 The effects of the fibre laser surface treatment by using various assist gases on topographical characteristics

5.3.1.2.1 O_2 assist gas

Figure 5.4 shows the surface topography of a Si_3N_4 sample fibre laser irradiated by using an O_2 assist gas. The laser treated zone (see Figure 5.4), is comprised of a newly formed (melted and solidified) surface layer with some degree of materials removal occurring as a result of the fibre laser surface treatment. The depth of the material removal was up to 257µm. The grey and white areas present in the laser treated zone indicate surface oxidation. This was further identified from the microscopic and the compositional analysis. The HAZ comprises of some degree of discoloration which is an indication of the distribution of heat. The surface finish in terms of Ra was measured to be 12.1µm within the laser treated zone. This points to a severe change occurring in the surface morphology of the laser treated zone. This is apparent from a comparison of the surface finish for the as-received sample which was measured to be 1.57 µm (Ra). The changes in the surface roughness occurred due to the formation of an uneven surface layer from the Si_3N_4 ceramic through material removal and decomposition which formed the asperities on to the surface as seen in Figure 5.4.

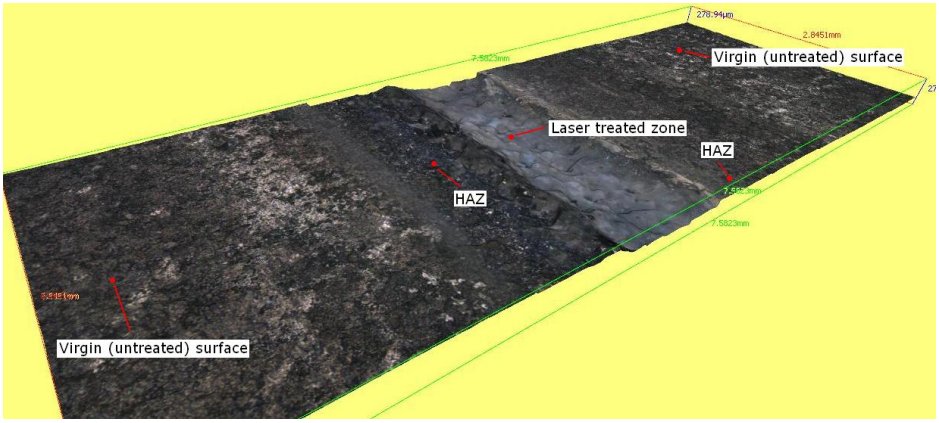

Figure 5.4 A 3-D topographical image of the surface profile of the Si_3N_4 engineering ceramic treated by the fibre laser irradiation by using an O_2 assist gas.

5.3.1.2.2 Compressed air assist gas

The upper surface profile of the Si_3N_4 sample treated with the fibre laser beam by using a compressed air assist gas is given in Figure 5.5. This shows significantly less material removal than that of the sample treated with an O_2 assist gas (see Figure 5.4). The depth of material removal was up to 169µm. This indicates that the laser-material interaction during the treatment was less reactive in comparison to the surface treated by the fibre laser by using the O_2 assist gas. The surface finish within the laser treated zone was 2.12µm (Ra) and was much smoother than that of the sample fibre laser irradiated with an O_2 assist gas, signifying a less effective surface treatment. This was because of the less interaction occurring between the fibre laser-Si_3N_4 and with using the compressed air. However, the whitening effect on the top surface of the track shows that oxidation took place, but not as much as the O_2/fibre laser irradiated sample. From comparison of the compressed air/fibre laser irradiated surface to the O_2/fibre laser irradiated surface of the Si_3N_4 engineering ceramic (see Figure 5.4), shows similar effects in the near (top) surface layer. Surface oxidation is apparent as well as formation of craters where the surface has become much smoother. Although, the average of the surface finish resulted to being much coarser due to the craters comprising of gradients. This confirmed the melting and the redistribution of the melt zone. More porosity and trapped air holes are also seen in this sample.

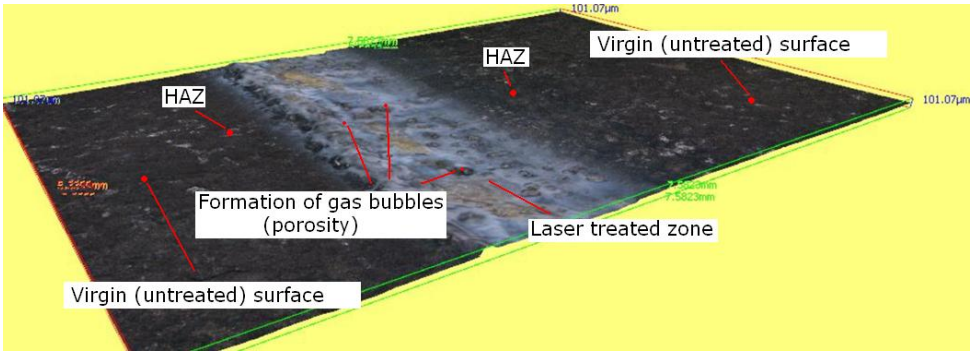

Figure 5.5 A 3-D topographical image of the surface profile of the Si_3N_4 engineering ceramic treated by fibre laser irradiation by using compressed air assist gas.

5.3.1.2.3 N_2 assist gas

Figure 5.6 shows that the sample fibre laser irradiated with an N_2 assist gas displayed a smaller laser treated track in comparison to the sample fibre laser irradiated with an O_2 assist gas (see Figure 5.4). This is due to N_2 being a non-reactive gas and therefore minimizing the effect of surface oxidation. The surface profile also presents evidence of some morphological changes on the surface of the ceramic resulting from the fibre laser treatment. The sample comprised of a smoother surface finish (0.701 µm) when compared to the as-received surface and the sample fibre laser irradiated with an O_2 assist gas. This led to less material removal in comparison with the samples treated by O_2 and was 116µm. The laser material interaction between the fibre laser by using N_2 on the Si_3N_4 ceramic may have been less in comparison to other gas types used in this study (see Figure 5.6).

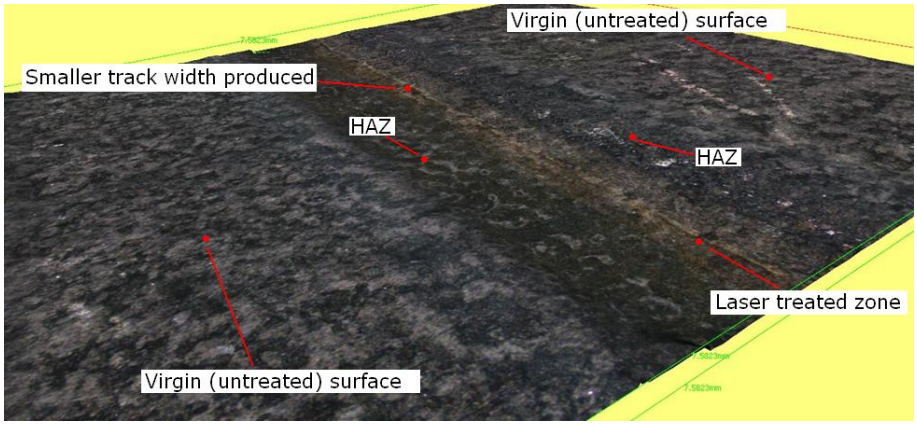

Figure 5.6 A 3-D topographical image of the surface profile of the Si_3N_4 engineering ceramic treated by fibre laser irradiation by using N_2 assist gas.

5.3.1.2.4 Ar assist gas

The surface of the sample fibre laser irradiated with an Ar assist gas (as shown in Figure 5.7), reveals similar effects compared to the surface of the sample treated with fibre laser irradiation and an N_2 assist gas (see Figure 5.6). This was, however, somewhat predictable as Ar is an inert gas which would also minimize the effect of oxidation and provide a much more protective treatment from atmosphere effects. The material removal in this case was 140µm and was slightly higher than the surfaces treated by the fibre laser irradiation by using a N_2 assist gas. The surface finish found was 1.61µm (Ra) after the laser treatment which again was rougher than that of the as-received surface.

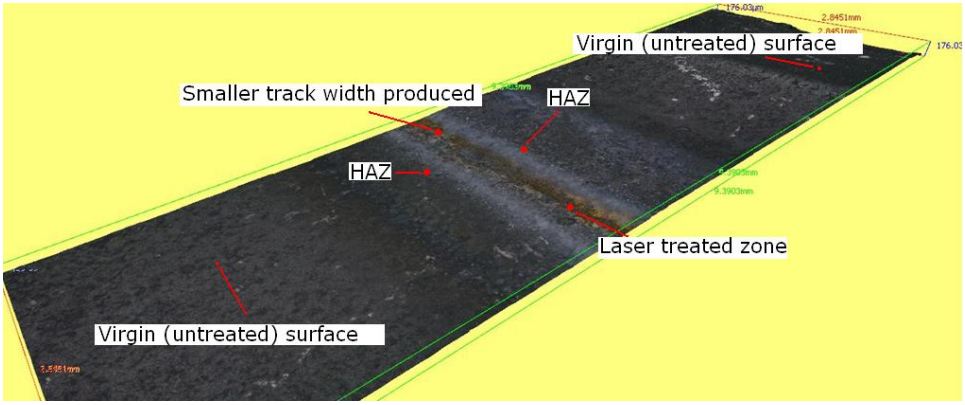

Figure 5.7 A 3-D topographical image of the surface profile of the Si_3N_4 engineering ceramic treated by the fibre laser irradiation by using Ar assist gas.

5.3.1.2.5 Ambient air (no assist gas)

The laser alone treated surface by using no assist gas produced similar result to that of the fibre laser surface treated by using the compressed air assist gas. This could be due to the compressed air having identical properties to the atmospheric gas properties which produced similar results during the laser alone treatment [120]. However, it can be observed from Figure 5.7 that there are also formations of trapped air holes on the laser treated zone. Those were not seen by using other gases

except compressed air and O_2 assist gasses. It can be gathered that the trapped air holes were formed as the surface melted and re-distributed leaving the trapped gas to form such a surface profile. The material removal was up to 162µm for this treatment (see Table 5.3). The surface finish was found to be 2.56µm (Ra) which in comparison with the as-received surface was much courser. This had occurred due to the melting and formation of the new surface layer.

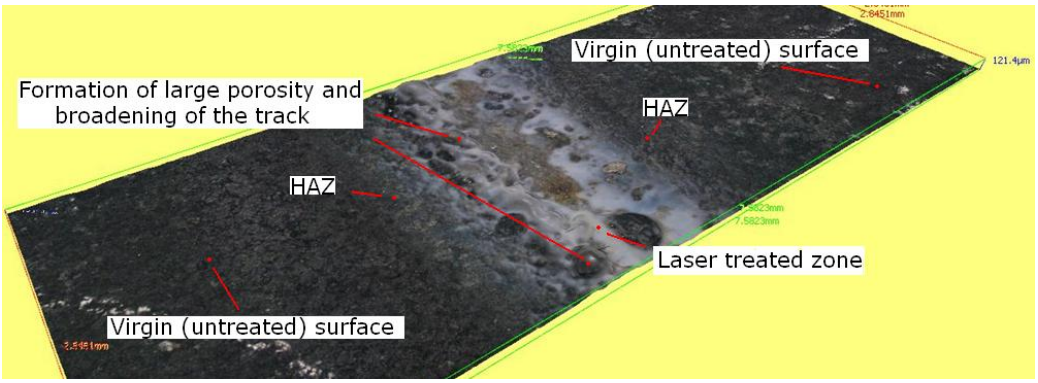

Figure 5.7 A 3-D topographical image of the surface profile of the Si_3N_4 engineering ceramic treated by the fibre laser irradiation by using ambient air (no assist gas).

Table 5.3 Summary of the effects of the material removal, the surface finish and the surface topography of the fibre laser irradiated Si_3N_4 engineering ceramic surfaces treated by using various assist gas compositions.

Condition	Material removal (µm)	Surface finish (Ra) µm	Topography			
			Presence of oxidation	Porosity	Treated Zone	HAZ
As-received surface	N/A	1.57	No	Minimal	N/A	N/A
Fibre laser treatment using O_2	257	12.1	High	Average	Large footprint	Large
Fibre laser treatment by using compressed Air	169	2.12	High	High	Large footprint	Large
Fibre laser treatment using N_2	116	0.701	Very Low	No	Fine footprint	Small
Fibre laser treatment by using Ar	140	1.61	Very Low	No	Fine footprint	Small
Fibre laser ambient air (no gas)	162	2.56	High	Very High	Large footprint	Large

5.3.1.3 The Effects of the Fibre Laser Irradiation by Using Various Assist Gases on the Morphology, Microstructure and Chemical Composition of the Si_3N_4 Engineering Ceramic

Observation of the SEM images of the sample treated by the fibre laser irradiation by using an O_2 assist gas showed a significantly modified surface profile which comprised of a newly formed surface layer (see Figure 5.9). This can also be seen with images from the other assist gases used but the effects are rather distinct from using O_2. The surface profile in this case was slightly different to that of the as-received surface as the fibre laser surface treatment had melted the top layer. The melted layer then redistributed unevenly and altered the surface finish and the chemical composition as further seen in this study. The HAZ of the surface treated with the fibre laser beam was also considerably broad in comparison with the samples treated by using other assist gases. This was because of O_2 being a reactive gas, where more chemical changes had occurred in comparison to using an inert gas. The reason for the sample treated with an O_2 assist gas producing large area of laser affected zones was due to the faster burning rate of the O_2 than the traverse speed of the laser beam as stated by Bass [121]. Bass also stated that non-metallic materials such as ceramics are more sensitive to chemical changes from using O_2. On account of this, a courser surface finish was found by using the O_2 in this investigation. If the burning rate of O_2 was slower than that of the fibre laser traverse speed, then the opposite reaction would occur where the laser treated zones would be narrow and produce a smoother surface finish. The processing temperature in this case would also be high. In general, the use of O_2 is appropriate for the fibre laser processing of ceramics if deep penetration or faster processing speeds are required. But if the surface roughness and the material removal are more important; then Ar or N_2 assist gases in particular are also ideal.

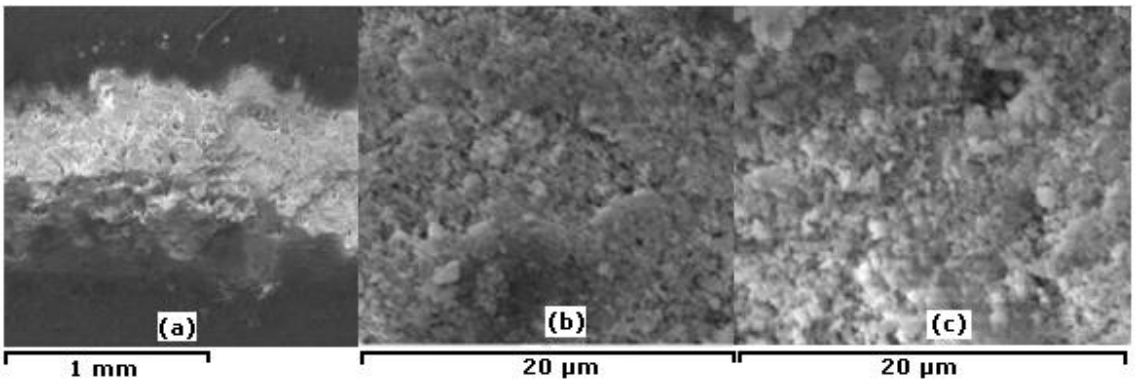

Figure 5.9 SEM images of the fibre laser irradiated surface of the Si_3N_4 by using O_2 assist gas at (a) ×50 magnification (b) ×3000 magnification and (c) the HAZ at ×3000 magnification.

The content of O_2 found on the surface of the sample fibre laser treated with an O_2 assist gas was reasonably high for obvious reasons. Up to 37 wt% of O_2 was observed and was the highest in comparison to the surfaces treated by using other assist gases. In comparison to the as-received surface the C content was reduced to 5.56 wt% and the Si content was 17.21 wt%, as further presented in Figure 5.14. There was also 17.70 wt% Y found in this sample. From this, it can be

observed that a chemical change has occurred after treatment with the fibre laser and an O_2 assist gas when compared to the as-received surface.

The fibre laser irradiated sample with a compressed air assist gas also showed significant level of morphological changes along with some de-composition (see Figure 5.10). The grains are exposed in comparison to that of the as-received sample. The level of oxidation is not in evidence as much as was the case with samples fibre laser irradiated with an O_2 assist gas. This was because of the O_2 content being lower in the elements found in the compressed air than that of the pure O_2. The chemical composition found when using compressed air was 24.39 wt% C, 37.72 wt% O_2, 30.43 wt% Si, and 4.21 wt% Y. The Si was decreased in comparison to the as-received surface, but not, however, as much as the surface fibre laser treated with an O_2 assist gas. This indicated that a compositional change had also occurred when performing the fibre laser surface treatment with using compressed air as an assist gas.

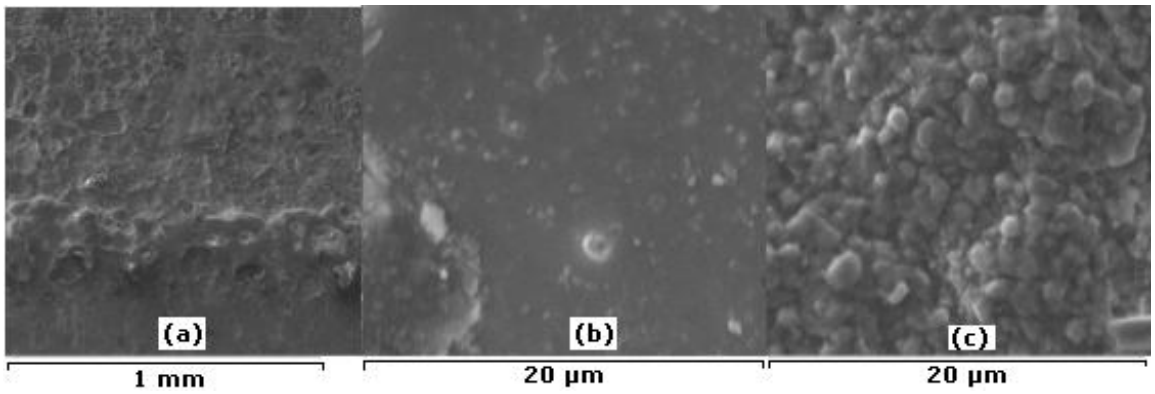

Figure 5.10 SEM images of the surface treated by fibre laser irradiation of the Si_3N_4 engineering ceramic by using compressed air assist gas at (a) ×50 magnification, (b) ×3000 magnification and (c) the HAZ at ×3000 magnification.

The morphology of a sample fibre laser irradiated with a compressed air assist gas is shown in Figure 5.10. It can be said that the surface has also undergone some de-composition due to the high temperatures produced during the laser-material interaction (in the region of over 2000°C). This in turn, produced material removal which intrinsically changed the surface morphology as the Si_3N_4 was exposed to the atmosphere at such high temperatures. The irregularity of the material removal during the de-composition of the ceramic should also be considered. This is because it has also contributed to the change in the surface morphology and the surface finish. Furthermore, the change in the morphology also depends on the how much the grains are covered and the level of bonding between the new surface layer produced by the fibre laser irradiation and the secondary phase of the Si_3N_4 ceramic. The sample treated in ambient air by using the fibre laser has some relation to the sample fibre laser irradiated with an O_2 assist gas. The laser alone (no assist gas) treated sample comprised of the highest O_2 content after the O_2 treated sample. Up to 42.60 wt% O_2 was found, as is

evident from the images shown in Figure 5.11(b) and Figure 5.11(c). This was the highest and probably occurred due to the lack of processing gas being supplied at the surface during the fibre laser-Si_3N_4 interaction and also because of the extra heat generated. This characteristically formed a high O_2 content within the surface layer treated by the fibre laser irradiation. Some areas of the treated zone also comprised of porosity that was produced from the formation of the new oxide layer. The oxide layer would have trapped the air from escaping during the solidification stage. The C content in the laser alone treated sample was 27.67 wt%, and Si being 27.73 wt%.

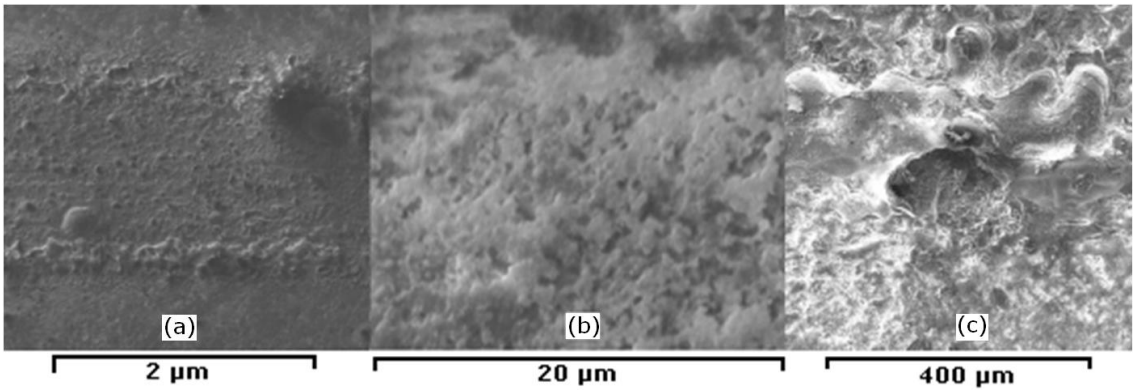

Figure 5.11 SEM images of the fibre laser alone irradiated surface of the Si_3N_4 by using no assist gas at (a) ×500 magnification, (b) ×3000 magnification and (c) the HAZ at ×3000 magnification.

SEM surface images of samples fibre laser irradiated with N_2 and Ar assist gasses are shown in Figure 5.12 and Figure 5.13, respectively. As one can see from these figures, the HAZ and the fibre laser irradiated area was much smaller and sharper when a N_2 assist gas was employed. The shape of the grains has also changed with N_2, as presented in Figure 5.12(b). This is where rod type grains have been formed in some areas which are not seen on other samples. There is also evidence of porosity formation in the interface between the HAZ and the laser treated area. This is not apparent in the surfaces treated by using the other assist gases, except for Ar. This was because of the increase in the cooling rate which allowed new surface layer be formed as gases were trapped from escaping. This was also seen in the work of Lawrence and Li [116]. It can be said that similar effects have been achieved when using N_2 and Ar, since they are both inert and less reactive to a chemical change in comparison to the other gases, including ambient air (no gas). This result is in good agreement with that of the Bass [121] and the findings of Minami *et al.* [114]. It is also believed that the temperatures reached during processing with N_2 and Ar assist gasses were much lower to those reached when using O_2, compressed air or ambient assist gasses. Yet at the same time, there was evidence of porosity found on the interface between the HAZ and the surface treated by the fibre laser irradiation for both samples that were treated with N_2 and Ar assist gasses, as can be seen in Figure 5.12 and Figure 5.13. The elemental analysis given in Figure 5.14 showed, 35.47 wt% O_2, 35.45 wt% Si, 6.99 wt% C and 10 wt% Y. The O_2 content within the sample laser treated with N_2 assist gas is the lowest in comparison to the other samples, but there is only a small amount of

difference between the O_2 content found within each of the samples. However, the use of N_2 as the assist gas certainly modified the surface profile as rod-like grains had began to form (see Figure 5.12(b)). The Si_3N_4 surface fibre laser irradiated with a N_2 assist gas also showed enlargement of the grains in comparison to the as-received surface.

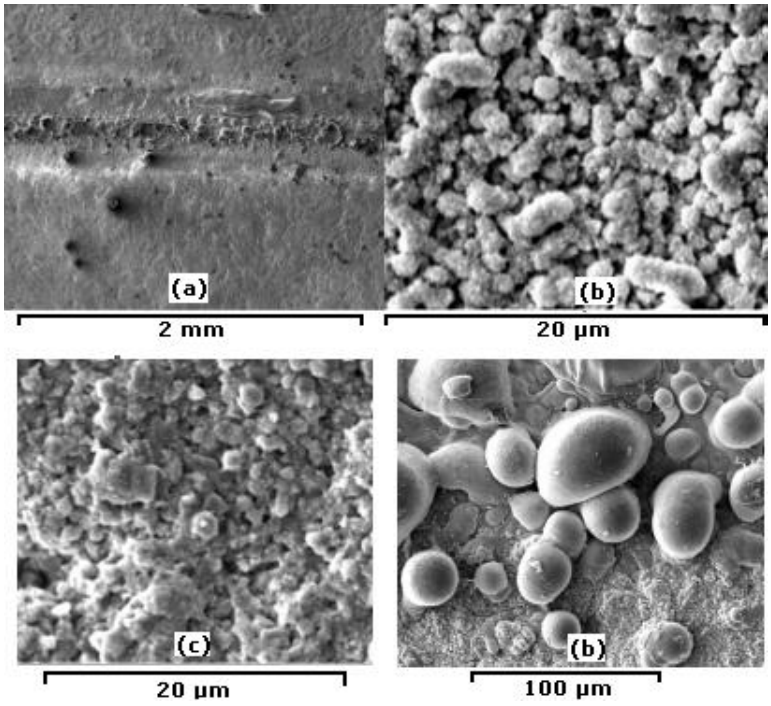

Figure 5.12 SEM images of the fibre laser irradiated surface of the Si_3N_4 by using N_2 assist gas in (a), (b) and (c) the HAZ and (d) the interface between the HAZ and the fibre laser irradiated zone.

The microscopic images in Figure 5.13(d) show evidence of the surface melting with using Ar assist gas. This in comparison to N_2 was somewhat different as the grain boundaries of the Si_3N_4 surface fibre laser irradiated with an Ar assist gas had began to bind into each other. The interface between the HAZ and the laser treated zone in Figure 5.13(c) also shows that porosity within the ceramic has been covered with the newly formed surface layer. This can relate to the concept of crack healing where the fibre laser irradiated surface areas were close to their melting temperatures and were solidified and covered the surface cracks and formed a new surface layer. Similar result was also reported by Sun *et al.* [15] during a CO_2 laser processing of a Si_3N_4 ceramics. The solidified surface however, particularly in the interface between the fibre laser irradiated surface and the HAZ showed evidence of splatter occurring from the melt-zone as the material was pushed to the side of the laser created track. This appears in all the fibre laser irradiated samples but is more present in the samples using N_2 and Ar assist gases. This indicates that there was less heat produced during the interaction of the fibre laser-Si_3N_4. Hence, the gas was being trapped before escaping between the HAZ and the fibre laser irradiated surface. The chemical composition found on this surface was 16.36 wt% C, 35.72 wt% O_2, 27.43 wt% Si and 11.70 wt% Y. The chemical composition herein is similar to that of the N_2 except with Ar/fibre laser irradiated sample. This was because there is more O_2 content

present due to the Ar not coupling well with the Si_3N_4 in comparison to N_2 so that the surface of the Si_3N_4 is protected from an atmospheric influence.

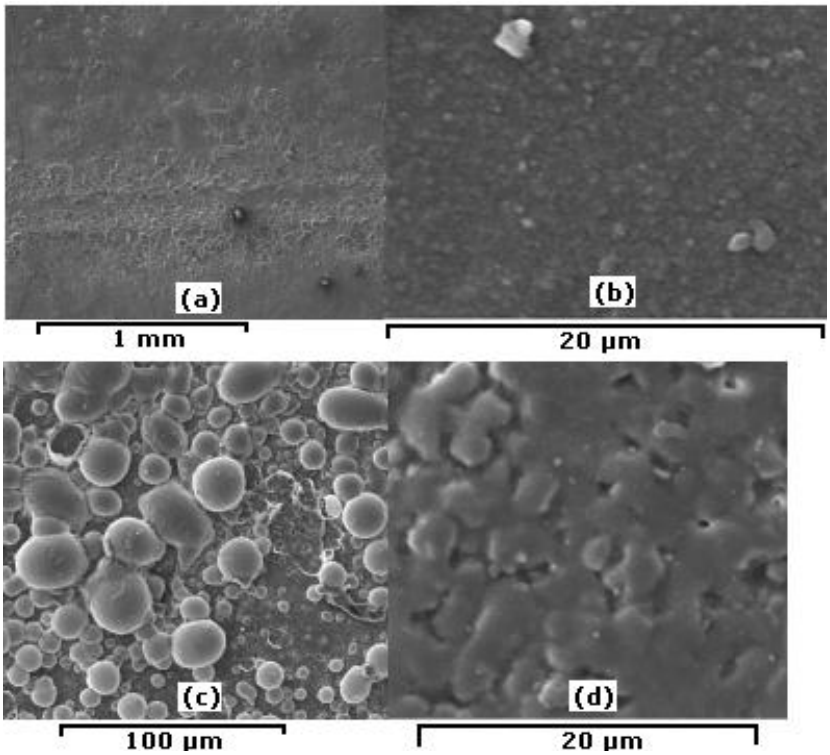

Figure 5.13 SEM images of the fibre laser irradiated surface of the Si_3N_4 engineering ceramic by using Ar assist gas in (a), (b) and (c) the interface between the HAZ and the laser treated zone and (d) the HAZ.

A chemical change has been observed on all surfaces treated by the fibre laser irradiation by using the variety of assist gases. Evidence of surface oxidation is also found with all treated samples. However, the effects are remarkable from using reactive gases in particular O_2. The sample treated in ambient condition by using no assist gas also showed similar results to that of the O_2 and compressed air assist gases. Over all, the increase in C and O_2 content has been seen for all laser processing gasses used (see Figure 5.14). This formed a new surface layer. From the five different conditions used, C, O_2 and Si as elements all appear within the treated surfaces to some extent. Owing to this, it can be said that a change in composition has taken place as the fibre laser irradiated surfaces of the Si_3N_4 engineering ceramic were altered to form SiO_2. The formation of SiO_2 was also discussed by Lysenko *et al.* [122], who reported that the SiO_2 results from heating silicon at elevated temperature (1600°C). The temperature during fibre laser processing in this study from using any of the gas compositions was much higher than 1600°C. This is evident from the topographical and the microscopic images where melt zones were found. This indicated that the formation of the SiO_2 layer was unavoidable even by using less reactive assist gases such as Ar and N_2.

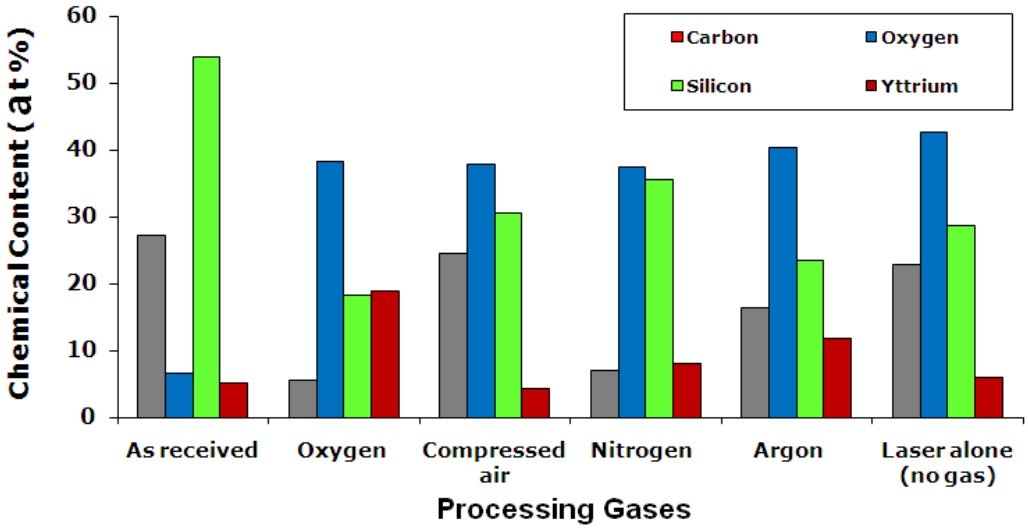

Figure 5.14 Chemical composition of the Si_3N_4 engineering ceramic in the as-received state and after fibre laser irradiation by using the different assist gas compositions.

5.3.2 Fibre Laser Surface Treatment of ZrO_2 Engineering Ceramic

5.3.2.1 Investigation of the HAZ of the fibre laser irradiated ZrO_2 engineering ceramic

It was found that a change in the surface hardness had occurred from measuring the hardness of the fibre laser irradiated surface of the ZrO_2 engineering ceramic. The hardness changed from within the laser unaffected zone to the HAZ and the fibre laser irradiated zone with all conditions applied. The hardness values are given in Table 5.4 and the depth of the diamond penetration in Table 5.5 for the various fibre laser irradiated surfaces ZrO_2 ceramics. It was found that the laser irradiated zone comprised of the softest surface layer. The hardness increased as the diamond indentation induced into the heat affected region. The interface between each zones and the untreated surface layer is also presented in Figure 5.15 where an example of the fibre laser irradiated surface by using the O_2 assist gas on the ZrO_2 is presented. The hardness was reduced to an average of 776 HV with the lowest being 756 HV and the highest being 945 HV, within the laser irradiated track as shown in the example in Figure 5.15. The hardness changed as the indenter was induces on the outer edges of the track and ranged between 1000 to 1200 HV for ZrO_2 ceramic. The induced diamond on the laser unaffected zone (as-received) surface was again different to that of the laser treated zone and the HAZ. The hardness on the laser unaffected zone was found to range between 1200 HV and 1250 HV. Table 5.4 shows the average, standard deviation and the range of the hardness values found within the respective zones investigated by using the five different treatment conditions. The change in the hardness over the fibre laser irradiated zone and the laser unaffected area established the position of the HAZ, the laser irradiated zone and the interface between each region on the surface of the ZrO_2 engineering ceramic.

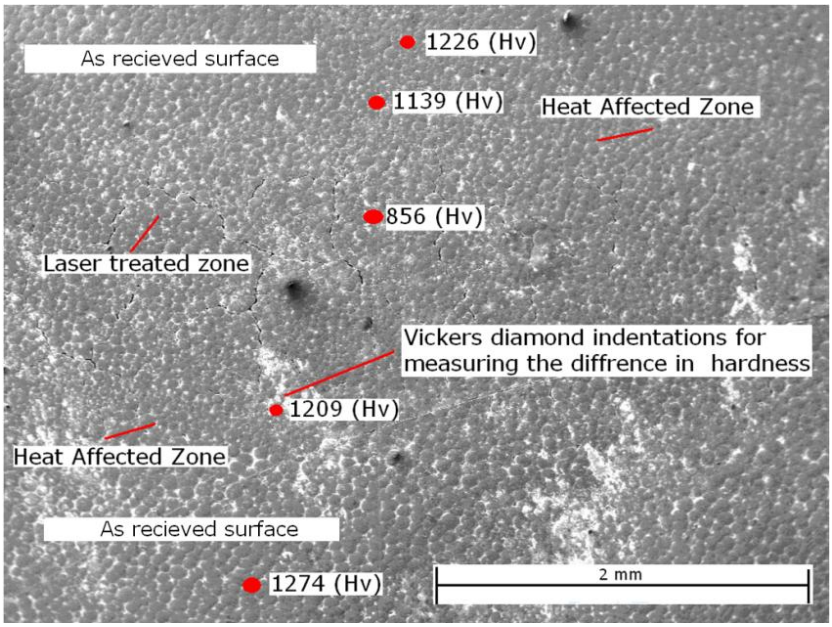

Figure 5.15 SEM image of the fibre laser irradiated surface by using O_2 assist gas, showing the HAZ, the laser unaffected zone as well as the interfaces between each zones for the ZrO_2 engineering ceramic.

Table 5.4 Change in the average hardness, STDEV and the range of hardness values found for the fibre laser irradiated zone (track) by using various assist gases, fibre laser unaffected zone and the HAZ of the ZrO_2 engineering ceramic.

Assist gases	Hardness values in various areas on the surface of the ZrO_2 engineering ceramic								
	Laser unaffected zone			Fibre laser irradiated track			HAZ		
	Average hardness (HV)	STDEV	Range	Average hardness (HV)	STDEV	Range	Average hardness (HV)	STDEV	Range
O_2	1270	50	1226 - 1325	944	32	797 - 974	1233	150	1047 - 1405
Ar	1257	70	1139 - 1337	1070	74	970 - 1104	1234	59	1129 - 1274
Compress-ed air	1205	46	1160 - 1263	1037	29	1256 - 1171	1206	75	1104 - 1261
N_2	1211	47	1261 - 1160	1076	134	1104 - 1261	1217	36	1170 - 1256
Ambient air (no assist gas)	1239	97	1119 - 1377	993	29	957 - 1016	1209	139	1029 - 1406

Table 5.5 Depth of penetration by the Vickers diamond indentation at 30 kg load inhibited on the fibre laser irradiated surfaces of the ZrO_2 engineering ceramic treated by using various assist gases.

Assist gases	Depth of penetration (µm)
O_2	30.55
Ar	29.65
Compressed air	31.77
N_2	30.37
Ambient air	31.24

5.3.2.2 The topographical effects of the fibre laser surface treatment of the ZrO_2 engineering ceramic by using various processing gases

Figure 5.16(a) presents topographical image of the fibre laser irradiated surface of the ZrO_2 ceramics by using various assist gas. The thermal energy induced by the fibre laser has led to some discoloration as shown in Figure 5.16(a-e). The discoloration of the laser irradiated ZrO_2 is expected due to the thermal energy induced. Thermal exposure of the ZrO_2 at elevated temperatures of over 2500°C would decompose and transpose the ceramic to black. In this case, the fibre laser irradiated ZrO_2 has transformed from white to light grey (as shown in Figure 5.16(a-e)). Melting of the surface is not apparent from the topographical images. However, further analysis by using the SEM has revealed some degree of surface melting which can allow one to postulate that the surface temperatures at the fibre laser-ZrO_2 interface would have ranged from 2300°C to 2500°C. The surface fibre laser irradiated by using the O_2 assist gas produced 73µm of material removal from the top (near) layer. This was the highest when compared to other conditions. This was because of the O_2 being a highly active gas which produced an exothermic reaction and supported the blackening of the near surface layer of the ZrO_2 ceramic. The surface finish found with the treated zone was 0.745µm (Ra). This was much smoother than the as-received surface indicating that the surface finish was enhanced after the fibre laser irradiation by using the O_2 assist gas. This is because the O_2 assist gas is much more reactive than other gas compositions. This would enhance the fibre laser-ceramic interaction which and would inherently generate higher processing temperature and create partial melting of the ceramic which is somewhat smother than the as-received surface layer. The result in a previous investigation by Minami *et al.* and Lawrence *et al*. also described O_2 to be a highly active assist gas for laser processing of ceramic tile grout.

The surface finish of the laser treated ZrO_2 by using compressed air (see Figure 5.16 (b)) was 0.561µm (Ra). The materials removal was up to 65µm. The surface finish was enhanced in comparison with the as-received surface. Though, it was not significantly different to the sample fibre laser irradiated by using O_2 assist gas. This was because the compressed air has similar

composition to that of the O_2 assist gas. This resulted in producing similar effects. The fibre laser treated track was found to be significantly large also along with a large HAZ in comparison to those surfaces fibre laser irradiated by using Ar and N_2 assist gases.

The surface of the sample fibre laser irradiated by using an N_2 assist gas (see Figure 3(c)) was 0.532µm (Ra). This showed little difference in comparison with the samples fibre laser treated by using the other gases. The surface finish was improved after the fibre laser treatment in comparison with the surface of the as-received sample. The material removal was slightly lower in comparison with the sample treated by O_2 and was up to 62µm. This was due to the N_2 assist gas being less reactive in comparison to O_2. Therefore, would produce less of the interaction between the fibre laser and the ZrO_2 engineering ceramic. Moreover, the processing temperature by using N_2 is also lower compared to the O_2 as an example. This would generate less heat and lower ablation.

The sample fibre laser irradiated by using an Ar assist gas also presented similar effects to those observed when using N_2 assist gas. This was perhaps to be expected as Ar is also an inert gas and would characteristically generate less of a reactive interaction zone between the fibre laser and the ZrO_2 engineering ceramic surface. The materials removal was 60µm with a surface finish of 0.469µm (Ra). The laser surface treatment using no assist gas (see Figure 5.16(d)) produced the roughest surface finish. The surface roughness value found was 0.736µm (Ra). Materials removal in this case was up to 63µm. This proved to be similar when compared to the other samples fibre laser irradiated by using reactive gases. This was due to the laser beam alone coupling with the atmospheric gas molecules to form a similar effect on the ZrO_2 ceramic as no assist gas was applied to compliment the surface treatment. The effects of the material removal, the surface finish and the surface topography of the fibre laser irradiated surface of the ZrO_2 engineering ceramic by using various assist gas compositions are presented in Table 5.6.

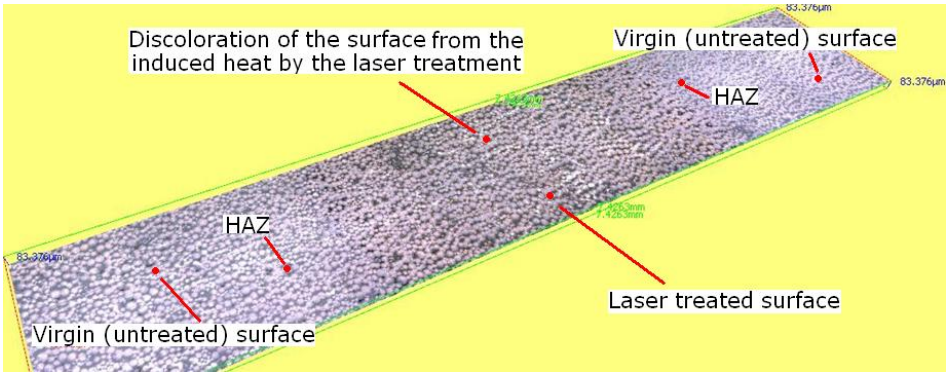

(a)

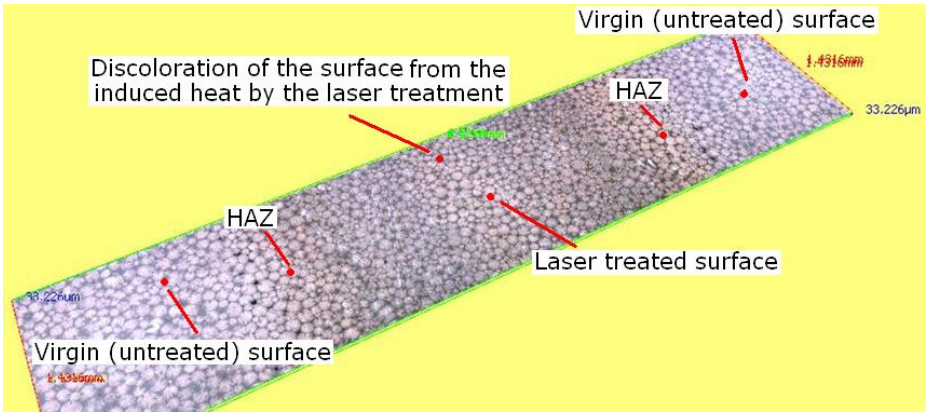

(b)

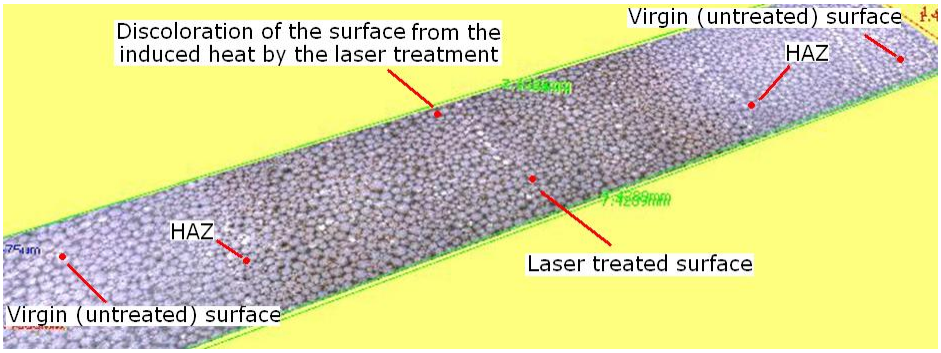

(c)

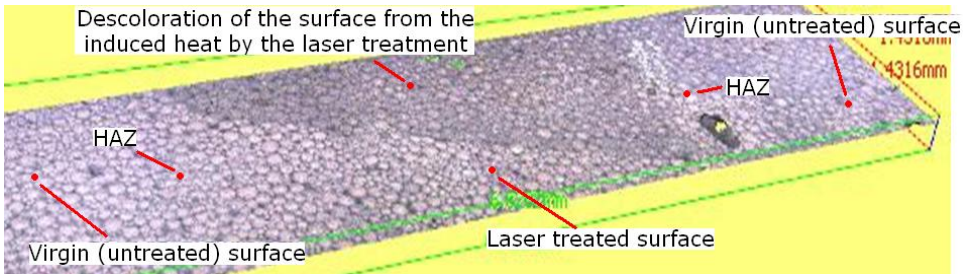

(d)

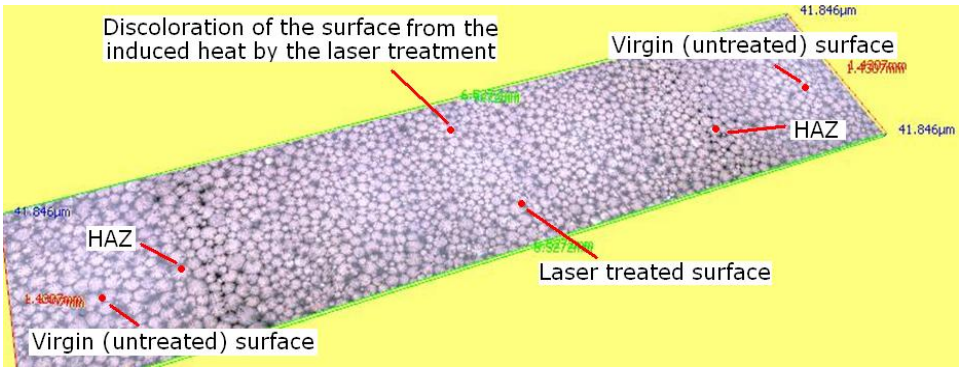

(e)

Figure 5.16 Topographical images of the surface profile of the ZrO_2 engineering ceramic treated with fibre laser irradiation when employing (a) an O_2 assist gas, (b) a compressed air assist gas, (c) a N_2 assist gas, (d) an Ar assist gas and (e) ambient air (no assist gas).

Table 5.6 Effects of the material removal, the surface finish and the surface topography of the surface treated with the fibre laser irradiation of the ZrO_2 engineering ceramic by using various assist gas compositions.

	Material removal (µm)	Surface finish (Ra) µm	Topography			
			Presence of oxidation	Porosity	Treated Zone	HAZ
As-received surface	N/A	1.56	low	Minimal	N/A	N/A
Fibre laser treatment by using O_2	73	0.74	low	Minimal	Large footprint	Large
Fibre laser treatment by using compressed Air	65	0.56	low	Minimal	Large Footprint	Large
Fibre laser treatment by using N_2	62	0.53	low	Minimal	Fine Footprint	Small
Fibre laser treatment by using Ar	60	0.46	low	Minimal	Fine footprint	Small
Fibre laser alone treatment (no gas)	63	0.73	low	Minimal	Large footprint	Large

5.3.2.3 Microscopic analysis and the effect of the fibre laser irradiation by using the various assist gases on the chemical composition of the ZrO_2 engineering ceramic

5.3.2.3.1 O_2 assist gas

The surface of the sample fibre laser irradiated when an O_2 assist gas was employed produced some melting of the top surface layer (see Figure 5.17). The grain boundaries herein had begun to close off and bind together. This inherently, produces an interlocking microstructure and enhanced the surface strength and resistance to fracture. This finding complimented the one in Chapter 6. The compositional analysis showed that the C content within the ceramic was increased to 12.77 wt% compared to the as-received sample by over 50%. This indicated that the laser processing resulted to the ceramic comprising of the C content because the C content generally existing in the atmosphere. The content of O_2 maintained in the same region to the as-received surface and was 24.49 wt% and Zr was 62.74 wt% as further presented in Figure 5.22.

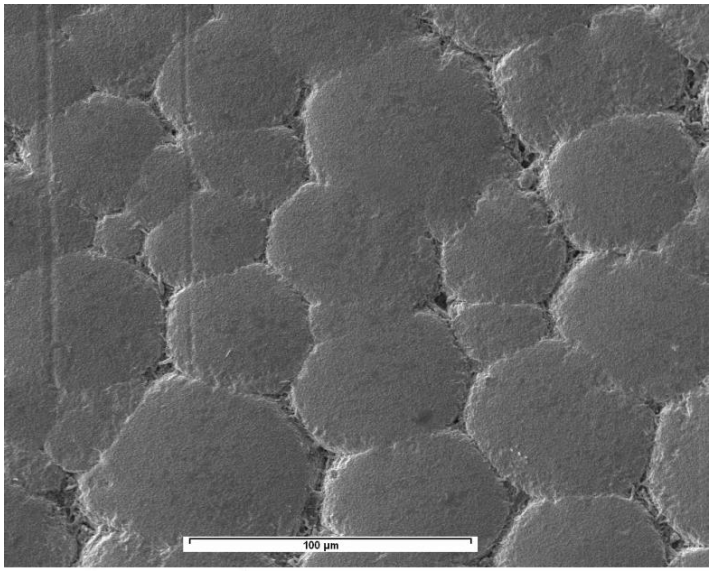

Figure 5.17 SEM image of the surface of a ZrO_2 engineering ceramic fibre laser irradiated by using an O_2 assists gas at x 500 resolution.

5.3.2.3.2 Compressed air assist gas

With using the compressed air as a processing gas, it was found that there was also some degree of surface melting that occurred during the laser-ZrO_2 interaction. This is shown on Figure 5.17(a) and (b), where the agglomerate boundaries have also begun to bond and interlock as the surface had partially melted. The C content increased to 9.52 wt% when compared to the laser unaffected surface. The O_2 content remains similar to that of the as-received surface and Zr content was 65.22 wt% (see Figure 5.22).

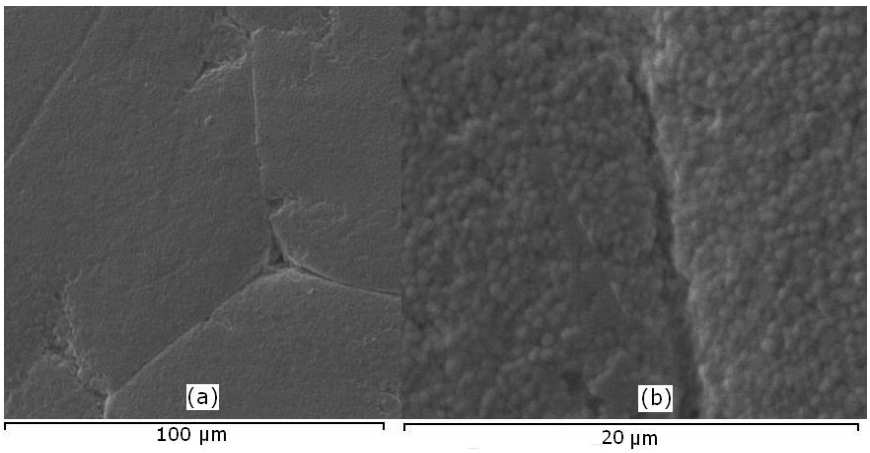

Figure 5.17 SEM image of the surface of a ZrO_2 engineering ceramic sample fibre laser irradiated by using compressed air assist gas at (a) x 500 and (b) x 3000 resolution.

5.3.2.3.3 N_2 assist gas

From observing the SEM images in Figure 5.19(a) and Figure 5.19(b) it can be gathered that the surface fibre laser irradiated with an N_2 assist gas showed the least amount of laser-material interaction. This was due to the surface melting (in this case) being minimal in comparison with

other samples. Yet, the gap between the agglomerate boundaries has decreased in comparison to the as-received surface, but generated minimal amount of material removal. The compositional analysis as presented in Figure 5.22 showed 12.76 wt% C, 22.73 wt% O_2 and 64.41 wt% Zr. The C content in this case increased with O_2. Thus, N_2 decreased in comparison to the as-received surface. The increase in the C content may have occurred during the melting, vaporization and material removal of the ZrO_2 engineering ceramic.

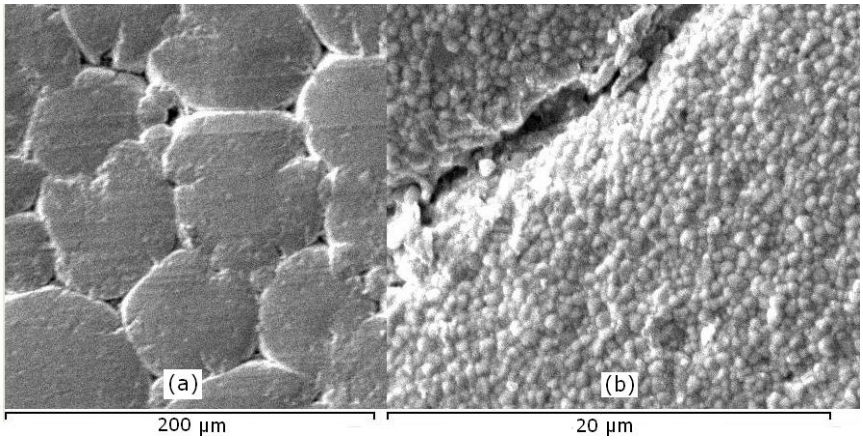

Figure 5.19 SEM image of the surface of a ZrO_2 engineering ceramic sample fibre laser irradiated by using N_2 assist gas at (a) x250 and (b) x3000 resolution.

5.3.2.3.4 Ar assist gas

The surface morphology of the sample fibre laser irradiated with an Ar assist gas showed considerable amount of modification to the near surface layer as shown in Figure 5.20(a) and Figure 5.20(b). The agglomerate boundaries showed some melting and redistribution. This had closed off the gaps that existed prior to the fibre laser surface treatment. This is markedly apparent in the sample treated by the fibre laser irradiation with an Ar assist gas in comparison to those treated under the other assist gases. Moreover, strengthening of the surface could occur due to a possibility of a phase transformation during heating (from ambient conditions) and close to melting temperature. This would have led phase transformation from the M-phase to the T-phase at around 1200ºC followed by a possible change to the C-phase (see Chapter 7 for phase transformation). Thus, during the transformation from M-phase to T-phase would have led to the binding of the agglomerate boundaries and enhanced surface strength. This was also documented in the work of Sakuma *et al.* [123], who showed that the fracture strength was achieved during an active dual phase transformation of T+M phase within a ZrO_2 ceramic during a sintering process. This in comparison with the other samples was the most influenced sample by the fibre laser irradiation when microstructure modifications are considered. This showed that the interaction of Ar with the other samples was better in surface modification ZrO_2 ceramic. The compositional study (see Figure 5.22) revealed 23.70 wt% O_2, 9.94 wt% C, and 66.36 wt% Zr.

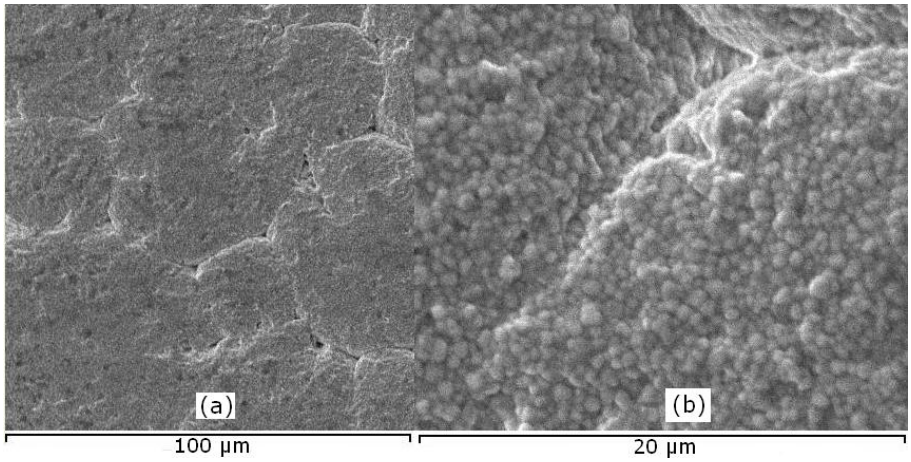

Figure 5.20 SEM image of the surface of a ZrO_2 engineering ceramic sample fibre laser irradiated by using an Ar assist gas at (a) x500 and (b) x3000 resolution.

5.3.2.3.5 Ambient air (no gas)

The fibre laser irradiated sample in ambient air (see Figure 5.21(a) and Figure 5.21(b)) proved to be less reactive as the gaps between the agglomerate boundaries were not greatly affected particularly when compared to samples treated by Ar, O_2, and compressed air. The samples fibre laser irradiated with N_2 illustrated similar results but in that case, the material removal and the surface roughness were both slightly higher. This indicated that the more interaction between the fibre laser and the ZrO_2 had also occurred. Hence, it can be summarized that the processing gas of a particular composition is required in order to achieve a considerable amount of effect during the fibre laser irradiation when micro-structural modifications are considered. The composition found on the fibre laser alone treated samples was 17.91 wt% C, 23.42 wt% O_2 and 57.66 wt% Zr as presented in Figure 5.22. The carbon content was the highest and Zr content was the lowest for this sample in comparison to all other samples. The content of Zr was found to have reduced in comparison to the as-received surface after the fibre laser surface treatment was performed by using ambient air and all other assist gases. The discolouration of all the surfaces (see Figure 5.16(a-e)) was a good indication of this to have occurred. This was because of the induction of the thermal energy as well as generation of the C content being absorbed within the top layer of the ZrO_2 engineering ceramic would have led the fibre laser treated surfaces to change colour and blacken.

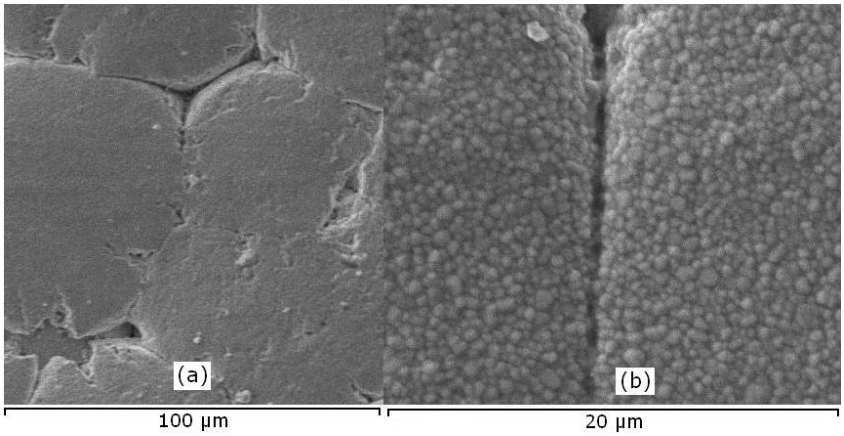

Figure 5.21 SEM image of the ZrO_2 engineering ceramic irradiated with fibre laser alone (no-assist gas) by using no processing gas, (a) at x500 and (b) x3000 resolution.

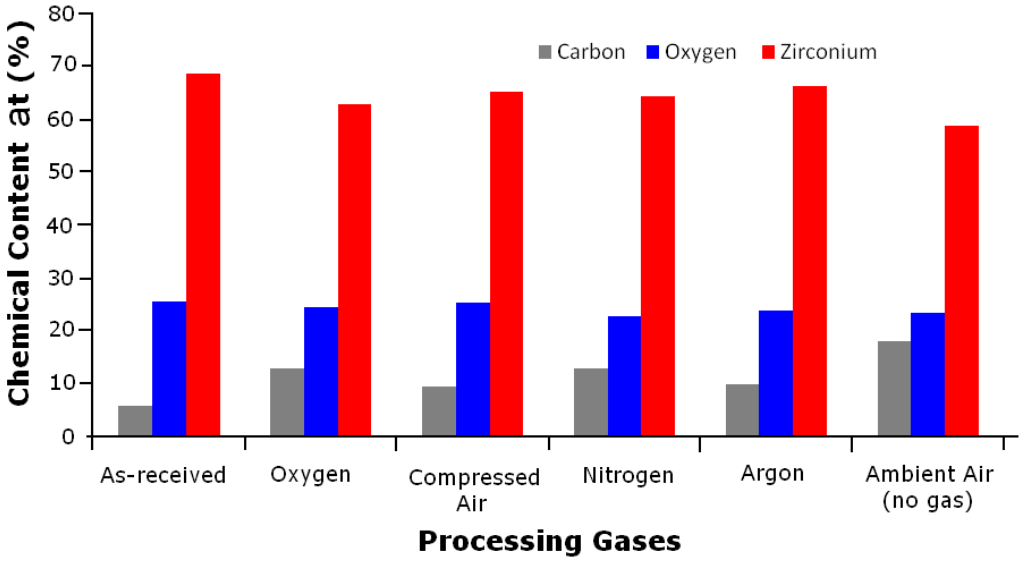

Figure 5.22 Chemical composition of the ZrO_2 engineering ceramic for the as-received, fibre laser alone and fibre laser treated surface by using different gases.

5.3.3 CO_2 Laser Surface Treatment of the Si_3N_4 Engineering ceramic

5.3.3.1 Investigation of the heat affected zone (HAZ) of Si_3N_4 engineering ceramic

By measuring the surface hardness of the CO_2 laser irradiated surface of the Si_3N_4 ceramic it was found that the CO_2 laser treatment resulted in a change in the surface hardness on the various zones of the Si_3N_4. This was also found for the fibre laser irradiated surface of the Si_3N_4 engineering ceramic. The hardness changed from within the untreated zone to the HAZ and the CO_2 laser irradiated zone. An example of the hardness values are given in Figure 5.23 and are further presented in Table 5.7. The CO_2 laser irradiated zone comprised of the softest surface layer. The hardness increased as the diamond indentation induced into the heat affected region, the interface between each zones and the untreated surface layer. The example shown in Figure 5.23 for the CO_2 laser irradiated surface by using compressed air showed that the hardness was reduced to 967 HV on the track and ranged between 730 to 1079 ±10% HV on the outer edges of the CO_2 laser treated track.

The hardness increased along the edges of the track indicating that the respective surface layer was less influenced. The untreated surface (see Figure 5.23) on both sides of the track, ranged from 1400 to 1600 HV ±10% HV.

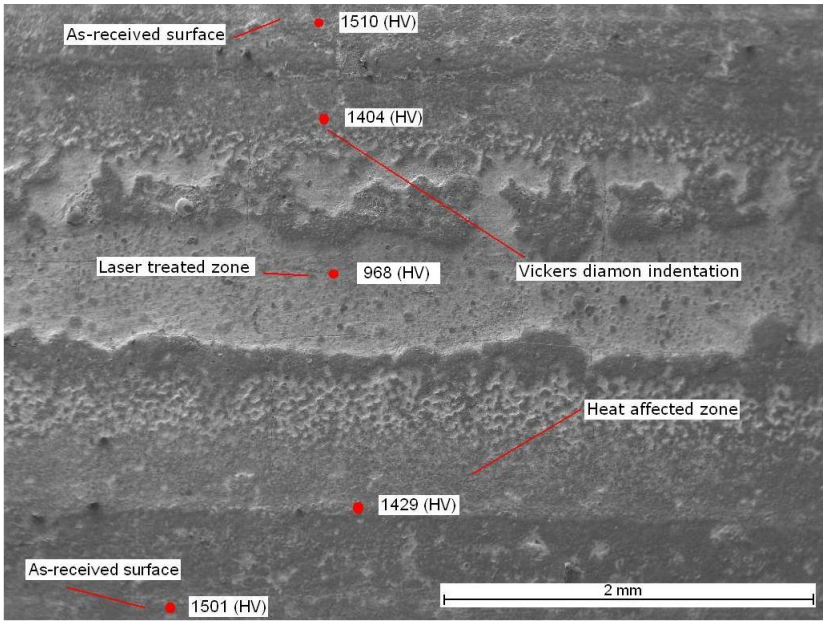

Figure 5.23 SEM image presents an example of the CO_2 laser irradiated surface of the Si_3N_4 by using compressed air showing the fibre laser unaffected surface, fibre laser irradiated surface and the HAZ.

The penetration depth of the Vickers diamond indentation for the various surfaces irradiated by the CO_2 laser and the different assist gases is presented in Table 5.8. Similarly to the fibre laser irradiated surfaces of the Si_3N_4 engineering ceramic; the CO_2 laser irradiated surface has also produced variation in the depth of the diamond indentation when using a 30 kg indentation load. This was also due to the formation of the SiO_2 layer. With the CO_2 laser irradiated surface, the SiO_2 layer was thicker and more distinct in comparison to that of the fibre laser irradiated surface of the Si_3N_4. Therefore, asperities and the changes in the surface morphology with the different gas compositions used were more extreme. The diamond indentation penetrated into the CO_2 laser irradiated surface in this case was the deepest for the CO_2 laser irradiated sample with compressed air followed by ambient air, O_2, N_2 and Ar being the lowest. Evidence of the SiO_2 layer can be found on each of the surface of the CO_2 laser irradiated track by using the different conditions. The change in the diamond indentation depth has occurred due to the variation in the thickness of the SiO_2 surface. The values in Table 5.7 correlates with the amount of O_2 content the CO_2 laser irradiated surfaces of the Si_3N_4 engineering ceramic has (see Figure 5.34). Increase in the O_2 content results to the SiO_2 layer being thicker and appears to be considerably softer to the laser unaffected surface (as-received) of the Si_3N_4. This had also occurred in comparison to the fibre laser irradiated surface of the Si_3N_4. Though, the softening effect of the CO_2 laser irradiated surface was much higher and the

hardness was also much lower for the CO_2 laser irradiated surface in comparison to the fibre laser irradiated surface. The reason for the larger laser being produced by the CO_2 laser surface treatment was because of more laser material interaction occurring at the surface of the Si_3N_4 ceramic in comparison to the fibre laser.

Table 5.7 Showing the change in the average hardness, STDEV and the range of hardness values found for the CO_2 laser irradiated zone (track) by using various assist gases, CO_2 laser unaffected zone and the HAZ of the Si_3N_4 engineering ceramic.

Assist gases	Hardness values in various areas on the surface of the Si_3N_4 engineering ceramic								
	Laser unaffected zone			CO_2 laser irradiated track			HAZ		
	Average hardness (HV)	STDEV	Range	Average hardness (HV)	STDEV	Range	Average hardness (HV)	STDEV	Range
O_2	1471	102	1377 - 1643	970	30	919 - 999	1371	62	1273 - 1433
Ar	1513	52	1574 - 1463	974	76	790 - 1099	1419	79	1324 - 1557
Compress -ed air	1470	75	1377 - 1557	917	166	730 - 1099	1411	33	1377 - 1463
N_2	1452	70	1377 - 1549	977	96	749 - 1079	1396	74	1509 - 1311
Ambient air	1501	102	1405 - 1643	946	63	749 - 1016	1433	106	1541 - 1261

Table 5.8 Depth of penetration by the Vickers diamond indentation at 30 kg load induced on the CO_2 laser irradiated surfaces of the Si_3N_4 treated by using various assist gases.

Assist gases	Depth of penetration (µm)
O_2	42.31
Ar	40.75
Compressed air	42.57
N_2	41.74
Ambient air	42.47

5.3.3.2 The effects of the CO_2 laser surface treatment by using various assist gases on topographical characteristics

5.3.3.2.1 O_2 assist gas

The topography of the CO_2 laser surface treatment of the Si_3N_4 engineering ceramic by using the O_2 assist gas is presented in Figure 5.24. The profile of the track shows a complete modification to the surface by formation of the oxide layer. This in comparison to that of the fibre laser treated sample by using O_2 assist gas is similar, but is more significant in terms of the width of the track and depth

of the oxide layer. Material removal of up to 560µm and surface roughness of 5.60µm was found as presented in Table 5.9. This in comparison with any other samples showed the highest materials removal as well as the surface roughness. This was due to the O_2 gas being more reactive along with the surface interaction of the Si_3N_4 ceramic with the CO_2 laser in terms of the wavelength was considerably higher in comparison to the fibre laser. The laser treated zone also showed high level of discolouration indicating that the surface was oxidized along with formation of porosity as further presented in Figure 5.24.

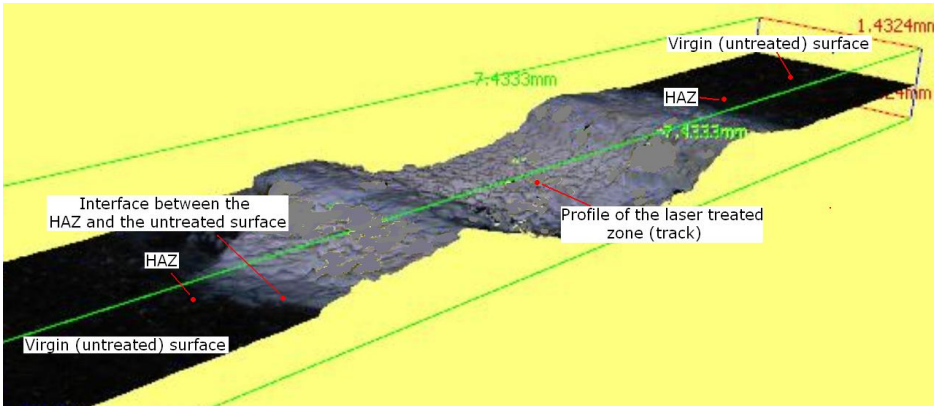

Figure 5.24 A 3-D topographical image of the surface profile of the Si_3N_4 engineering ceramic treated by CO_2 laser irradiation by using O_2 assist gas.

5.3.3.2.2 Compressed air assist gas

Surface profile of the Si_3N_4 ceramic irradiated by the CO_2 laser by using compressed air is illustrated in Figure 5.25 and showed a much smother surface finish (2.19µm (Ra)). The materials removal was up to 124µm and was smaller than that of the O_2/CO_2 laser treated sample. Considerable amount difference in the material removal was found when compared to the sample CO_2 laser irradiated by using O_2 assist gas. This occurred due to O_2 being more reactive than compressed air. Sufficiently thick oxide layer was produced from the CO_2 laser irradiated surface of the Si_3N_4 ceramic by using the compressed air assist gas. This in comparison to the surface treated with other conditions was thicker except the sample CO_2 laser irradiated by using the O_2 assist gas. The surface finish had become smoother in this instance in comparison to the sample CO_2 laser irradiated with O_2 assist gas and had possibly occurred as there was much lower material removal. This in turn, would have led to producing a lower surface roughness in comparison. However, in any case the CO_2 laser produced a rougher surface finish in comparison to the as-received surface. This was due to the uneven oxide layer created which was thicker in some areas than others.

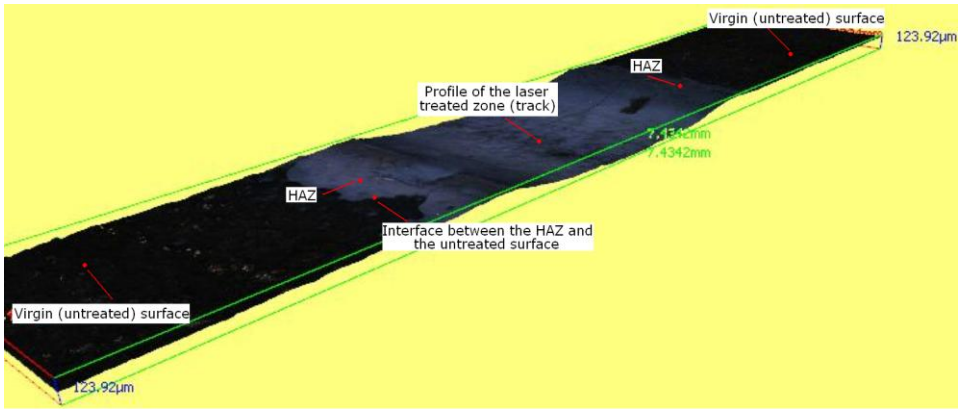

Figure 5.25 A 3-D topographical image of the surface profile of the Si_3N_4 engineering ceramic treated by CO_2 laser irradiation by using compressed air assist gas.

5.3.3.2.3 N_2 assist gas

The CO_2 laser irradiated surface by using the N_2 assist gas is presented in Figure 5.26 and showed over 121µm of material removal and a surface finish of 1.03µm (Ra). Both values were much bigger in comparison with the surface treated by the Ar but not O_2 or compressed air. From observing the CO_2 laser treated track; it can be seen that the depth of the track was not significantly large as opposed to the other CO_2 laser irradiated samples of the Si_3N_4 by using the various assist gases. The surface roughness was somewhat enhanced in comparison to the as-received surface and the CO_2 laser irradiated surface of the Si_3N_4 ceramic by using all the gases except Ar. The effect of oxidation in general was also smaller in this sample in comparison to the more reactive gases such as O_2, compressed air and ambient air.

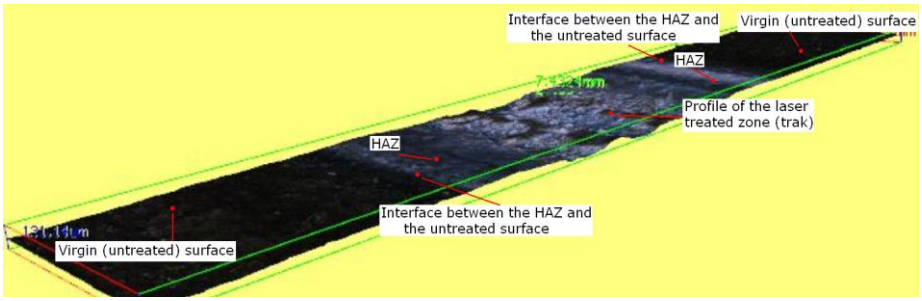

Figure 5.26 A 3-D topographical image of the surface profile of the Si_3N_4 engineering ceramic treated by CO_2 laser irradiation by using N_2 assist gas.

5.3.3.2.4 Ar assist gas

CO_2 laser treatment of Si_3N_4 by using Ar produced over 110µm of material removal. The roughness found after the treatment was 0.60µm (Ra). This was the smoothest from all the samples and comprised of the lowest material removal. The surface had changed colour and was affected by oxidation but the effect was somewhat smaller in comparison to the reactive gases. This was so due to the Ar being an inert gas. It can be observed from Figure 5.27 that the surface was not affected by oxidation in comparison to the samples treated by the reactive gases. This is expected as Ar being an

inert gas would have minimized the effects caused by the atmosphere that are present in the other treated samples.

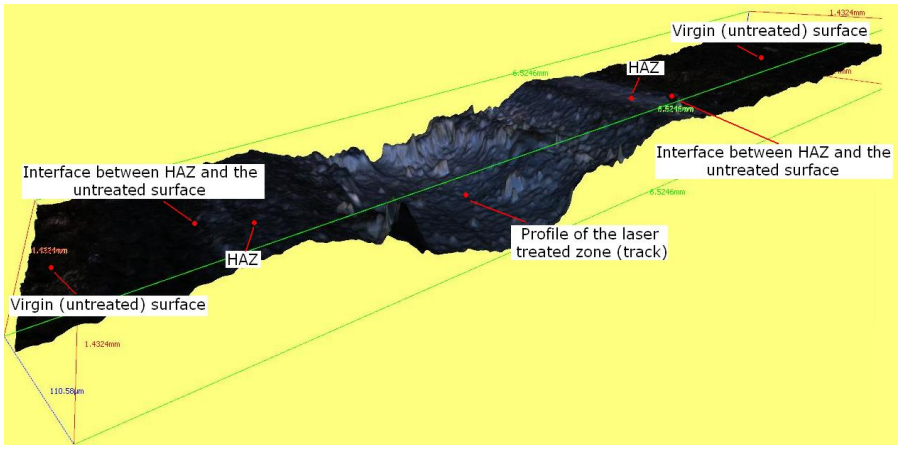

Figure 5.27 A 3-D topographical image of the surface profile of the Si_3N_4 engineering ceramic treated by CO_2 laser irradiation by using Ar assist gas.

5.3.3.2.5 Ambient air (no assist gas)

Figure 5.27 illustrates the topographical view of the CO_2 laser irradiated surface by using the ambient air assist gas. Considerable amount of oxidation was also gathered within the CO_2 laser irradiated track and with significant level of deformation of the surface where the laser beam made the interaction. The materials removal for this particular sample was 153µm with a surface roughness of 3.60µm (Ra). The surface roughness and the material removal were both second highest for this sample, followed by the sample CO_2 laser irradiated by using O_2 assist gas.

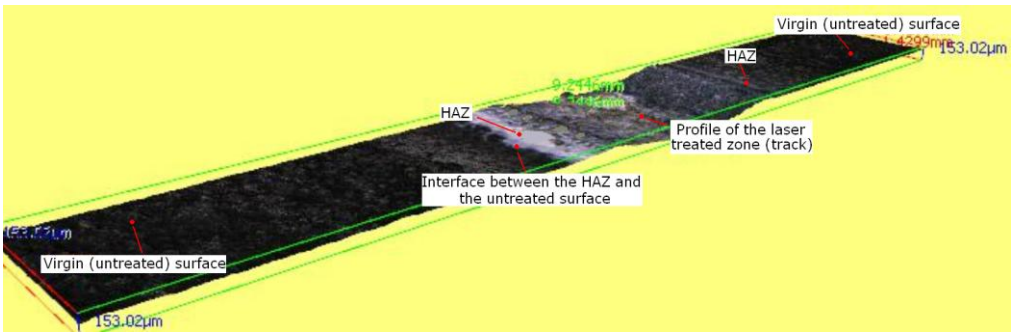

Figure 5.27 A 3-D topographical image of the surface profile of the Si_3N_4 engineering ceramic treated by CO_2 laser irradiation by using laser alone assist gas.

Table 5.9 The effects of the material removal, the surface finish and the surface topography of the CO_2 laser irradiated Si_3N_4 engineering ceramic surfaces treated by using various assist gas compositions.

Condition	Material removal (µm)	Surface finish (Ra) µm	Topography			
			Presence of oxidation	Porosity	Treated Zone	HAZ
As-received surface	N/A	1.57	No	Minimal	N/A	N/A
CO_2 laser treatment using O_2	560	5.60	High	Average	Large footprint	Large
CO_2 laser treatment using compressed Air	124	2.19	High	High	Large footprint	Large
CO_2 laser treatment using N_2	121	1.03	Very Low	Minimal	Fine footprint	Small
CO_2 laser treatment using Ar	110	0.60	Very Low	Minimal	Fine footprint	Small
CO_2 laser ambient air (no gas)	153	3.60	High	Very High	Large footprint	Large

5.3.3.3 The effects of the CO_2 laser irradiation by using various assist gases on morphological characteristics, microstructure and chemical composition

5.3.3.3.1 O_2 assist gas

The formation of porosity after the CO_2 laser surface treatment has also occurred and is presented by the SEM micrograph in Figure 5.29. This surface in comparison with the surface of the as-received Si_3N_4 (see Figure 5.1) shows a significant difference after the CO_2 laser treatment. It can be gathered that surface melting has occurred when comparing the laser treated and as-received surfaces. The overall surface roughness has increased due to the formation of porosity and formation of the uneven oxide layer. From comparing the SEM images of the fibre laser irradiated surface of the Si_3N_4 with O_2 assist gas (see Figure 5.9) and the CO_2 laser irradiated Si_3N_4 with O_2 assist gas (see Figure 5.29), it is found that the effects of the CO_2 laser surface treatment were greater than that of the fibre laser on the surface as a larger laser affected zone was discovered. The compositional analysis showed the surface comprised of 42.25 wt% O_2, 22.57 wt% C, and 35.16 wt% Si as presented in Figure 5.34. The content of O_2 was much higher from all the elements found within the CO_2 laser irradiated sample by using O_2 assist gas. This in comparison with the as-received surface was somewhat

different as N_2 was lost after the treatment along with increase in the O_2 content and decrease in the C content. The results herein agrees with the results found with the work conducted by Lawrence *et al*. [116] and Minami *et al.* [114] by using the HPDL.

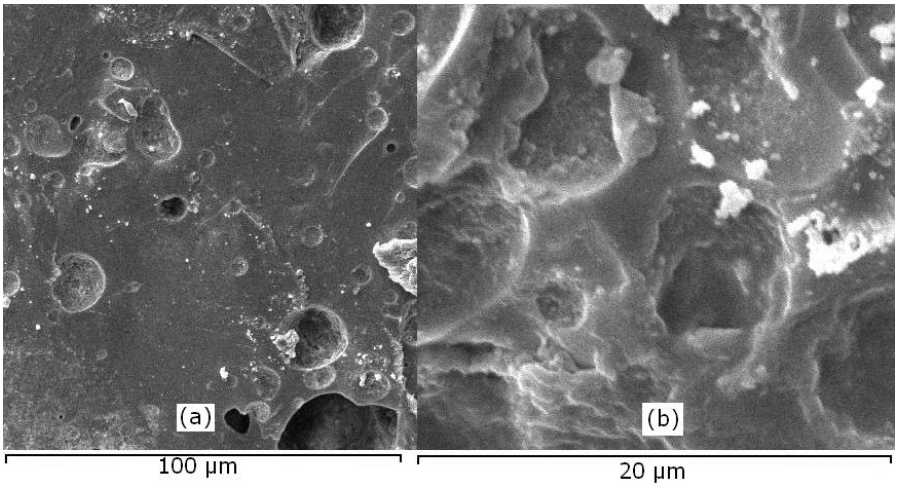

Figure 5.29 SEM images of the CO_2 laser alone irradiated surface of the Si_3N_4 engineering ceramic by using O_2 assist gas at (a) ×500 magnification and (b) ×3000 magnification.

5.3.3.3.2 Compressed air

The formation of pores on the surface of the CO_2 laser irradiated Si_3N_4 ceramic by using the compressed air assist gas can be seen from Figure 5.30(a). Modification of the surface morphology is also evident as the oxide layer has been formed on the top surface layer after the CO_2 laser surface treatment was conducted by using the compressed air assist gas. The compositional analysis showed that 42.26 wt% O_2, 21.77 wt% C, and 35.96 wt% Si was found. The O_2 content was not much different to that of the sample CO_2 laser irradiated by using the O_2 assist gas.

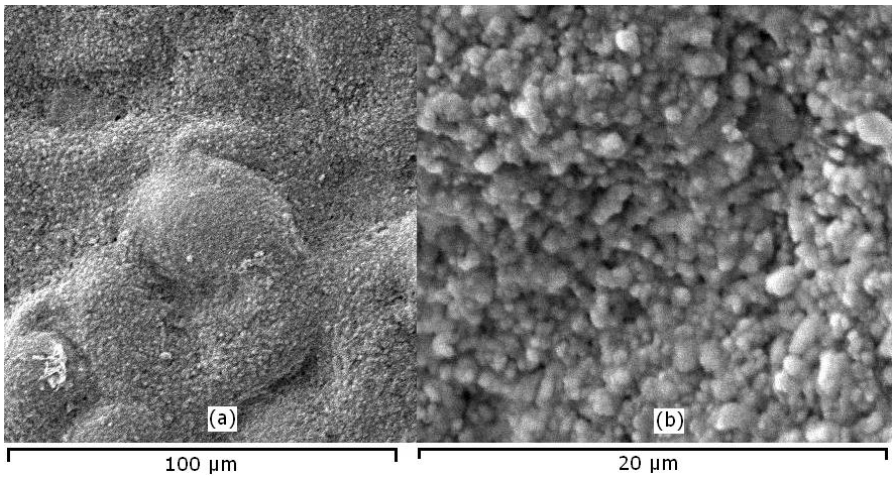

Figure 5.30 SEM images of the CO_2 laser alone irradiated surface of the Si_3N_4 engineering ceramic by using compressed air assist gas at (a) ×500 magnification and (b) ×3000 magnification.

5.3.3.3.3 N_2 assist gas

The SEM image in Figure 5.31 shows that the surface of the CO_2 laser irradiated sample of the Si_3N_4 ceramic by using N_2 gas assist. The CO_2 content within this sample was one of the lowest as the N_2 being a non-reactive gas would have minimized the oxide layer that was present in the samples CO_2 laser irradiated with reactive gases. The O_2 content found was 25.67 wt% which was somewhat higher in comparison to the as-received surface, but this is expected as the Si_3N_4 generally has the tendency to oxidize when placed in at atmospheric conditions at high temperature such as the laser treatment. The C content was reduced to 20.52 wt% in comparison with the as-received surface and Si was found to be 36.77 wt% and was different to the samples CO_2 laser irradiated by using O_2 and compressed air assist gases as more of the Si atoms had oxidized in comparison.

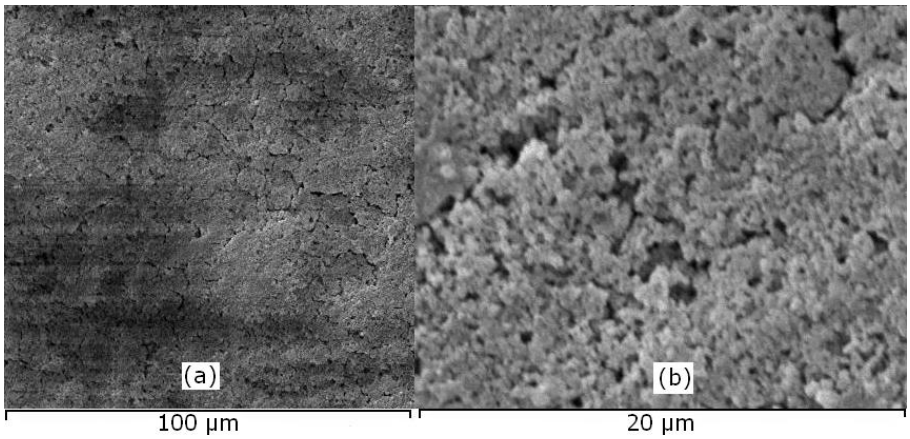

Figure 5.31 SEM images of the CO_2 laser alone irradiated surface of the Si_3N_4 engineering ceramic by using N_2 assist gas at (a) ×500 magnification and (b) ×3000 magnification.

5.3.3.3.4 Ar assist gas

The Si_3N_4 surface CO_2 laser irradiated with Ar assist gas in Figure 5.32 was somewhat similar to the CO_2 laser irradiated with N_2 assist gas. The surface, however, comprised of porosity which did not exist prior to the CO_2 laser treatment when compared to the as-received surface. The CO_2 laser treatment has also developed a level of oxide layer but was much thinner in comparison to the one produced by the more reactive gases. The compositional analysis showed that there was 16.07 wt% C, 21.41 wt% O_2 and 62.49 wt% Si. This treated sample had shown the lowest O_2 content from all the Si_3N_4 samples treated with the CO_2 laser by using the various conditions. This further confirmed that with using the inert gas would be more protective from atmospheric effects which the Si_3N_4 would otherwise undergo. The C was also reduced in comparison to the as-received and other treated samples. In addition, the content of Si was found to be the highest, which meant that the Si atoms were not disturbed and remained unchanged. Ar as a protective gas has worked well with conjunctions to the laser beam in order to form a protective surface treatment as well as finer track when compared to the other conditions applied with the CO_2 laser.

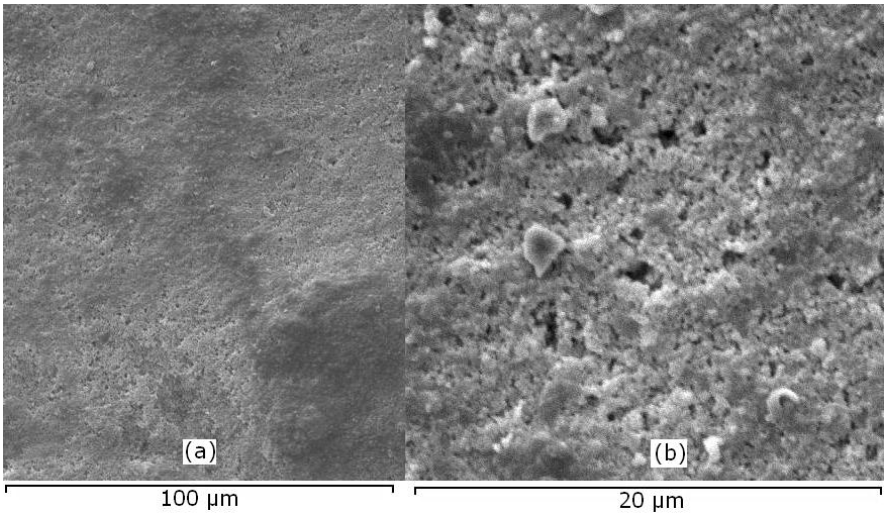

Figure 5.32 SEM images of the CO_2 laser alone irradiated surface of the Si_3N_4 engineering ceramic by using Ar assist gas at (a) ×500 magnification and (b) ×3000 magnification.

5.3.3.3.5 Ambient air (no assist gas)

The sample CO_2 laser irradiated with using the no assist gas had produced the most porous surface as shown in Figure 5.33. Due to lack of assist gas being introduced at the laser-Si_3N_4 interface, it is possible that the surface temperature herein was somewhat higher in comparison to the samples CO_2 laser irradiated with other conditions. This is why the material removal in this sample was also one of the highest in comparison to the CO_2 laser irradiated sample by using other conditions. The CO_2 laser has considerably exposed the pores within this sample which is not seen to that affect in other samples. The Si content for this sample had reduced after the CO_2 laser irradiation to 22.34 wt%, with O_2 increasing to 30.74 wt% in comparison to the as-received surface. Highest amount of C content (46.93 wt%) was found in this sample which can be said to have occurred from the lack of gas applied during the interaction between the CO_2 laser and the Si_3N_4.

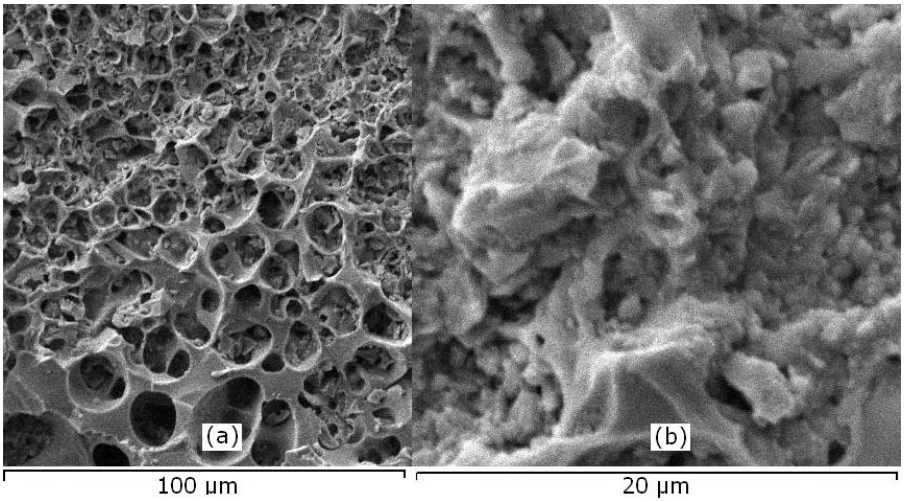

Figure 5.33 SEM images of the CO_2 laser alone irradiated surface of the Si_3N_4 engineering ceramic by using no assist gas at (a) ×500 magnification and (b) ×3000 magnification.

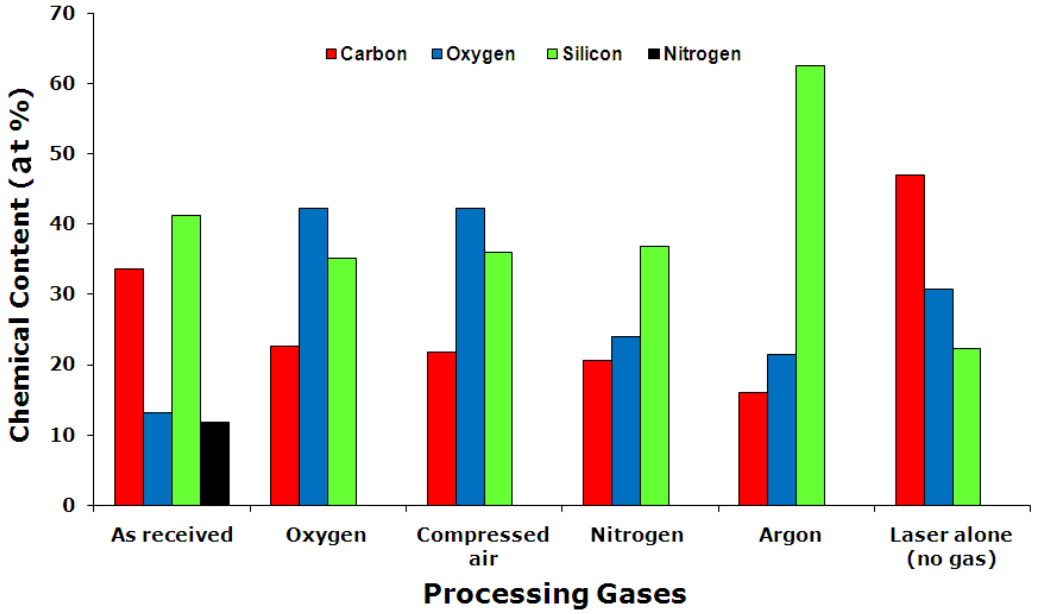

Figure 5.34 Chemical composition of the Si_3N_4 engineering ceramic in the as-received state and after CO_2 laser irradiation by using the different assist gas compositions.

5.3.4 CO_2 Laser Surface Treatment of ZrO_2 Engineering ceramic

5.3.4.1 Investigation of the Heat Affected Zone (HAZ) of the ZrO_2 Engineering Ceramic

From measuring the hardness of the CO_2 laser irradiated surface of the ZrO_2 engineering ceramic, it was found that a change in the surface hardness had also occurred. The hardness changed from within the laser unaffected zone to the HAZ and the fibre laser irradiated zone with all conditions applied. The hardness values are demonstrated in Table 5.35 for the ZrO_2 ceramics. This was similar to the effect produced by the fibre laser irradiation as the CO_2 laser irradiated zone also comprised of the softest surface layer. However, the hardness has decreased more in the case for the CO_2 laser irradiated sample in comparison to that of the fibre laser. As the diamond indentation induced into the HAZ, the hardness began to increase. The interface between each zones and the untreated surface layer are not shown in Figure 5.35. This is because the whole image covers the CO_2 laser irradiated area though the HAZ and the as-received surface are both indicated for the ZrO_2 ceramic CO_2 laser treated by using ambient air assist. The hardness was decreased from an average of up to 1250 HV to an average of up to 614 HV with the lowest being 579 HV and the highest being 639 HV within the CO_2 laser irradiated track as shown in the example in Table 5.10. The induced diamond on the laser unaffected zone (as-received) surface was remarkably different to that of the laser treated zone. The HAZ and was found to range between 1200 HV and 1250 HV. The HAZ showed increase in hardness from the CO_2 laser irradiated track, but was somewhat lower than that of the laser unaffected zone. Table 5.9 shows the average hardness, standard deviation and the range of the hardness values found within the respective zones investigated by using the five different laser surface treatment conditions. The change in the hardness over the CO_2 laser irradiated zone and the laser unaffected area established the position of the HAZ, the laser irradiated zone and the interface

between each region on the surface of the ZrO_2 engineering ceramic. The SEM image in Figure 5.35 shows a profile of the Gaussian shaped beam in the centre part of the image. Though, a large part of the image is laser treated since the beam is of 3mm diameter which covers most of the surface shown in Figure 5.35. However, the part in the centre is partially melted due to the footprint of the Gaussian shaped beam producing partial melting in the central area (just under a 1mm) but not the whole diameter of the beam.

The microstructure of the surface presented in Figure 5.35 is somewhat different to that presented in the latter part of the thesis (see Figure 8.7, Chapter 8). This is because the SEM images in this Chapter represents the unpolished laser treated surfaces of the ZrO_2 engineering ceramics, whereas the FEGSEM images in presented in Chapter 8 shows the ground, polished and thermal etched surface. Thermal etching herein was not conducted due to inaccessibility of a correct technology and equipment generally used for etching ceramics to reveal the microstructure during that time.

Furthermore, a spray drying step is used for the preparation of the ceramic powders for processing. In this step the powders dispersed in a liquid medium is sprayed into hot air so that the droplets will dry leading to the formation of spherical agglomerates. These agglomerates improve the flow-ability of the powder and would inherently increase the processing speed during the preparation of the green body (ceramic products) by pressing. It is then sintered to get the final product (the rectangular bar in Figure 4.1 used for the work in this thesis). The agglomerates would generally crush during the preparation of the green body by pressing. But, this is not always the case. Some agglomerates will only get flattened especially those near the surface of the sample as presented in the SEM images of the ZrO_2 engineering ceramic. The lower magnification image in this Chapter shows these agglomerates in comparison to the FEGSEM images. The grains are further seen with higher magnification for the ZrO_2 once by observing through the agglomerates as shown in the images in Chapter 8 for the ZrO_2 engineering ceramic.

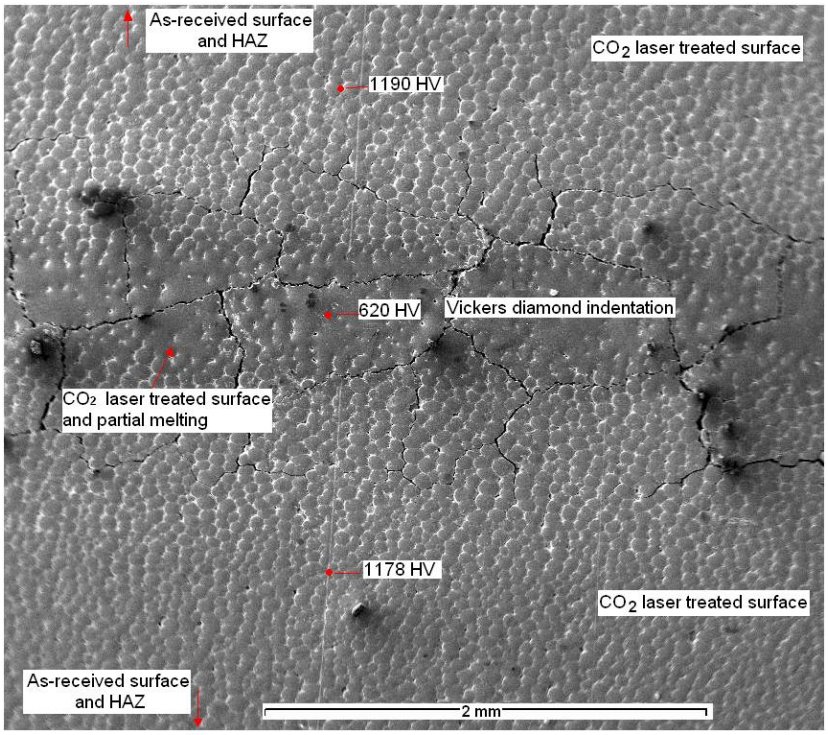

Figure 5.35 SEM image of the CO_2 laser irradiated surface by using O_2 assist gas; showing the HAZ, the laser unaffected zone as well as the interfaces between each zones for the ZrO_2 engineering ceramic.

Table 5.10 The change in the average hardness, STDEV and the range of hardness values found for the CO_2 laser irradiated zone (track) by using various assist gases, CO_2 laser unaffected zone and the HAZ of the ZrO_2 engineering ceramic.

Assist gases	Hardness values in various areas on the surface of the ZrO_2 engineering ceramic								
	Laser unaffected zone			CO_2 laser irradiated track			HAZ		
	Average hardness (HV)	STDEV	Range	Average hardness (HV)	STDEV	Range	Average hardness (HV)	STDEV	Range
O_2	1277	71	1204 - 1391	639	37	670 - 576	1195	37	1149 - 1250
Ar	1231	101	1149 - 1391	697	70	570 - 701	1176	77	1261 - 1052
Comp-ressed air	1203	56	1261 - 1149	610	14	590 - 626	1159	45	1099 - 1203
N_2	1254	67	1149 - 1324	655	64	573	1143	62	1052 - 1226
Ambient air	1219	113	1079 - 1391	614	22	579 - 639	1176	129	1079 - 1391

Table 5.11 Depth of penetration by the Vickers diamond indentation at 30 kg load induced on the CO_2 laser irradiated surfaces of the ZrO_2 treated by using the CO_2 laser and various assist gases.

Assist gases	Depth of penetration (µm)
O_2	42.21
Ar	40.05
Compressed air	43.14
N_2	41.74
Ambient air	43.02

5.3.4.2 The effects of the CO_2 laser surface treatment by using various assist gases on topographical characteristics

5.3.4.2.1 O_2 assist gas

The surface of the ZrO_2 ceramic as presented in Figure 5.36 showed that the CO_2 laser treated zone by using O_2 assist gas was effective in terms producing surface modification as considerable discolouration of the surface occurred. When compared to the same surface irradiated by the fibre laser the effect was somewhat greater and showed that the CO_2 laser wavelength was having more influence at least at the surface of the ZrO_2 engineering ceramic. The surface in Figure 5.36 showed 120µm of material removal and a surface finish of 0.71µm (Ra). The roughness was much smoother than the roughness of the as-received surface which showed that there was some degree of modification after the CO_2 laser irradiation took place. The CO_2 laser irradiated track however, by using the O_2 assist gas was fairly broader in comparison to any other track created by the CO_2 laser irradiation of the ZrO_2. This was also the case when compared to the results of the fibre laser irradiated sample of the ZrO_2 ceramic.

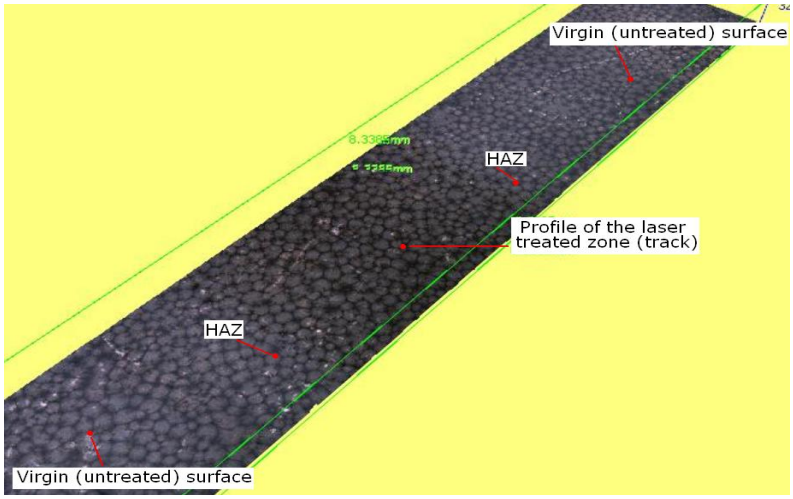

Figure 5.36 A 3-D topographical image of the surface profile of the ZrO_2 engineering ceramic treated by the CO_2 laser irradiation by using O_2 assist gas.

5.3.4.2.2 Compressed air assist gas

The sample CO_2 laser treated by using compressed air in Figure 5.37 showed that the surface had cracked when using the same parameters compared to the sample treated by O_2 gas. The generation of the crack tends to occur from the thermal shock being induced from the laser surface treatment. However, it is indicative that the temperature at the surface during the CO_2 laser interaction with ZrO_2 ceramic and compressed air was somewhat higher than the temperature produced during the CO_2 laser irradiated sample by using the O_2 assist gas. The cracking was a result of the thermal shock induced from the CO_2 laser treatment. However, the surface in this occasion has also changed form as the ZrO_2 had been modified to some degree to produce an amorphous glassy mixture. The amount of material removal found on this surface was up to 91µm with a surface finish of 0.70µm (Ra).

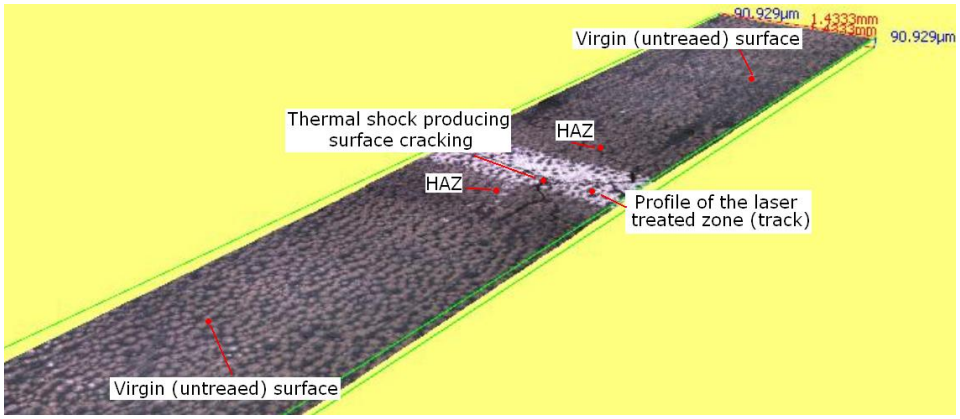

Figure 5.37 A 3-D topographical image of the surface profile of the ZrO_2 engineering ceramic treated by the CO_2 laser irradiation by using compressed air assist gas.

5.3.4.2.3 N_2 assist gas

The CO_2 laser irradiated sample of the ZrO_2 ceramic by using the N_2 assist gas is illustrated in Figure 5.37. The materials removal was found up to 77µm and the surface finish obtained was 0.91µm (Ra). This was slightly higher than the surface of the other treated sample of ZrO_2 with the CO_2 laser.

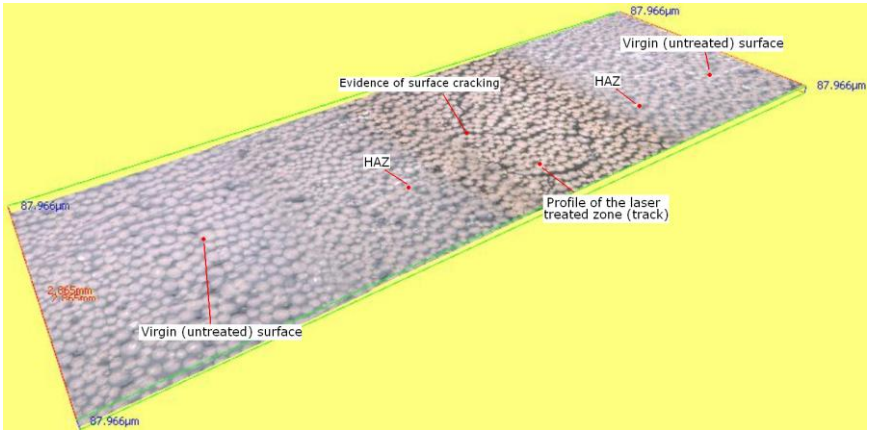

Figure 5.37 A 3-D topographical image of the surface profile of the ZrO_2 engineering ceramic treated by the CO_2 laser irradiation by using N_2 assist gas.

5.3.4.2.4 Ar assist gas

The CO_2 laser irradiated surface by using Ar assist gas (see Figure 5.39) also showed some degree of surface cracking. Ar being inert gas would have resulted in the similar effect to those accrued by that of the N_2 treated sample. Thus, cracking was somewhat more significant in comparison. The surface finish found with this sample was 0.77µm (Ra) and the materials removal was over 90µm. In comparison to the other samples CO_2 laser irradiated by using N_2, compressed air and O_2 assist gases, the material removal was slightly higher but was still considerably lower than that of the as-received surface of the ZrO_2 engineering ceramic.

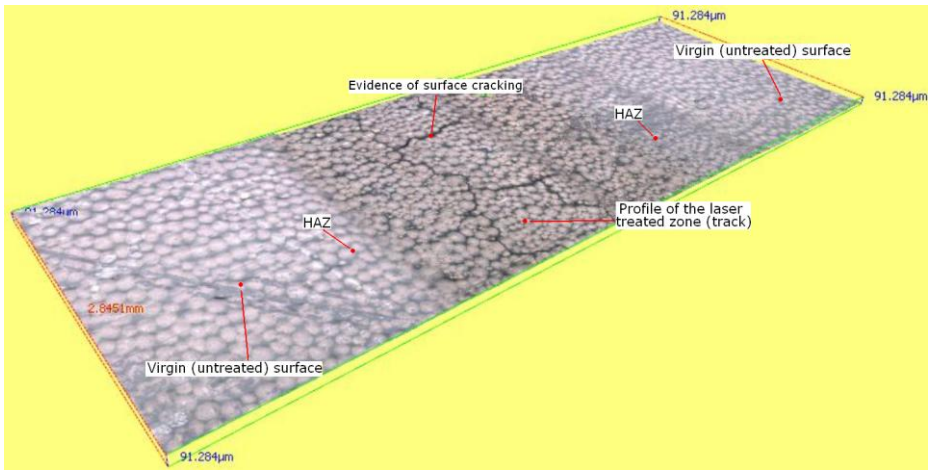

Figure 5.39 A 3-D topographical image of the surface profile of the ZrO_2 engineering ceramic treated by the CO_2 laser irradiation by using Ar assist gas.

5.3.4.2.5 Ambient air (no assist gas)

The sample treated by using the CO_2 laser in ambient air (no gas) is shown in Figure 5.40. This has also proved to have a significant change in the surface topography of the ZrO_2 ceramic. It can be seen that the CO_2 laser alone has created a thin layer of glassy profile through surface melting and solidification. However, due to no gas being applied the region of cracked area was considerably large and continuous due to excessive heat being inducted into the ceramic. The materials removal in this case was up to 79µm and the surface finish was 1.03µm. This was the highest from all ZrO_2 samples treated by using various gases by employing the CO_2 laser.

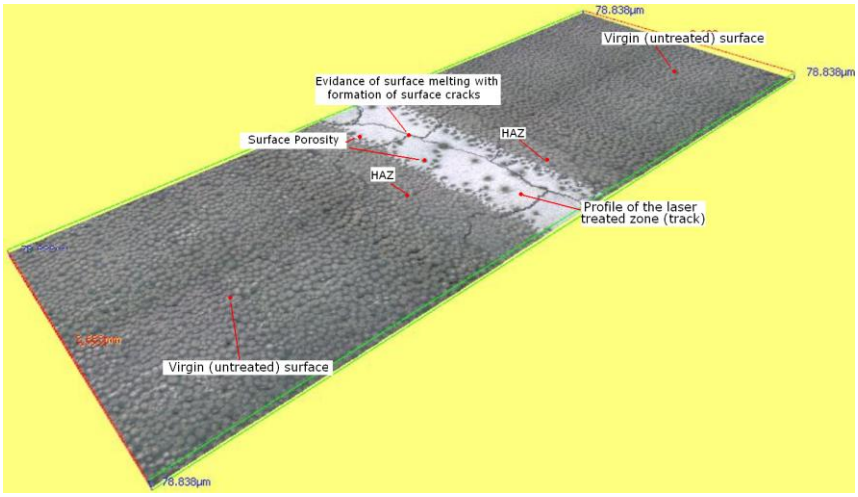

Figure 5.40 A 3-D topographical image of the surface profile of the ZrO_2 engineering ceramic treated by CO_2 laser irradiation by using laser alone (no assist gas).

Table 5.12 The effects of the material removal, the surface finish and the surface topography of the CO_2 laser irradiated ZrO_2 engineering ceramic surfaces treated by using various assist gas compositions.

	Material removal (µm)	Surface finish (Ra) µm	Topography			
			Presence of oxidation	Porosity	Treated Zone	HAZ
As-received surface	N/A	1.56	Very low	Minimal	N/A	N/A
CO_2 laser treatment using O_2	120	0.71	Very low	Very low	Large footprint	Large
CO_2 laser treatment using compressed Air	91	0.70	Very low	Medium	Large footprint	Large
CO_2 laser treatment using N_2	77	0.91	Very low	low	Fine footprint	Small
CO_2 laser treatment using Ar	90	0.77	Very low	low	Fine footprint	Small
CO_2 laser alone treatment (no gas)	77	1.03	Very low	Medium	Large footprint	Large

5.3.4.3 Microscopic analysis and the effect of the CO_2 laser irradiation by using the various assist gases on the chemical composition of the ZrO_2 engineering ceramic

5.3.4.3.1 O_2 assist gas

From comparing the SEM images of the as-received and the CO_2 laser irradiated surface by using the O_2 assist gas, it can be observed that the formed agglomerates on the microstructure of the ZrO_2 are affected from the CO_2 laser surface treatment. The effect which occurred with the fibre laser treatment of the ZrO_2 also occurs with the CO_2 laser surface treatment. However, the surface presented in Figure 5.41 is much influenced by the laser treatment due to the higher wavelength

exhibited with the CO_2 laser. This caused more interaction to take place particularly at the surface where the CO_2 laser-ZrO_2 interaction had taken place. This was confirmed by the bigger HAZ and partial surface melting which pushed the agglomerates together as the agglomerate boundaries began to melt and bind together. The chemical analysis presented in Figure 5.46 showed that there were 12.77 wt% C, 24.49 wt% O_2, and 62.74 wt% Zr found. The C content was found to be as twice as much as that of the as-received surface. The O_2 content remained unchanged along with Zr content decreasing to 6 wt% as opposed to the as-received surface.

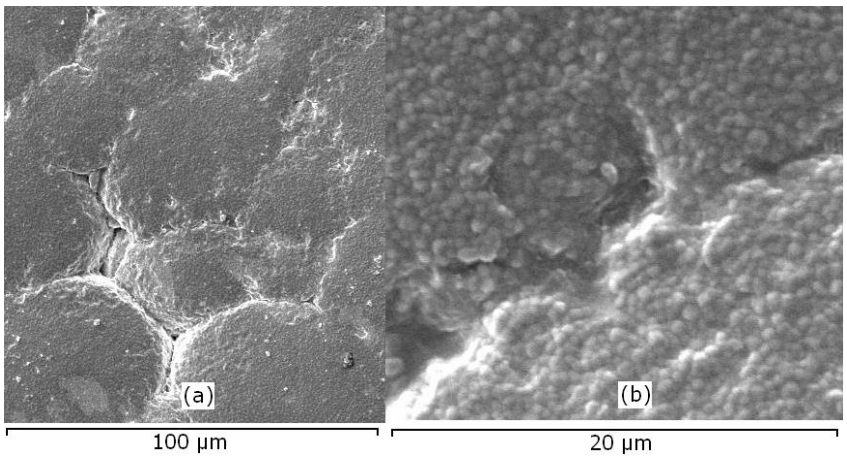

Figure 5.41 SEM image of the surface of a ZrO_2 engineering ceramic sample CO_2 laser irradiated by using O_2 assist gas at (a) x500 and (b) x3000 resolution.

5.3.4.3.2 Compressed air assist gas

From observing the SEM image in Figure 5.42 of the CO_2 laser irradiated surface of the ZrO_2 ceramic by using compressed air, it can be observed that there was evidence of the agglomerate boundaries were melting and binding into each other as seen in Figure 5.42(a). The image at x3000 resolution (see Figure 5.41 (b)) shows that the microstructure comprising of agglomerates are modified and have become much closer in comparison to the as-received surfaces and O_2 treated sample. This meant that there was more induction of heat during the laser ceramic interaction with compressed air. This in turn would have generated some surface cracks by using the compresses air assist gas. However, the thermal energy had further melted the localized the surface which caused the boundaries of the agglomerates to begin to bond into each other. The elemental analysis shows that 9.52 wt% C, 25.26 wt% O_2 and 65.22 wt% Zr was found. This in comparison with the as-received surface did not show a significant difference except that the C content was increased by over 4% and the Zr content was reduced by 3% when using the compressed air as assist gas.

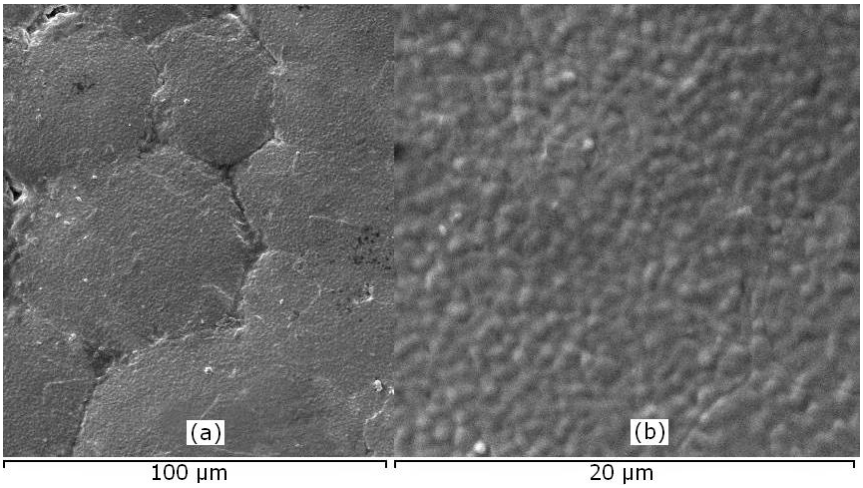

Figure 5.42 SEM image of the surface of a ZrO_2 engineering ceramic sample CO_2 laser irradiated by using compressed air assist gas at (a) x500 and (b) x3000 resolution.

5.3.4.3.3 N_2 assist gas

The bonding of the agglomerates was also observed within the sample CO_2 laser irradiated with N_2 assist gas (see Figure 5.43). This is predicted to have occurred by localized melting of the top surface layer and further allowed a more interlocking microstructure. The gap between the agglomerates has closed off when compared with the as-received sample in Figure 5.2. The compositional analysis on this surface showed 22.3 wt% C, 14.96 wt% O_2 and 63.01 wt% Zr. This in comparison to the ZrO_2 sample CO_2 laser treated with O_2 and compressed air did not differ too much. However, when compared to the as-received surface, the content of C was increase after the laser treatment. This was possibly due to the surface melting and inducing the C content into the surface by generation of the plasma plume that was inhibited into the engineering ceramic.

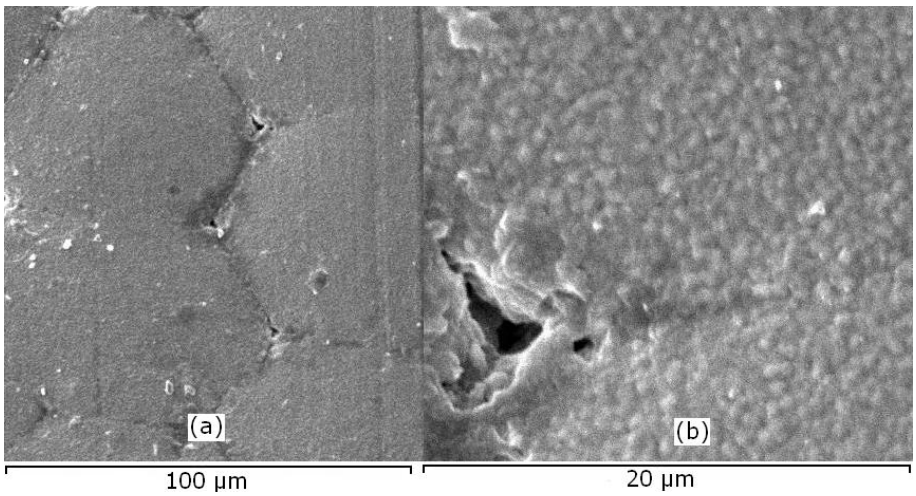

Figure 5.43 SEM image of the surface of a ZrO_2 engineering ceramic sample CO_2 laser irradiated by using N_2 assist gas at (a) x500 and (b) x3000 resolution.

5.3.4.3.4 Ar assist gas

Similar effects were found with the surface CO_2 laser irradiated by using Ar assist gas when compared to the surface of CO_2 laser irradiated sample by using N_2. The regime of surface being melted was also seen since the agglomerates in this sample has also began to bond together and the distance between them had considerably reduced as shown in Figure 5.44(a). The compositional study showed that there was 17 wt% C, 16.01 wt% O_2, and 65 wt% Zr. The level of the C content was the lowest by using Ar. However, in comparison to the as-received surface the C content was slightly higher, but the difference was only 2 wt%. This would have again resulted from the laser-ZrO_2 interaction as the plasma plume was absorbed into the ceramic.

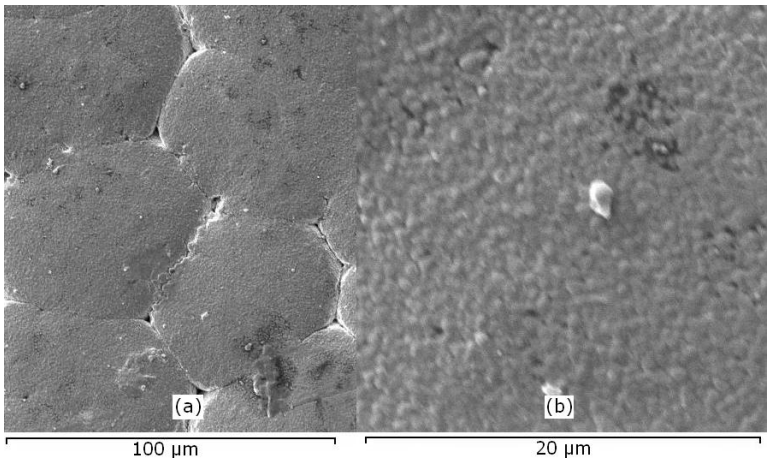

Figure 5.44 SEM image of the surface of a ZrO_2 engineering ceramic sample CO_2 laser irradiated by using an Ar assist gas at (a) x500 and (b) x3000 resolution.

5.3.4.3.5 Ambient air (no assist gas)

Figure 5.45 illustrates the CO_2 laser irradiated sample with ambient air (no assist gas). From observing the topography of the surface and the surface cracks which occurred, it was indicative that the due to no assistance given by the processing gas the CO_2 laser-ZrO_2 interaction temperature was considerably high. This resulted to the a bigger melt zone in comparison to that of the other treated samples of ZrO_2 ceramic irradiated with different conditions. In addition, it resulted in changing the surface morphology at microscopic level as it can be seen from Figure 5.45(a) that the local surface has melted and created a newly formed agglomerates which further appeared to be different (see Figure 5.45(b)) to those of the other samples previously shown. The formation of new microstructure was much closer with an indication of an interlocking microstructure. This also indicated that laser alone processing of the ZrO_2 engineering ceramic can be used to severely modify the surface profile and morphology of the ZrO_2. The compositional analysis showed 11.45 wt% C, 17.19 wt% O_2 and 70.56 % Zr. The C content was fairly low in comparison with the surfaces CO_2 laser irradiated with O_2, N_2, and compressed air but not Ar.

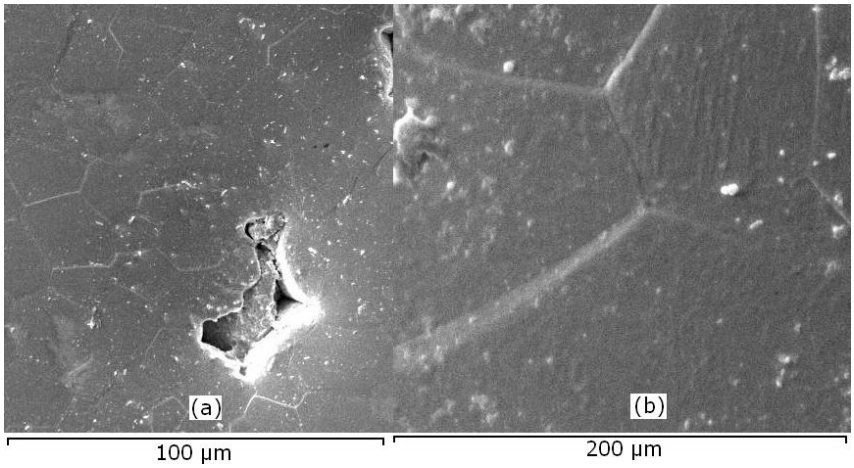

Figure 5.45 SEM image of the surface of a ZrO_2 engineering ceramic sample CO_2 laser irradiated by using no assist gas at (a) x500 and (b) x3000 resolution.

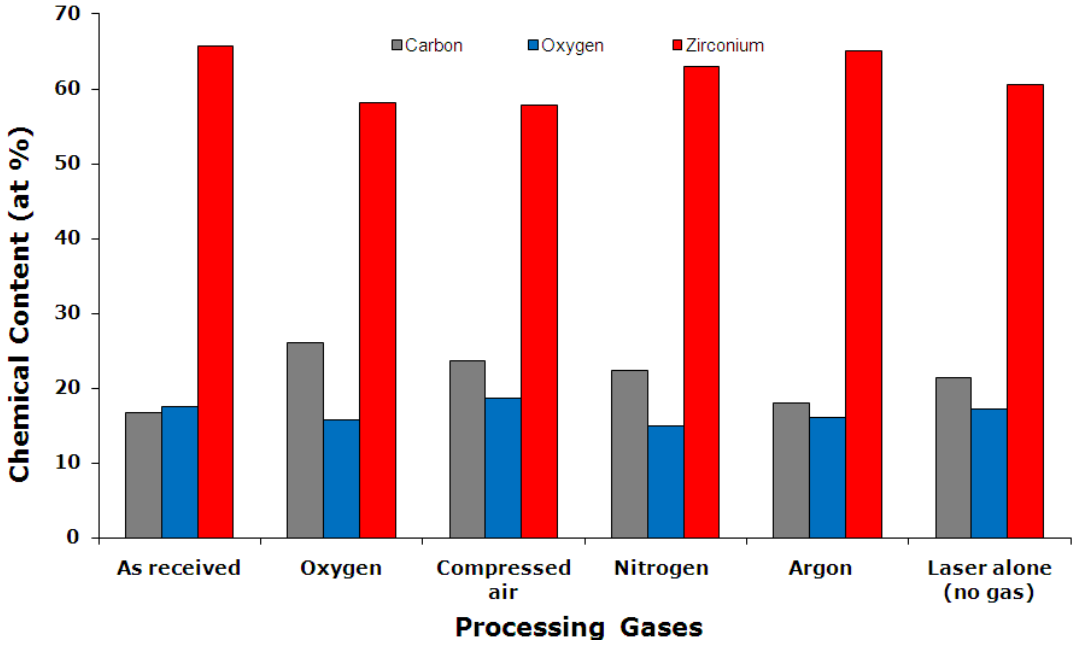

Figure 5.46 Chemical composition of the ZrO_2 engineering ceramic in the as-received state and after CO_2 laser irradiation by using the different assist gas compositions.

5.3.5 Change in Composition and the Mechanism of C Absorption After the CO_2 and the Fibre Laser Irradiation of the Si_3N_4 and ZrO_2 Engineering Ceramics

From observing the behavior of the chemical elements within the Si_3N_4 and the ZrO_2 engineering ceramics prior to and after the CO_2 and the fibre laser surface treatment, it can be seen that all samples of the ZrO_2 would characteristically comprise of zirconium and O_2 content. This is because both elements form the main composition of the ZrO_2 ceramic. For the Si_3N_4 it would be Si, N_2 and Yi which would pre-exist within its main chemical composition. Various percentage of the main elements are lost within the surfaces as the C and O_2 are introduced during and after the CO_2 and the fibre laser after the laser surface treatment of the two ceramics. The C content generally exists for all the fibre laser irradiated surfaces and also when using the inert assist gases. Though, when using Ar

the C content is fairly low but unavoidable as C exits in the atmosphere and could only be avoided if the laser treatment was conducted in vacuum conditions. In general, it can be seen that the laser surface treatment has led to some degree of change in the composition of the ZrO_2 to ZrC (zirconia carbide) due to induction of the C content and Si_3N_4 to SiO_2 due to introduction of O_2 at high temperatures [122]. For the ZrO_2 engineering ceramic, it is indicated that through induction of carbon the fibre laser irradiated layer of the ZrO_2 engineering ceramic would have transformed the ceramic to zirconia carbide (ZrC) through the induction of high carbon vacancies. Therefore, it indicated that the ZrO_2 would have deemed to comprise less O_2 content with an increased C content where the ZrO_2 can be further classified as $ZrO_{>2}$ (less than the original content of zirconia oxide). Furthermore, since the highest content of carbon is about 27% by observing all the conditions used, the ZrO_2 is estimated to be about $ZrO_{1.80}$. This shows a lower O_2 content in comparison to the as-received surface.

The C content has generated from the event of the laser interaction with the two ceramics. This is illustrated by the schematic in Figure 5.47. The energy delivered by the laser would generate high temperature rise at the ceramic surfaces during the interaction and would further lead to generating a keyhole and then lead to some degree of melting, material removal through vaporization. During this instance, the vaporized substance mixes with the assist gas to form a plasma plume as mentioned by Hoffman *et al.* [122], Raciukaitis *et al.* [125] and Boulmer *et al.* [127]. As the plasma plume comprises of the gas mixture, the main source of C induction occurs from the assist gas molecules [127]. Moreover, the plasma plume is in close contact with the ceramic and is active with the atmosphere. This forms a bridge which then allows the C atoms to create bonds with the surface and within the sub-surface (1µm depth) of the ceramic in order to saturate into the surface and to the sub-surface of the ceramic from the atmosphere [125]. The type of assist gas used would also influence the saturation of the C within the ceramic. This is because more reactive gases such as O_2, compressed air, and ambient air would produce an exothermic reaction with increased surface temperatures by creating a higher interaction zone and producing a bigger plasma plume. This is more likely to absorb deeper into the surface of the ZrO_2. This is why the C content was found to be high for conditions where O_2 and ambient air was used when compared to the results of non-reactive gases such as N_2 and Ar.

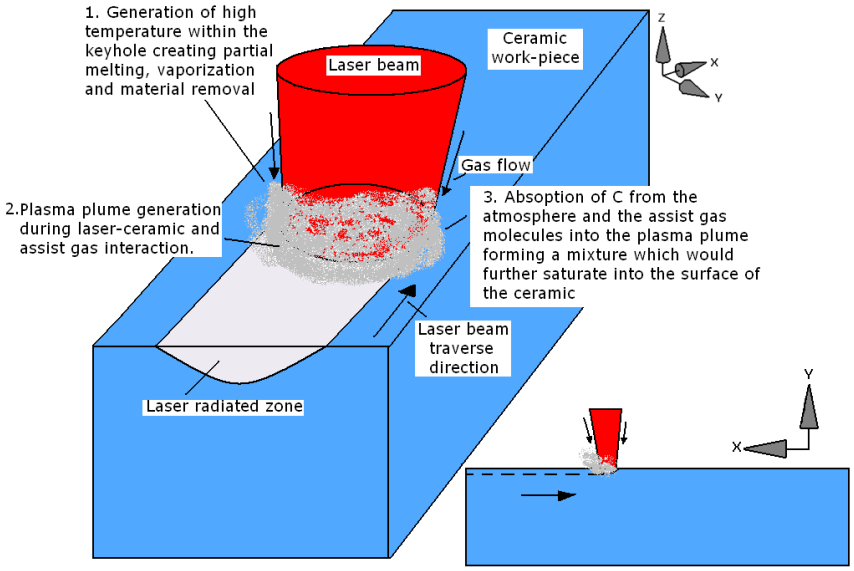

Figure 5.47 Schematic diagrams illustrating the generation of the plasma plume and C absorption within the surface of the Si_3N_4 and the ZrO_2 engineering ceramics.

5.3.6 Rational for the Change in Hardness

The CO_2 and the fibre laser irradiated surfaces had both softened the laser affected zone in comparison to the as-received surface and the HAZ of the two ceramic as presented earlier in this Chapter. The reduction in the hardness was more significant when O_2 assist gas was used followed by ambient air, compressed air, Ar and N_2 for both the engineering ceramics. The hardness then increased within the interface and the respected untreated areas. This ensured the location of the different zones found from the result of the laser surface treatment of the both the Si_3N_4 and ZrO_2 engineering ceramics. The change in hardness occurred due to the formation of the ZrC and SiO_2 within the laser treated regions. This was somewhat softer in comparison to the laser unaffected regions or the as-received surface of the two ceramics. Owing to this, a reduction in the surface hardness was found and indicated that the CO_2 and fibre laser irradiated surface had softened the top (near) surface layer of the Si_3N_4 and ZrO_2 by forming a modified surface layer. However, the effects were more significant with the results produced by the CO_2 laser as the oxide layer produced by the fibre laser particularly on the Si_3N_4 ceramics was significantly thicker. The formation of the new surface layer for the ZrO_2 ceramic occurred through partial melting, induction of carbon vacancies and formation of a glassy amorphous zone. This was during and after the laser/ceramic and the particular assist gas interaction took place as can be seen by the SEM micrographs. The Si_3N_4 was decomposed to some extent whilst being heated over 1900°C. During this phase, the Si_3N_4 has the tendency to react with ambience and oxidize itself to various degrees depending on its absorption of the wavelength applied and the processing temperature which it is exposed to. Through these aspects would have caused a localized ductile surfaces to have formed along with change in the surface composition which was softer than that of the laser unaffected zone for Si_3N_4 engineering ceramic.

The change in hardness found on both ceramics irradiated by the CO_2 and fibre laser had demonstrated that the diamond indentation induced into the ceramic was somewhat larger as the laser irradiated surface had become softer than the as-received surfaces. This meant that the ceramics were less prone to cracking under the influence of a load or an impact. This also indicated that the laser treated ceramics would comprise of improved fracture resistance. This is further investigated in Chapter 6 which elucidated the fracture toughness property (K_{1c}) modifications of the ZrO_2 and the Si_3N_4 engineering ceramics following the CO_2 and the fibre laser surface treatment.

5.3.7 Selection of the Assist Gases

The decision for choosing a particular assist gas is purely dependant on the specific needs for the application when considering the different effects that result from using the various assist gases. If large surface track is desired with high laser-ceramic surface interaction and high material removal, then CO_2 laser by using reactive assist gas such as O_2 is more desirable with both ceramics. This is particularly so for the ZrO_2 ceramic as the CO_2 laser showed considerable change in the surface microstructure of the ZrO_2. This is because the ZrO_2 is more absorbing the MIR wavelength as opposed to the NIR wavelength of the fibre laser. This was not the case for fibre laser processing of the Si_3N_4 engineering ceramic as considerable change was observed within the surface morphology. In general, the use of Ar and N_2 assist gases resulted in producing the finest surface finish with a lower material removal. This was in comparison with the sample treated by using other conditions with both CO_2 and fibre laser processing of the ZrO_2 engineering ceramics. This was because of both processing gases being non-reactive. Hence, protecting the Si_3N_4 and the ZrO_2 ceramic from too much atmospheric influence as well as generating lower surface temperatures in comparison to the other assist gases used. Fibre laser processing with N_2 however, showed a considerably modified surface in comparison to Ar as small sized elongated rod-like grains were found. These types of grains were not seen from other results. A compositional change was yet apparent but to a lesser extent despite N_2 and Ar showed less influence of the atmospheric effects such as oxidation. From the compositional study, it was observed that the Si_3N_4 was transformed to SiO_2 and the ZrO_2 was transformed to ZrC. The oxidation effect within the ZrO_2 ceramic was somewhat less as it contains large percentage of O_2. However, the oxidation of Si_3N_4 is unavoidable as the CO_2 and the fibre laser treatment was conducted in an atmospheric condition. Therefore, such conditions would drive the Si to oxidize within the atmosphere at elevated temperatures and form the new SiO_2 layer.

5.4 Summary

The following conclusions were drawn from applying various processing gases during fibre and CO_2 laser surface treatment of Si_3N_4 and ZrO_2 engineering ceramics:

- Fibre laser irradiated surfaces of the Si_3N_4 and ZrO_2 engineering ceramics were both reduced in hardness when applying all assist gases within the laser treated track. The effect was more

significant with using O_2 followed by compressed air, ambient air, N_2 and then Ar. The hardness then increased within the interface and the respected untreated areas.

- The change in hardness occurred due to the formation of the SiO_2 within fibre laser treated regions. This was somewhat softer in comparison to the laser unaffected regions or the as-received surface. Similarly, the surface of the ZrO_2 engineering ceramic was also modified to ZrC which could have resulted to the hardness reduction.

- Reactive gases produced the highest materials removal and the roughest surface finish along with a high level of oxidation and average porosity for both laser surface treatments on the ZrO_2 and the Si_3N_4. Large surface profile of the treated and the HAZ were also observed by using reactive gases (particularly with the CO_2 laser). This was because of the content of the particular compositions within these conditions were highly reactive and allowed porosity, oxidation, larger surface treated zones and larger HAZ to occur.

- The use of Ar and N_2 assist gases resulted in producing the finest surface finish with a lower material removal in comparison with the sample treated by using other conditions. N_2, however, showed a considerably modified surface in comparison to Ar as small sized elongated rod-like grains within the Si_3N_4 were found. Such microstructure was not seen from other results. A compositional change was yet apparent but to a lesser extent despite N_2 and Ar showed less influence of the atmospheric effects such as oxidation. The compositional study confirmed that the Si_3N_4 was transformed to SiO_2.

- The compositional study revealed the formation of the ZrC surface layer within the ZrO_2 occurred with both laser surface treatments. This was saturated into the surface of the ceramics with the support of the plasma plume being generated during the laser-ceramic interaction. The plasma plume comprised of partially melted and solidified mixture and acted as a bridge between the surface and ambience. This further allowed the C atoms to mix with the surface to form a new top (near) surface layer.

PART 3

MECHANICAL AND THERMAL ASPECTS

CHAPTER 6
Assessment of a Suitable Method for the Evaluation of Fracture Toughness Parameter (K_{1c}) of Laser Surface Treated Engineering Ceramics

This Chapter consists of the techniques used to determine the fracture toughness property (K_{1c}) of CIP Si_3N_4 and ZrO_2 engineering ceramics and the effects thereon of the CO_2 and a fibre laser surface treatment. Vickers macro hardness indentation method was employed for the investigation prior to and after the laser surface treatment to observe the near surface changes in the ceramics hardness. Optical microscopy was then used to observe the ceramics near surface integrity along with flaw sizes (crack lengths) and its geometry. Computation and analytical methods were then used to determine the ceramics K_{1c}. Enhancement of the K_{1c} was found for both ceramics by applying the CO_2 and the fibre laser irradiation, however, with differing mechanisms for the increases as further demonstrated in the Chapter.

6.1 Introduction

Crack sensitivity and low fracture toughness can limit the use of ZrO_2 and Si_3N_4 engineering ceramics, particularly for demanding applications. Nevertheless, the applications of ZrO_2 and Si_3N_4 have gradually increased on account of the desirable physical properties and longer functional life which often gives the engineering ceramics a commercial advantage over the conventional materials in use. Conventional metals and alloys especially can be replaced by engineering ceramics such as ZrO_2 and Si_3N_4 due to its exceptional mechanical and thermal properties offered. Now, ZrO_2 and Si_3N_4 ceramics in particular are predominantly being used to manufacture components in the aerospace, automotive and motorsports industrial sectors [37-43]. Various components used within these sectors were previously mentioned (see Chapter 1, Section 1.5). For such applications, fracture toughness is an essential property since low fracture toughness in comparison to metals and alloys is one of the disadvantages of the ceramic. Inherently, an increase in the fracture toughness would therefore, lead to an enhancement in the components functional life and better performance. This in turn leads to reduction in the maintenance time and cost of the component/part and or the system.

Fracture toughness is considered to be an important property for both of the ZrO_2 and the Si_3N_4 as well as other ceramics in general due to their high hardness and brittleness. Materials such as metals and alloys are soft and ductile. This in turn would resist cracks at higher stress levels and loading [13, 117, 127-131], whereas hard and brittle materials such as a Si_3N_4 ceramic posses a low fracture toughness and allow crack propagation to occur at lower stresses and loading. The fracture toughness

for the ZrO_2 ceramic is fairly high in comparison to the Si_3N_4 but not in comparison to metals and alloys. This is due to their low ductility, high hardness, caused by the closely packed grains along with a porous structure which increases the crack-sensitivity. This characteristically prevents these ceramics from increasing the movement of dislocations in comparison to that of metals [130-132]. Dislocations are hard to generate within the ceramics due to its strong and highly directional covalent bonds which make it difficult to move the atoms from its lattice positions. Mechanical yielding of the ZrO_2 or the Si_3N_4 is also limited due to the porosity and the surface flaws make it crack-sensitive and eventually lead to a much lower resistance to fracture. K_{1c} is a parameter of fracture toughness and is low for both the ceramics in comparison with metals and alloys so it would be an advantage if the K_{1c} of the ceramic is enhanced. Through improvement of K_{1c}, it is possible to make way for new applications where metals and metal alloys fail due to their low hardness, thermal resistance, co-efficient of friction and wear rate.

This Chapter investigated the use of empirical equations from the literature to calculate the fracture toughness property (K_{1c}) of a ZrO_2 and a Si_3N_4 engineering ceramic and observed the effects thereon of the CO_2 and the fibre laser irradiation to effect surface treatment. A change in the K_{1c} has an influence on the materials functionality or diversity to its applications. By improving the K_{1c} of materials can enhance its functional capabilities such as longer functional life, improved performance under higher cyclic and mechanical loading particularly for demanding applications as previously mentioned. This study also demonstrates a technique to calculate the K_{1c} by employing Vickers indentation test for laser treated CIP ZrO_2 and Si_3N_4 ceramics. All tested samples were investigated for their top surface hardness, generated crack profiles from the diamond indentations and microstructural changes before and after the fibre laser surface treatment.

Despite the use of industrial lasers such as CO_2, Nd:YAG, HPDL and an excimer to process various technical ceramics; no other investigation, hitherto, has employed the fibre laser to process engineering ceramics and to investigate the K_{1c}. Moreover, the fibre laser was selected because of its shorter wavelength radiation in comparison to the conventional lasers previously used for ceramic processing [14-16, 96, 133-139]. Also the selection of the CO_2 laser was made so a contrast of two different wavelengths can be seen. It would be interesting to investigate further the effect of short wavelength on the surface properties of the ZrO_2 and Si_3N_4 engineering ceramic. Moreover, the effects of the fibre laser are different to that of the CO_2 laser due to the differing wavelength, beam conditions as well as the beam delivery system despite applying identical parameters. This is why, a broader investigation was carried out by using the CO_2 and the fibre laser on the ZrO_2 and the Si_3N_4 engineering ceramic. Furthermore, despite the Nd:YAG laser wavelength being in the same region as that of the fibre laser, the Nd:YAG laser does not function stably in the CW mode. This is required for minimizing the thermal shock induced into a ceramic. Fibre lasers also produce high brightness in comparison to the more conventional CO_2 and Nd:YAG lasers. This generally inhibits deeper

penetration, capability of producing finer spot sizes, longer depth of focus, as well as low cost per wattage being exhibited due to it high brightness. As one can see, this investigation is timely as limited research has been conducted by employing fibre lasers to conduct the surface treatment of materials, especially of engineering ceramics.

6.2 Calculating the Ceramics Fracture Toughness Parameter (K_{1c}) by means of an Indentation Technique

Vickers indentation along with single edge notched beam (SENB), chevron notched beam (CNB) and double cantilever beam (DCB) techniques can be employed to determine the fracture toughness of ceramics. The use of Vickers indentation method to determine the fracture toughness parameter (K_{1c}) of ceramics and glasses from empirical relationships has been demonstrated previously [140-146]. The Vickers indentation test has several advantages such as the cost effectiveness and easy set-up as well as being simple and less time consuming in comparison to other indentation techniques.

Measured hardness and the crack lengths from the Vickers indentation test are placed into an empirical equation to calculate the materials K_{1c} [13, 127, 129]. The results from the Vickers indentation test can then be applicable to the empirical equations which were derived by Ponton [127, 129], Chicot [142] and Liang *et al.* [143]. The equations derived by Ponton *et al.* [127, 129] originated from various other authors [144-155]. The equations were however modified and applied specifically to hard and brittle materials such as ceramics and glass by Ponton *et al*. [127, 129]. The equations have a specific empirical value. This is particularly suitable for different ceramics. However, Ponton *et al.*'s work does not make it clear with regards to which empirical value and equation is more applicable for different ceramics. Preparations of the samples involve polishing in order to create a reflective surface plane (this would mean that the surface has been well polished) [13, 127] prior to applying the Vickers indentation process. There are still constraints with the Vickers indentation techniques as reported by Gong *et al.* [156], over the more conventional technique applied such as SENB and double-torsion (DT) method as mentioned elsewhere [140, 157-159]. The constraints are: (a) the dependence of the crack geometry on the applied indentation load and the properties of the material; (b) indentation deformation (non-uniform fracture progression or rapid fracture growth) such as lateral cracking; and (c) unsuitable consideration of the effect of Young's modulus and the material hardness. Table 6.1 presents the literature K_{1c} values for comparison from using the SENB, CNB and DCB technique to determine the fracture toughness of a ZrO_2 and Si_3N_4 engineering ceramics [13, 160, 161].

Table 6.1 Fracture toughness values of Si_3N_4 and ZrO_2 engineering ceramics obtained by using the various indentation fracture methods.

Indentation Fracture Methods	Vickers		SENB		CNB		DCB	
	Si_3N_4	ZrO_2	Si_3N_4	ZrO_2	Si_3N_4	ZrO_2	Si_3N_4	ZrO_2
K_{1c} (MPa $m^{1/2}$)	6.37 [13]	12 [117]	9 [50]	13.6 [120]	7.9 [49]	12.3 [117]	4.0 [52]	12.5 [117]

The procedure and steps in order to produce a genuine Vickers indentation test result and produce genuinely valid K_{1c} values are: (a) each indentation must be performed at a sufficient distance from one another. This would avoid the formed cracks to inter-connect and bridge with the other diamond indentations performed on the ceramic surface [119, 162]; (b) a minimum load of 50 N is recommended; (c) it is ideal to coat the test surface with gold so performed indentations are visible and (d) the test samples should be around 1.5 times larger than the diagonal length of the diamond indentation and comprise of minimum porosity. The author also stated that the adjacent indents should be no closer than four times the size of the diamond indentation.

6.3 Generation of the Cracking Profiles during the Indentation Test

Liang *et al.* [143] investigated the K_{1c} of ceramics by using the indentation method, followed by applying several equations by various authors as listed in [143]. Liang *et al.* stated that equations differ as the crack geometry changes (from Palmqvist to median half-penny cracks). He introduced a new equation which was said to be more universal as opposed to the previous work conducted. Ponton *et al.*'s formula in comparison was much simplified and was easy to apply. Chicot *et al.* [142] conducted further investigation by applying two other equations to produce results using materials such as tungsten carbide (Nickel phosphorus treated) and pure silicon. He uses the concept of median half-penny crack and a Palmqvist crack system to determine the most applicable equation [142]. It was stated that high indenter loads produce a median half-penny crack within the material which is on the edges of the diamond indentation (footprint produced). This type of crack will always remain connected. A Palmqvist crack is produced during low indenter loading and is of a smaller scale in comparison. The Palmqvist crack will always appear at initial stage of the crack generation during the indentation process. Then, a median half-penny crack is produced once the impact of the indenter is exerted. It can be assumed that a median half-penny crack may be the result, since the ceramics comprise of high hardness, indicating that high indenter loads are required in order to induce visible and measurable diamond footprints.

Orange *et al.* [167] investigated the K_{1c} of Al_2O_3-ZrO_2 by comparing the notched beam and the Vickers indentation techniques. Cracking behaviour was observed as Palmqvist and median half-penny crack geometries were found. Low indentation loading produced Palmqvist cracks and with

increasing loading median half-penny cracks were found. High microcracking was also found with Vickers indentation technique when a fine grain size (0 to 3µm) ceramics were tested and with increasing grain size (0 to 5µm), the micro cracking was reduced with increase in the K_{1c}. With the notched beams technique a higher K_{1c} value was also achieved with a larger grain size [157]. From the work of Orange *et al.* [157] it can be gathered that notched beam indentation technique produced better results in comparison with the Vickers indentation method. Although, reasons behind this was not well justified.

Median half-penny shaped cracks occur when high indentation loads are applied [142, 163, 164]. The profile of a median half-penny shaped crack is illustrated in Figure 6.1(a). It can be predicted that the outcome for most of the crack profiles in this study would be of median half-penny shape. For cracks that are of median half-penny shape the applicable equations differ (see Equations 6.1-6.15) [13, 127, 129]. The indention load at which the median half-penny crack occurs for most ceramics is 3N [142]. This was lower for the loads applied for this investigation. Therefore, it would be reasonable to assume that the generated cracks would always be of a half-penny median type crack profile. This indicated that only equation particularly applicable for median-halfpenny cracks should be utilised for this study in order to determine the K_{1c}. Figure 6.1(b) illustrates a profile of a Palmqvist crack which tends to occur at low indentation loads [142, 165].

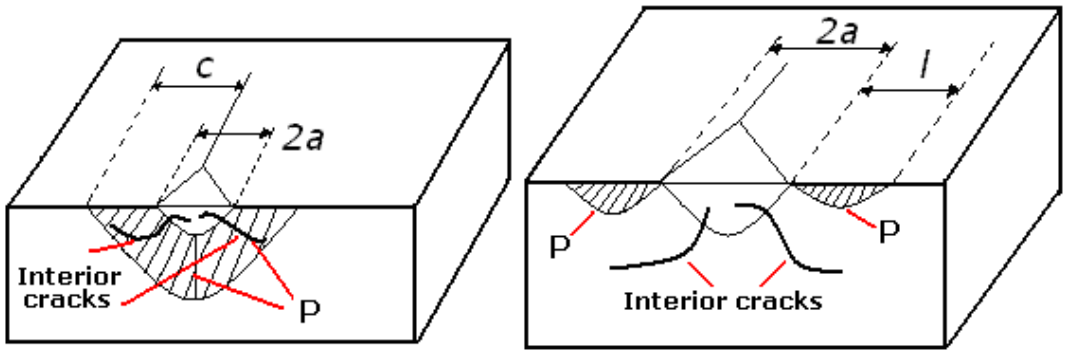

(a) **(b)**

Figure 6.1 Median Half-penny crack in (a) and Palmqvist crack (b).

Note: l is the surface crack length, 2a is the length of the diamond indent, c is the centre of the diamond to the end of the crack tip and P is the load impact.

A Palmqvist crack is part of the median-half penny crack system because when a load above 3N is applied the indenter "pop in" occurs, while the already produced Palmqvist crack further develops into a median half-penny crack [142, 165]. These cracks are shallow and lie in the axis of the indenter as there would be a small extension at the edge of the diamond indenter [165]. Up to 50N of indentation loads were used for this work and so it is likely that a Palmqvist crack occur, leading to the half-penny median crack geometry.

6.4 Determination of the K_{1c} by Using the Empirical Equations

Equations for median half penny-shaped cracks are usually used for high indenter load applications [147, 149, 152]. One equation is selected to calculate the K_{1c} value for the treated and as-received samples from applying the equations to real experimental values. The equations were derived by the ceramics geometrical values that were obtained from experimental means, of ceramics and glass [127, 129]. Equations 6.1 to 6.15 were mentioned in the literature to be applicable for ceramics and glass type materials. However, no such equation was defined as applicable for a certain ceramic type. Hence, the suitability of applying the various equations to the ZrO_2 and the Si_3N_4 engineering ceramics was not particularly defined. This is why it was required that an investigation was carried out in order to determine the most employable equation prior to investigating the K_{1c} modifications through the laser irradiated ceramics. There were 10 equations selected in this study from various equations discussed in [127, 129, 140], to first determine the K_{1c} of the as-received surfaces of the ZrO_2 and the Si_3N_4 and then the laser treated surfaces. The selected equations applicable to calculate the $K_{1c,}$ by using the Vickers indentation methods are [127]:

$\mathbf{K_{1c} = 0.0101\ P/\ (ac^{1/2})}$	**[162]**	(6.1)
$\mathbf{K_{1c} = 0.0724\ P/c^{3/2}}$	**[166]**	(6.2)
$\mathbf{K_{1c} = 0.0515\ P/c^{3/2}}$	**[147]**	(6.3)
$\mathbf{K_{1c} = 0.0134\ (E/HV)^{1/2}\ (P/c^{3/2})}$	**[149]**	(6.4)
$\mathbf{K_{1c} = 0.0330\ (E/HV)^{2/5}\ (P/c^{3/2})}$	**[152]**	(6.5)
$\mathbf{K_{1c} = 0.0363\ (E/HV)^{2/5} (P/a^{1.5})\ (a/c)^{1.56}}$	**[167]**	(6.6)
$\mathbf{K_{1c} = 0.095\ (E/HV)^{2/3}\ (P/c^{3/2})}$	**[167]**	(6.7)
$\mathbf{K_{1c} = 0.022\ (E/HV)^{2/3}\ (P/c^{3/2})}$	**[167]**	(6.7)
$\mathbf{K_{1c} = 0.035\ (E/HV)^{1/4}\ (P/c^{3/2)})}$	**[169]**	(6.9)
$\mathbf{K_{1c} = 0.016\ (E/HV)^{1/2}\ (P/c^{3/2})}$	**[161]**	(6.10)
$K_{1c} = 0.079\ (P\ /a^{3/2})\ log\ (4.5\ a/c) \quad for\ 0.5 \leq c/a < 4.5$	[170]	(6.11)
$K_{1c} = 0.4636\ (P/a^{3/2})\ (E/HV)^{2/5}\ (10^{F})$	[170]	(6.12)
$K_{1c} = 0.0141\ \ (P/a^{3/2})\ (E/HV)2/5\ log\ (7.4^{a}/c)$	[167]	(6.13)
$K_{1c} = 0.0232\ [f\ (E/HV)]\ P/(\ ac^{1/2})$ † *for* $c/a \leq \approx 2.7$	[167]	(6.14)
$K_{1c} = 0.417\ [f\ (E/HV)]\ P/\ (a^{0.42}\ c^{1.07})$ † *for* $c/a \geq \approx 2.$	[169]	(6.15)

Note: Equations highlighted in bold were deemed to be appropriate for this investigation. Where P is load (kg), c is average flaw size (μm), a is 2c, m is length (m), HV is the Vickers material hardness value and E is the Young's modulus.

Ponton *et al.* [130] state that Equation 6.10 as used by Kelly *et al.* [155] was 30 to 40 % accurate for ceramics which are well behaved in their indentation response. However, it is first required that the propagation of the crack geometry is understood from performing the Vickers indentation test on the as-received ZrO_2 and the Si_3N_4 ceramics as further justified in this Chapter. It is not made clear as to why this equation was particularly used for the ceramic. It was therefore, required that some of the relevant equations that were applied to the tested values from this experiment to determine what sort of results are obtained. Ten equations were employed as previously stated to establish which particular equation type produces the K_{1c} value that is the nearest to the known value for the as-received Si_3N_4 ceramics which is normally between 4 and 6 MPa $m^{1/2}$ and 7 to 12 MPa $m^{1/2}$ for the ZrO_2 ceramic.

6.5 Experimental Procedure and Analysis

6.5.1 Experimental Material

The materials used for the experimentation were presented in Chapter 4, Section 4.1, Figure 4.1. A smoother surface than 1.56μm for the Si_3N_4 and 1.57μm for the ZrO_2 ceramics would have much lower surface flaws and microcracks and would perform better under the diamond indentation as the resulting crack growth from the Vickers indentation would be smaller but initial experiments showed that polished shinier surfaces (below 1.56μm for Si_3N_4 and 1.57μm for the ZrO_2) would reflect the beam and would, therefore, reduced beam absorption into the ceramics. Hence, the surfaces were not ground and polished.

6.5.2 CO_2 and Fibre Laser Surface Treatment

The details of the fibre laser used for the experiments are presented in Chapter 4, Section 4.3, Figure 4.2 and Section 4.4, Figure 4.3 for the CO_2 laser surface treatment. The experiments were conducted in ambient condition at a known atmospheric temperature (20°C) by using the compressed air at the rate of 25 l/min for both the CO_2 and the fibre laser.

6.5.3 Application of the Vickers Indentation Technique

An indenter of a specific shape made from a diamond was used to indent the surface of the Si_3N_4 under investigation [13, 14, 117, 127-132]. The diamond was initially pressed on to the as-received surface and the load was then released. A diamond indentation was created. Thus, on the surface which was then measured in size. Thereafter, the surface area of the indentation was placed in to Equation 6.16 to calculate the hardness value:

$$HV = 2P \sin [\theta/2] / D^2 = 1.7544P / D^2 \quad (6.16)$$

Where P is the load applied (kg), D is the average diagonal size of the indentation in mm and θ is the angle between the opposite faces of the diamond indenter being 136° with less than ±1° of tolerance. Indentation load of 5, 20 and 30 kg, were applied. The indented surface and the resulting crack lengths were measured using the inbuilt optical microscope of the Vickers indenter (Amstrong Engineers Ltd). This method was then implemented for both the CO_2 and the fibre laser irradiated surfaces of ZrO_2 and Si_3N_4 ceramics. The test samples were placed under the macro indenter and were initially viewed by using the built in microscope to adjust the distance between the surface of the work-piece and the diamond indenter. This maintained a sufficient distance during each indentation and allowed a standardized testing method which complied to ISO 6507-1 [119].

6.5.4 Measurement of the Crack Lengths

The crack lengths generated by employing the Vickers diamond indentation test as presented in Figure 6.2 (a) and (b) were measured by using a contact-less, co-ordinate measuring machine (CMM), Flash 200. The ceramic samples were placed under a traversing lens of the optical microscope. The lens traverses in the y-direction and to adjust the magnification it is also able to move in the z-direction. Motion in the y-direction is provided by the bed on which the test-piece is mounted for analysing the surface. The accuracy of the motion system in the x- and y-direction was ± 4.37µm and ± 5.25µm in the z-direction. The image appears on the screen as the optical lens traverses above the surface of the test-piece. The scale resolution of the lens was 0.5µm. The diamond indentations and the resulting crack lengths were measured by moving the lever in the x- and y-directions and selecting a starting point on the screen where the crack ends (crack tip) and stopping on the edge of the diamond indentation footprint (where the crack starts). Then measuring the length or the width of the diamond footprint, followed by measuring the crack length on the other side of the diamond indentation from the edge of the diamond indentation (where the crack starts) to the crack tip (where the crack ends). This measurement was carried out in both the x- and y-directions.

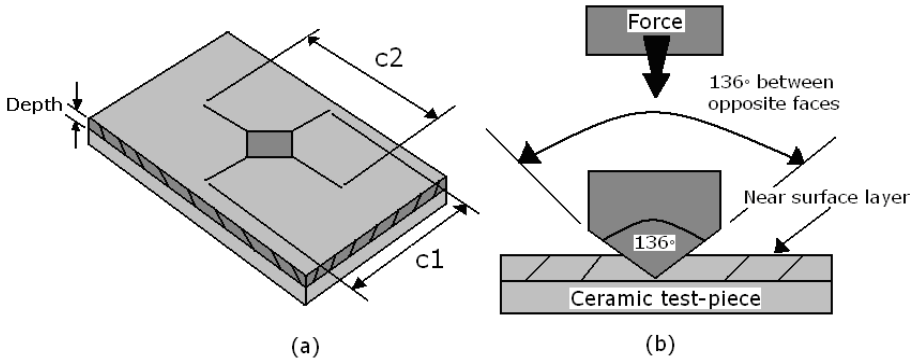

Figure 6.2 A schematic diagram of a Vickers diamond indentation with propagation of the cracks (a) and (b) the concept of diamond indentation employed.

6.5.5 Calculation of the Fracture Toughness Parameter (K_{1c})

Initial investigation used 15 equations to determine which equation type was best suited for calculating the K_{1c} [127-129]. The as-received surfaces of the ZrO_2 and the Si_3N_4 engineering ceramics were first tested for its hardness. Fifty indentations were made on one surface plane of various test samples of the ZrO_2 and the Si_3N_4 ceramics. Measured hardness values were then recorded and a average was taken for the as-received surfaces. Each indentation and its crack lengths were then viewed at microscopic level by the aid of the optical microscope (Optishot; Nikon Ltd.) to observe the surface morphology. The crack lengths were measured by using a co-ordinate measuring machine (CMM - Smartscope Flash 200; OGP Ltd.) CMM and crack geometry was observed by a 3 dimensional (3-D) surface topography by using a focus variation technique (Infinite focus; IFM 2.15, Alicona Ltd.). The crack lengths, produced by the indentations were then placed into the various K_{1c} equations with its measured average hardness. Cracking geometries were then observed in order to confirm that the cracks generated by the diamond indentation at 5 kg were of median half-penny crack profile. This insured that equations (6.1) to (6.10) used for median half-penny crack profile were correct. Equation (6.11) to (6.15), are used for Palmqvist type crack profile and were not used. Figure 6.3 to Figure 6.6 presents an example of a typical surface profile produced from the Vickers diamond indentation using a 5 kg and 20 kg loads for both the ZrO_2 and Si_3N_4 engineering ceramics. Both showed evidence of median half-penny type crack profiles where an indenter "pop in" indicated in Figure 6.4 for the Si_3N_4 and in Figure 6.6 for the ZrO_2 ceramics were exerted and then linear cracks were produced. A Palmqvist crack profile tends to occur with lower indentation loads and had occurred (as indicated from the indenter "pop in") already in this crack geometry. The concept was more present with higher indentation loading as presented in Figure 6.4 for the Si_3N_4 and Figure 6.6 for the ZrO_2 ceramic.

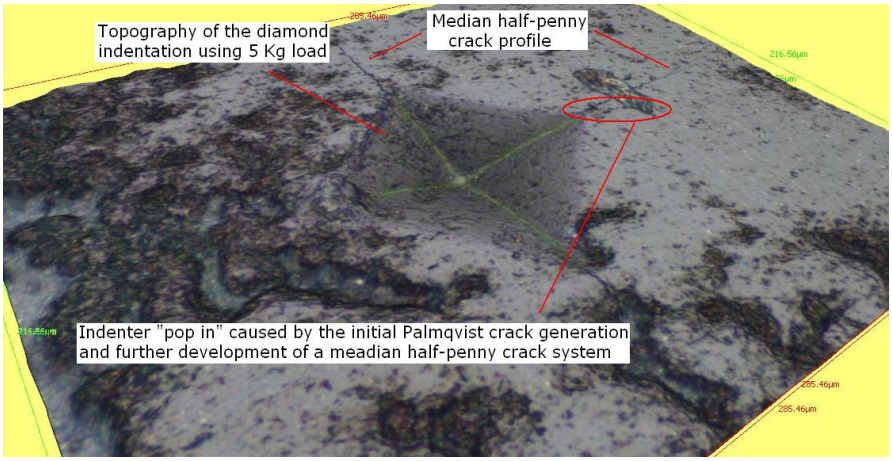

Figure 6.3 Topography of the Vickers diamond indentation on the as-received surface of the Si_3N_4 ceramics indented at 5 kg, illustrating a median half-penny crack geometry.

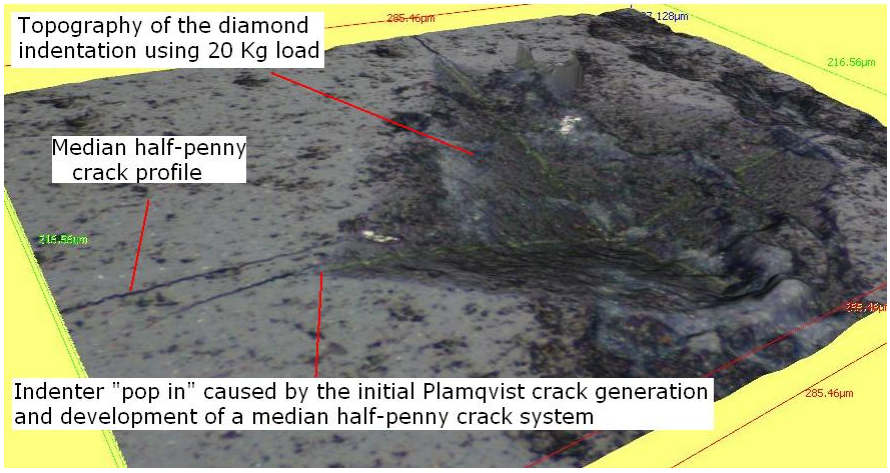

Figure 6.4 Topography of the Vickers diamond indentation on the as-received surface of the Si_3N_4 ceramics indented at 20 kg, illustrating a median half-penny crack geometry.

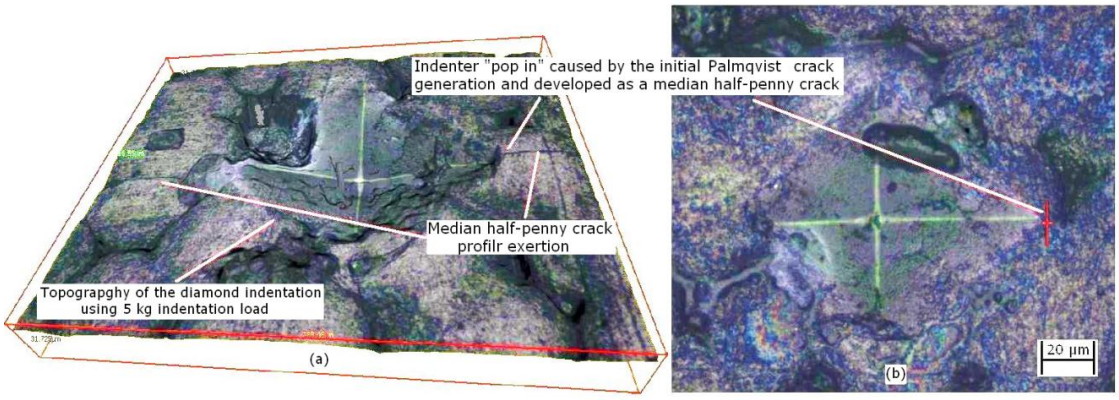

Figure 6.5 Topography of the Vickers diamond indentation of the as-received surface of ZrO_2 ceramics indented at 5 kg, illustrating a median half-penny crack geometry.

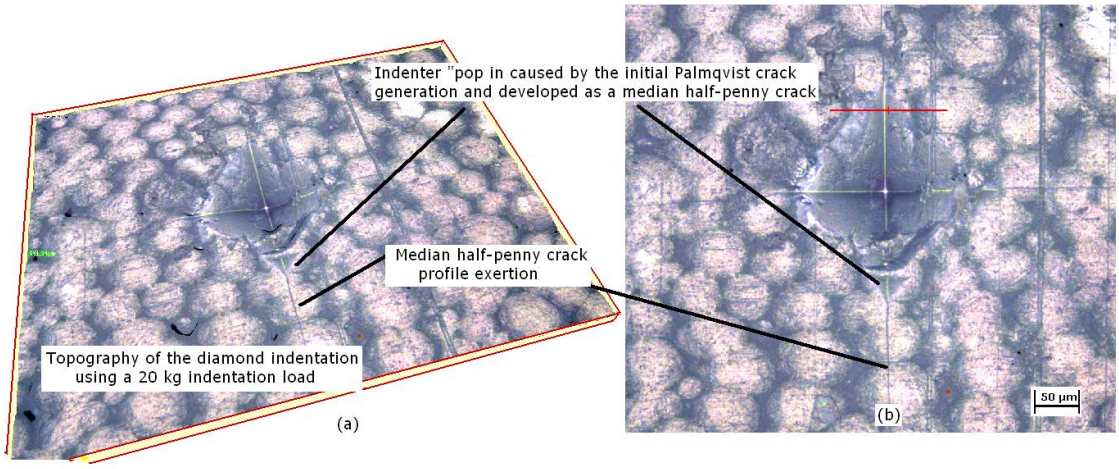

Figure 6.6 Topography of the Vickers diamond indentation of as-received surface of ZrO_2 indented at 20 kg, illustrating a median half-penny crack geometry.

Equations 6.1 to 6.10 for half-penny median crack system are presented in Table 6.2 and were initially used to calculate the K_{1c} of the as-received ZrO_2 and the Si_3N_4 engineering ceramics to

investigate the most appropriate equation that can be applied to the experimental values for both, the as-received and the laser treated surfaces of the ZrO_2 and the Si_3N_4 engineering ceramic. The results have been tabulated and are as presented in Table 6.3 and Table 6.4. The equations were set-up by using Microsoft Excel which made it easy to be able to input parameters from the full equation. These values were hardness, crack length, Vickers indention load and the Young's modulus. The Young's modulus for the as-received surface and the laser irradiated surfaces was kept to 310 GPa for the Si_3N_4 and 210 GPa for the ZrO_2. It can be seen that all the values which range between 4 to 6 MPa $m^{1/2}$ [42] for the Si_3N_4 and 7 to 12 MPa $m^{1/2}$ for the ZrO_2 [42], would generally allow the equation to be useable for calculating the K_{1c} for the both CO_2 and the fibre laser treated and the as-received surfaces of the two ceramics.

Table 6.2 The ten equations used to calculate the K_{1c} for the as-received surface of ZrO_2 and Si_3N_4.

Equation Number	Equations	Equation Origin
6.1	$K_{1c} = 0.0101\ P/(ac^{1/2})$	Lawn & Swain [162]
6.2	$K_{1c} = 0.0724\ P/c^{3/2}$	Lawn & Fuller [166]
6.3	$K_{1c} = 0.0515\ P/C^{3/2}$	Evans & Charles [147]
6.4	$K_{1c} = 0.0134\ (E/Hv)^{1/2}\ (P/c^{3/2})$	Lawn, Evans & Marshall [149]
6.5	$K_{1c} = 0.0330\ (E/Hv)^{2/5}\ (P/c^{3/2})$	Niihara, Morena and Hasselman [152]
6.6	$K_{1c} = 0.0363\ (E/Hv)^{2/5} (P/a^{1.5})\ (a/c)^{1.56}$	Lankford [167]
6.7	$K_{1c} = 0.095\ (E/Hv)^{2/3}\ (P/c^{3/2})$	Laugier [167]
6.7	$K_{1c} = 0.022\ (E/Hv)^{2/3}\ (P/c^{3/2})$	Laugier [167]
6.9	$K_{1c} = 0.035\ (E/Hv)^{1/4}\ (P/c^{3/2})$	Tanaka [169]
6.10	$K_{1c} = 0.016\ (E/Hv)^{1/2}\ (P/c^{3/2})$	Anstis, Chantikul, Lawn & Marshall [161]

Where P is load (kg), c is average flaw size (µm), a is 2c, m is length (m), HV is the Vickers material hardness value and E is the Young's modulus. (Young's modulus for the as-received Si_3N_4 was kept to 310 GPa $m^{1/2}$). Range (required equation accuracy) is 4 to 6 MPa $m^{1/2}$ for Si_3N_4 [42] and 7 to 12 MPa $m^{1/2}$ for the ZrO_2 [42]. For all tested samples, the indentation load was 5 and 30 kg. Average of the K_{1c} was obtained by using values from fifty different Vickers indentation tests on one particular surface plane per sample. This allowed more consistency in calculating the K_{1c} since the values can be used from a bigger pool of data.

The literature value of K_{1c} for the as-received engineering ceramics (as stated before) that do not lie between the range given were not considered as acceptable and therefore, those equations were proved to be less accurate in obtaining the values close to or within the range. The K_{1c} values found by using Equation 6.10 were reasonably close to the range for both the ZrO_2 and the Si_3N_4 in comparison to the values obtained by the other equations so this equation was most appropriate for

use. Based on this, other equations were not taken into consideration since the K_{1c} values produced by those equations were far from being within or close to the range.

The Vickers diamond indenter was induced fifty times into the as-received surface plane of the ZrO_2 and the Si_3N_4 engineering ceramics. Hardness values from the indentation test were recorded and the resulting crack lengths were then measured to first calculate the K_{1c} of the as-received surface. This produced fifty K_{1c} values that were obtained from one surface plane. The experimental values obtained were an input into the set Excel spreadsheet such as the indentation load, crack lengths produced by the Vickers diamond indentations and the measured hardness. The equation that generated the closest value within the range (4 to 6 MPa $m^{1/2}$ for the Si_3N_4 and 7 to 12 MPa $m^{1/2}$ for the ZrO_2) after fifty indentation tests was Equation 6.10. The results of the equation are presented in Table 6.3 and Table 6.4 along with their average, standard deviation and range. Despite the average K_{1c} values of the as-received ceramics being out of the range (see Table 6.3 and Table 6.4), the values obtained by using Equations 6.10 were the closest to the fracture toughness range for the ZrO_2 and the Si_3N_4 ceramics in comparison with the other equations. Consequently, this equation was used for all as-received, CO_2 and the fibre laser irradiated ZrO_2 and Si_3N_4 engineering ceramics to determine the K_{1c}.

Table 6.3 The end K_{1c} values with its standard deviation and range for 5 and 30 kg load from employing the ten equations for the as-received Si_3N_4 engineering ceramic.

Equation Number	Average K_{1c} value using 30 kg load (MPa $m^{1/2}$)	Standard deviation	Range (MPa $m^{1/2}$)	Average K_{1c} value using 5 kg load (MPa $m^{1/2}$)	Standard deviation	Range (MPa $m^{1/2}$)
6.1	0.64	0.14	0.97-0.40	0.10	0.03	0.04 - 0.20
6.2	2.32	0.51	1.47-3.15	0.26	0.11	0.14 - 0.73
6.3	3.71	0.73	2.35-5.67	0.577	0.17	0.22 -1.17
6.4	19.71	4.70	10.90 - 29.51	3.71	1.27	1.07 - 5.94
6.5	46.47	9.57	26.75 - 67.72	9.04	17.33	4.57-13.25
6.6	474.67	100.27	323.74 - 676.21	131.67	57.69	49.29 -315
6.7	2162.22	594.10	1357.40 - 3477.21	557.51	214.00	206.26 - 919.9
6.7	467.94	137.57	240.13- 727.97	131.49	70.26	54.52 -379.27
6.9	746.04	217.77	372.03-1152.66	21.60	11.37	9.07 -61.50
6.10	7. 70	1.71	13.16 – 5.43	1.71	0.59	3.66 - 0.56

Note: Young's modulus is 310 GPa (as-received surface), average hardness at 30 kg load is 1479 HV (14.60 GPa) with a range of 1575 to 1207 HV (15.44 - 11.75 GPa) and standard deviation of 69.54 HV (0.67 GPa); average a is 0.000356 m; standard deviation 0.0000553 m and average c is 0.000177 m and standard deviation of 0.000273 m; average hardness at 5 kg load is 1106 HV (11.32 GPa) with a range of 707 to 1524 HV (6.93 to 14.95 GPa) and standard deviation of 201.69 (1.97

GPa); average a is 0.000756 m; average c 0.000193 m with a standard deviation 0.0000427. The density was 3.15 g/cm^3 [37, 42], and the average grain size of 2µm for the as-received surface.

Table 6.4 The end K_{1c} values with its standard deviation and range for 5 and 30 kg load from employing the ten equations for the as-received ZrO_2 engineering ceramic.

Equation Number	Average K_{1c} value using 30 kg load (MPa $m^{1/2}$)	Standard deviation	Range (MPa $m^{1/2}$)	Average K_{1c} value using 5 kg load (MPa $m^{1/2}$)	Standard Deviation	Range (MPa $m^{1/2}$)
6.1	0.90	0.17	0.67-1.27	0.16	0.057	0.060-0.29
6.2	3.25	0.67	2.36-4.61	0.57	0.21	0.21-1.95
6.3	5.20	1.07	3.77-7.37	0.96	0.34	0.034-1.72
6.4	22.24	5.07	14.64-35.5	4.77	1.64	1.76-9.04
6.5	411.97	120.74	293-647	103.56	42.37	36-247
6.6	472.41	137.45	277-779	117.76	47.60	41-273
6.7	1976.63	579.32	1164-3679	496.92	203.34	205-1177
6.7	457.74	134.16	269-752	115.07	47.09	40-274
6.9	727.23	213.43	429-1355	173.07	74.91	64-437
6.10	12.65	2.67	7.52 -17.11	2.51	0.90	0.92-4.76

Note: Young's modulus is 210 GPa (as-received surface); average hardness at 30 kg load is 1141 HV (11.19 GPa) with a range of 793 to 1346 HV (7.22 to 13.20 GPa) and standard deviation of 115 HV (1.12 GPa); average a is 0.000275 m; standard deviation 0.0000370 m and average c is 0.0001425 m and standard deviation of 0.000174 m; average hardness at 5 kg load is 973 HV (9.64 GPa) with a range of 707 to 1329 HV (6.93 to 13.03 GPa) and standard deviation of 141 HV (1.37 GPa); average a is 0.000279 m; standard deviation 0.000707 m; average c 0.00013927 m with a standard deviation 0.0000353. The density was 6.30 g/cm^3 [37, 42].

6.6. Results and Discussion

6.6.1 Analysis of the As-received Surfaces

6.6.1.1 Analysis of Si_3N_4 engineering ceramic by using a 5 and 30 kg indentation load

The average hardness value of the Si_3N_4 ceramic by using a 30 kg load was 1479 HV with the highest value being 1674 HV above the mean and lowest being 1326 HV below the mean. Figure 6.7 illustrates the footprint of the as-received surface of the Si_3N_4 indented by using a 30 kg load. The hardness of the Si_3N_4 from applying a 5 kg load was much lower than the hardness values obtained after applying a load of 30 kg. This was because of the 5 kg load applied to the material resulted into lower penetration of the diamond indentation into the Si_3N_4 as well as the surface area of the diamond footprint also being smaller in dimension which resulted in generating a lower hardness value. An average hardness deduced by using a 5 kg load was 1106 HV. The highest value found on the surface of the Si_3N_4 was 1647 HV and the lowest value below the mean was 707 HV. This

fluctuation is considerable and well outside the expected range of ± 10% [117]. This wide fluctuation in the hardness values is however, not unusual and resulted from surface scaring and pre-existing cracks, porosity, as a result of the manufacturing process [164] as well as impurities on the near surface layer in comparison with the bulk hardness frequently produced non-uniform results.

The results showed minimal difference in the generated crack lengths for the Si_3N_4 from applying a 5 kg load in comparison with the results from applying a 30 kg load. The crack lengths ranged between 227µm to 499µm with an average of 376µm. Crack lengths has a close relationship with the hardness of a ceramic. High hardness inherently leads to a high level of cracking and materials with low hardness produces smaller sized cracks. This directly relates to the final K_{1c} value as materials with high hardness will give rise to long crack lengths. This in turn will generate lower K_{1c} values. Materials with low hardness are softer and more ductile and will therefore produce shorter crack lengths through resistance to indentation and produce high K_{1c} values. Despite the indentation load and the applied force being much smaller in comparison with the 30 kg load, the material was still cracking in equivalent measure to the results of the trials conducted by using a higher load. This clearly indicated that the surface did not exhibit a good response during the indentation test. This could mean that a smoother surface finish was required for the indentation test in order to overcome this problem so that the surface scaring and microcracks pre-existing on the Si_3N_4 were minimized and the strength of the top surface layer could be further enhanced for a better indentation response. This also has a possibility of increasing the surface hardness, yet at the same time would reduce the resulting cracks from the Vickers diamond footprints and avoid crack connecting from the diamond footprint and the pre-existing surface microcracks.

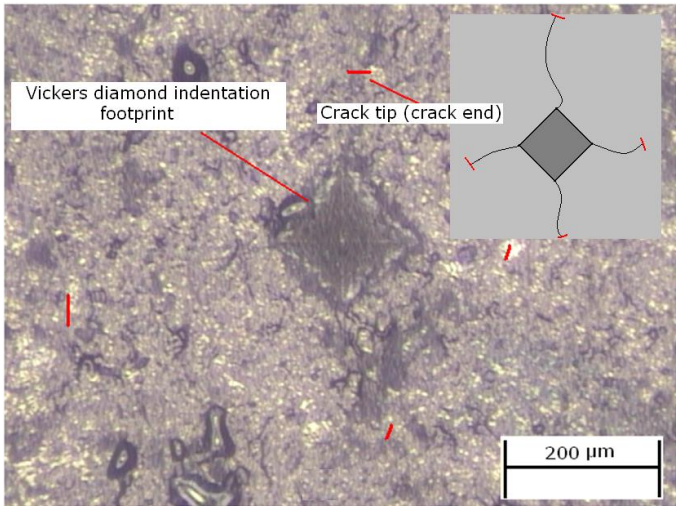

Figure 6.7 As-received surface of Si_3N_4 ceramic indented with by a 30 kg load (hardness = 1292 HV (12.67 GPa), crack length = 371µm, K_{1c} = 5.45 MPa $m^{1/2}$).

Ponton and Rawlings [129] suggested that a minimum loading of 50N must be pressed in order to produce a diamond indent. The minimum loading used herein agrees to the work of Ponton and

Rawlings [129]. Although, the loading herein was 49.05N and we yet see a diamond indentation with a median half-penny shape profile as presented in Figure 6.7. Initial experiments by using lower indentation loads such as 24.5N and 9.7N also presented a sufficient indented footprint from the Vickers hardness test. The diamond indentation in Figure 6.7 is smaller in size when compared with the indentation created by the 30 kg load. However, the average crack lengths found from using a 5 kg indentation load to some extent were in the same region. The differences between the average values for two test results were 4.3% and less when considering a larger pool of data. From this, it can be gathered that macro hardness indentation test may be more stable at higher indentation loads than lower, particularly with hard brittle materials such as Si_3N_4. The overall average K_{1c} by using a 30 kg load was found to be 7.70 MPa $m^{1/2}$ for the Si_3N_4 as presented in Figure 6.7, also showing the highest value being 12.77 MPa $m^{1/2}$ and the lowest being 5.34 MPa $m^{1/2}$.

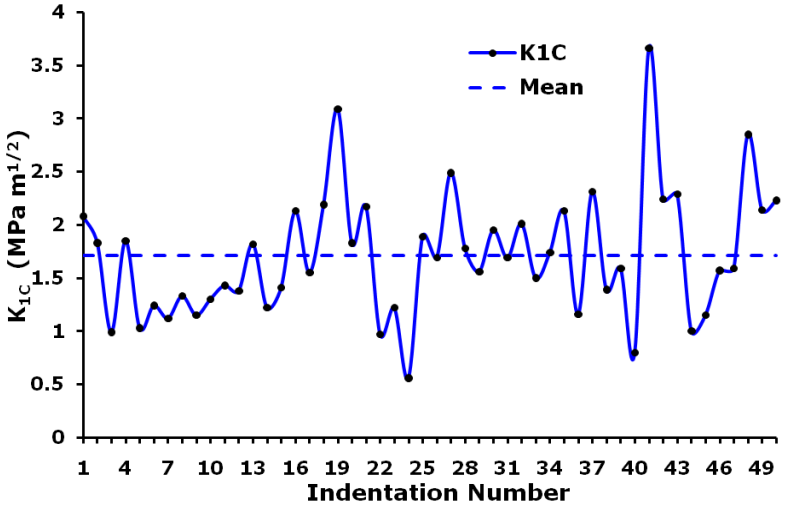

Figure 6.7 K_{1c} of the as-received surfaces of the Si_3N_4 ceramics after applying a load of 30 kg.

The result found for hardness when employing a 30 kg indentation load match with the values provided by the manufacturer and proves that the method used for the hardness calculation and measurement of the crack lengths was valid. Although, the values for the hardness are much smaller than the values provided in the manufacturer's specification when using a 5 kg load. This was due to the fact that the indentation load was much smaller and produced smaller footprints (see Figure 6.9) of the diamond which exerted lower force to the surface and reduced the end value of the K_{1c}. The average K_{1c} was found to be 1.71 MPa $m^{1/2}$ for the Si_3N_4 as presented in Figure 6.10 also showing the highest value being 3.06 MPa $m^{1/2}$ and the lowest being 0.55 MPa $m^{1/2}$.

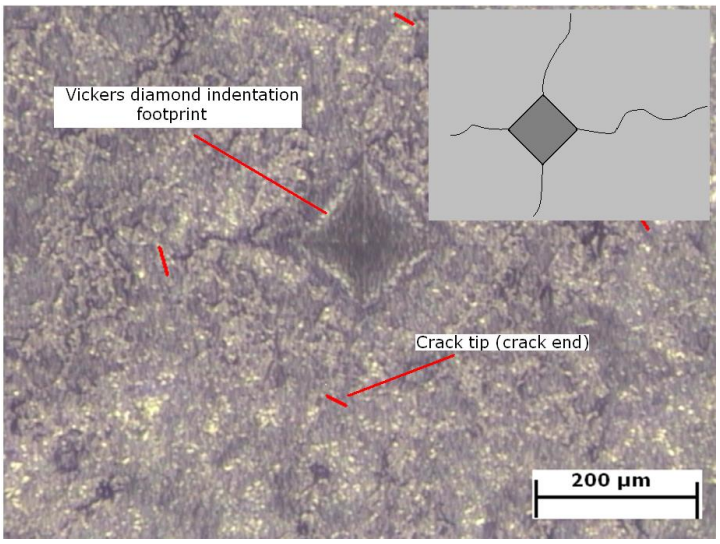

Figure 6.9 As-received surface of the Si_3N_4 ceramic indented by a 5 kg load (hardness = 900 HV (7.73 GPa), crack length = 391µm, K_{1c} = 1.66 MPa $m^{1/2}$.

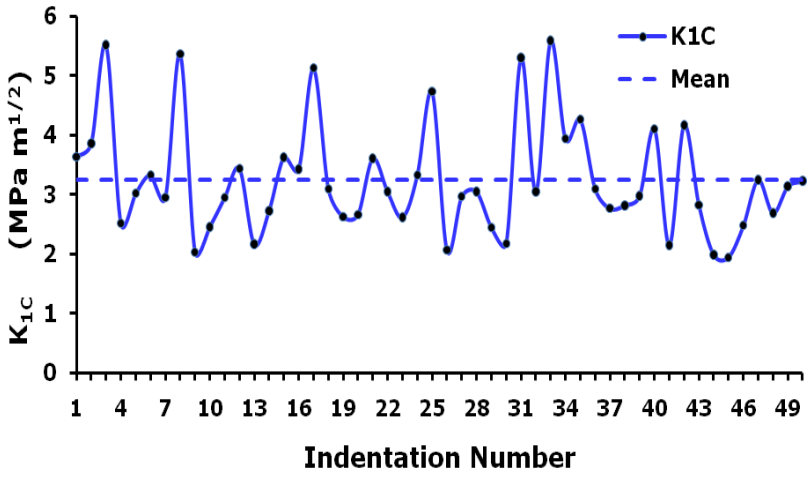

Figure 6.10 K_{1c} of the as-received surfaces of the Si_3N_4 ceramics from applying a 5 kg indentation load.

The hardness can become much higher if the surfaces were ground and polished prior to the Vickers indentation test as previously stated. This would minimizes the surface microcracks and result in obtaining a better consistency in achieving the hardness value and the resulting crack lengths but surfaces could not be ground and polished in this case as the initial studies showed that grinding and polishing resulted to the Si_3N_4 ceramic becoming smooth and shiny. This in turn has the tendency to produced high laser beam reflection. Furthermore, grinding and polishing could not be conducted after the fibre laser surface treatment as it removed the newly formed surface layer and would also induce some degree of residual stress into the ceramic as stated by Sun Li *et al*. [15]. This would not do justice to the laser irradiated surface during the Vickers indentation test and therefore, all surfaces were tested as-received for the indentation study prior to and after the laser surface treatments.

6.6.1.2 Analysis of ZrO_2 engineering ceramic by using a 5 and 30 kg indentation load

The average surface hardness of the as-received ZrO_2 was found to be 1141 HV for ZrO_2 (see Figure 6.11) when applying a 30 kg indentation load. The values provided by the manufacturer for the as-received surfaces were 700-1200 HV for ZrO_2. The highest value of 1129 HV and lowest was 757 HV when an indentation load of 30 kg was applied. This fluctuation has occurred due to several factors such as porous structure, the ceramics response to the diamond indentation, surface flaws and microcracks pre-existing on the ceramic, operator and machine accuracy in measuring the sizes and footprints of the diamond indentations. Operator accuracy depends purely on the ability of the operator to locate and measure the size of the diamond footprint through the inbuilt lens of the Vickers indentation machine. Such errors were minimized in the work herein as the diamond footprints and the resulting crack lengths were both measured by using computational means. However, the machine accuracy of 775 nm for a load of 5 kg and 1471.5 nm for a load 30 kg must be taken into consideration when conducting the Vickers indentation test [119].

The fluctuations found in the mean hardness from the results of this study were up to 11%. This in comparison with the values for ZrO_2 given in the literature were 1% higher from the ± 10% range (error) given in [117]. Error of 1% between the hardness values found in this study and the literature can be an exempt from being a non-conformance and may be considered to pass through the quality requirements if the hardness test was used for a (real life) ZrO_2 engineering ceramic component/product.

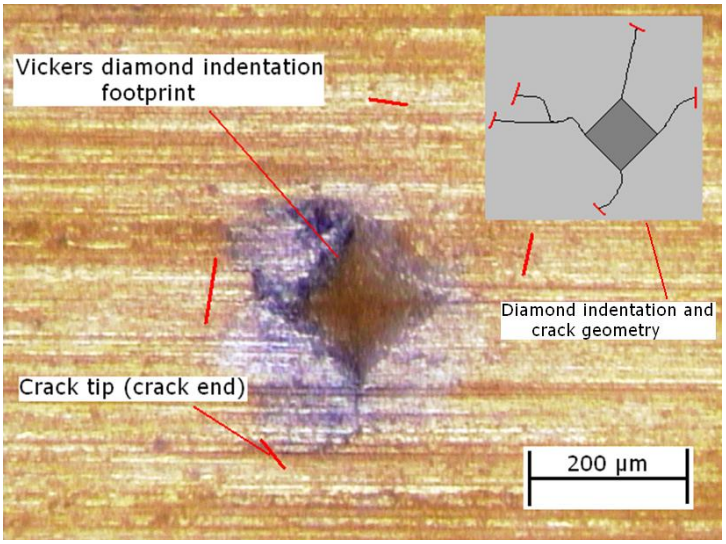

Figure 6.11 An example of the as-received surface of the ZrO_2 indented by using a 30 kg load (hardness =926 HV (9.07 GPa), crack length = 437µm, K_{1c} = 6.94 MPa $m^{1/2}$).

The average crack length produced from the Vickers indentation test was 270µm for ZrO_2. Results from 50 indentations present that the crack lengths range from 221µm as the lowest and 335µm being the highest for ZrO_2. The variation from its mean value was wide due to the microcracks pre-

existing on the ZrO_2's surface. If the surfaces were well polished the results of the crack lengths would be much lower as the surface would be less prone to cracking after grinding and fine polishing of the ZrO_2. However, a smoother surface would prevent the laser from being absorbed sufficiently into the material surface and often has the tendency to reflect more than absorb and so the surfaces were not polished and were tested as-received from the manufacturer as mentioned previously.

From applying a 30 kg load it was found that the cracks were significantly large due to the amount of force exhibiting on the surface area of the ZrO_2. An example of such crack profile is shown in Figure 6.13. It was therefore interesting to investigate the crack lengths produced with a lower indentation load, which predictably would have a smaller effect on the end value of the K_{1c} of the ZrO_2 engineering ceramic. As such, a 5 kg indentation load was used due to the force over the surface area being much lower. This would produce a smaller footprint of the diamond and the resulting crack lengths. This would therefore, result to producing a lower K_{1c} value than the literature and the manufacturers range given for the ZrO_2.

The K_{1c} values for the as-received surfaces after applying an indentation load of 30 kg as presented in Figure 6.12 showed that the values obtained complied with the values given in the literature [37]. The average K_{1c} for ZrO_2 was found to be 12.52 MPa $m^{1/2}$. It is indicative from the graph in Figure 6.12 that there is a significant level of fluctuation for the values above and below the mean range.

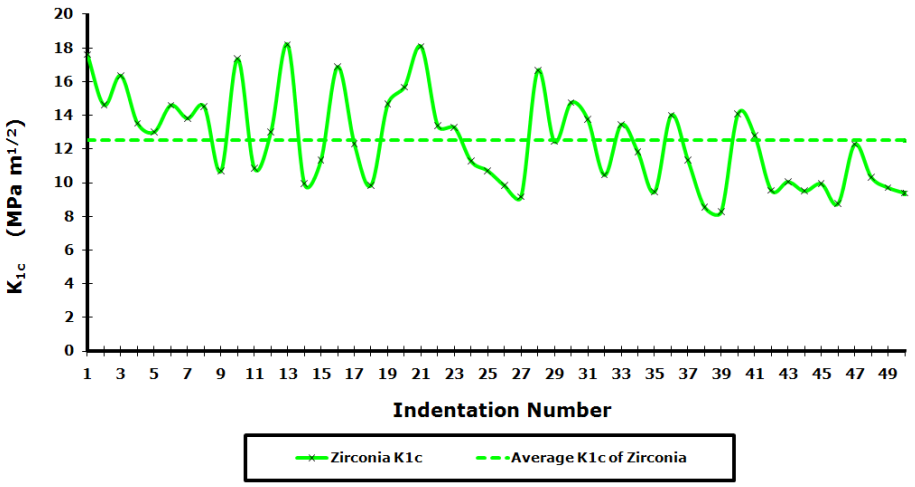

Figure 6.12 K_{1c} of the as-received surface of the ZrO_2 after applying a load of 30 kg.

The highest value above the mean was found to be 17.20 MPa $m^{1/2}$ and the lowest value above the mean was 7.29 MPa $m^{1/2}$. This has occurred due to the following factors: (a) a change in the material hardness influences the end K_{1c} value. The change in the hardness by ± 100 HV resulted into a change in the final K_{1c} value by ± 0.34 MPa $m^{1/2}$ (according to Equation 6.10); (b) change in the crack length (being the major parameter in the equation as used in this work (Equation 6.10)) by ± 100μm resulted into change in the end K_{1c} value over ± 6.31 MPa $m^{1/2}$ if the hardness was up to 1250 HV as a particular input parameter in the calculation. Hence, the crack length has a bigger influence

on the K_{1c} end value in comparison to the hardness; (c) the surface microcracks and porosity pre-existing on the ZrO_2 surface, making it prone to cracking and reduces the ceramics resistance to fracture and (d) the response of ZrO_2 to diamond indentation as some of the areas within the ZrO_2 produced fluctuating values as opposed to other areas from the view point of the crack length, porosity and the surface flaws. The surface condition should also be considered as the surface roughness for the ZrO_2 was exceptionally high for conducting the Vickers indentation test and this would have resulted in producing higher crack lengths that further resulted to reduction in the ZrO_2's K_{1c} value. Similarly, these aspects should also be taken into consideration with the Si_3N_4 engineering ceramics.

The hardness of ZrO_2 from applying a 5 kg load was much lower than the hardness values obtained after applying a load of 30 kg. This was because of the 5 kg load applied to the material's surface area resulted into lower penetration of the diamond indentation into the ZrO_2 as well as the surface area of the diamond footprint also being smaller in dimension that resulted in generating a lower hardness value. The average hardness value for the ZrO_2 was 973 HV with the highest value being 1330 HV above the mean and lowest being 707 HV below the mean. The hardness values of the ZrO_2 by using a 5 kg load comply with the hardness values provided by the manufacturer. However, they were found to be towards a bottom limit. A possible cause of this vast fluctuation in the values may have occurred due to the ZrO_2 comprising of microcracks, porosity and impurities on the near surface layer in comparison with the bulk hardness often produced fluctuating results.

The results showed minimal difference in the generated crack lengths for the ZrO_2 from applying a 5 kg load in comparison with the results from applying 30 kg load. The average crack length was 277µm ranging between 170µm to 512µm. Despite the indentation load and the applied force being much smaller in comparison with the 30 kg load, the material was still cracking in equivalent measure to the results of the trials conducted by using a higher load. As with the Si_3N_4, the ZrO_2 also indicated that the surface did not exhibit a good response during the indentation test. This indicated that that a smoother surface finish was more ideal when conducting the diamond indentation test so that surface scaring and microcracks pre-existing on the ZrO_2 were minimized and the strength of the top surface layer is further enhanced for a better indentation response. This in turn would also increase the surface strength and avoid cracks from the diamond indentation to interconnect with the pre-existing surface flaws and microcracks.

Ponton and Rawlings [129] suggested that a minimum loading of 50N must be pressed in order to produce a diamond indent. The minimum loading used herein agrees to the work of Ponton and Rawlings [129]. Despite, the loading herein was 49.05N, we yet see a diamond indentation as presented in Figure 6.13 with a median half-penny shape profile. Previous experiments by employing lower indentation loads such as 24.5N and 9.7N also created a sufficient footprint from the Vickers

diamond indentation. The diamond indentation in Figure 6.13 is smaller in size when compared with the indentation created by the 30 kg load. However, the average crack lengths found from using a 5 kg indentation load were equally the same size as that of the 30 kg. The differences between the average values for two test results were 3% and less when considering a larger pool of data. From this, it can be gathered that macro hardness indentation test may be more stable at higher indentation loads than lower particularly with hard brittle materials such as ZrO_2.

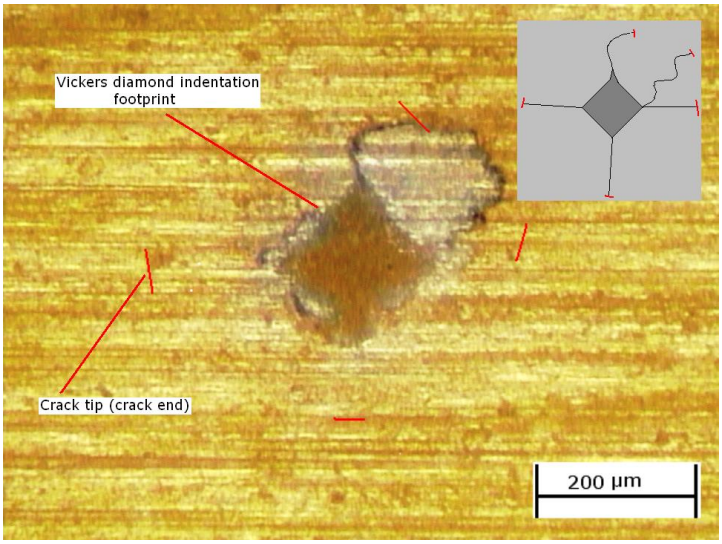

Figure 6.13 An example of the as-received surface of ZrO_2 indented with by a 5 kg load (hardness =1120 HV (10.97 GPa), crack length = 425 µm, K_{1c} = 1.10 MPa $m^{1/2}$).

The result found for hardness herein when employing a 30 kg indentation load match with the values provided by the manufacturer and proves that the method used for the hardness calculation and measurement of the crack lengths was valid. Although, the values for the hardness are much smaller than the values provided in the manufacturer's specification when using a 5 kg load. This was due to the fact that the indentation load was much smaller and produced smaller footprints of the diamond which exerted lower force to the surface and reduced the end value of the K_{1c}. The average K_{1c} was found to be 2.45 MPa $m^{1/2}$ for the ZrO_2 as presented in Figure 6.13 also showing the highest value being 4.42 MPa $m^{1/2}$ and the lowest being 0.92 MPa $m^{1/2}$. The hardness can become much higher if the surfaces were ground and polished prior to the Vickers indentation test as previously stated. This would minimize the surface micro-cracks and resulted in obtaining a better consistency in achieving the hardness value and the resulting crack lengths. The surfaces were tested as-received due to the comparison made with the laser treated surface as the ground and polished surfaces would enhance the materials reflectivity to the laser beam and would minimize the laser beam absorption into the ZrO_2; consequently a compromise was required to be made.

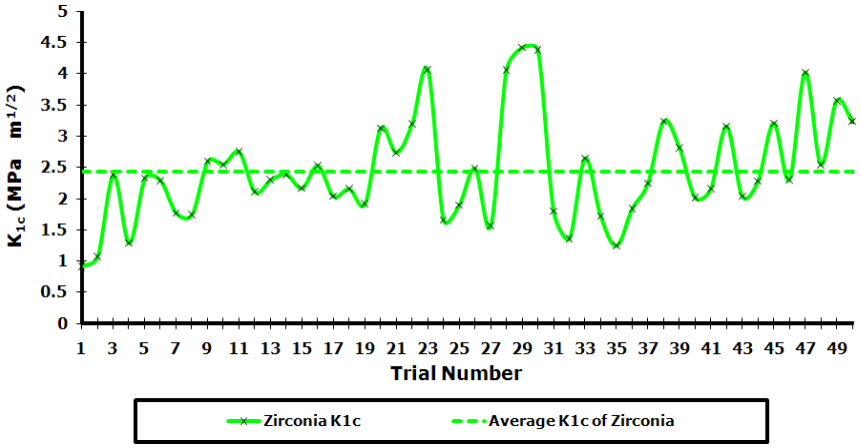

Figure 6.14 K_{1c} of the as-received surfaces of the ZrO_2 from applying a 5 kg indentation load.

6.6.2 Fibre Laser Surface Treatment of the Si_3N_4

The mean hardness found was 1179 HV on the fibre laser treated Si_3N_4. The highest value above the mean was 1449 HV and the lowest being 751 HV. There was a 4% difference between the average hardness values obtained from the fibre laser treatment in comparison with the average hardness values obtained by the as-received surface (see Section 4.1). This is somewhat inconsiderable as there is a tendency for the hardness to fluctuate within ±10% of the average value particularly by using the Vickers indentation method [118]. Through, in general, an increase in the hardness of a material indicates that the surface has become more brittle and therefore was prone to cracking and fracture. This would manifest as longer crack lengths on the corners of the diamond indentations. This however, did not occur as the average crack lengths on the fibre laser treated surface were much reduced in comparison to the crack length of the as-received surface, 242µm compared to 377µm respectively. The fibre laser treated surfaces also comprised of much smaller cracks during the Vickers indentation test in comparison to that of the as-received surface as is evident in Figure 6.15.

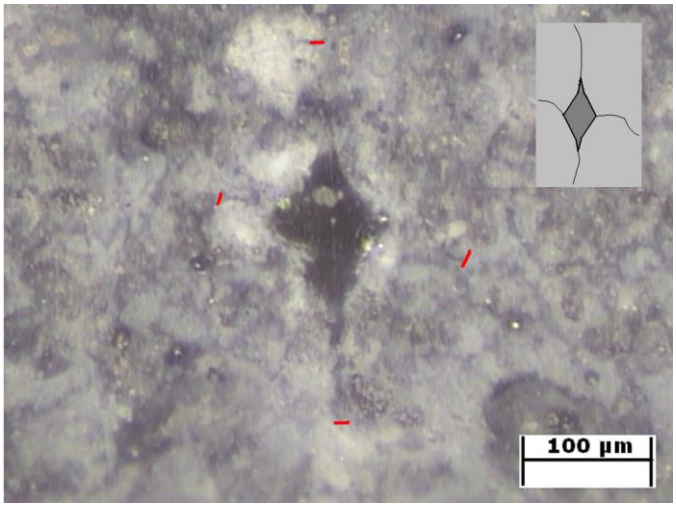

Figure 6.15 Fibre laser treated surface of the Si_3N_4 engineering ceramic indented by a 5 kg load, laser power = 150 W, 100 mm/min, 3mm post size, (hardness = 7.73 GPa, crack length = 247µm, K_{1c} = 3.59 MPa $m^{1/2}$).

The 4% increase in hardness but a decrease in the crack lengths following the fibre laser surface treatment would have occurred by the event of strain hardening taking place as result of the fibre laser-Si_3N_4 surface interaction. The strain hardening through movement of dislocations, at elevated temperatures in turn would have induced compression into the surface and sub-surface of the ceramic and through the effect of transformation hardening.

If one considers the heat generated from irradiation by the fibre laser beam is likely to have caused transformation toughness where the Si_3N_4 to transform from the α to β state at 1600°C, as stated by Jiang *et al.* [171]. This in turn would have caused the observed increase in the hardness of the Si_3N_4 to 3600 HV. Since, the temperature during the fibre laser surface treatment has been found to be much higher than 1600°C, as indicated from the surface melting and decomposition which would imply that the ceramic was heated to around a temperature of about 1900°C or above where phase transformation of α-β phase will inherently occur after the fibre laser surface treatment of the Si_3N_4.

An investigation by Moon *et al.* [172] found that the fracture toughness of Al_2O_3 and Si_3N_4 ceramics was improved considerably by generating dislocations within the ceramics by plastic deformation (shot blasting) and then annealing to temperatures of 1500°C. Owing to the assumption that the heating temperature is around 2000°C and the decomposition temperature is around 1900°C for the Si_3N_4, the fibre laser surface treatment induced compression (see Figure 6.16); the tension would have needed to overcome the compression in order to produce a fracture. Therefore, the cracking of the Si_3N_4 was much smaller in comparison to the as-received surface. This meant that the tension induced by the 5 kg load to produce the crack on the fibre laser treated surface was much smaller than the induced compression. This rational goes some way to explaining the reason why smaller crack lengths have been found on the fibre laser treated Si_3N_4 surface in comparison with the as-received surface.

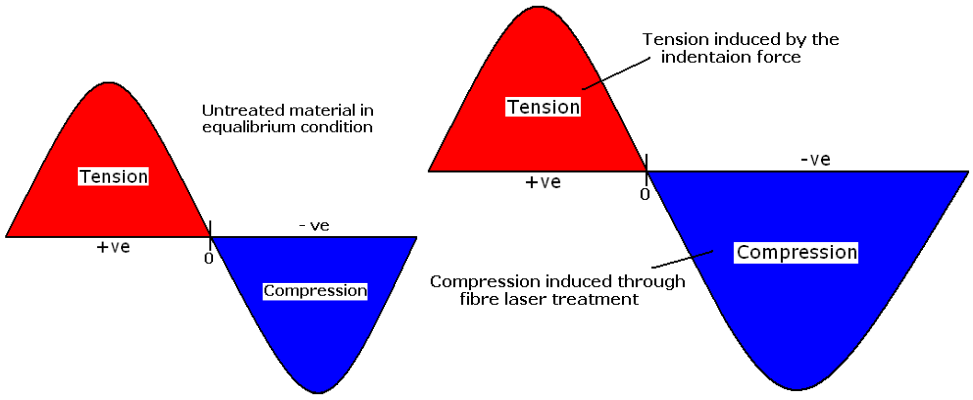

Figure 6.16 Diagram of the tension and compression concept where (a) is the state of the ceramic under equilibrium condition and (b) showing the increase in induced compression from the fibre laser surface treatment.

Residual stress is generally found by using the X-ray diffraction (XRD) method on the Si_3N_4 ceramics [173]. However, in this case, the fibre laser treated surface of the Si_3N_4 ceramic becomes amorphous after decomposition of the Si_3N_4 at 1900°C. Although, X-rays diffract from the amorphous layer, there are yet no sharp diffraction peaks that can be found and an amorphous hump with a broad profile is found whose position can be determined by the average intermolecular spacing. But, this is not ideal for residual stress measurement and therefore a possible increase in the compressive residual stress was only predicted mainly based on the decrease in the Vickers indented crack length of the ceramic after the fibre laser treatment in this study.

The average K_{1c} value for the Si_3N_4 after the fibre laser surface treatment was 3.25 MPa $m^{1/2}$. The highest K_{1c} value obtained above the mean was 6.03 MPa $m^{1/2}$. The lowest value below the mean was 2.20 MPa $m^{1/2}$ for the Si_3N_4 as presented in Figure 6.17 and Table 6.5. The K_{1c} values for the fibre laser treated Si_3N_4 were improved by 47% in comparison with that of the as-received surfaces under the measured conditions. The values in Figure 6.17 mainly fluctuate due 37% reduction in the crack lengths found for the fibre laser treated. In those areas where the K_{1c} is high, indicate that the localized near surface layer has more resistance to crack propagation under cyclic loads or during the onset of any tensile stresses.

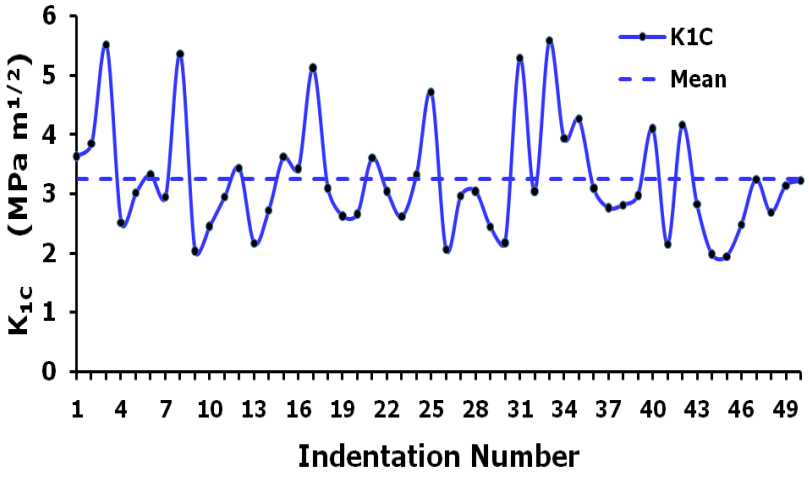

Figure 6.17 K_{1c} of the fibre laser treated surfaces of the Si_3N_4 from applying 5 kg indentation load.

Indentation fracture toughness method is heavily dependent on the local microstructural changes and its influence. Hence, the microstructure of the fibre laser irradiated and as-received surfaces of the Si_3N_4 ceramic are presented in Figure 6.17 (a) – (d). Surface flaws, cavity and micro porosity as well as morphology are also present in the image. Figure 6.17 (c) and (d) show the microstructure of the fibre laser irradiated Si_3N_4 ceramics and is somewhat different to that of the as-received surface. It can be seen that considerable amount of material removal has occurred from the laser beam interaction after some degree of decomposition taking place. The removal of the surface was around 101µm by using compressed air assist gas. This has produced a degree of oxide layer from the exposure to the atmosphere and would have also changed the composition of the laser treated area of

the Si_3N_4 as previously shown in Chapter 5. The surface morphology also shows a reduction in the porosity and the surface flaws that are apparent particularly in Figure 6.17(a). This may have caused the increase in hardness with reduced crack length. This in turn increases the K_{1c} under the measured conditions.

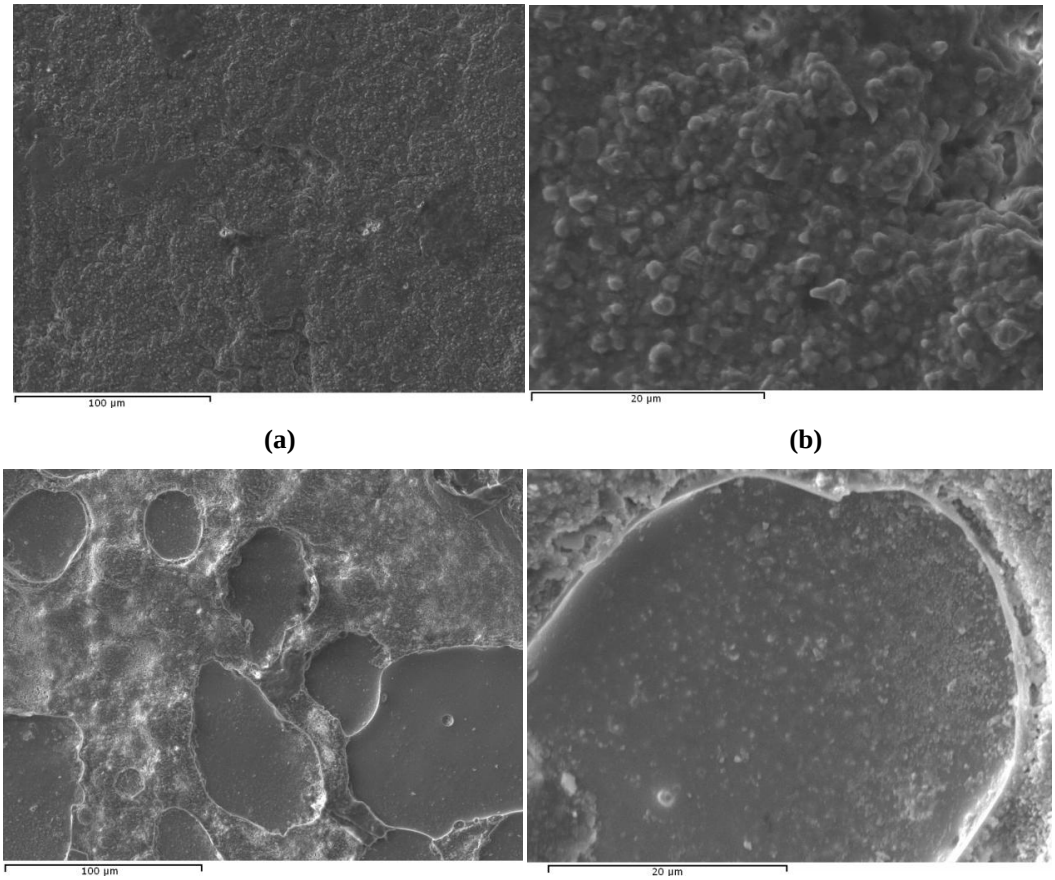

Figure 6.17 SEM image of the microstructure of the as-received surface Si_3N_4 engineering ceramic presented in (a) at x500 and (b) at x3000 resolution as well as the surface morphology and the microstructure of the fibre laser surface treated surface of the Si_3N_4 engineering ceramic at x500 and (b) at x3000 resolution.

Consideration should also be given to the processing conditions of the ceramic as this will vary the depth of indentation and the relative cracking geometry underneath the diamond indenter depending on the sintering conditions of the ceramic and the relative density. In this case the Si_3N_4 was not sintered and therefore was not fully dense (3.15 g/cm^3) [174] compared to a fully sintered Si_3N_4 (3.60 - 3.70 g/cm^3) [42]. The partially sintered or un-sintered Si_3N_4 would be more porous in comparison to that of a fully sintered Si_3N_4 and therefore would be low in strength. This also means that the cracking geometry would be longer in comparison to the fully dense Si_3N_4. The depth of the indentation is dependent on the indentation load applied. At 30 kg the depth of the indentation was around 30.05µm on the laser treated track. At 5 kg of load, the depth was 14.74µm on the laser

treated track. The depth of the laser treated track ranged from 100 to 120µm and in relation to the diamond indentation depth was much deeper. This meant that the diamond indentation was not fully penetrating through the fibre laser irradiated surface to make contact with the sub-surface where the condition of the sub-surface microstructure would fully affect the cracking geometry of the fibre laser irradiated surface. The condition of the sub-surface would affect the crack geometry for the instance where the diamond indenter is penetrating through the modified surface layer.

Table 6.5 (see end of the Chapter) presents the results obtained by the as-received surface and the fibre laser treated surface of the Si_3N_4 engineering ceramic. Values for the fibre laser treated surface were compared to the values of the as-received and the CO_2 laser irradiated surface indented by using a 5 kg load to determine the percentage rise and decrease. A load of 5 kg was used after discovering that the 30 kg load would produce a bigger diamond indent which would overlap the microcracks which exist on the surface of the ceramics after the laser treatment. Vickers indentation method offers many advantages for calculating the K_{1c}. Nevertheless, it has many flaws. Those are the results obtained from the hardness test heavily depending on the operator's ability to detect the crack lengths and its geometry. The ceramics ability to the indentation response and the surface conditions that were used during the indentation test as smoother surfaces would result to higher surface strength and influences the hardness value and the resulting crack lengths. The K_{1c} results could be much more accurate if a consistent surface hardness value was obtained along with its crack geometry which could be found from employing other indentation techniques as well as various other methods by using other existing equations would also produce variation in the K_{1c} value.

The K_{1c} value would also be affected if the effect of Young's modulus is to be considered. The fibre laser irradiation would increase the stress and strain ratio of the ceramic on one plane in comparison to the other planes. This may then produce anisotropy within the plane that is normal to the direction of the laser treatment as opposed to the remaining untreated material in other planes. The ceramic would also become anisotropic as the grain structure found from the SEM (see Figure 6.17) images does not show any regularity in comparison to the one of the as-received surface. This would indicate that the laser treated surface may be anisotropic. As well as the changed composition and reduction in porosity, the change in the Young's modulus would also occur due to an interlocking the microstructure produced by the fibre laser irradiation. The interlocked microstructure will produce refinement in surface flaws and covering of the microcracks. This in turn, will create a denser surface layer and affect the elastic property by increasing the stress resistance. If the Young's modulus is raised due to such effects then the end K_{1c} value would also increase as the Young's modulus is an effective parameter into the K_{1c} equation. So, it is likely that the influence of the Young's modulus would be significant in calculating the K_{1c} values in this investigation.

6.6.3 CO_2 Laser Irradiated Surfaces of Si_3N_4

The average hardness of the CO_2 laser treated surface was 1010 HV - a reduction of 7.5% from the as-received surface. This reduction in the surface hardness indicated that a softer surface layer was produced by CO_2 laser treatment. This resulted in a surface that would be more resistant to cracking and fracture. The hardness values ranged between 666 HV and 1373 HV. From the range, it can be gathered that the fluctuation in the hardness value was large. This was due to the surface containing an oxide layer of around 123µm thickness (presented in the Chapter 5, Section 5.3.3.2.2 , Figure 5.25) which was somewhat softer and more uneven in comparison to the laser unaffected surface. As such, the diamond indenter penetrated deeper into the surface in some of the regions than in others. This is why the diamond indentation in Figure 6.19 is not symmetrical in comparison to that of the as-received surface.

Reduction of the surface hardness from the CO_2 laser surface treatment led to a reduction in the cracks lengths induced by the Vickers diamond indenter to an average of 216µm. This was 43% lower in comparison to the as-received surface of the Si_3N_4 engineering ceramic. The crack lengths ranged between 179 to 463µm. Vast fluctuations resulted from the newly formed, uneven oxide layer after the CO_2 laser surface treatment. This was also seen with the Si_3N_4 ceramic irradiated by using the fibre laser surface treatment. However, the oxide layer appeared to be somewhat larger in width and in depth of the CO_2 laser irradiated surface of the Si_3N_4 as seen in Figure 6.19.

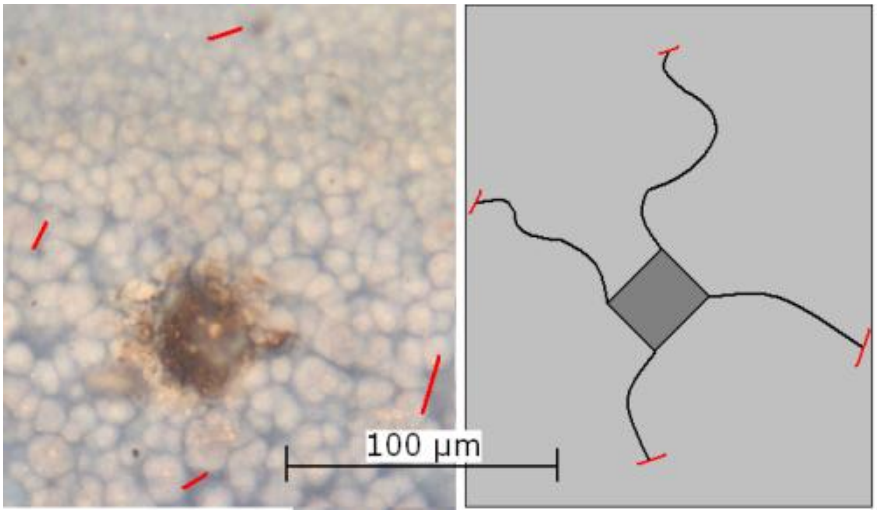

Figure 6.19 Microscopic image (left) and the crack profile (right) of the CO_2 laser treated surface of the Si_3N_4 engineering ceramic.

It can be seen from Figure 6.19 that the diamond indentation was larger than that of the as-received surface of the Si_3N_4 engineering ceramic (see Figure 6.9) by about 7µm. The indentation size measured was 117µm, with a hardness of 666 HV and the crack length of 160µm. The topographical image in Chapter 5, Section 5.3.3.2.2, Figure 5.25 of the CO_2 laser treated surface, presents the newly formed surface layer comprising of surface oxidation along with the heat affected zone (HAZ)

and the laser unaffected zone. The new surface was formed from the result of the Si_3N_4 engineering ceramic being exposed to the atmosphere at high temperatures. This would have led to a possible compositional change where the Si_3N_4 was changed to SiO_2. The change in composition of the Si_3N_4 was also confirmed from a previous investigation by Lysenko *et al.* [122]. The average K_{1c} of the CO_2 laser treated surface was found to be 3.16 MPa $m^{1/2}$ and ranged between 1.95 and 5.30 MPa $m^{1/2}$ as presented in Figure 6.20. These values also fluctuate considerably due to the variations found in the hardness and the crack lengths that led to generating an uneven surface profile after the CO_2 laser surface treatment.

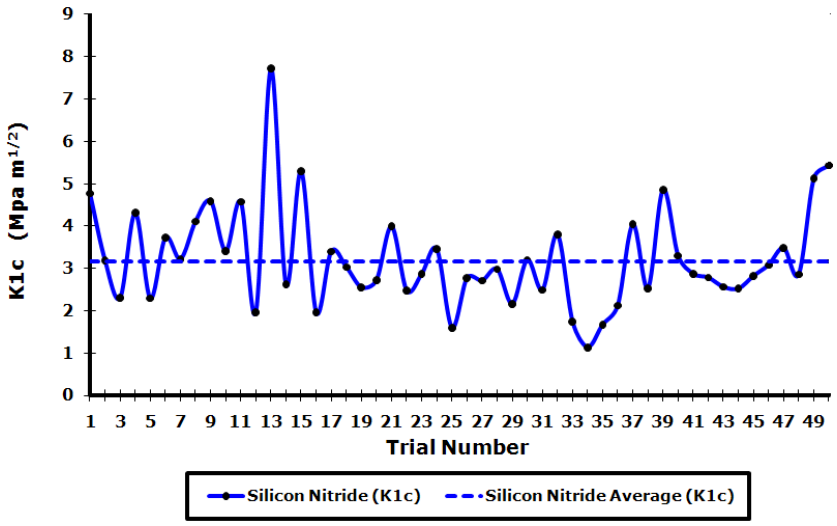

Figure 6.20 K_{1c} of the CO_2 laser treated surface of the Si_3N_4 ceramic.

6.6.4 Analysis of the Fibre Laser Treated Surfaces of the Si_3N_4 by Using a 5 kg Indentation Load

The mean hardness found was 940 HV on the fibre laser treated ZrO_2. The highest value above the mean was 1079 HV and the lowest being 726 HV. There was a 4.5% difference between the average hardness values obtained from the fibre laser treatment in comparison with the average hardness values obtained by the as-received surface. The fibre laser had decreased the hardness in comparison to that of the as-received surface of the ZrO_2. The average crack length of the fibre treated ZrO_2 was 170µm. The highest above the mean was 243µm and the lowest being 112µm. The crack length was much reduced in comparison with the crack length of the as-received surface which was 270µm. The fibre laser treated surfaces also comprised of much smaller cracks in comparison with the as-received surface (see example in Figure 6.21). Reduction in the surface hardness indicated that the laser surface treatment had softened the top (near) surface layer of the ZrO_2. From this, it can be assumed that some degree of melting and solidification may have taken place during the laser-ceramic interaction. Through this, would have caused a localised ductile surface to have formed along with change in the surface composition.

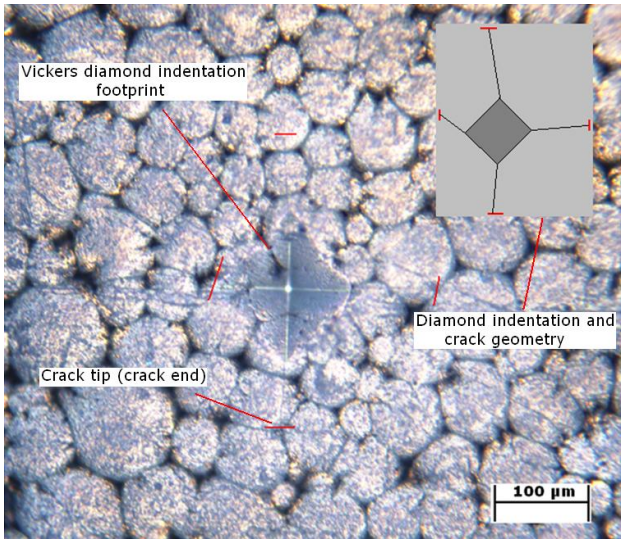

Figure 6.21 An example of the fibre laser treated surface of the ZrO_2 indented by a 5 kg load, laser power = 150 W, 100 mm /min, 3mm post size, (hardness = 654 HV (6.41 GPa), crack length = 232µm, K_{1c} = 3.97 MPa $m^{1/2}$).

The average K_{1c} value for the ZrO_2 after the fibre laser treatment was 5.05 MPa $m^{1/2}$. The highest K_{1c} value obtained above the mean was 7.76 MPa $m^{1/2}$. The lowest value below the mean was 2.67 MPa $m^{1/2}$ for ZrO_2 as presented in Figure 6.21. The K_{1c} values for the fibre laser treated ZrO_2 under the conditions measured were enhanced by 56% in comparison with that of the as-received surfaces. The values in Figure 6.22 fluctuate due to the softening of the treated surface that would have generated lower cracks during the indentation test. In those areas where the K_{1c} is high, indicate that the localised near surface layer has more resistance to crack propagation under cyclic loads or during the onset of any tensile stresses.

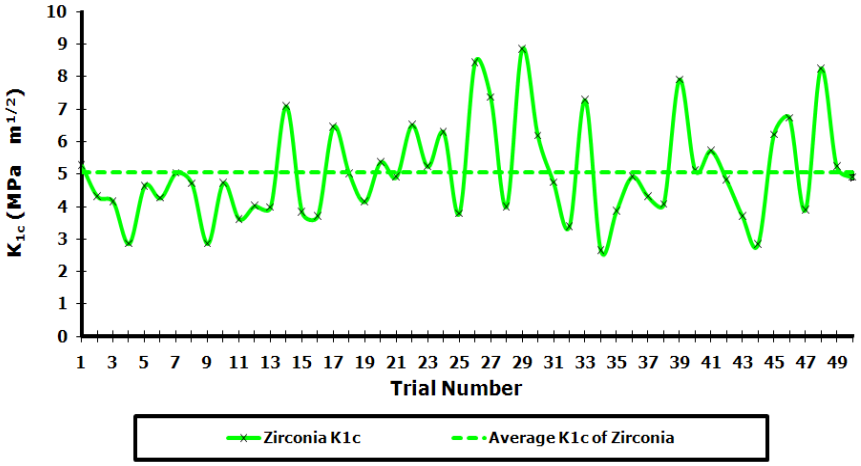

Figure 6.22 K_{1c} of the fibre laser treated surfaces of the ZrO_2 from applying 5 kg indentation load.

6.6.5 Analysis of the CO_2 Laser Treated Surfaces of the ZrO_2 by using a 5 kg Indentation Load

The mean hardness found was 754 HV on the CO_2 laser treated ZrO_2 ceramic. The highest value above the mean was 1120 HV and the lowest being 473 HV. It can be said that there is certainly a

vast amount of difference between the highest hardness value and the lowest. This was due to the difference in absorption and lack of penetration of the beam in some area in comparison to the other areas of the ZrO_2 surface where there was sufficient CO_2 laser beam interaction occurring with the ceramic. This made the more CO_2 laser affected areas to allow the diamond indentation to penetrate than other which consequently had affected the surface hardness and resulted to a difference between the hardness of the CO_2 laser irradiated surface of the ceramic and the fibre laser irradiated surface of just over 10%.

Figure 6.29 illustrates the diamond footprint of the CO_2 laser irradiated surface of the ZrO_2 engineering ceramic along with its cracking geometry. Average crack length of the CO_2 laser treated surfaces was 216µm with the highest value above the mean being 333µm and the lowest being 143µm as presented in Figure 6.29. This was interesting when compared to the crack lengths obtained by the fibre laser surface treatment of the ZrO_2 which were considerably low. It is usually expected that the softer surface with low hardness would result to producing low cracking. This was not the case with the CO_2 laser treated ZrO_2 when compared to the crack length obtained by the fibre laser surface of the ZrO_2 which comprise of 27% lower cracks. Justification for this phenomenon is given later in this Chapter.

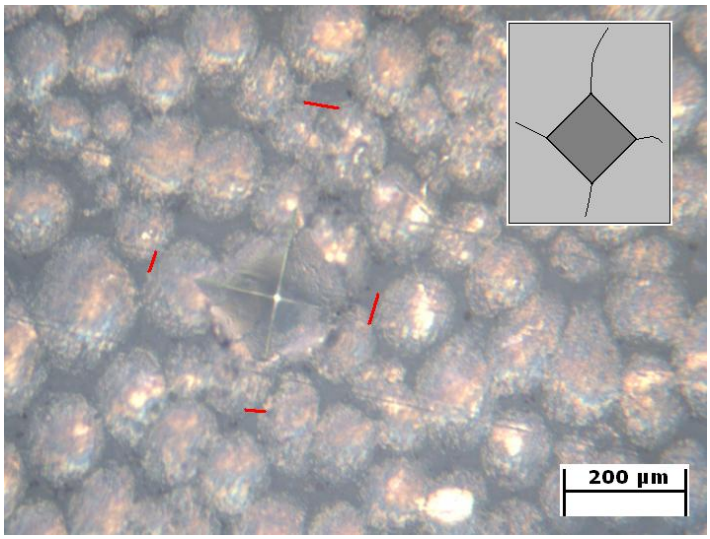

Figure 6.23 Optical image of the CO_2 laser irradiated surface of the ZrO_2 ceramic indented by a 49.05 N load; 600 mm/min; 3mm post size; (hardness = 650 HV; crack length = 297µm; K_{1C} = 2.75 MPa $m^{1/2}$).

Figure 6.24 illustrates the K_{1c} values obtained for the CO_2 laser irradiated surface of the ZrO_2 engineering ceramic showing an average K_{1c} value of 3.75 MPa $m^{1/2}$. The highest above the mean was found to be 6.77 MPa $m^{1/2}$ and the lowest was found to be 1.69 MPa $m^{1/2}$. The vast fluctuation is also expected with the results for this sample since the fracture toughness property K_{1c} is a reflection of the surface hardness and the cracking geometry of the diamond indentation which also produced significant fluctuation in the values found. The K_{1c} of the CO_2 laser irradiated surface of the ZrO_2

ceramic was however, significantly higher than the as-received surface. This meant that a level of surface modification and increase in the K_{1c} under the measured condition was found up to 50% which is remarkable in general.

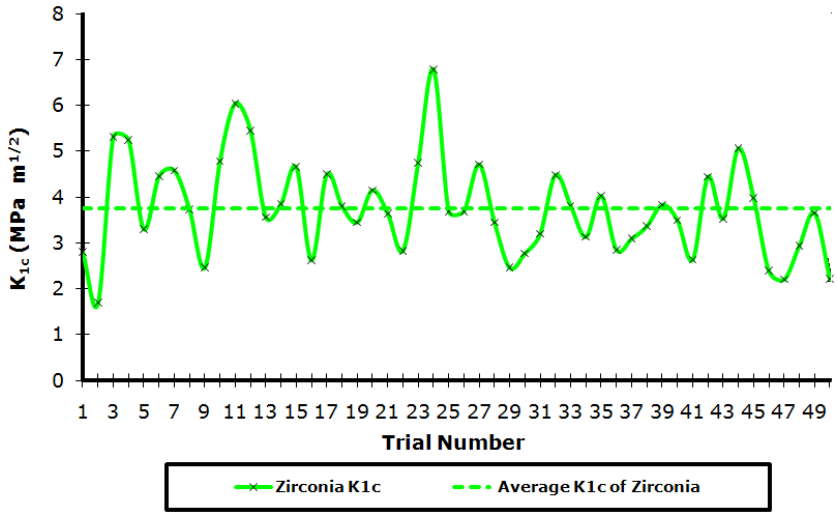

Figure 6.24 K_{1c} of the CO_2 laser treated surfaces of the ZrO_2 from applying 5 kg indentation load.

6.6.6 Comparison of CO_2 Laser Surface Treatment and Fibre Laser Surface Treatment of the Si_3N_4 Engineering Ceramic

6.6.6.1 Change in the surface hardness

The average hardness of the CO_2 laser irradiated surface of the Si_3N_4 was 1027 HV which was - a reduction of 13% from the fibre laser irradiated surface (1154 HV). This reduction in the surface hardness indicated that a softer surface layer was also produced by the CO_2 laser irradiation in comparison to that of the fibre laser irradiation. The hardness values ranged between 264 HV and 1449 HV for the CO_2 laser irradiated Si_3N_4 and between 777 HV to 1449 HV for the fibre laser irradiated Si_3N_4 as shown in Figure 6.24. It is evident from Figure 6.23 that the fluctuation in the hardness value was large. The reason for this was due to the surface containing an oxide layer of around 100 to 150µm thickness resulting from both laser treatments. This was somewhat softer and more uneven in comparison to the laser unaffected surface. As such, the diamond indenter penetrated deeper into the surface in some of the regions than in others. This is why the diamond indentation shown in Figure 6.15 and Figure 6.19 are not symmetrical.

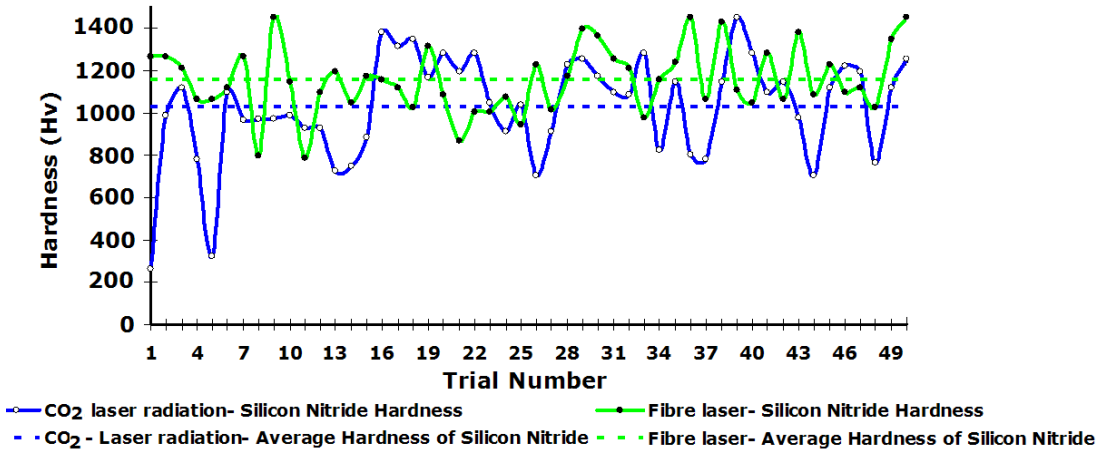

Figure 6.25 Hardness of the Si_3N_4 ceramic treated by the CO_2 and a fibre laser irradiation.

It can be seen from the footprint of the diamond indentation produced by the CO_2 and the fibre laser that the footprint of the CO_2 laser irradiated Si_3N_4 is larger than that of the fibre laser irradiated surface. Both the CO_2 and the fibre laser treated surface of the Si_3N_4 genuinely showed evidence of surface oxidation. The new surface was formed from the result of the Si_3N_4 ceramic being exposed to the atmosphere at high temperatures. This would have led to the possible compositional change where the Si_3N_4 was changed to SiO_2. Moreover, the occurrence of the white phase as illustrated in Figure 6.15 and Figure 6.19 would also lead to some modification in the microstructure of the Si_3N_4 ceramic as the white oxide layer would be formed above the normal surface of the Si_3N_4. This in turn would generate in-filling of the surface cracks in various areas and also cover the grains that would normally appear on the top surface layer. The change in composition of the Si_3N_4 was also confirmed from a previous investigation [124]. A reduction in the crack length obtained on the CO_2 laser irradiated surface occurred due to the oxide layer being somewhat thicker in various areas in comparison which showed lower surface hardness and the resulting crack lengths.

6.6.6.2 Change in the crack length

The crack lengths obtained from both of the laser irradiated surfaces are presented in Figure 6.26. The average crack length obtained from the CO_2 laser irradiation was 277µm and ranged between 179µm to 463µm. This in comparison to the cracks produced by the Vickers indentation test of the fibre laser irradiated Si_3N_4 was 16% lower. An average crack length found was 242µm with a highest of 307µm and the lowest of 160µm for the fibre laser irradiated surfaces. The fluctuation from the values in Figure 6.26 has resulted from the newly formed, uneven oxide layer after both of the laser surface treatments.

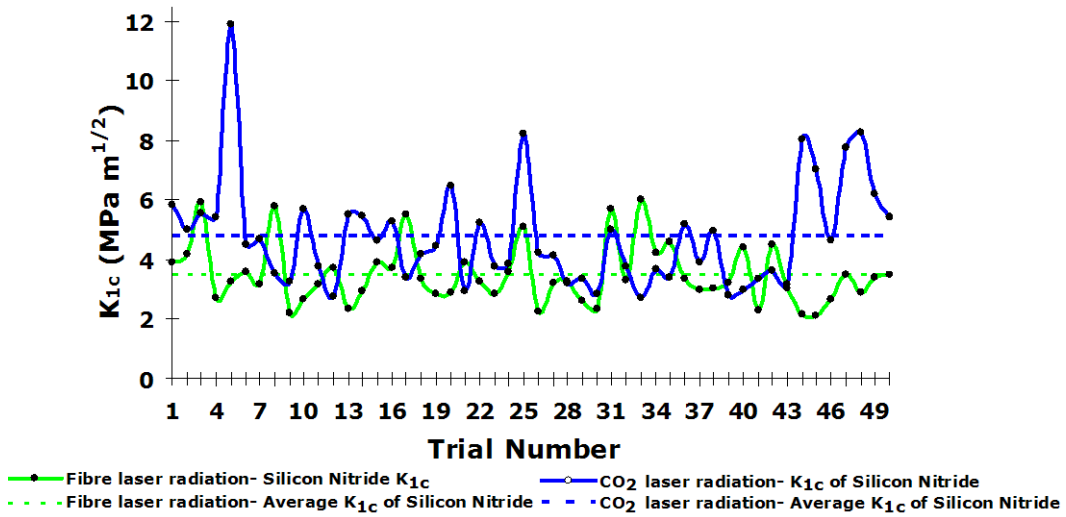

Figure 6.26 K_{1c} of the CO_2 laser treated surface of the Si_3N_4 ceramic.

6.6.6.3 Change in the K_{1c}

The average K_{1c} of the CO_2 laser treated surface was found to be 4.77 MPa $m^{1/2}$ and ranged between 2.74 MPa $m^{1/2}$ and 11.90 MPa $m^{1/2}$. This was 26% higher in comparison to that of the fibre laser irradiated surface of the Si_3N_4 ceramic. The average K_{1c} value for the Si_3N_4 after the fibre laser treatment was 3.51 MPa $m^{1/2}$. The highest K_{1c} value obtained above the mean was 6.03MPa $m^{1/2}$. The results are shown in Figure 6.27. The values also fluctuate considerably due to the variations found in the hardness and the crack lengths that led to generating an uneven surface profile as mentioned earlier in this study.

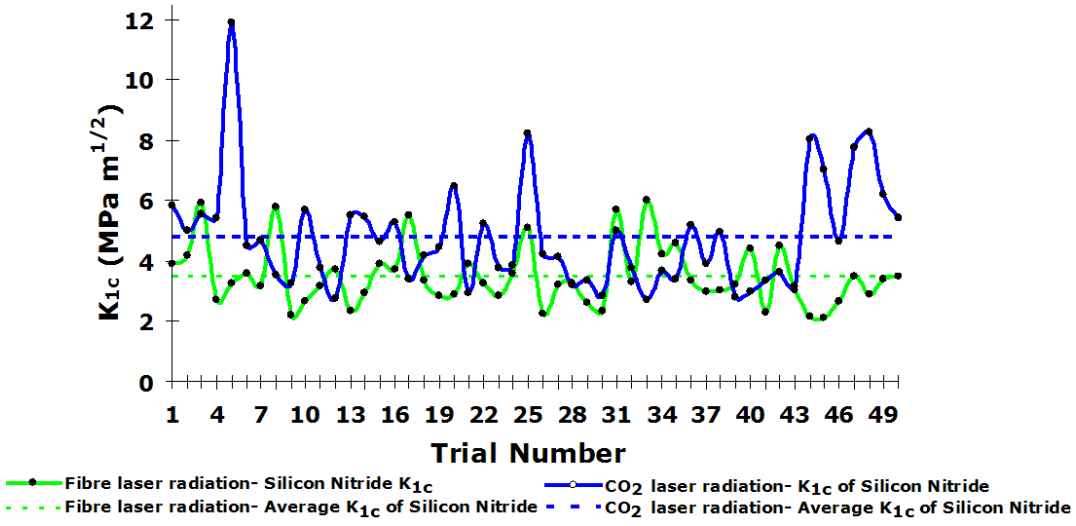

Figure 6.27 K_{1c} of the CO_2 laser treated surface of the Si_3N_4 ceramic.

6.6.7 Comparison of CO_2 Laser Surface Treatment with Fibre Laser Surface Treatment of the ZrO_2 Engineering Ceramic

6.6.7.1 Change in the surface hardness

Figure 6.27 presents the fluctuations in the hardness of the CO_2 and the fibre laser irradiated surfaces of the ZrO_2 ceramics along with its mean hardness value over 50 indentation tests that were conducted on one surface plane. As one can see that the hardness of the CO_2 laser irradiated surfaces was considerably lower than that of the fibre laser irradiated surface. The average hardness of the CO_2 laser irradiated ZrO_2 was 754 HV with the highest value being 1120 HV and the lowest being 473 HV. The average hardness for the fibre laser irradiated surface of the ZrO_2 was 940 HV. The highest value above the mean was 1079 HV and the lowest being 726 HV for the ZrO_2 ceramic. The hardness values fluctuated in both of the curves due to an uneven surface being produced from material removal as well as melting and solidification. The hardness of the CO_2 laser irradiated surface was up to 22% lower than that of the fibre laser. This showed that the CO_2 laser irradiation had softened the surface of the ZrO_2 in comparison to that of the fibre laser irradiated surface.

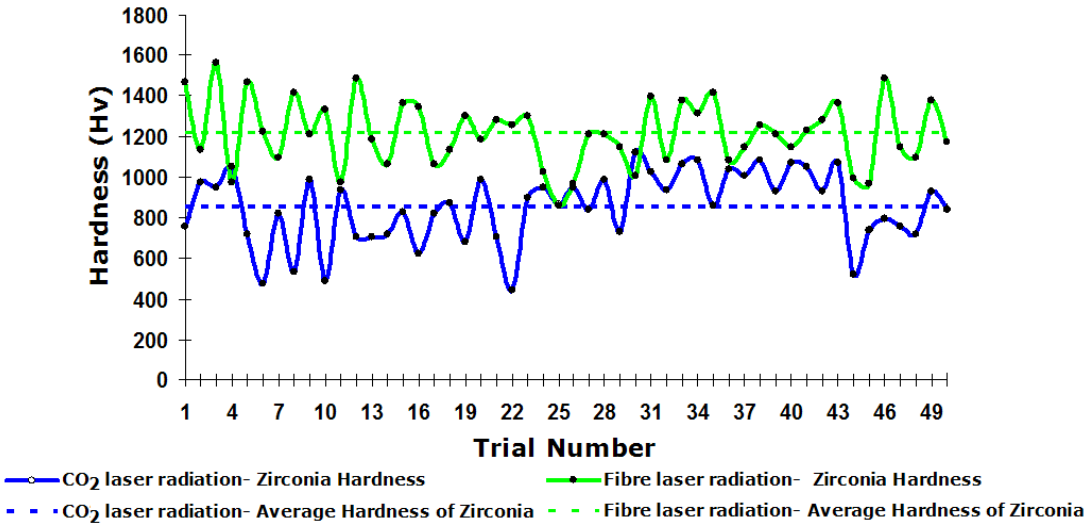

Figure 6.27 Hardness of the ZrO_2 ceramic treated with a CO_2 and a fibre laser irradiation.

6.6.7.2 Change in the crack length

Average crack length of the CO_2 laser treated surfaces was 216µm with the highest value above the mean being 333µm and the lowest being 143µm as presented in Figure 6.29. The average crack length of the fibre laser irradiated surface of the ZrO_2 was 171µm. The crack length was much reduced in comparison with the crack length of the CO_2 laser irradiated surfaces. Despite the increase in hardness produced by the fibre laser irradiated surface, a 21% decrease in crack length was found from the fibre laser irradiation. This can be seen from Figure 6.21 and Figure 6.23 where the diamond indentation produced by the CO_2 laser irradiation was larger due to the softening of the surface but produced high cracking profiles. In comparison, the indentation created by the fibre laser irradiated surface was smaller due to surface hardening and yet produced a considerably smaller

cracking geometry. The expected result was larger crack length due to smaller indentation footprint produced. From this, it can be postulated that compressive residual stress could have been induced during the fibre laser surface irradiation which caused lower crack propagation as further explained in this Chapter.

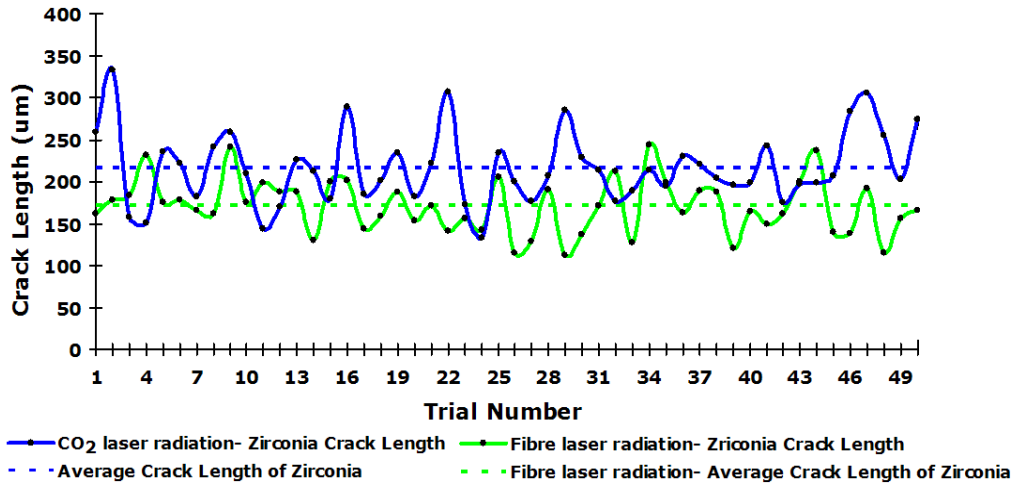

Figure 6.29 Crack length of the ZrO_2 ceramic obtained after a CO_2 and a fibre laser irradiation.

One can see from the optical micrographs in Figure 6.21 and Figure 6.23 that surface oxidation is not apparent. The ZrO_2 ceramic is less sensitive to the effect of surface oxidation during the exposure to the laser beam irradiation. This was due to the majority of the ZrO_2 ceramics comprising of Zr + O_2. It can also be seen from the optical micrographs that the ZrO_2 has been changed in colour especially in Figure 6.21 due to the thermal energy being induced. It is possible however, that the ZrO_2 had undergone a degree of compositional change since it has been exposed to the environment at high temperatures during both CO_2 and the fibre laser irradiation. A compositional change from ZrO_2 to ZrC is likely to have occurred during the laser surface interaction. This would bring changes in the fracture resistance of the ZrO_2 and is deemed to have influenced the K_{1c} values after the laser surface treatments.

6.6.7.3 Change in the surface K_{1c}

Figure 6.30 presents the K_{1c} of the CO_2 and the fibre laser treated ZrO_2 ceramics which showed that the K_{1c} of the fibre laser irradiated surfaces was 29% higher than that of the CO_2 laser irradiated surface. The average K_{1c} of the CO_2 laser irradiated surface of the ZrO_2 was 5.63 MPa $m^{1/2}$ with the highest value being 9.75 MPa $m^{1/2}$ above the mean and the lowest being 2.97 MPa $m^{1/2}$ below the mean. The average value found for the CO_2 laser irradiated surface of the ZrO_2 was 4.16 MPa $m^{1/2}$ with the highest value being 7.54 MPa $m^{1/2}$ and the lowest being 1.79 MPa $m^{1/2}$. The values for both laser treated surfaces fluctuated due to the variation in the surface hardness and the differing crack geometries. The surface finish of the ceramics prior to the laser treatment should also be considered

where the unpolished (as-received) surface is more prone to cracking during the diamond indentation due to pre-existing manufacturing surface flaws and microcracks, which was the case in the study.

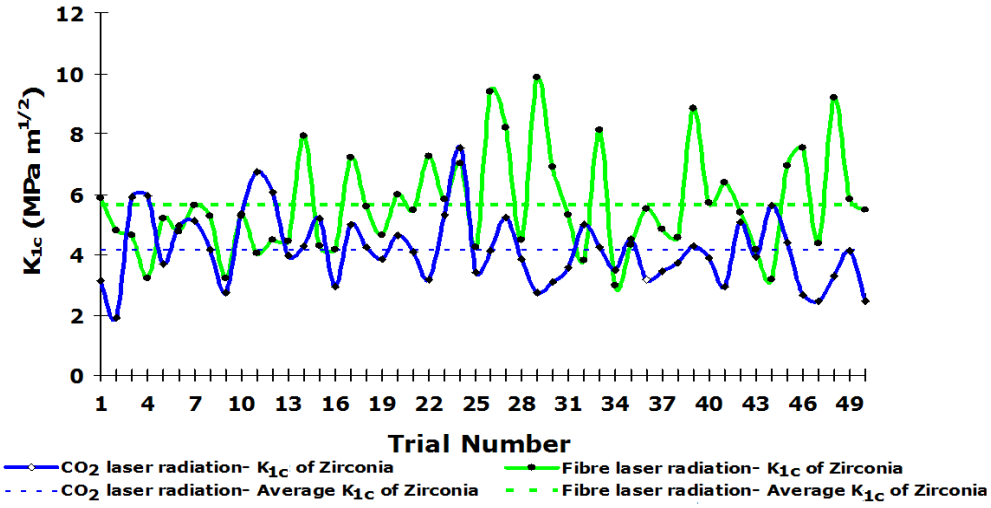

Figure 6.30 K_{1c} of the ZrO_2 ceramic obtained after the CO_2 and a fibre laser irradiation.

6.6.7 Differences between the CO_2 and the Fibre Laser Surface Treatment and the Effects on the Hardness, Crack Lengths and the K_{1c} of the Engineering Ceramics

6.6.7.1 Rationale for the change in the hardness

The results showed that a change in the hardness occurred from both of the laser treatments to the ZrO_2 and the Si_3N_4 engineering ceramics. However, the hardness produced by the CO_2 laser in comparison to the fibre laser was somewhat lower. This was due to the difference in the absorption of the MIR wavelength of the CO_2 laser and the NIR wavelength of the fibre laser. Both the CO_2 and the fibre laser wavelength, however, penetrate to a significant depth within the ceramics. The CO_2 laser has the tendency to produced high interaction zones at the surface, whereas the fibre laser is penetrated deeper into the ceramic layer for the Si_3N_4 ceramic in particular. This produces more compositional change at the top surface irradiated by the CO_2 laser as the white SiO_2 layer is produced. This layer is somewhat softer in comparison to the parent surface. For the ZrO_2 ceramic, the fibre laser wavelength is somewhat transparent. Hence, the interaction is lower in comparison to the CO_2 laser interaction with the ZrO_2. This in turn will produced high local temperature and larger melt pool at the surface, but yet it is still shallow in comparison to the fibre laser irradiated surface. The larger melt zone intrinsically produces a bigger diamond indentation footprint in comparison to the fibre laser irradiated surface and therefore has slightly lower hardness in comparison. This finding relate to the work of White *et al.* [175] who reported that an increase in the hardness of boron carbide ceramic by processing with the NIR wavelength of a Nd:YAG laser was found which comply with the higher hardness found with the NIR wavelength of the fibre laser.

6.6.7.2 Rationale for the change in the crack lengths and the end K_{1c} of the ceramics

The increase in the hardness usually manifests as an increase in the crack length due to the ceramic becoming more brittle. However, this did not occur with the surfaces of both CO_2 and the fibre laser irradiation. A likely cause for this would be the effect of crack healing as the pre-existing surface microcracks on the ceramic were filled and covered particularly by the fibre laser irradiation. Also, the event of phase transformation would have occurred for both ceramics. This would have led to a change in the K_{1c} values.

Consideration must also be given to the event of strain hardening taking place as result of the fibre laser-ceramic surface interaction. The effect of strain hardening through movement of dislocations at elevated temperatures, inherently, could induce compression into the surface and the sub-surface of the ceramic and through the effect of transformation hardening. If one considers the heat generated from the fibre laser beam radiation is likely to have caused the Si_3N_4 in particular to transform from the α to β state at 1600°C, as stated by Jiang *et al.* [171]. This intrinsically, would have caused the observed increase in the hardness of the Si_3N_4 to 3600 HV in particular. Since, the temperature during the fibre laser processing has been found to be much higher than 1600°C [171] for both ceramics, phase transformation of α-β phase will inherently, occur within the Si_3N_4 and from M-phase to an active T-phase would occur within ZrO_2 during the fibre laser irradiation.

An investigation by Moon *et al.* [172] found that the fracture toughness of Al_2O_3 and Si_3N_4 ceramics was improved considerably by generating dislocations within the ceramics by plastic deformation (shot blasting) and then annealing to temperatures of 1500°C. It is postulated that during the ceramic being processed at elevated temperature would have led to an increase in the hardness as the movement of dislocations at high temperatures would have induced a degree of residual stress into the ceramic in the form of compression.

In account of the fibre laser induced compression, the tension would have needed to overcome the compression in order to propagate a crack. Therefore, the cracking of the ceramics was much smaller with the fibre laser irradiated surface in comparison to that of the CO_2 laser irradiation. This meant that the tension induced by the 49.05N load to produce a crack on the fibre laser treated surface was much smaller than the induced compression. This rational goes some way to explaining the reason why smaller crack lengths have been found on the fibre laser treated ceramic (particularly with Si_3N_4) surfaces in comparison with the CO_2 laser treated surface. Values obtained for the hardness, crack length and the K_{1c} for the Si_3N_4 and the ZrO_2 ceramics treated by both the fibre laser and the CO_2 laser are presented in Table 6.5.

6.6.9 Other Influential Aspects Affecting the K_{1c} of the Laser Treated Ceramics

6.6.9.1 Differences in laser parameters

The differences within the K_{1c} results achieved by the CO_2 and the fibre laser surface treatment have occurred due to several aspects which should be considered. Those are the material absorption; laser beam delivery system; wavelength and the brightness (power per unit area) and the beam quality factor (M^2 = 1.3) as well as the Gaussian beam mode of the CO_2 laser (TEM_{01}) whereas the fibre laser M^2 value was 1.2 and the Gaussian beam mode of TEM_{00} indicating that the beam quality of the fibre laser was better and the Gaussian beam mode higher. Therefore, the effect of the beam quality factor is minimal. However, it is important to consider the way in which the Gaussian beam of TEM_{00} is delivered, as this would have an influence on the interaction between the ceramics and the specific laser used. Since the CO_2 laser is delivered by a galvanometers and stationary mirrors the beam is focused at a fine spot size, whereas the fibre laser beam is delivered by a fibre cable which is less focused. It is required that a larger laser-beam spot diameter is used for ceramic surface treatment so that the laser beam is distributed evenly onto the ceramic. In this case a fibre laser with a low focused beam in comparison to that of the CO_2 would be more ideal especially for the surface treatment of the ceramics.

The material absorption co-efficient is varied with different laser wavelengths. As some wavelength are better absorbed by the ceramics than others. The CO_2 laser wavelength absorption with ceramics is about 77%, whereas the fibre laser wavelength absorption is about 92% [91, 126]. This means that the fibre laser wavelength is more absorbed into the material and exhibits better interaction zone. This produces more photon energy that is induced onto the ceramic surface. This in turn, produces high temperatures during the fibre laser processing. This allows the ceramics to undergo phase and compositional changes and affect the hardness and the resulting crack geometries in different ways and has also affected the end K_{1c} result from the two different lasers used.

The difference in the laser brightness (luminance) between the two lasers used would also have an effect during the ceramic interaction as the fibre laser is much brighter than the CO_2 laser. This indicates that there is more power per unit area being executed at the ceramic surface. On account of this, it is indicative that the luminance at high power per unit area is larger with the fibre laser and produces more interaction, high processing temperatures and rather leads to transformation hardening of the ceramics. This is not seen with the CO_2 laser surface treatment. Chapter 8 further presents the effect of the fibre laser-beam brightness on the ZrO_2 engineering ceramic to demonstrate this effect.

6.6.9.2 Influence of the ceramics surface condition

The CO_2 and the fibre laser both were executed on the as-received surfaces of the ZrO_2 and the Si_3N_4 ceramics which comprised of some degree of surface flaws such as porosity and microcracks and machine induced scaring prior to the laser surface treatment. Due to this, the possibility of crack propagation increases during the diamond indentation tests. If the surface flaws were minimized in this study by introducing grinding and polishing of the near surface layer of the ceramics, then the crack propagation during the indentation test would have been somewhat low. This is also true because the ground and polished surfaces are free from the surface impurities and has the tendency to induce compressive stress and allow the ceramics to be more resistant to cracking [176]. This in turn, also increases the surface K_{1c} as the resulting crack lengths from the indentation tests are reduced. This indicates that the surfaces of the ceramics are less prone to cracking.

6.6.9.3 Effects of phase transformation and change in composition

A new surface was formed especially on the top surface of the Si_3N_4 ceramic after being irradiated by both CO_2 and the fibre laser (see Chapter 5, Section 5.3.1.2.2, Figure 5.5 and Section 5.3.3.2.2, Figure 5.25). This was because of the Si_3N_4 ceramic being exposed to the atmosphere at high temperatures and led to a possible change in the composition as the Si_3N_4 was changed to SiO_2. Consequently, the effects with ZrO_2 were also identical after conducting both the CO_2 and the fibre laser surface treatments. A change in composition within the ZrO_2 would have also taken place where the top surface of the ZrO_2 was changed to ZrC. A compositional change within the laser irradiated ZrO_2 and the Si_3N_4 was also previously confirmed in Chapter 5. A change in composition after the fibre laser surface treatment in turn, would affect the hardness of the ceramics. This inherently, influenced the crack geometry during the Vickers indentation test and furthermore, the end K_{1c} values.

6.6.9.4 Effects of the Vickers indentation test and parameters used within the K_{1c} equation

The Vickers indentation method is easy to set-up and cost effective but it still has several flaws such as the results obtained from the hardness test heavily depending on user's ability to detect the crack lengths and its geometry. The K_{1c} values could be much improved if the surface hardness values and the resulting crack geometries were consistently balanced with minimal fluctuation. The fluctuations found in the mean hardness from the results of this study were up to 11%. This in comparison with the values for the ceramics given in the literature were 1% higher from the ± 10% range (error) given in [119]. Error of at least 1% (minimum) between the hardness values found in this study and the literature can be an exempt as mentioned earlier in the this Chapter.

Calculation of fracture toughness is somewhat difficult due to various uncertainties such as the selection of the most appropriate equation; input parameters which compliment the equation used; the surface conditions of the ceramics and the ceramic response during the diamond indentations test.

Consideration should be given to two parameters that can influence the K_{1c} of the ceramics herein and on a general note. Those parameters are; the indentation load and the Young's modulus. The indentation load was kept constant in this study, so the effects of this parameter were zero. However, the Young's modulus would influence the K_{1c} of the Si_3N_4 since an increase in the ratio of stress and strain would increase the Young's modulus value and affects the end K_{1c} value. If the effect of Young's modulus was ignored then the K_{1c} value for the CO_2 laser treated surfaces would be reduced to 6% on average.

6.7 Summary

Fracture toughness property K_{1c} of the as-received, CO_2 and the fibre laser surface treated Si_3N_4 and ZrO_2 engineering ceramics was investigated and the following conclusions were raised:

- Various empirical equations were used to calculate the K_{1c} of the as-received surfaces of the Si_3N_4 and ZrO_2 engineering ceramics to investigate the most suitable equation. It was found that equation: $K_{1c} = 0.016 (E/Hv)^{1/2} (P/c^{3/2})$ was the most relevant to use.

- Modification in hardness and the crack length demonstrated that the hardness acted as an influential parameter in changing the surface K_{1c} of the engineering ceramics.

- Comparison of the as-received surface with the CO_2 and the fibre laser treated surface showed improvement in the K_{1c} of the top surface layer of both laser treated ZrO_2 and Si_3N_4 engineering ceramics under the applied conditions.

- CO_2 laser surface treatment resulted to considerable softening of the treated layer of the two ceramics leading to an increased K_{1c}. On the other hand, the fibre laser increased the hardness only by 4% but produced a reduction in the crack length was found. This led to an increased K_{1c} values under the applied conditions.

Table 6.5 Surface hardness, crack lengths and the K_{1c} values found by using a 5 kg indentation load, from the experimental investigation of both the Si_3N_4 and the ZrO_2 engineering ceramics, treated by the CO_2 and the fibre laser irradiation.

	Average Surface hardness (Hv)						Average surface crack length (µm)						Average surface K_{1C} (MPa $m^{1/2}$)					
	Si_3N_4	STDEV	Range	ZrO_2	STDEV	Range	Si_3N_4	STDEV	Range	ZrO_2	STDEV	Range	Si_3N_4	STDEV	Range	ZrO_2	STDEV	Range
As-received surface	1106	201	707 - 1647	973	141.37	707- 1330	376	765	227 - 499	277	707	177 - 512	1.71	0.59	0.55 - 3.06	2.45	0.73	0.92 – 4.42
CO_2 laser treatment	1019	216	666 - 1379	754	177	473 - 1120	277	609	179 - 463	216	434	144 - 333	3.16	1.17	1.13 - 5.30	3.75	1.05	1. 69 - 6.77
Fibre laser treatment	1154	159	777 - 1449	940	60	726 - 1079	242	407	160 - 307	170	328	112 - 243	3.25	0.94	1.95 - 5.52	5.05	1.51	2.67 - 7.76

CHAPTER 7
Thermal Analysis of Laser Surface Treated Engineering Ceramics

The thermal effects of CO_2 and fibre laser surface treatment on the Si_3N_4 and the ZrO_2 engineering ceramic were studied by using a computational finite element model (FEM). Temperature increases on the surface and the bulk of the ceramics during the laser surface treatment were measured by using an IR thermometer and specifically located thermocouples. The FEM was used to reveal the temperature distribution at various stages of the laser surface treatment of the two ceramics. By utilizing data obtained from a thermo, gravimetry-differential scanning calorimetry (TG-DSC), the FEM predictions of the temperature distribution were used to map phase transformations and significant events occurring during the fibre laser surface treatment in particular of the two ceramics. The mapping revealed that the laser surface treatment generally resulted in a phase transformation of the ceramics at various temperatures changes as further elucidated in this Chapter.

7.1 Introduction

Laser interaction with any material is a complex phenomenon and this is especially so with engineering ceramics since the laser process involves multi-factors such as power density; traverse speed; instantaneous heating; ablation; rapid cooling and solidification. To analyse such events; thermal analysis by means of employing the experimental, analytical and computation approaches can be useful to investigate the laser-ceramic surface interaction.

Previous research by several workers has revealed ways of predicting and calculating the surface and the bulk temperature of various laser processing methods by using numerical means. Cline and Anthony [177] conducted one of the first investigations to determine the temperature profiles of a metallic alloy during CO_2 laser processing. They presented an analytical model by using the Greens's function for a Gaussian laser beam traversing at a constant velocity. Lax [178, 179] investigated a one-dimensional numerical integral of a solid material by the temperature rise during an onset of a Gaussian laser beam when applying a steady-state solution and by taking in account of the constant and the temperature-dependent thermo-physical properties for the solid. Nissim *et al.* [180] also used the Greens's function to calculate temperature profiles of an elliptical laser beam during annealing of a silicon gallium arsenide (semiconductor). Their results showed that with prior knowledge of the thermal conductivity, accurate temperature can be calculated and are valid for any material. Moody and Handel [181] as well used a CW elliptical laser beam by using an improved formalism of the Kirchhoff transformation to evaluate the temperature profiles on a silicon substrate. Thermal conductivity, diffusivity, and the surface reflection were considered as important functions

in the analysis. Their findings showed variation in the temperature profiles within the molten, the semi liquid and the solid regions.

Sanders [182] adopted the steady state solution of a Gaussian laser beam on a solid substrate to approximate the onset of the surface temperatures. Kar and Mazumber [183] implemented the 3-D transient heat conduction equation to generate temperature predictions as well as a FEM of a Gaussian laser beam chemical vapour deposition process thereof on a pure titanium work-piece. The 3-D model showed a relationship between the variation in the temperatures at fluctuating laser powers and the traverse speeds. Kar [184] then followed an investigation by using a quasi-steady-state heat conduction model to analyse the laser heating of a solid substrate with rectangular, square, multimode, and single or multiple laser beams. Their findings presented a 3-D quasi-steady-state thermal model and an approximation of the temperature spread during the laser heating with a single or multiple beams by using a rectangular spots.

Cheng and Kar [185] then conducted a theoretical investigation to study the densification of ZrO_2 ceramic coating processed with a moving transmission electron microscopy (TEM_{00}) mode laser beam. They produced a 3-D quasi-steady state heat conduction model by applying the Fourier integral transform method to show that the depth of the HAZ, the influence of laser power, spot size and the processing speed on the densification of the ZrO_2 ceramic. The use of both computational and an experimental model in this study was adopted rather than a numerical model for calculating the temperature distribution was because of simplicity, to obtain accuracy and also because it is less time consuming particularly, with the adopting the computational FEM approach. The temperature measurement by using the experimental approach would also lead to achieving a realistic values as oppose to a analytical model, which does not consider the physical aspects such as the heat transfer from the work-piece to the clamps or the processing table (as a second body) in contact with the test-piece. This can have a considerable effect on the temperature distribution as opposed to a finite body in space used without any constraints in the analytical models.

Experimental measurement of the processing temperatures during the laser surface treatment is rather difficult with hard, brittle engineering ceramics and often requires a lengthy and time consuming preparation for drilling holes, positioning and mounting the temperature sensors or thermocouples. However, this method is ideal for measuring the temperature changes in the bulk. Thus, it is not suitable for measuring the surface temperatures so pyrometers or contact-less devices are also employed, as demonstrated by Zhang *et al.* [186], Hao & Lawrence [187] and Ignatiev *et al.* [188]. Ignatiev *et al.* also stated that such measuring techniques are helpful to detect the material's phase transformation. This approach is also adopted for the investigation herein as further revealed. Temperature measurement during the laser surface treatment is important as the measured temperatures are used as an input parameter into the computational models for determining features

such as deformation, bending, tensile and compressive stresses as well as the thermal heat map and distribution of heat.

Several researches have been published on finite element analysis (FEA) by using design software such as ABAQUS and ANSYS for investigating the residual stress and thermal distribution of various laser processing technique applied on conventionally used metals and alloys. Braisted and Brockman [189]; Yongxiang *et al.* [190]; Ocana *et al.* [191] and Chen *et al.* [192] who studied the laser surface treatment through shock peening and constructed a 3-D model of the process which led to the determination of residual stress fields and surface deformation. The steady heat transfer equation to model the evaporating laser cutting process by using a 3-D computational finite element model was studied by Kim [193]. Shiomi *et al.* [194] analysed a laser rapid prototyping of metallic powders with the aid of a FEA. Investigation of the temperature fields and the stress state during laser welding by the aid of a simulated FEM and the thermal heat map produced to improve the laser welding process was conducted by Carmingnani *et al.* [195]; Spina *et al.* [196]; Yilbas *et al.* [197]; Zain-Ul-Abdein *et al.* [198] and Naeem *et al.* [199]. Much work has been conducted with modelling various laser processes with metals. However, very little work has been published with finite element modelling of laser surface treatment of engineering ceramics.

Considerable amount of research has also been conducted within the field of phase transformation of the ZrO_2. The phase transformation of the ZrO_2 ceramic occurs when it is exposed to increasing/decreasing or changing temperatures as stated by Zakurdaev and Huang [200]; Luping *et al.* [201] as well as Holand and Beall [202]. With respect to the changing temperature being introduced during the laser surface treatment; it is important to understand the thermal effects of the laser irradiation upon the crystal phases of the ZrO_2 ceramics. ZrO_2 ceramic comprise of three phases within its crystal structure. Upon heating at 700°C the transition from M-phase to the T-phase begins to occur. At 1100°C, the ZrO_2 ceramic fully transforms from M-phase to the T-phase. Furthermore, the T-phase becomes active until 2370°C. The reverse order takes place upon cooling of the ceramic. This was presented in the work of Garvie *et al*. [203]; Porter and Heuer [204]; Sergio [205]; Zhou *et al*. [206]; Sato *et al.* [207]; Haraguchi *et al.* [208]; Shackelford and Doremus [209]; Richardson [37]; Huang *et al*. [210] and Lee and Rainforth [211].

There are several events that take place within a ceramic during phase transformation. Previous research has shown the change in ZrO_2 phases by introducing heat treatment such as sintering and annealing at temperatures up to 1500°C. Sintering at temperatures up to 1500°C would result to an increase in hardness and toughness as found by Xigeng *et al.* [212] and Nayak *et al*. [213]. Changes in volume, strength and the grain boundaries depending on the concentration of the additive and the critical temperature applied was also reported by Sato and Ohtaki [214] as well as decreasing the

grain size of the ZrO_2 reduces the amount of T to M phase transformation. Zhu [215] stated that the grain size of a 2 mol% ZrO_2 ceramic was dependant on the transformation temperature.

Considerable amount of research has also been conducted within the field of phase transformation of the Si_3N_4 ceramics as described in the numerous literatures on the phase transition of the Si_3N_4 ceramic [216-223]. The phase transformation of the Si_3N_4 ceramic occurs when it is exposed to mainly increasing temperatures. With respect to the increasing temperature being introduced during the laser surface treatment; it is important to understand the thermal effects of the laser irradiation upon various phase changes within the Si_3N_4 ceramic. Phase transformation of the Si_3N_4 ceramic during laser surface processing is however, not been widely published in the literature. Phase transformation of the Si_3N_4 ceramics is complex in comparison to other ceramics such as a ZrO_2. This is because the behaviour of the Si_3N_4 during the heating process involves densification *via* particle arrangement, solution diffusion-precipitation and coalescence. These aspects are required for a full α-phase to β-phase conversion [216].

Messier *et al.* [217] investigated the phase transformation of powder Si_3N_4 and reported that a change of α-phase to β-phase occur at 1600°C. Effect of this transition also leads to formation of fine log-shaped grains with hexagonal symmetry being formed. Messier *et al.* also stated that α-phase was generally formed at low temperature. Ziegler and Hasselman [218] investigated the phase transformation of hot pressed Si_3N_4 (HPSN) and reaction sintered Si_3N_4 (RSSN) ceramic and reported that different morphology is formed with change in phase with respect to the increase in the temperature. The β-phase grain structure has the tendency to increase to a rod-like grain. These types of grains are usually formed at about 1499°C. Sarin [216] also commented on the increased grain size of the ceramics and occurrence of wiskar rod-type grains with high aspect ratio forming at 1770°C during sintering of the ceramics for up to 4 hours. Formation of the rod-like grains and transition to β-phase was also confirmed by the work of Sajgalik and Galusek [219]. Rouxel *et al.* [220] reported a phase transformation of the Si_3N_4 ceramic from α-phase to β-phase between sintering temperatures of 1549°C to 1649°C. Increase in the fracture toughness *via* decrease in the hardness and the Young's modulus was also reported in Rouxel *et al.*'s investigation. Such modifications occurred through microstructural changes that were found in the work of previous researchers. Yang *et al.* [221] also investigated the change in phases occurring with the Si_3N_4-MgO-CeO_2 ceramic and found that densification of the ceramic occurred at 1500°C. This was followed by the phase transition of the Si_3N_4-MgO-CeO_2 from α-to-β occurring at 1500°C and endings at 1600°C. Dai *et al.* [222] conducted an in depth study of the phase transformation behaviour of the Si_3N_4 at temperature between 1600°C to 1700°C. It was reported that α-to-β transformation occurred when heating the ceramic to 1600°C. This finding also complied with the finding of Jiang *et al.* [223] and the work of various authors reviewed previously. Dai *et al.* also reported that SiO_2 was formed during the α-phase to β-phase transition.

This research attempts to look at the underlying effects during such phase changes and how the Si_3N_4 and the ZrO_2 engineering ceramics are evolved from the CO_2 and the fibre laser irradiation. Thermal distribution and the change in the characteristics of the two ceramics during the CO_2 and the fibre laser surface treatment were under investigation. This was done by performing an experimental investigation of the temperature exhibited during the CO_2 and the laser irradiation within the bulk and the surface of the ZrO_2 engineering ceramics. Consequently, mapping of the heat distributed within engineering ceramics by an experimental model and by using a FEM with the aid of Unigraphics Nx-5 Nastran design and simulation software by Sham [224] is presented herein. In addition, verification of the experimental model in comparison to the FEM; phase transformation within the ZrO_2 and the Si_3N_4 engineering ceramics was speculated at various temperatures prior to, during and after the fibre laser surface treatment of the both the engineering ceramics. The experimental value was used as the input parameter for constructing a FEM. This was then used for postulating any changes within the Si_3N_4 and the ZrO_2 ceramics such as phase transformations, through data obtained from a thermo, gravimetry-differential scanning calorimetry (TG-DSC). No other investigation hitherto adopts the combination of employing the Unigraphics NX 5 Nastran software for conducting the analysis and fibre laser processing of the ceramics in particular as this was the first time.

7.2 Mathematical Model Development of the CO_2 and the Fibre Laser Surface Treatment of the Si_3N_4 and ZrO_2 Engineering Ceramics

7.2.1 Thermal Modelling

It is important to study the event during the laser interaction with the ceramics. The laser beam with a given power density and a constant traverse speed (see Section 4.2, Chapter 4) is passed on the top surface of the ceramics. During this time, the laser energy is absorbed by the ceramics to about 90% as reported by Zhang and Modest [186]. The absorbed light in form of heat causes a degree of surface heating. This leads to a degree of melting, followed by some level of ablation through vaporization and finally solidifies during its cooling process to ambient temperatures. Phase changes during such events also occur at certain temperature gradients as mentioned earlier in this study. Furthermore, an analytical solution as presented in Equation 7.1 onwards can be adopted to evaluate an analytical model.

$$\partial^2 (k\theta)/\partial x^2 + \partial^2 (k\theta)/\partial y^2 + \partial^2 (k\theta)/\partial z^2 + qb = \rho c_p \partial\theta/\partial t \qquad (7.1)$$

and θ is the temperature and k_{ij} are the conductivity co-efficient. The variable ρ, c_p and q_b are mass density, the specific heat and the rate of heat generation per unit volume. The thermal energy acting on the surface of the engineering ceramics due to convection to the environment is governed by

$$q = - h (\theta - \theta^0), \qquad (7.2)$$

where q is the heat energy across the surface, h is a reference film co-efficient, θ is the temperature at this point on the surface and θ^0 is a reference temperature value. The thermal energy on the ceramic is due to radiation to the environment and is governed by

$$q = A\,[(\theta - \theta^Z)^4 - (\theta^0 - \theta^Z)^4], \tag{7.3}$$

where q is the thermal energy across the surface of the ceramic, A is the radiation constant, θ is the temperature at this point on the surface, θ^0 is an ambient temperature value and θ^Z is the value of absolute zero on the temperature scale being used. Therefore, the radiation constant is defined as:

$$A = \varepsilon\sigma, \tag{7.4}$$

Where ε is the emissivity of the surface and the σ is the Stefan Boltzmann constant. In a situation where phase change occurs, particularly so for a pure substance, then the following boundary conditions of Rolph and Bathe [225] is applied at the phase transition interface at the solid-liquid interface:

$$\theta = \theta_f, \tag{7.5}$$

$$\Delta\, q_s\, dS = -\rho L\, dV/dt \tag{7.6}$$

where θ_f, ρ and L are the phase change temperatures, mass density and latent heat per unit mass of the material undergoing phase change and V is the volume. The heat is absorbed at a rate proportional to the volumetric rate of conversion of the material, dV/dt, at the solid liquid interface as stated by Equation 7.6. The heat must also be balanced by the heat flow, $\Delta\, q_s$, from the interface. The –ve sign is used for a situation where absorption of heat during melting occurs. The steps to construct the FEM by using a computational method of steady state solution are further presented with its 3-D geometry.

7.2.2 FEM Development

A FEM was constructed by using Unigraphics, NX 5.0, Nastran designing software. The model presents the thermal distribution of the CO_2 and the fibre laser irradiated heat distribution over the sample. This is compared to the experimental heat distribution model by the two lasers. This is to investigate if there is a correlation between the experimental and the FEM. The steps taken for the finite element analysis (FEA) are illustrated in Figure 7.1.

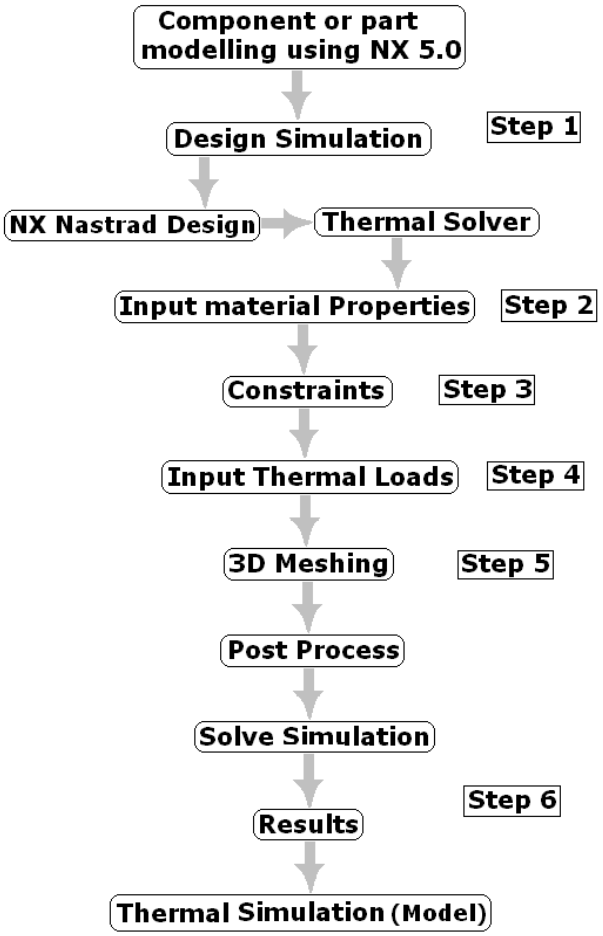

Figure 7.1 A schematic diagram of the steps taken to construct the FEM.

The component part was first designed which represented the experimental work-piece (see Figure 7.2). It comprised of a 3mm diameter blind hole with a depth of 100µm, equivalent to the footprint of the CO_2 and the fibre laser beams used. A depth of 100µm was assigned for the blind hole as the minimal penetration of the laser beam. It was necessary to introduce the blind hole to the model to assign a heat load acting on the work-piece as opposed to assigning the laser beam as a heat load. This is because the laser beam is not a solid object and does not have the required physical properties for the model to function correctly. This also helped to minimize the computational time and the model complexity during the simulation.

The second step to construct the model was to assign the material properties. However, the user must ensure that the correct software functions are selected. Those are namely: the design simulation followed by NX Nastrad design and the thermal solver. The materials properties are presented in Table 7.1 and then assigned to the work-piece. Young's modulus; Poisson's ratio; shear modulus; thermal expansion coefficient and the thermal conductivity are predominant properties directly affecting the model and hence, were assigned in all three x-y and z-directions by using the orthotropic material function of the NX Nastrad design, (thermal solve). This was because the characteristic of the ceramic does not remain the same in all axis of its orientations due to certain

manufacturing impurities and further modifications to have occurred during processing of the ceramics. Also, the ceramic was exposed to the laser beam (thermal energy). This would have lead to induction of further changes within the material from the induced thermal stress.

Table 7.1 Input of the properties assigned to the Si_3N_4 and the ZrO_2 engineering ceramic to construct the FEM.

Material Properties	Value (Units)	
	Si_3N_4	ZrO_2
Mass Density	3200 kg/m^3	6050 kg/m^3
Reference Temperature	25°C	25°C
Specific Heat	900 J/kg-k	425 J/(kg*$^\circ$C)
Young's Modulus	320000 MPa	270000 MPa
Poisson's Ratio	0.27	0.27
Shear Modulus	110000 MPa	55000 MPa
Thermal Expansion Coefficient	3.25 u / $^\circ$C	7×10-6 / $^\circ$C
Thermal Conductivity	15 W/m-k	1.75 W/(m*$^\circ$C)
Thermal capacity	3200 kg/m^3	400 J/(kg*$^\circ$C)

After assigning the material properties, the third step of the FEM was to give constraints (see Figure 7.2(b)) to the work-piece or to set the boundary conditions. The constraint is in form of a thermal constraint and is assigned to the work-piece in positions where the sample is connected to another body (i.e mounted to the processing table by using putty). A putty was used since mechanical clamping is not always ideal for holding hard brittle ceramics due to the risk of inducing mechanical tensile stress which often leads propagation of fractures. Furthermore, the use of putty provided a firm fixation and avoided any vibrations when the working table was in motion during the fibre laser surface treatment. A thermal constraint of 25°C was applied to the positions shown in Figure 7.2(c) on both edges of the work-piece. This meant that the work-piece was held firm in those positions and was in contact with another body during the CO_2 and the fibre laser surface treatment. The temperature of the thermal constraint was applied at an atmospheric temperature of 25°C. Step four of the FEA involved applying a heat load to the work-piece. This is where the following heat loads were applied as dependant on the various processing conditions of the CO_2 and the fibre laser surface treatment of the ZrO_2 and the Si_3N_4 engineering ceramics:

- Experimental temperature of 2473°C found for the fibre laser irradiated ZrO_2 ceramic and applied on the 3mm diameter blind hole (see Figure 7.2(c)) on the work-piece at the laser power density of 3717.44 W/mm^2.

- Experimental temperature of 1752°C found for the CO_2 laser irradiated ZrO_2 ceramic and applied on the 3mm diameter blind hole on the work-piece at the laser power density of 1736.11 W/mm^2.
- Experimental temperature of 2269°C found for the fibre laser irradiated Si_3N_4 ceramic and applied on the 3mm diameter blind hole on the work-piece at the laser power density of 3979.16 W/mm^2.
- Experimental temperature of 1935°C found for the CO_2 laser irradiated Si_3N_4 ceramic and applied on the 3mm diameter blind hole on the work-piece at the laser power density of 5556 W/mm^2.

This was the maximum power density induced by the 3mm diameter beam of the CO_2 and the fibre laser according to the threshold of the ceramics. The surfaces of the ceramics were assigned a view factor of 1. This is the amount of heat being passed on from one surface to another. In this case, the thermal energy irradiated by the laser beam was only being passed onto one surface during the heat transfer as described by Cengel and Turner [120]. Absorption of 90% was assigned to the model by taking in consideration of the absorption values found in a previous investigation by Zhang and Modest [186]. An emissivity of 0.40 was used as it is a typical value for all ceramics.

Once a thermal load was applied the FEM is then ready to be meshed. Furthermore, a fine 3-D mesh of tetrahedral by using 10 nodes, with an overall element size of 1mm was created on the work-piece (see Figure 7.2(d)). The final step of the FEA is to create a simulation by using the post processing function of the NX 5.0 Nastran software. This generated a solution from the input data and produced a simulation in form of a FEM. This was also animated to investigate the distribution of heat during, prior to, and after the laser process as presented further in this chapter by the aid of screen shots of the animation.

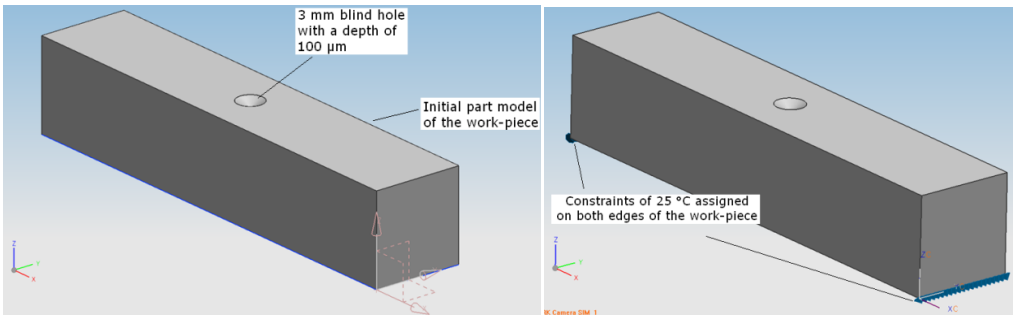

(a) **(b)**

Figure 7.2 Screen shot images of the part design showing a 3mm diameter blind hole at a depth of 100µm in (a) and (b) the thermal constraint of 25°C applied on both edges to the work-piece.

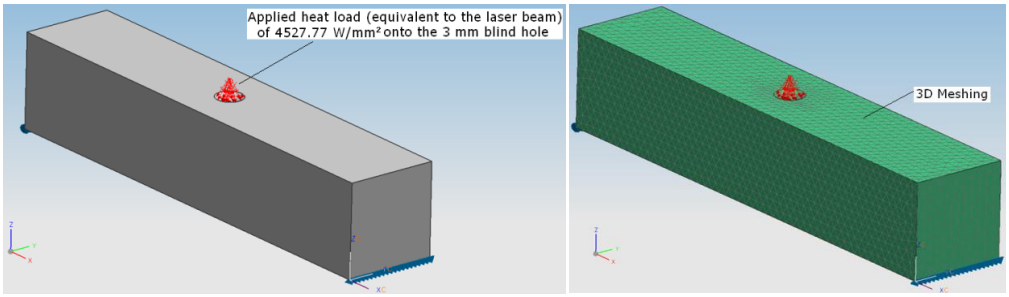

(c) **(d)**

Figure 7.2 Screen shot images of the part design showing application of the heat load to both the Si_3N_4 the ZrO_2 ceramics in form of the laser beam in (c) and (d); an image of the full 3-D mesh showing the assigned heat load to both the Si_3N_4 and the ZrO_2 engineering ceramics.

7.3 Experimental Techniques and Analysis

7.3.1 Experimental Material

Details of the materials used for the experimentation are presented in Chapter 4 (see Section 4.1, Figure 4.1).

7.3.2 CO_2 and Fibre Laser Surface Treatment

The details of the fibre laser used for the experiments are presented in Chapter 4, Section 4.3 and Section 4.4 for the CO_2 laser surface treatment. Figure 7.3 and Figure 7.4 illustrate the schematic diagram of the set-up of the two lasers used.

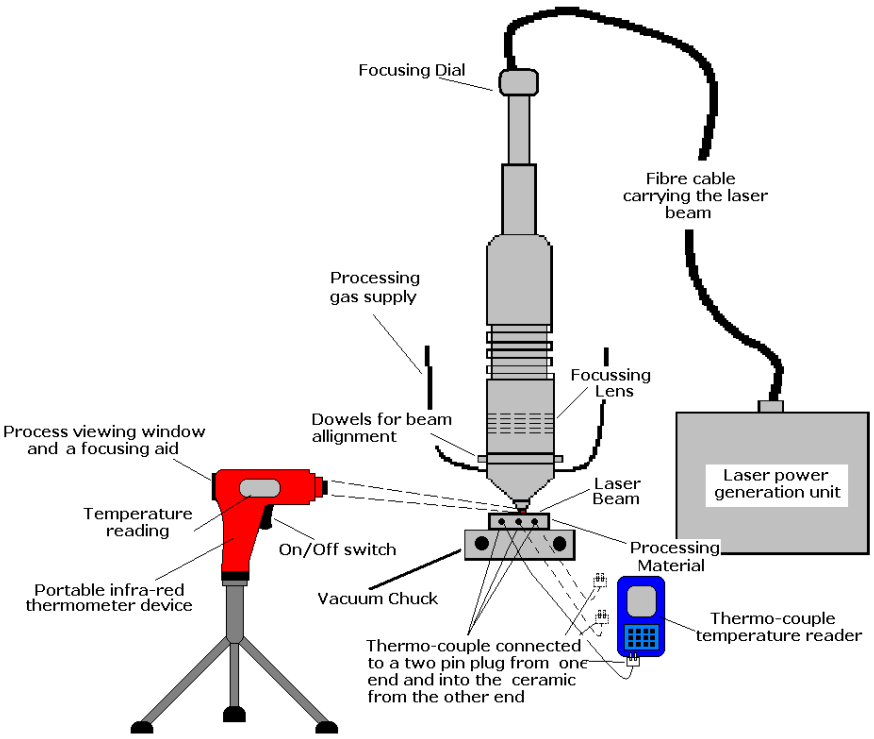

Figure 7.3 A schematic diagram of the experimental set-up of the fibre laser surface treatment of the Si_3N_4 and ZrO_2 engineering ceramics.

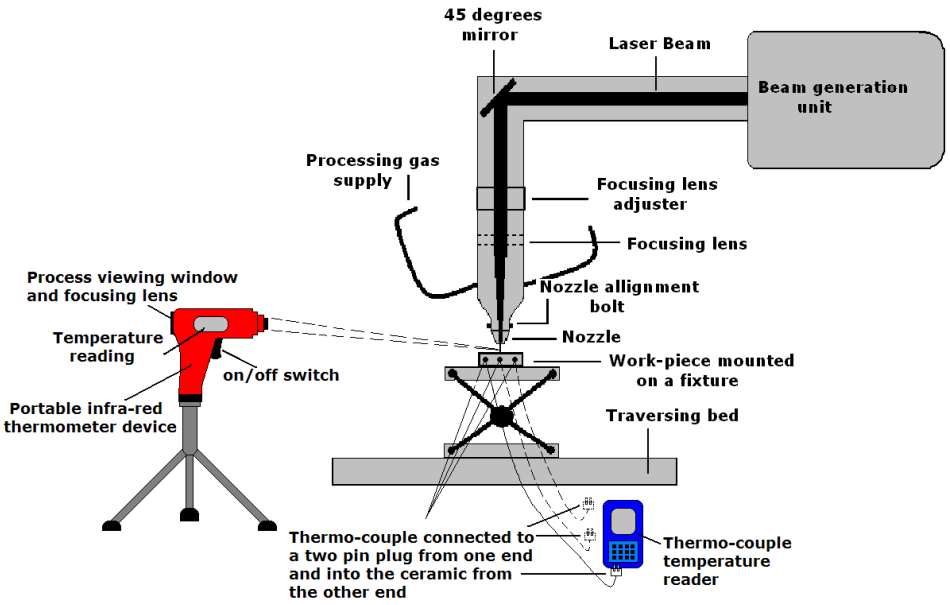

Figure 7.4 A schematic diagram of the experimental set-up of the CO_2 laser surface treatment of the Si_3N_4 and ZrO_2 engineering ceramics.

7.3.3 Temperature Measurements

7.3.3.1 Infra-red (IR) thermometer

The surface processing temperature was measured by using a portable IR thermometer (Cyclops 100 B; Land instruments international Ltd). The device was bolted on a tripod and positioned 1m away from the processing area (see Figure 7.3 and Figure 7.4). The IR thermometer was then aligned with the work-piece by means of a He-Ne beam of the CO_2 and the fibre laser as indicated in Figure 7.5. Thereafter, the laser beam was switched on for the surface treatment to take place. The IR thermometer was then switched on shortly after and followed the laser ceramic interaction as the laser processing began. The IR thermometer was switched off before the CO_2 or the fibre laser surface treatment was completed (see Figure 7.5). This procedure was adopted for every measurement that was taken for the experiment. This allowed an average temperature to maintain closer to the real temperature of the processing area. However, it was important that the operator constantly monitored the processing area through the viewing window of the lens of the IR thermometer whereby the traversing laser beam was followed in order to accurately measure the temperature during the laser surface treatment. The temperature measurement was conducted on five different areas of the surface of the ceramic work-piece as indicated in Figure 7.5. The measurement on the surface was conducted as the beam traversed on the surface of the work-piece. Each area was measured in one pass of the laser beam. The average reading of the temperature was taken from five passes of the laser beam executed on five samples. This enabled to produce consistent values of the temperature measurement.

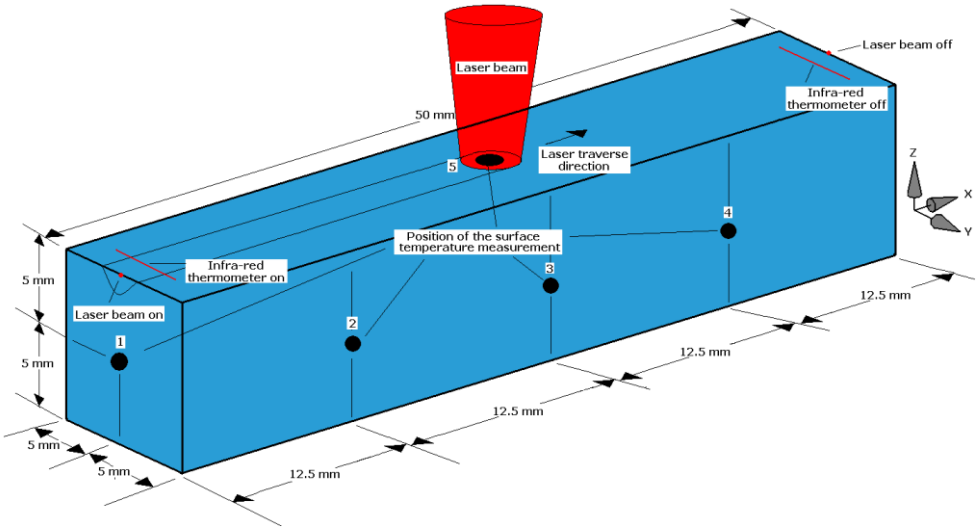

Figure 7.5 A schematic diagram of the positions used to measure the surface temperature of the Si_3N_4 and ZrO_2 engineering ceramic during the fibre laser surface treatment.

7.3.3.2 Digital temperature reader

The bulk temperature measurement was taken by using a precision fine wire (0.20mm diameter x 152mm in length), R-type, thermo-couples, capable of reading up to 2300°C (P13R, Omega Instruments Ltd.) and were precisely mounted at various positions within the bulk of the sample as illustrated in Figure 7.6. Each of the fine wire thermocouples set was wired to a two pin plug which connected to a digital temperature reader (N9002-Thermometer; Comark Ltd.) for receiving the feedback in of a temperature reading. Three holes were drilled into the ceramic by using the ultrasonic drilling method, after which the tip of the thermocouples were mounted into the holes at 3, 6, 7mm from the surface (see Figure 7.6). The holes were then filled by using filler (paste) made of organic type material that is stable during high temperature processing. This assured firm fixation for the thermo-couples during the laser surface treatment. Measurement was taken in three different passes of the laser surface treatment. This was because one pass could only measure the temperature from a single set of thermocouple positioned in a single hole. A new sample was used with each pass of the fibre laser and five identical readings were recorded for each of the positioned hole to achieve consistency in the bulk temperature measurement.

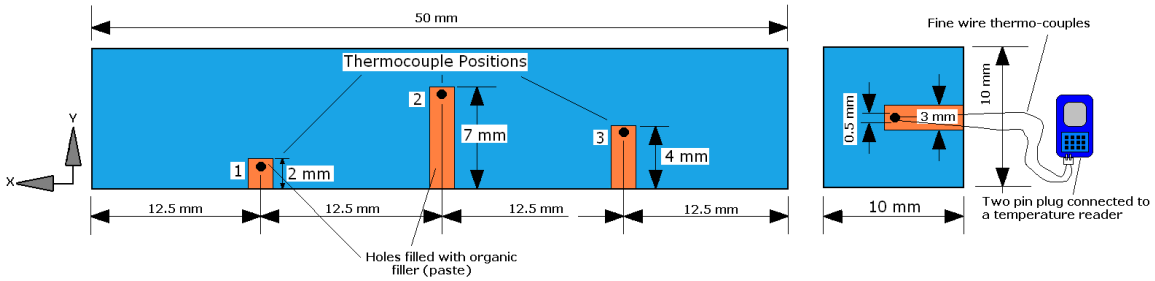

Figure 7.6 A schematic diagram of the mounting position of the thermo-couples into the Si_3N_4 and the ZrO_2 engineering ceramics during the CO_2 and the fibre laser surface treatment.

7.3.4 Thermogravimetry-Differential Scanning Calorimeter (TG-DSC) Analysis

TG-DSC analysis (1500 DSC; Stanton Redcroft, Ltd.) was conducted on the as-received and fibre laser irradiated samples of the Si_3N_4 and the ZrO_2 engineering ceramics. The average surface area of the samples was approximately $2mm^2$ for both of the samples and the mass was 26mg for the Si_3N_4 and 29.45mg for the ZrO_2 engineering ceramic. The samples were placed into an Al_2O_3 crucible and N_2 was used as a purge gas at 50 ml/min. Once in place, the samples were heated up to 1500°C at a rate of 10°C/min to measure the mass flow as the temperature increased. The samples were then cooled to ambient temperature at the same rate by using the same parameters to measure the mass flow as the temperature reduced. The heat flow through the as-received and the laser treated samples was recorded for any changes during the heating and cooling cycles and are shown in Figure 7.16, Figure 7.34 and Figure 7.35. From this, recording it was then possible to identify specific phase events that occurred in both the Si_3N_4 and the ZrO_2 engineering ceramics during heating at what temperature these events take place.

7.4 Results and Discussion

7.4.1 Fibre Laser Surface Treatment

7.4.1.1 Experimental temperature readings of the ZrO_2 engineering ceramic

The average temperatures found on the surface after five passes of the fibre laser are presented in Figure 7.7(a) and (b) for the surface temperature and the bulk for the ZrO_2 engineering ceramic. At the laser-ceramic interface the surface temperature was found to be 2473°C. This is close to the manufacturer's specification of the melting temperatures (2550°C) in comparison. The difference between the two readings was 2.5%. This difference could be justified by the accuracy and the operator error that may have occurred during the experimentation. This is above the melting temperature of the ZrO_2 which indicated that there is some degree of melting which occurred. This was also supported by the evidence in Chapter 5 where grain boundaries have began to bind together and inter-lock as result of partial melting. The surface temperature on the side of the sample (away) from the laser treated zone was found to be much lower than the melting temperature. This would obviously be high due to the heat transferring through the bulk of the ceramic. Interestingly, the temperature readings should result to being stable throughout one surface plane. However, this was not the case as the difference between position 2, 3 and 4 was sufficiently large (251°C).

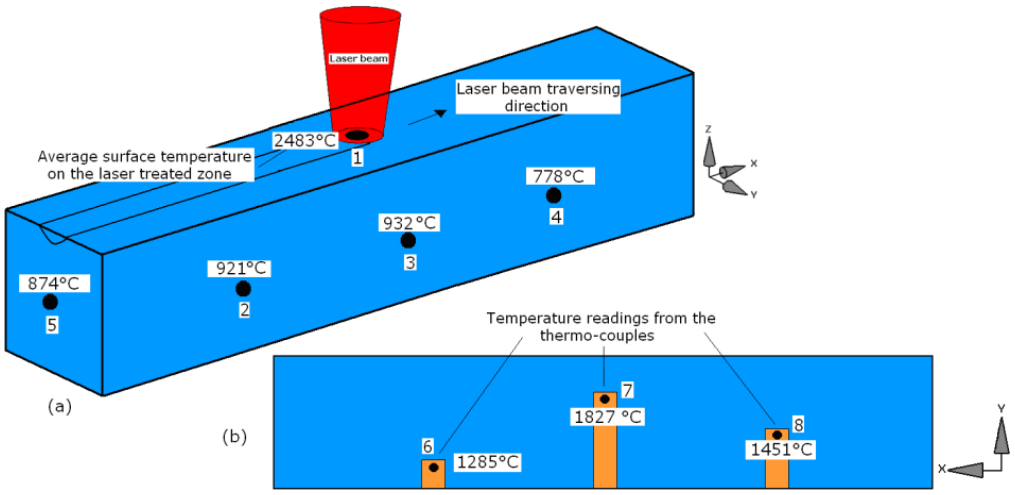

Figure 7.7 A schematic of the surface temperature reading in (a) and (b) the bulk temperature of the ZrO_2 engineering ceramic during fibre laser surface treatment.

The temperature measurements taken from using the thermo-couples within the bulk of the ZrO_2 ceramic are presented in the Figure 7.7(b). The average bulk temperature after five readings in position 6, 7 and 8 were 1275°C, 1727°C, and 1451°C. This result agrees with the surface temperature presented in Figure 7.7(a) that 3mm below the surface due to the heat transfer; the temperature is above 400°C lower. At 6mm below the surface, the measured temperature was considerably lower (1225°C). In this position, the temperature has begun to decrease as the heat was distributed throughout the surface. Moreover, the temperature at 7mm below the surface was 1007°C as the heat was passed on from the bulk of the ceramic to the surface.

In Figure 7.8(a) and (b), both of the graphs are constructed from the experimental values found. This was for a situation where the fibre laser was incident at 25mm length (centre) from the edge of the ZrO_2. The distribution of heat is presented in Figure 7.8(a). This illustrated the surface temperature over the length of the ZrO_2 sample at 25mm. At the length of 0mm the experimental temperature was instantaneously ramped up to 1604°C and gradually increases as it comes closer to the incident beam. The peak temperature found was 2473°C at 25mm length (centre of the work-piece) of the focused laser beam upon the ZrO_2 test-piece. The temperature reduced to 1935°C at 37.5mm in length and was recorded at 1739°C at the edge of the sample at 50mm.

The graph in Figure 7.8(b) presents the experimental temperatures obtained in the bulk of the ceramic particularly at 3, 6 and 7mm. Temperatures at various other positions can also be calculated from these three values as shown in Figure 7.7(b). In general the curve in Figure 7.8(b) has declined due to the reduction of the temperature through the bulk of the ceramic. The temperature is reduced from 2473°C at the depth of 0mm (surface) to 2015°C at 3mm, 1225°C at 6mm and 1007°C at 7mm depth. From this, the temperature at the depth of 10mm can be predicted as shown in Figure 7.8(b).The experimental investigation would now be used as a base to construct the FEM. The results

found herein are also compared to the FEM for validation and confirmation of the level of accuracy or error in the temperature measurements in this study.

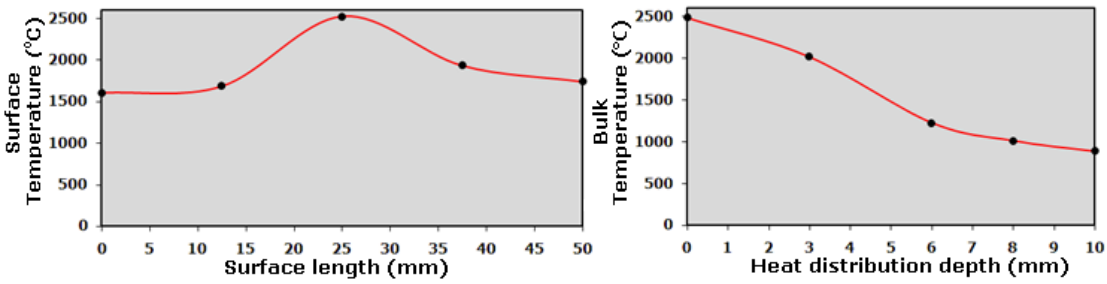

(a) **(b)**

Figure 7.8 Experimental temperature distributions over the surface length in (a) and (b) the temperature distribution through the bulk of the fibre laser surface treatment of the ZrO_2 engineering ceramic.

7.4.1.2 FEM temperature reading

A FEM was constructed which revealed the surface and the bulk temperature maps by taking in account of the surface and the bulk temperatures measured from the experimentation. The surface maps are presented in Figure 7.9, 7.11 and 7.13. Because of the laser beam traversing as a CW beam; it is always ideal to construct the model so that it illustrates the FEM of a moving laser beam. However, in this case, a stationary spot was used for the analysis to observe the effect of the thermal radiation. The total time to cover the whole area of the sample was 30 sec at a traverse speed of 100 mm/min. This would cover 1.66 mm/sec. In Figure 7.9, the first point of contact with the ceramic and the laser beam has been demonstrated. The impact on the beam is only 1.5mm onto the surface despite comprising of a spot size of 3mm diameter. A heat map is illustrated for this condition and is compared with the values for the experimental temperature readings that were found. It can be observed that the maximum temperature found at the laser-material interface on the FEM was 2354°C. The temperature here was lower than the temperature from the real experimental value by 5.47%. Error of the computational method within ±10% can be considered to be in good agreement with the experimental values. In Figure 7.9(b); the laser beam is only concentrated at 50% of its diameter because it is focused on the edge of the sample (start of the laser surface treatment). This enabled the cross-sectional distribution of heat to be analysed. From observing the cross-sectional heat map, it can be seen that the near to melting temperature found through the bulk of the ceramic ranges between 100 to 200µm.

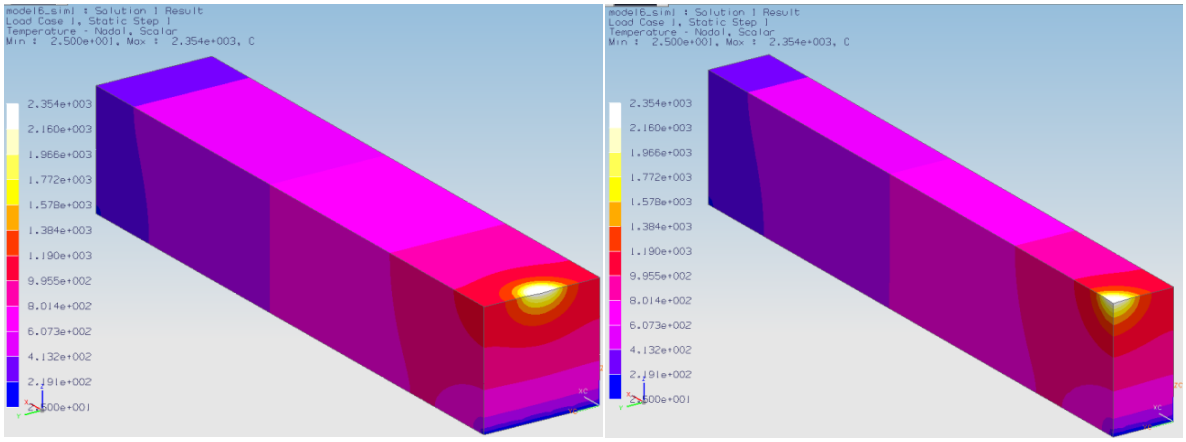

(a) **(b)**

Figure 7.9 FEM of the heat distribution of the fibre laser focused at 0mm from the edge (position 1) of the ZrO_2 engineering ceramic work-piece (start of the laser treatment) in (a) and (b); the cross-sectional view.

From observing the results from the model in Figure 7.9(a) and (b), the determination of temperature distribution over the surface at various lengths and through the bulk at various depths are presented in the graph in Figure 7.10(a) and Figure 7.10(b). In this model, the incident beam at the start of the surface treatment is covering 0 to 1.5mm radius. The temperature within this area as seen on Figure 7.11(a) is up to 2350°C. During this time the temperature distribution over the rest of the surface is lower. This is due to the heat transfer taking effect over the surface. At 25mm in the centre of the work-piece, the temperature was up to 710°C and at 50mm (edge of the sample) the temperature was much lower (120°C). The result of the FEM at this position appears to be in good agreement with that of the experimental result. However, from observing the depth of the distribution from the model in Figure 7.9(b); the surface temperature at 0mm is 2350°C and reduces to 1190°C at the depth of 2mm, 1000°C at 4mm, 794°C at 7mm and finally reducing to 25°C at 10mm (room temperature).

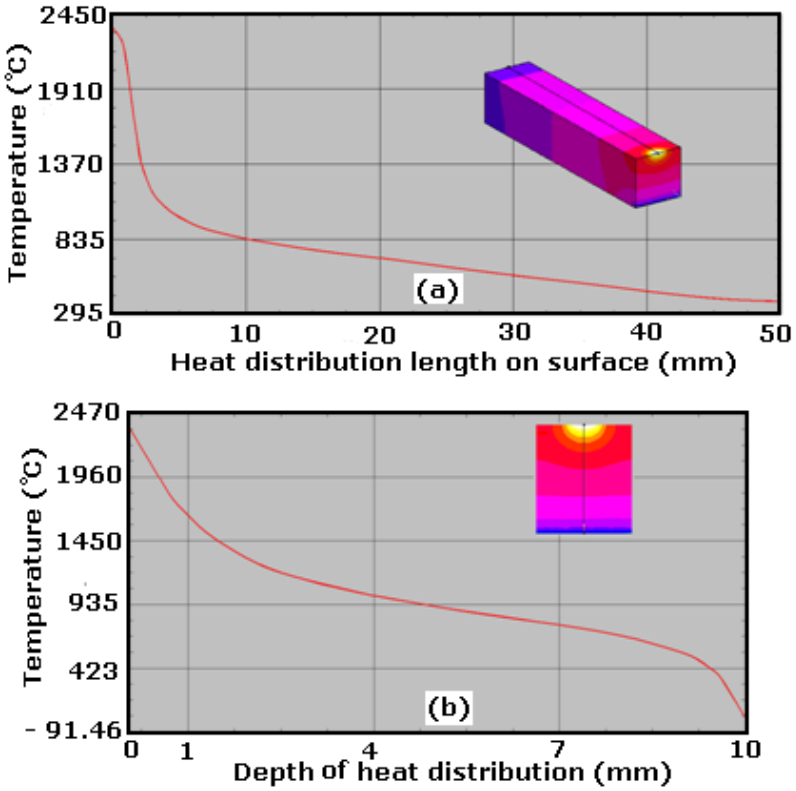

Figure 7.10 Temperature curves from the FEM of the initial stage at 0mm from the edge (position 1) of the fibre laser surface treatment of the ZrO_2 engineering ceramic for (a) the heat distribution over the length of the sample and (b) the heat distribution through the depth of the sample.

The FEM in Figure 7.11(a-c) showed that the temperature pattern was somewhat different to that of the one found at the start of the laser treatment (see Figure 7.9) as the average heat input began to increase over the total surface area of the ZrO_2 engineering ceramic. Despite the effect of surface melting during the laser interaction and the rapid cooling effect taking place; the temperature at the laser irradiated zone has increased on the surface and through the bulk as presented in the graph in Figure 7.10(a) and Figure 7.7(b).

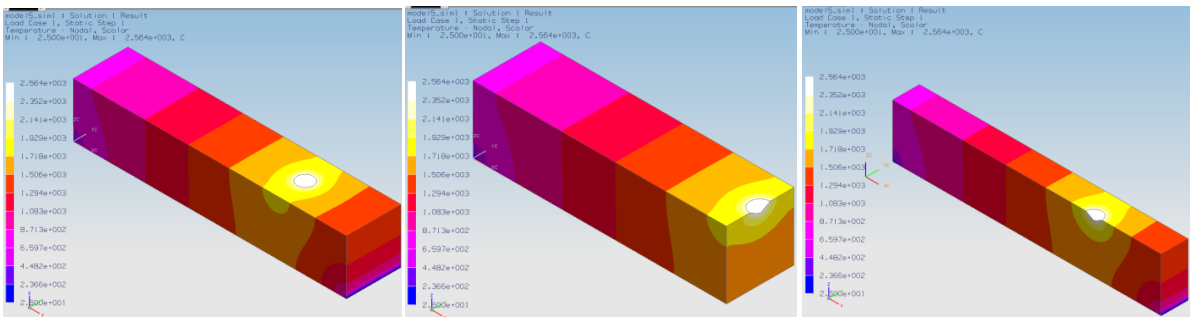

(a) **(b)** **(c)**

Figure 7.11 FEM of the heat distribution of the fibre laser focused at 12.5mm from the edge (position 2) of the ZrO_2 engineering ceramic in (a) and the cross-sectional view in (b) and (c).

The traversing laser beam is paused in time at 12.5mm from the edge in order to show the effects at that position. At 12.5mm as presented the temperature is at its highest which is 2564°C (see Figure 7.12). Gradually, the temperature begins to decrease to 1347°C at 25mm, 1017°C at 37.5mm and 750°C at 50mm. The temperature through the bulk has increased in comparison with the bulk temperature during the start of the fibre laser surface treatment due to the increase in time that the laser beam has spent on the ceramic. This in turn would have caused a sufficient level of heat to be produced. From melting temperatures at 0mm (surface); the temperature reduces to 1675°C through the bulk during the laser-ceramic interaction at 12.5mm in length after the start of the treatment.

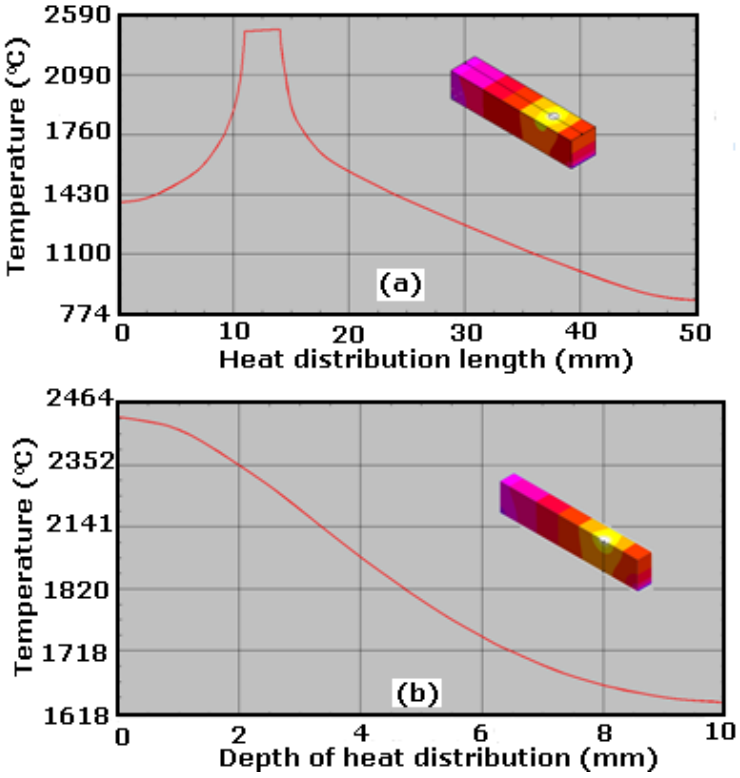

Figure 7.12 Temperature curves from the FEM of the fibre laser surface treatment at 12.5mm from the edge (position 2) of the ZrO_2 engineering ceramic for (a) the heat distribution over the length of the sample and (b) the heat distribution through the depth of the sample.

The illustrations in Figure 7.13(a), (b) and (c) show the FEM of the laser-ceramic interaction in the centre of the work-piece (25mm from the edge). In this position the distribution of heat is different to the interaction during the initial stages as previously shown. The ZrO_2 ceramic in this position is in thermal equilibrium since the temperature distribution is well balanced. At 25mm the heat is at its peak (2577°C) near to the melting temperature of the ZrO_2 ceramic. During this time, the slope gradually increases to the highest position, maintains for 3mm and then declines and has the opposite effect where the temperature curve is declined.

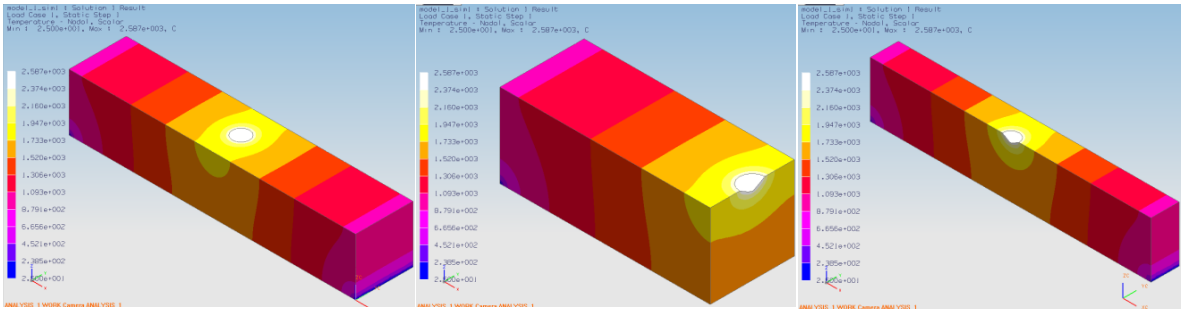

(a) **(b)** **(c)**

Figure 7.13 FEM of the heat distribution of the fibre laser beam focused in the centre (position 3) of the ZrO_2 engineering ceramic in (a) and in the cross-section in (b) and (c).

From this point onwards; as the laser beam traverses furthermore on to the sample, the effect of heat distribution is similar to that of the one presented in previous FEM's. The temperature distribution over the surface was similar to that of the FEM presented in Figure 7.14 as well as the results obtained from the experimental model. The difference between the experimental model and the computational FEM was up to 5% particularly for the temperature predictions over the surface length. The bulk readings for the two compared models were also in good agreement. However, consideration should be given to the accuracy of thermometer device used for measuring the experimental temperature (±10%) as well as the distance which the temperature measurement was taken from. The distance of the temperature measurement changes as the laser beam traverses away from the focused IR beam of the thermometer device (see Figure 7.1). This would also cause some fluctuation in the results found.

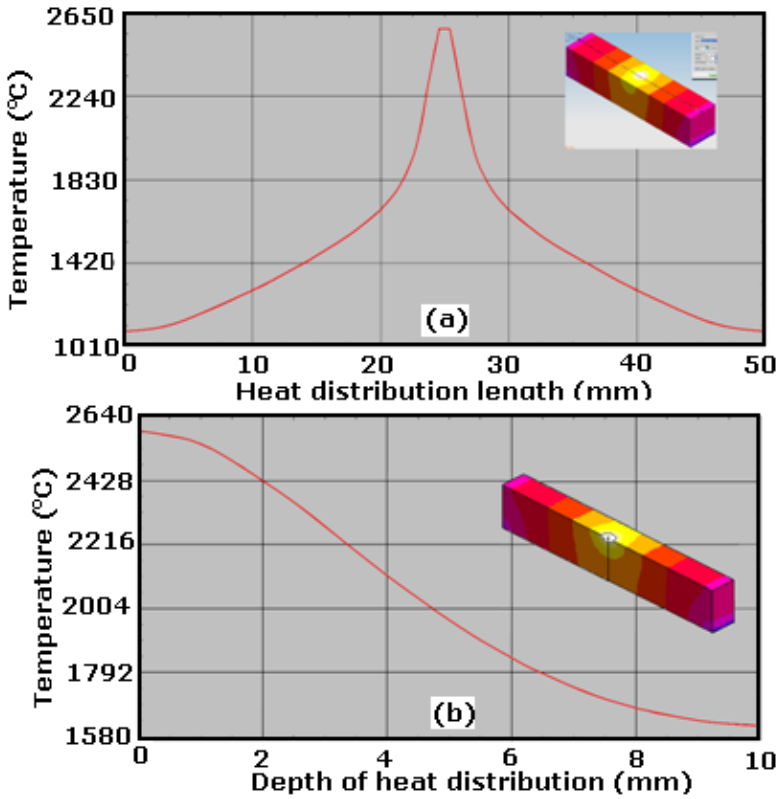

Figure 7.14 Temperature curves from the FEM of the fibre laser surface treatment at 25mm from the edge (position 3) of the ZrO_2 engineering ceramic for (a) the heat distributed over the length of the sample and (b) the heat distribution through the depth of the sample.

7.4.1.3 Comparison of the experimental and the FEM produced by the fibre laser surface treatment

At the laser-ceramic interface the surface temperature was found to be 2473°C (see Figure 7.7). This result is in good agreement with results found in Chapter 5, where it was found that fibre laser surface treatment of the ZrO_2 resulted in some degree of melting of the top (near) surface layer. Interestingly, the temperature readings would be expected to be stable throughout a plane, but this was not the case as up to 16% difference in temperatures between Positions 2 to 3 and 4 to 5 was observed. The difference between the two results may have resulted from the following:

(i) The error in reading the temperature resulting from the contact-less IR thermometer device;

(ii) Fluctuation in the laser power during the processing stage (although, stable output powers were recorded prior to the laser surface treatment);

(iii) The ceramic material being somewhat inhomogeneous.

The temperature is expected to be fairly high in at the edges of the samples in position 5, (where the average temperature was measured at 1772°C) and on the same surface plane in position 2, 3, and 4 as it is at the edge of the sample indicating that there is less area for the heat to travel. This created

sufficient heat at the surface. Still, the experimental surface temperature measurements agree with those of the FEM (reference to Figure 7.12) with a +10% error. Further modification to the temperature measurement settings would improve the consistency in obtaining more accurate temperature readings.

The average temperatures measured within the bulk of the ZrO_2 after five readings also agree with the bulk temperatures predicted by the FEM. At 3mm below the surface the temperature was up to 2035°C. The FEM by comparison gave a temperature of over 1900°C, and agreement of just over 7%. The temperature in Position 7 (see Figure 7.7) was found to be 1451°C. This in comparison to the FEM was 79°C lower, indicating an error of 5.5%. Finally, at Position 6 the temperature recorded was 1275°C, while the temperature predicted by the FEM was 245°C lower, a difference of 19%. It is clear that the bulk material temperatures measured experimentally were slightly lower than those produced from the FEM. This may have resulted due to three known factors:

(i) Heat loss through the 3mm holes drilled into the sample;

(ii) Lack of contact of the thermocouples to the material surface;

(iii) The thermocouple response time. Such aspects were not taken into account by the FEM and so the FEM results will always be higher.

7.4.1.4 Development of extended parameters from the FEM

Based on the results obtained from the FEM a range of possibilities are presented in Figure 7.15(a-g) for traverse speed; power density; depth of heat distribution; temperature; and time, in relationship to one another. From this, one can predict and gauge the input parameters during fibre laser surface treatment of the ZrO_2 engineering ceramic at various input parameters.

As with all laser processes, the results herein show that a lower traverse speed at high power density would generate high processing temperatures. This in turn would lead to a deeper distribution of the thermal energy. The effects are opposite when the processing speed increases or the power density decreases. This is when the surface temperature is also reduced with lower penetration of the thermal energy into the bulk of the ceramic. Consideration of power density would also allow one to gauge the effect of the laser spot size as an additional parameter, since the spot is a function of the power density applied. Typically, a smaller spot size than 3mm by using the same power input (137.5 W) would produce a much bigger power density and would further compliment the models that are presented in this study.

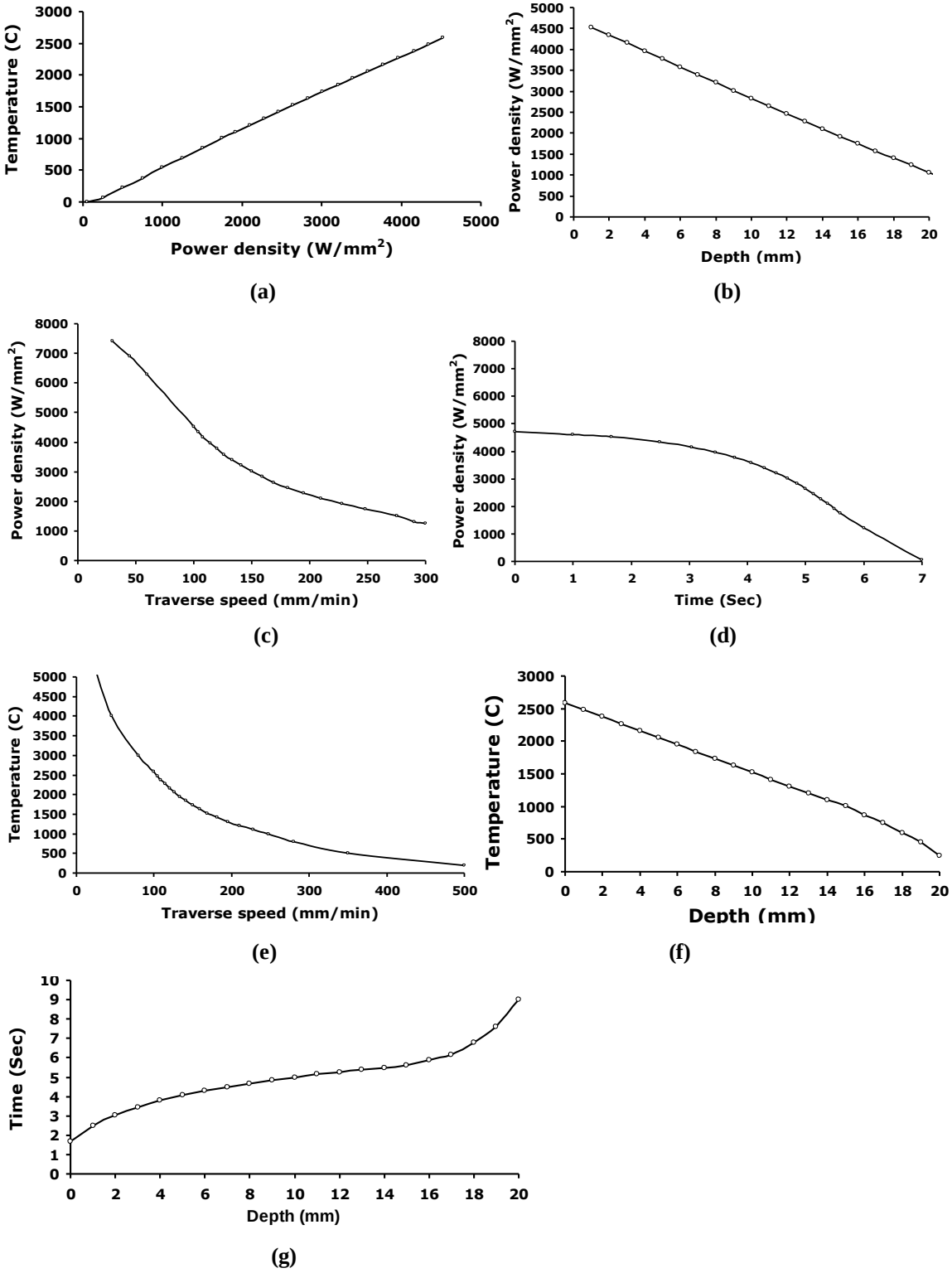

Figure 7.15 Parameters obtained from the FEM of the fibre laser treated surface of the ZrO_2 engineering ceramic, showing the coloration of various factors with one another; (a) power density *versus* temperature; (b) depth *versus* power density; (c) power density *versus* traverse speed; (d) power density *versus* time; (e) traverse speed *versus* temperature; (f) depth *versus* temperature and (g) depth *versus* time.

7.4.1.5 Phase transformation of ZrO_2 engineering ceramic

The TG-DSC analysis is presented in Figure 7.16. The heating curve for the as-received ZrO_2 surface shows an exothermic peak at 50°C and a corresponding reduction in mass flow of 7mW. This indicated a possible release of moisture. At 700°C the small peak observed suggests a possible phase change where the mixture of M+T could have occurred. At 1290°C a further change in the curve indicated a phase transformation of M-T. The mass flow reduced as the sample reached 1500°C during the heating cycle. During the cooling process mass flow was much higher and similar effects took place to that of the heating curve. At 1205°C the curve showed an additional peak. This may have occurred due to the change in the phase transformation from the T to the T+M phase.

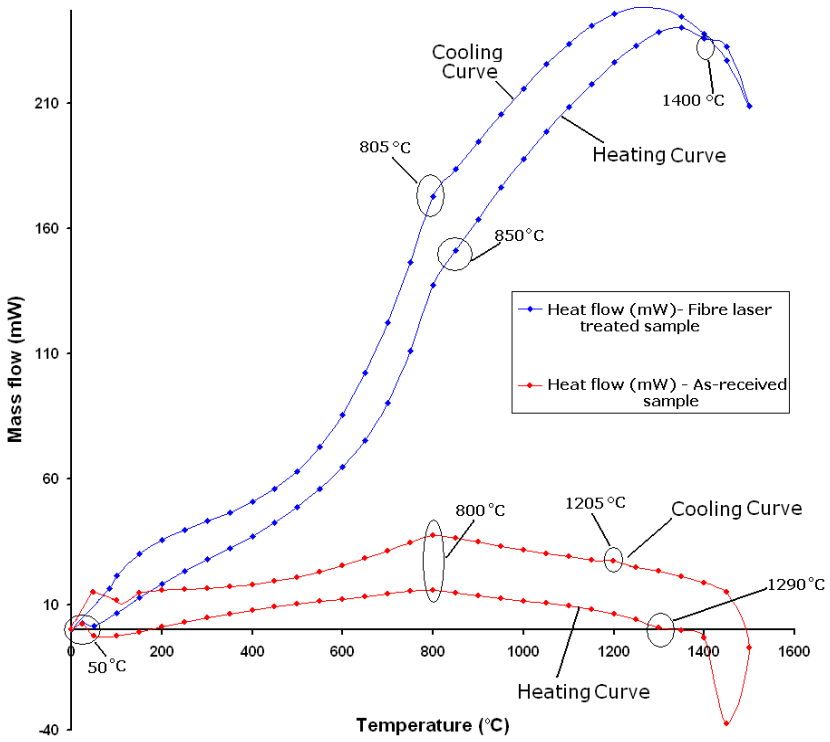

Figure 7.16 TG-DSC curves for the as-received and the fibre laser treated ZrO_2 engineering ceramic.

The curve produced by the fibre laser treated ZrO_2 sample was somewhat different to that of the as-received sample as more heat will have flowed through the bulk due to air blocks or cavities within the as-received sample. This in turn would cause a decline in the mass flow. During the heating cycle the curve produced for the fibre laser treated ZrO_2 showed changes at 750°C, which marks the beginning of the M+T phase change. At 1400°C the curve showed a minor change, indicating that the T transformation had fully occurred. This is different to the effect of the as-received sample and that of a previous finding by Porter and Heuer [204]. A possible cause of this would be due to the ceramic changing its composition after the fibre laser surface treatment. Hence, the observed increase in mass flow was to be seen. During the cooling cycle there were no changes to be seen until 705°C. This is a sign that the ZrO_2 had transformed back to the M state. The TG-DSC analysis

only investigated changes up to 1500°C. Since the temperatures measured experimentally and predicted from the FEM were much higher, we can only surmise the effects beyond 1500°C.
From observing the temperature distribution obtained experimentally and from the FEM (see Figures 7.9, 7.11 and 7.13); it can be seen that the distribution of heat varies in different positions on the ZrO_2 engineering ceramic as the fibre laser beam is frozen in one position in order to investigate the heat distribution for this study. From this, one can see that the rapid surface and the bulk heating occur. This is followed by the rapid cooling effect which took place where the ZrO_2 is transformed from M →M+T →T →T+C during heating. It is then instantaneously transformed back from T+C →T →T+M →M.

Figure 7.17 presents a conventional phase diagram of the ZrO_2 engineering ceramic with the percentage of molar content of Y_2O_3. The vertical dotted line shows that the ZrO_2 used for this work comprised of 4 mol% as stated by the manufacturer. On account of this, one can see the changes in the phases as the ZrO_2 ceramic is being heated by the fibre laser irradiation. Furthermore, the phase change of the ZrO_2 can be predicted during the laser-ceramic interaction where the M+C phase of the ZrO_2 begins to change phase at 500°C and transforms to a mixture of M and T-phase. The M+T phase fully transforms to T at about 700°C as presented in Figure 7.17. The ZrO_2 ceramic with 4% Y_2O_3 at about 1300°C changes phase from T to T+C and then forms the C-phase at about 2200°C. Further increase in the temperature of about 2750°C transforms the ZrO_2 into a mixture of L+C phase. Results in Chapter 5 illustrated that the grain boundaries of the ZrO_2 engineering ceramic treated by the fibre laser where binding due to melting and re-solidification were to be seen. This indicated that the phase transformation of the ZrO_2 would be in the region of L+C state. The changes in the phase during the cooling process are reasonably symmetrical to that of the heating. However, the time it takes to heat the ceramic is much faster than the rate of cooling so the rate of phase change is much slower during the solidification stage. The TG-DSC results reveal the changes within the ZrO_2 ceramic during heating and cooling up to 1500°C. However, the changes in the phase beyond 1500°C can only be predicted from using the FEM and the experimental model as well as the phase diagram presented in Figure 7.17. In addition, from observing the event of the laser material interaction, it can be stated that the ZrO_2 ceramic is certainly not in a thermal equilibrium. This is simply due to the focused laser beam executing a high power density in a small spot size which is producing a melt zone at the processing zone, whilst the other areas of the ceramic are much cooler. This goes to show that due to the temperature difference during the fibre laser surface treatment leads to the variations in the phase changes within the ZrO_2 where the fibre laser-ZrO_2 interaction zone maybe L+C phase, whilst the other phases of the ceramic may be a mixture of M, M+T, T, T+C and C at the same time.

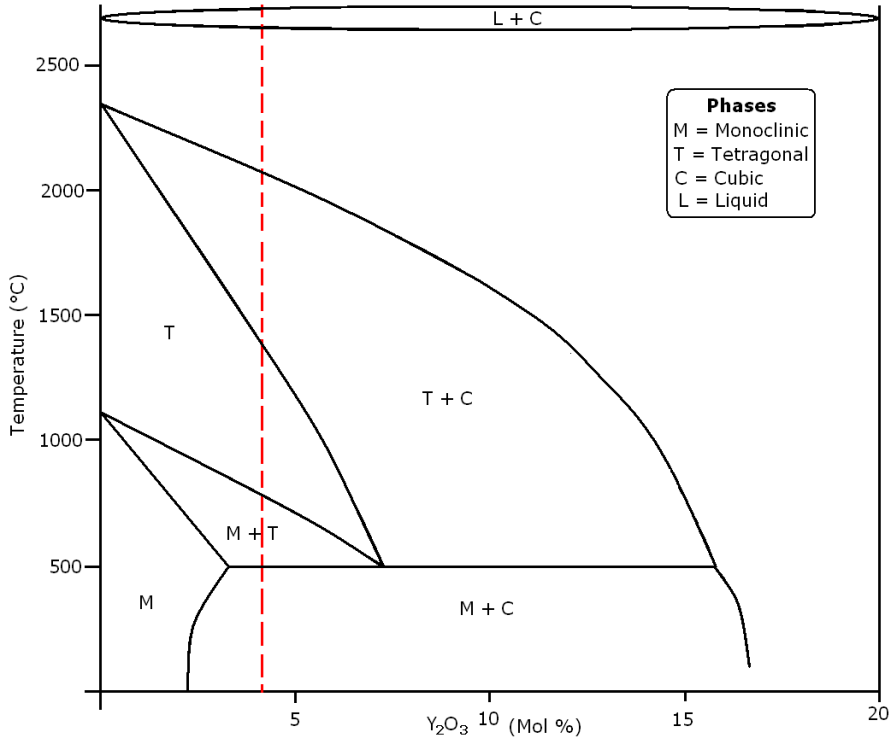

Figure 7.17 A phase diagram of the ZrO_2 engineering ceramic showing the change in phase with changing temperature of 4 mol% of Y_2O_3 content within the ZrO_2 engineering ceramic used in this research.

7.4.2 CO_2 Laser Processing of the ZrO_2 Ceramic

7.4.2.1 Experimental temperature readings

An experimental model of the temperature distributions of the CO_2 laser over the ZrO_2 engineering ceramic is illustrated in Figure 7.18(a) and (b). The temperature on average during the CO_2 laser and the ZrO_2 surface interaction was 1752°C. The surface temperature on the outer edges of CO_2 laser irradiated ZrO_2 ceramic is presented in Figure 7.18(a). The highest surface temperature measurement was found to be 776°C in position 4 (see diagram in Figure 7.18) and the lowest was 679°C - a 97°C of difference in the same surface plane. As described previously, the temperature measurements were different on one plane when they should be the same in general. However, this difference can be justified when considering the inhomogeneous material and the errors in measurement as previously discussed. The bulk temperature as shown in Figure 7.18(b) illustrates the temperature reading at various positions with the ZrO_2. The temperature measurements were found to be 325°C, 677°C and 1034°C at 8mm, 6mm, 2mm beneath the surface. Despite the temperatures being different to the temperature distribution pattern over the surface and through the bulk of the CO_2 laser irradiated ZrO_2 ceramic in comparison to the fibre laser irradiated surface of the ZrO_2 was somewhat the same as it can be seen from Figure 7.19(a) and Figure 7.19(b). The experimental temperature value of the bulk are used from Figure 7.18(b) to construct a graphical representation of the bulk temperature from the surface at 0mm to 10mm through the bulk and showed gradual decline as the heat was distributed into bulk of the ZrO_2 ceramic.

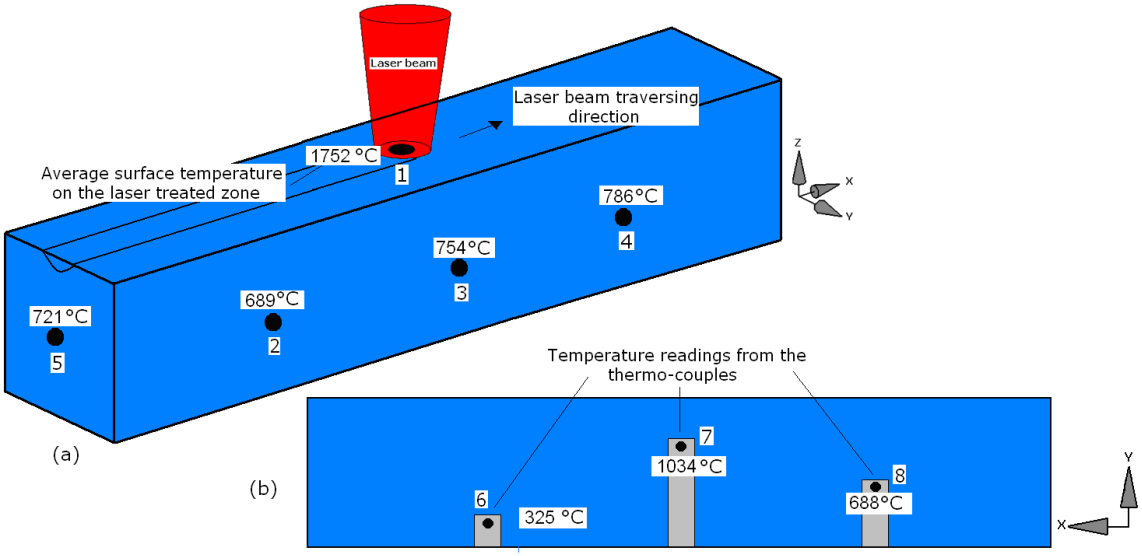

Figure 7.18 A schematic diagram of the surface temperature readings in (a) and (b) the bulk temperature of the CO_2 laser irradiated ZrO_2 engineering ceramic.

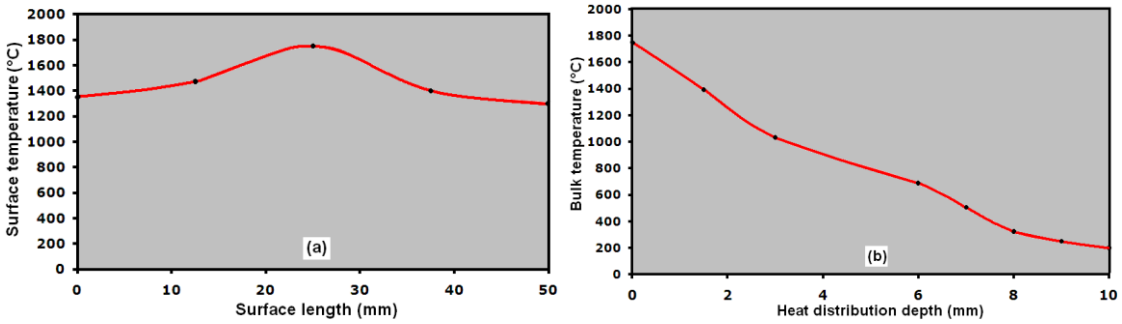

Figure 7.19 Experimental temperature distributions over the surface length in (a) and (b) the temperature distribution through the bulk of the CO_2 laser surface treated ZrO_2 engineering ceramic.

7.4.2.2 FEM temperature readings

The FEM of the CO_2 laser irradiated surface of the ZrO_2 ceramic is presented in Figure 7.20(a) for the surface and the bulk in Figure 7.21(b). The maximum temperature found from the FEM was 1795°C which was not far from the experimental temperature findings. The difference in the temperature was only 43°C. This was a + 2.5 % difference. However, the difference increases as the CO_2 laser beam traverses further over the surface of the ZrO_2 ceramic as further seen in the FEM representing the heat distribution of the later positions. The temperature distribution showed in Figure 7.20(b) and Figure 7.21(b) was found at 1795°C at the surface and then began to decline to 724°C at 4mm, 579°C at 7mm and then 79°C at 10mm beneath the surface.

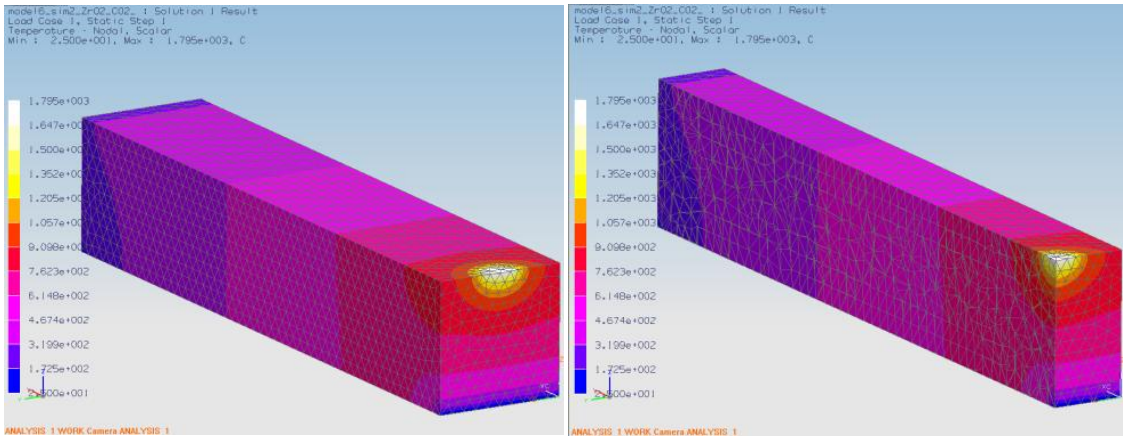

(a) **(b)**

Figure 7.20 (a) FEM of the heat distribution of the CO_2 laser focused at 0mm from the edge (position 1) of the ZrO_2 engineering ceramic (start of the laser treatment) and (b) the cross-sectional view.

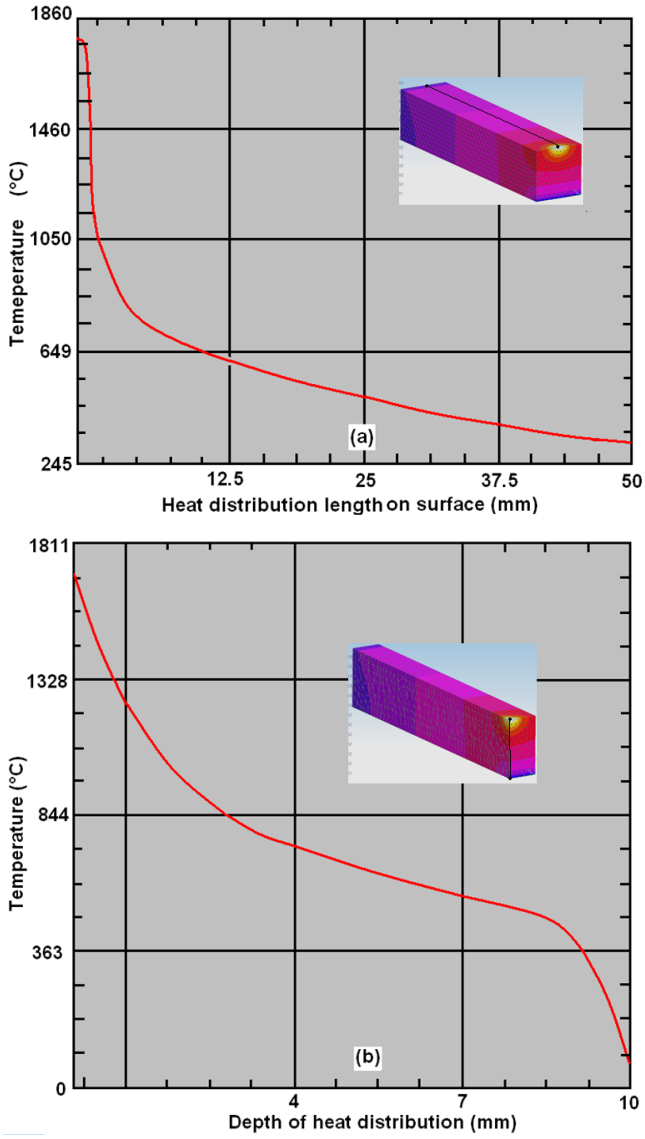

Figure 7.21 Temperature curves from the FEM of the initial stage at 0mm from the edge (position 1) of the CO_2 laser irradiated surface of the ZrO_2 engineering ceramic for (a) the heat distribution over the length and (b) the heat distribution through the depth of the sample.

The FEM for the CO_2 laser irradiated ZrO_2 ceramic in position 2 is presented in Figure 7.22(a) and (b) and furthermore in the graphical format in Figure 7.23(a) and (b) for the surface and the bulk. The maximum surface temperature in this position was 1741°C and was somewhat larger than the experimental model and the FEM temperature map in position 2. This was because of the increase in temperature of the ceramic since the CO_2 laser beam was active on the ceramic for a longer period of time. The difference in the FEM and the experimental model was 5% and is generally predicted due to the FEM not taking in factors such as the environment and the heat loss to the parent surface in contact which the ceramic is mounted on. The bulk temperature was found to range from the highest of 1741°C on the surface, 1194°C at 5mm and 1144°C at 10mm below the surface. The FEM value in this case for the bulk temperatures were about + 17% higher than that of the experimental model.

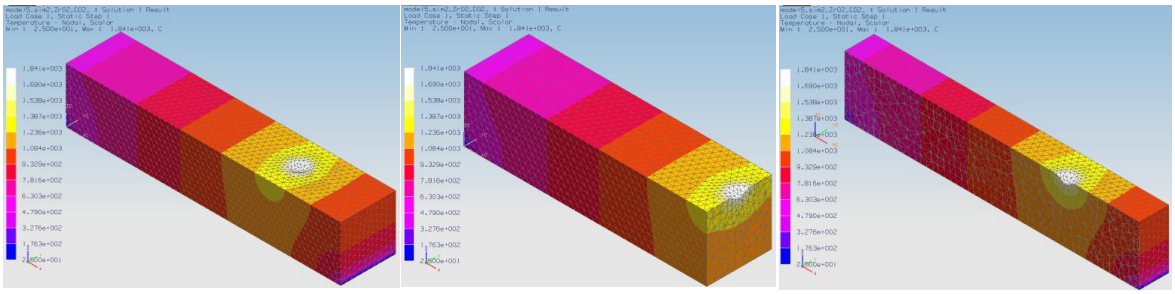

(a) **(b)** **(c)**

Figure 7.22 FEM of the heat distribution of the CO_2 laser focused at 12.5mm from the edge (position 2) of the ZrO_2 engineering ceramic and (b and c) the cross-sectional view.

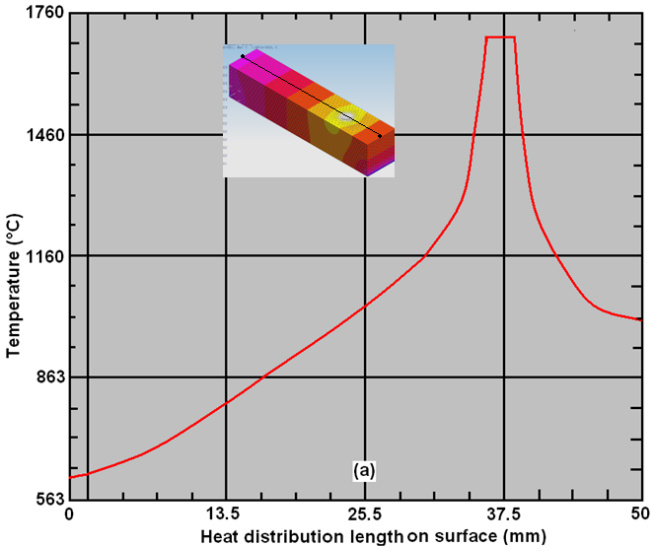

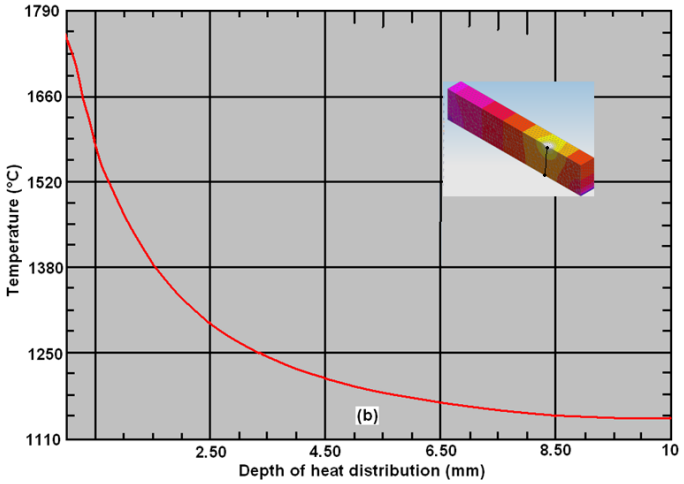

Figure 7.23 Temperature curves from the FEM of the CO_2 laser irradiation at 12.5mm from the edge (position 2) of the ZrO_2 engineering ceramic for (a) the heat distribution over the length of the sample and (b) the heat distribution through the depth of the sample.

The FEM for position 3 in the centre of the sample is presented in Figure 7.23(a) for the surface and Figure 7.23(b) and (c) for the bulk of the CO_2 laser irradiated ZrO_2 ceramic. The maximum temperature on the surface of the ZrO_2 irradiated with the CO_2 laser was found to be 1747°C. This was also somewhat larger than the temperature obtained by the experimental model and the temperature map in the position 1 and 2 from the FEM. The temperature distribution pattern showed in Figure 7.24(a) was similar to the previous pattern found in the fibre laser irradiated surface of the ZrO_2 as the temperature was balanced on both sides of the active CO_2 laser beam over the surface of the ZrO_2. The difference between the FEM in position 1 and 2 was +3% and +1%. This is not large but showed an increase in the temperature as the CO_2 laser beam traversed onto the surface of the ceramic. However, the difference between the FEM herein and the experimental temperature reading was + 95°C which was about 5.5%. The bulk temperature shown in Figure 7.25(a) show a balance of the temperature on both sides of the sample as the CO_2 laser beam was focused on the centre at 25mm (see Figure 7.24(a)) with the temperature distributed evenly on the ZrO_2 as shown by the curve. Gradual decline in the curve can be seen with the bulk temperature reading as the temperature was reduced from 1747°C on the surface to 1230°C at 5mm and then 1160°C.

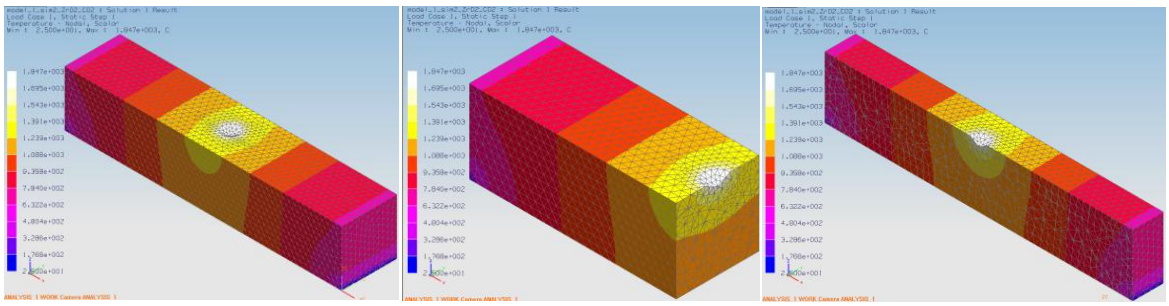

(a) **(b)** **(c)**

Figure 7.24 FEM of the heat distribution of the CO_2 laser beam focused in the centre (position 3) in (a); and the cross-section of the ZrO_2 engineering ceramic work-piece in (b) and (c).

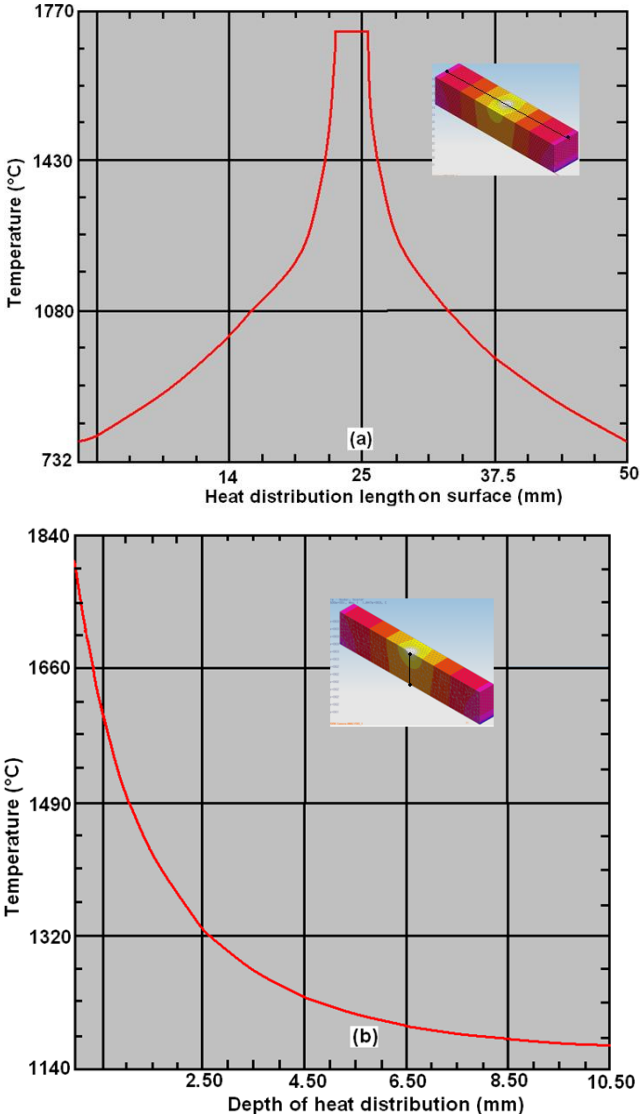

Figure 7.25 Temperature curves from the FEM of the CO_2 laser irradiation at 25mm from the edge (position 3) of the ZrO_2 ceramic for (a) the heat distributed over the length of the sample and (b) the heat distribution through the depth of the sample.

7.4.2.3 Comparison of the experimental and the FEM

The experimental temperature at the CO_2 laser-ZrO_2 interface was found to be 1752°C. This in comparison to the FEM in position 3 was 95°C lower. It was also found that the temperature difference throughout one surface plane were not the same for the CO_2 laser irradiated sample of the ZrO_2 engineering ceramic. The difference was under 5% which can be classified as being within an exceptional range. The reason for this difference has been mentioned earlier in this Chapter (see Section 7.4.1.3).

The average temperatures measured within the bulk of the ZrO_2 after five readings at 3mm below the surface the temperature was up to 1034°C. The FEM by comparison gave a temperature of about 1250°C. This was with an error of about 20%. The temperature in Position 7 (see Figure 7.18) was found to be 677°C. This in comparison to the FEM was twice that of the experimental temperature.

Lastly, in Position 6 the temperature recorded was 325°C, while the temperature predicted by the FEM was 1170°C. This was considerably, higher than the bulk temperature. It can be seen that the bulk temperatures measured experimentally were to some extent a lot lower for the CO_2 laser irradiated ceramic in comparison to that of the FEM. Along with the factors previously mentioned, a valid point should be considered. This is the fact that the FEM model does not consider the processing speed of the laser. The FEM was generated as it was to be focused on one particular area. However, in case of the CO_2 laser irradiated surface of the ZrO_2, the speed was increased as larger cracking was found. Hence, the measured surface temperature was recorded to be lower. Another point to be considered is the absorption of the ZrO_2 engineering ceramic with that of the CO_2 laser. This is further discussed in the latter part of this Chapter.

7.4.2.4 Development of extended parameters

Figure 7.26 illustrates the prediction of various laser parameters by considering factors such as power density, surface and bulk temperatures, depth, time and traverse speed for the CO_2 laser surface treatment of the ZrO_2 engineering ceramic.

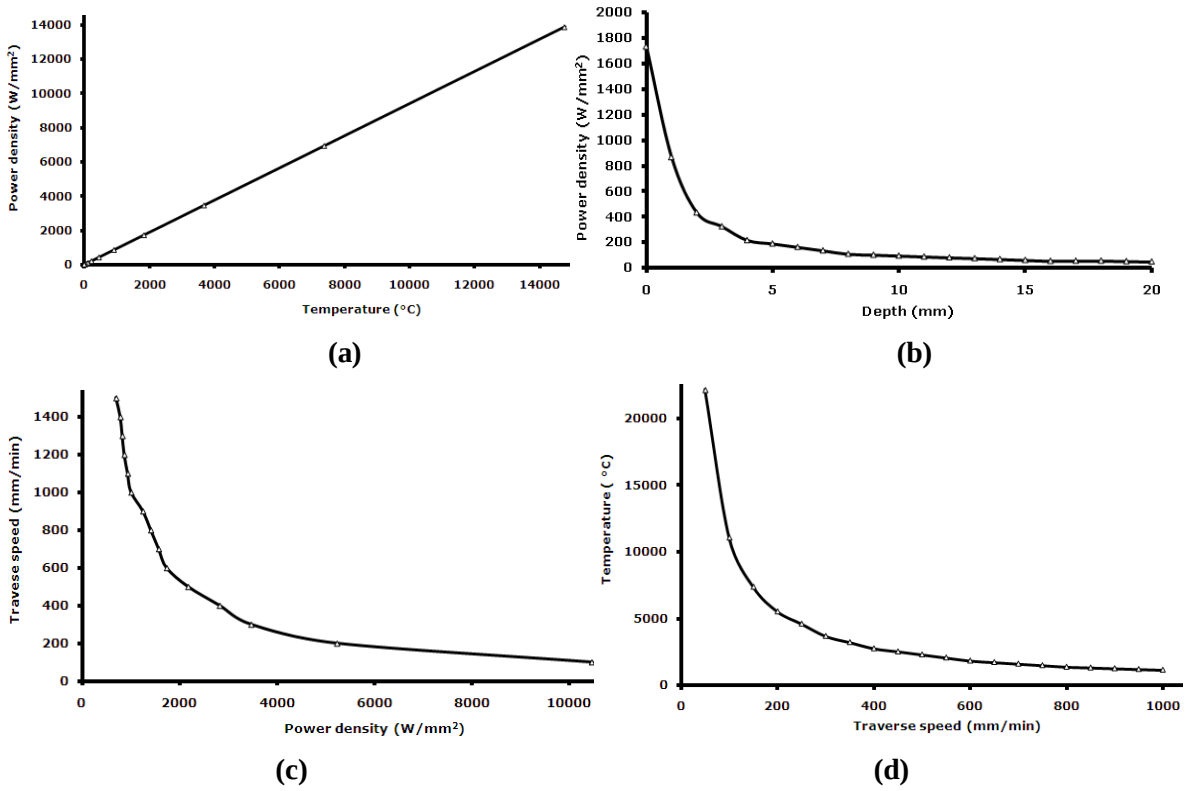

Figure 7.26 Parameters obtained from the FEM of the CO_2 laser surface treated ZrO_2, showing the correlation of various factors with one another: (a) power density *versus* temperature, (b) depth *versus* power density, (c) power density *versus* traverse speed and (d) power density *versus* time.

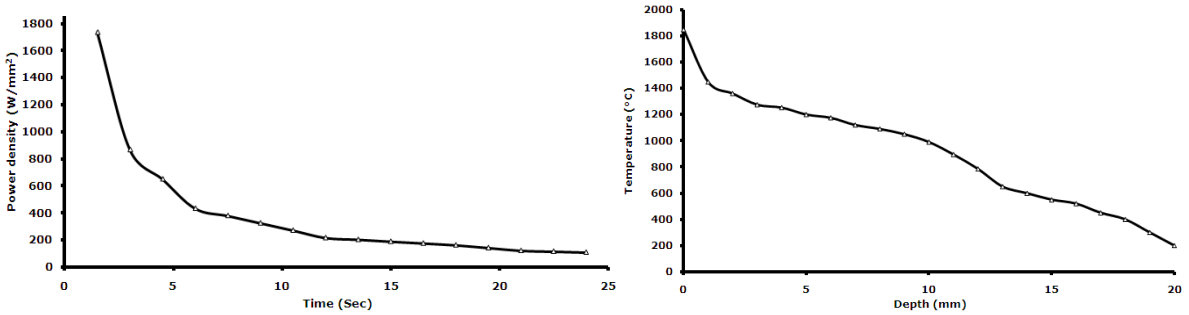

(e) **(f)**

Figure 7.26 Parameters obtained from the FEM of the CO_2 laser surface treated ZrO_2, showing the correlation of various factors with one another: (e) traverse speed *versus* temperature and (f) depth *versus* temperature.

7.4.3 Fibre Laser Surface Treatment of the Si_3N_4 Engineering Ceramic

7.4.3.1 Experimental temperature readings

The average temperatures found on the surface of the Si_3N_4 engineering ceramic after five passes of the fibre laser are presented in Figure 7.27(a) and (b); the surface temperature and the bulk temperature of the Si_3N_4 ceramic. At the laser-ceramic interface the surface temperature was found to be 2269°C. This was considerably higher than the general melting temperature of the ceramic (1900°C) [42] in comparison. This is when the Si_3N_4 ceramic undergoes decomposition. The difference between the two readings was 19.5%. This undoubtedly showed that the fibre laser surface treatment temperature was sufficiently higher than that of the decomposition temperature of the Si_3N_4. The surface temperature on the side of the sample (away) from the laser treated zone was found to be much lower than the melting temperature. This would obviously be high due to the heat transferring through the bulk of the ceramic.

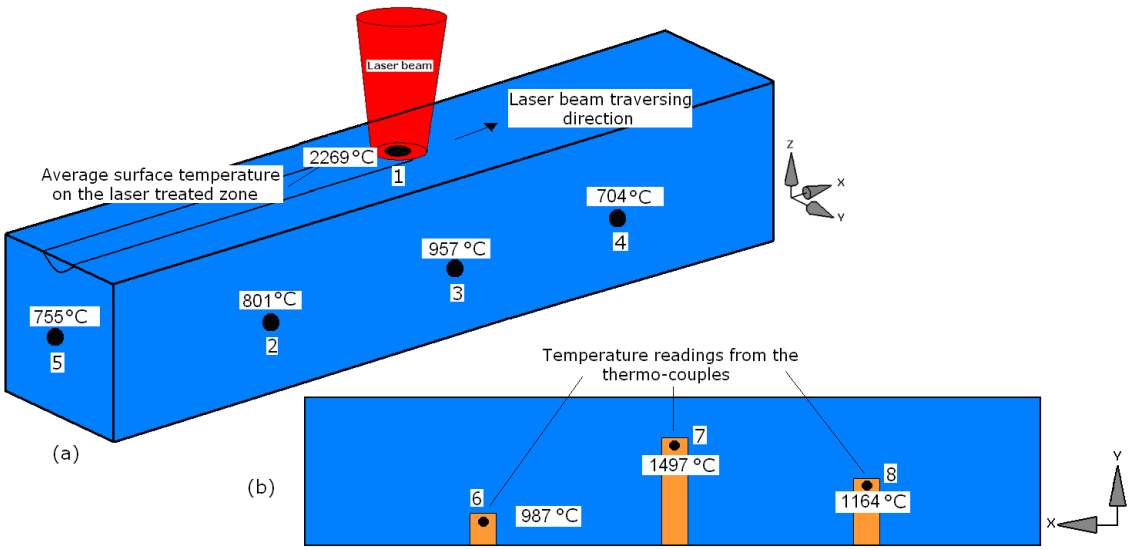

Figure 7.27 Schematics of the surface temperature reading in (a) and (b) the bulk temperature of the Si_3N_4 engineering ceramic.

The temperature measurements taken from using the thermo-couples within the bulk of the Si_3N_4 engineering ceramic are presented in the Figure 7.27(b). The average bulk temperature after five readings in position 6, 7 and 8 were recorded to be 976°C, 1497°C, and 1164°C. This result agrees with the surface temperature presented in Figure 7.27(a) that 3mm below the surface due to the heat transfer; the temperature is above 400°C lower. At 6mm below the surface, the measured temperature was considerably lower (1164°C). In this position, the temperature has begun to decrease as the heat was distributed throughout the surface. Moreover, the temperature at 7mm below the surface was 977°C, as the heat was passed on from the bulk of the ceramic to the surface.

In Figure 7.28(a) and (b), both of the graphs are constructed from the experimental values. This was for a situation where the fibre laser was incident at 25mm length (centre) from the edge of the Si_3N_4 ceramic. The distribution of heat is presented in Figure 7.28(a). This illustrated the surface temperature over the length of the Si_3N_4 sample at 25mm. At the length of 0mm the experimental temperature was instantaneously ramped to just less than 700°C and gradually increases as it comes closer to the incident beam. The peak temperature found was 2269°C at 25mm length (centre of the work-piece) of the focused laser beam on the Si_3N_4. The temperature reduced to 730°C at 37.5mm in length and was recorded at 750°C at the edge of the sample at 50mm.

The graph in Figure 7.28(a) and (b) presents the experimental temperatures obtained on the surface and the in the bulk of the ceramic. In general the curve in Figure 7.28(b) has declined due to the reduction of the temperature through the bulk of the ceramic. The temperature is reduced from 2269°C at the depth of 0mm (surface) to 1500°C at 3mm, 1235°C at 6mm and 1195°C at 7mm depth. From this, the temperature at the depth of 10mm can be predicted as shown in Figure 7.28(b).The experimental investigation would now be used as a base to construct the FEM. The results found herein are also compared to the FEM for validation and confirmation of the level of accuracy or error in the temperature measurements in this study.

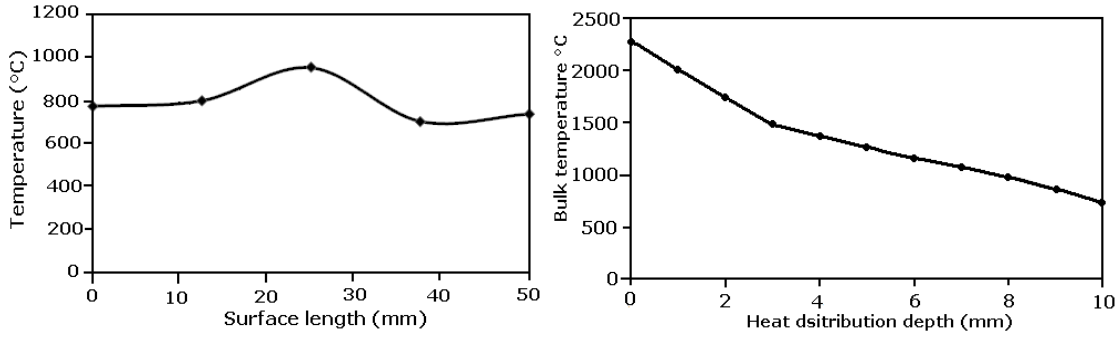

(a) **(b)**

Figure 7.28 Experimental temperature distributions over the surface length in (a) and (b) the temperature distributions through the bulk of the fibre laser irradiated Si_3N_4 engineering ceramic.

7.4.3.2 FEM temperature reading

A FEM was constructed which revealed the surface and the bulk temperature maps by taking in account of the surface and the bulk temperatures measured from the experimentation. The surface maps are presented in Figure 7.29, Figure 7.31 and Figure 7.33. The impact on the beam is only 1.5mm onto the surface despite comprising of a spot size of 3mm diameter. It is seen that the maximum temperature found at the laser-Si_3N_4 interface on the FEM was 2236°C. The temperature here was lower than the temperature from the real experimental value by only 1.5%. In Figure 7.29(b); the laser beam is only concentrated at 50% of its diameter because it is focused on the edge of the sample which is the start of the laser treatment. This allowed the cross-sectional distribution of heat to be analysed.

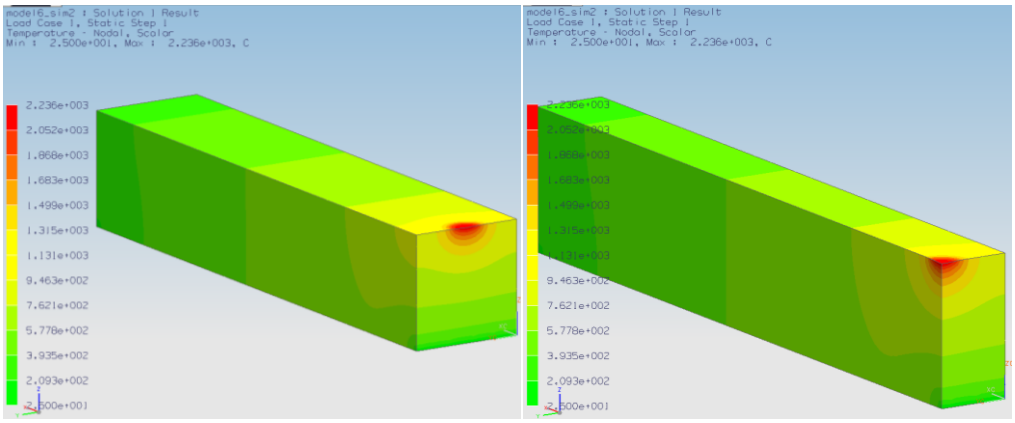

(a) **(b)**

Figure 7.29 FEM of the heat distribution of the fibre laser focused at 0mm from the edge (position 1) of the Si_3N_4 ceramic (start of the laser treatment) in (a) and (b); the cross-sectional view.

From observing the results from the model in Figure 7.29(a) and (b), the determination of temperature distribution over the surface at various lengths and through the bulk at various depths are presented in the graph in Figure 7.30(a) and (b). In this model, the incident beam at the start of the surface treatment is covering 0mm to 1.5mm radius. The temperature within this area as seen on Figure 7.30(a) is up to 2227°C. During this time the temperature distribution over the rest of the surface is lower. This is due to the heat transfer taking effect over the surface. At 25mm in the centre of the work-piece, the temperature was up to 573°C and at 50mm (edge of the sample); the temperature was much lower. The result of the FEM at this position appears to be in good agreement with that of the experimental result. However, from observing the depth of the distribution from the model in Figure 7.30(b); the surface temperature at 0mm is 2250°C and reduces to 790°C at the depth of 2mm, 650°C at 4mm, 470°C at 7mm and finally reducing to around 300°C at 10mm.

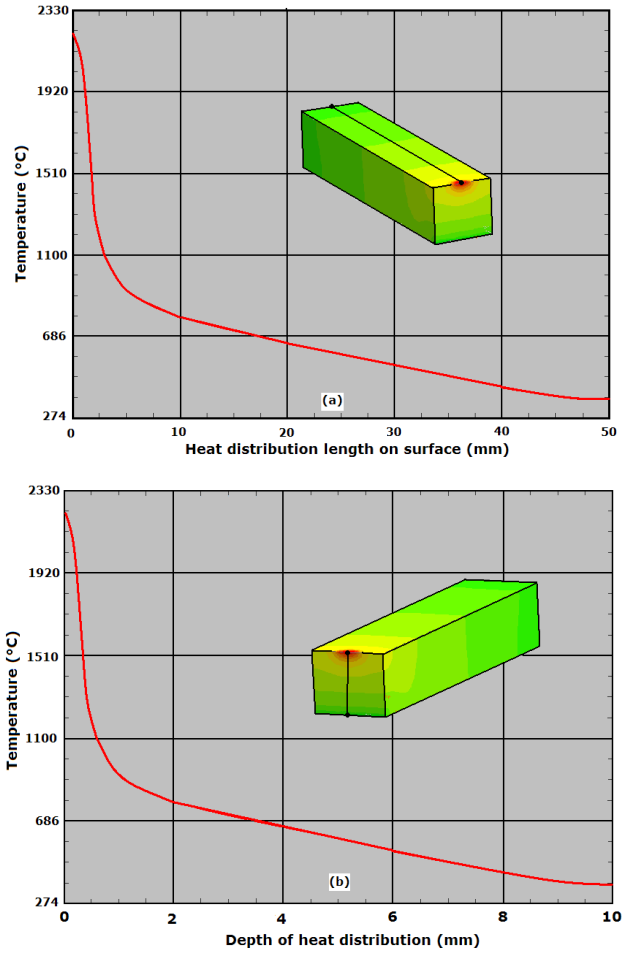

Figure 7.30 FEM temperature distribution curves of the initial stage at 0mm from the edge (position 1) of (a) the heat distributed over the length of the sample and (b) the heat distribution through the depth of the sample for the fibre laser irradiated surface of the Si_3N_4 engineering ceramic.

The FEM in Figure 7.31(a-c) showed that the temperature pattern was somewhat different to the one found at the start of the fibre laser surface treatment as the average heat input begun to increase over the total surface area of the Si_3N_4. Despite the decomposition and surface melting occurring during the laser interaction and the rapid cooling effect taking place; the temperature at the laser irradiated zone has increased on the surface and through the bulk as presented in the graph in Figure 7.32.

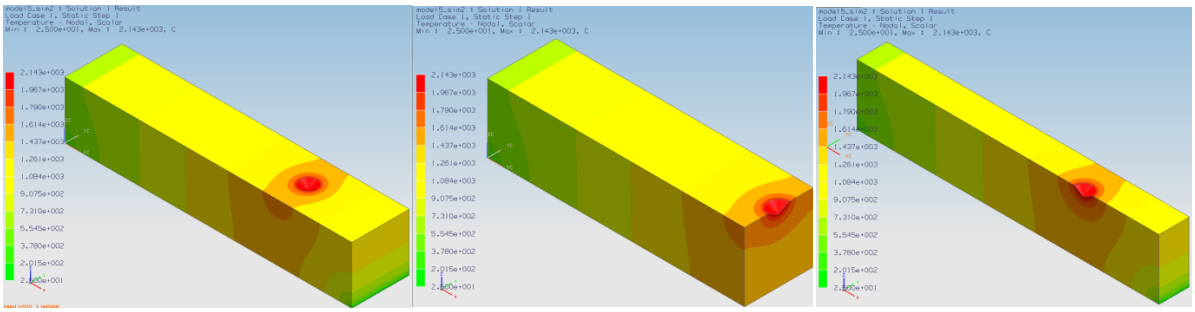

(a) **(b)** **(c)**

Figure 7.31 FEM of the heat distribution of the fibre laser focused at 12.5mm from the edge (Position 2) of the Si_3N_4 in (a) and the cross-sectional view in (b) and (c).

The traversing laser beam is paused in time at 12.5mm from the edge in order to show the effects at that position. At 12.5mm the highest temperature on the surface was found to be 2143°C. Gradually, the temperature begins to decrease to 1167°C at 25mm, 953°C at 37.5mm and 729°C at 50mm. The temperature through the bulk has increased in comparison with the bulk temperature during the start of the fibre laser surface treatment due to the increase in time that the laser beam has spent on the ceramic. This would have caused a sufficient level of heat to be produced. From melting temperatures at 0mm on the surface; the temperature reduces to 1355°C through the bulk at the bottom surface layer as the heat is passed on during the laser-ceramic interaction at 12.5mm in length after the start of the treatment.

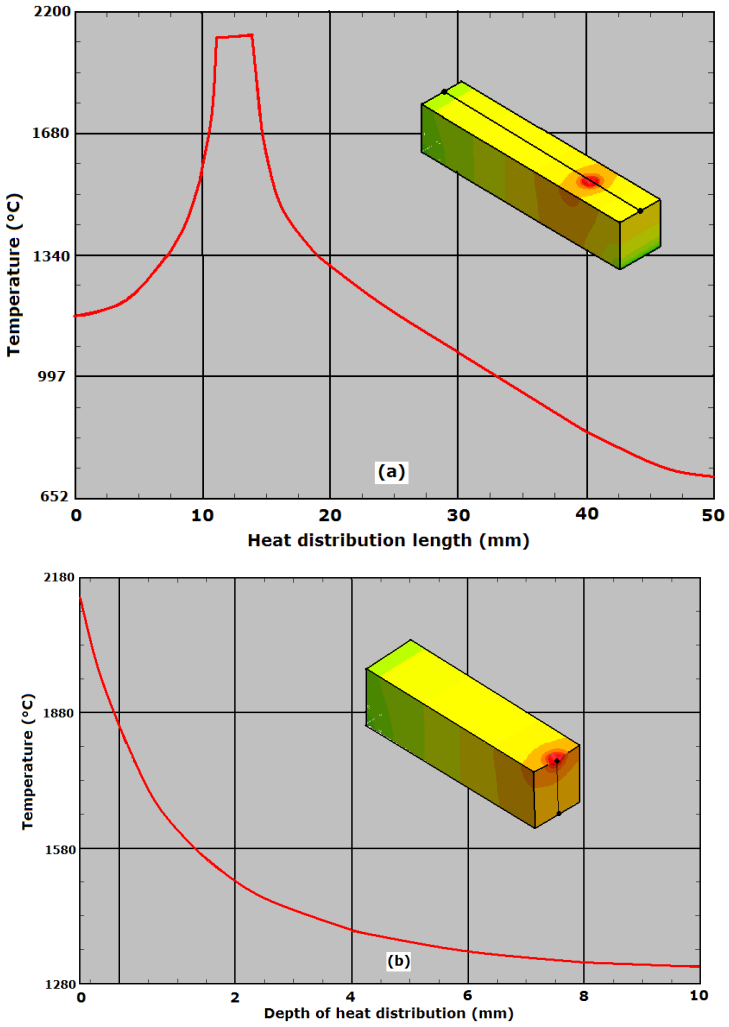

Figure 7.32 Temperature curves from the FEM of the fibre laser irradiation at 25mm from the edge (position 3) of the Si_3N_4 ceramic for (a) the heat distributed over the length of the sample and (b) the heat distribution through the depth of the sample.

The illustrations in Figure 7.33(a), (b) and (c) show the FEM of the laser-ceramic interaction in the centre of the work-piece (25mm from the edge). In this position the distribution of heat is different to the interaction during the initial stages as previously shown. The Si_3N_4 ceramic in this position is in thermal equilibrium since the temperature distribution is well balanced as presented in Figure

7.33(a). At 25mm the heat is at its peak (2277°C) near to the melting temperature of the Si_3N_4 ceramic. During this time, the temperature slope gradually increases to the highest position as shown in Figure 7.34(a) and maintains for 3mm, then has the opposite effect where the temperature curve is declined.

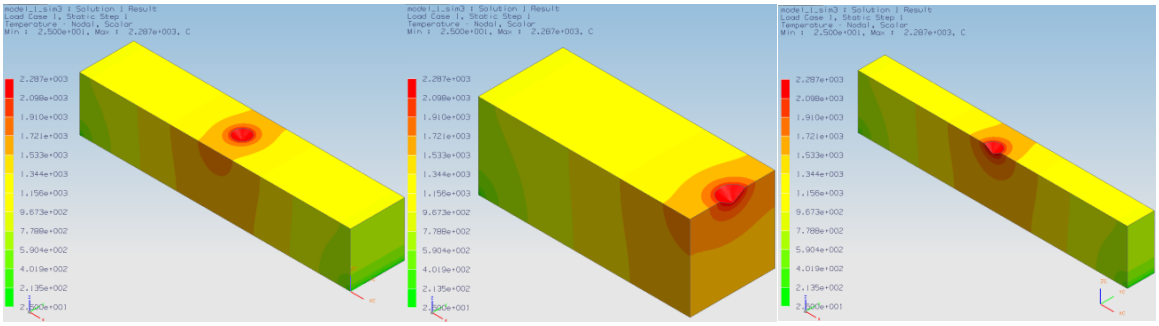

(a) **(b)** **(c)**

Figure 7.33 FEM of the heat distribution of the fibre laser beam focused in the centre (position 3) of the Si_3N_4 ceramic in (a) and in the cross-section in (b) and (c).

From this point onwards - as the laser beam traverses furthermore on to the sample, the heat distribution is similar to that of the one presented in previous FEM's. The temperature distribution over the surface was similar to that of the FEM presented in Figure 7.33, as well as the results obtained from the experimental model. The difference between the experimental model and the computational FEM was less than 1% particularly for the temperature predictions over the surface length. The bulk readings for the two compared models were also in good agreement. However, consideration should be given to the accuracy of thermometer device used for measuring the experimental temperature (±10%) as well as the distance which the temperature measurement was taken from. This is because such factors will have a considerable effect on the experimental readings. The distance of the temperature measurement changes as the laser beam traverses away from the focused IR beam of the thermometer device (see Figure 7.6). This would also cause some fluctuation in the results found.

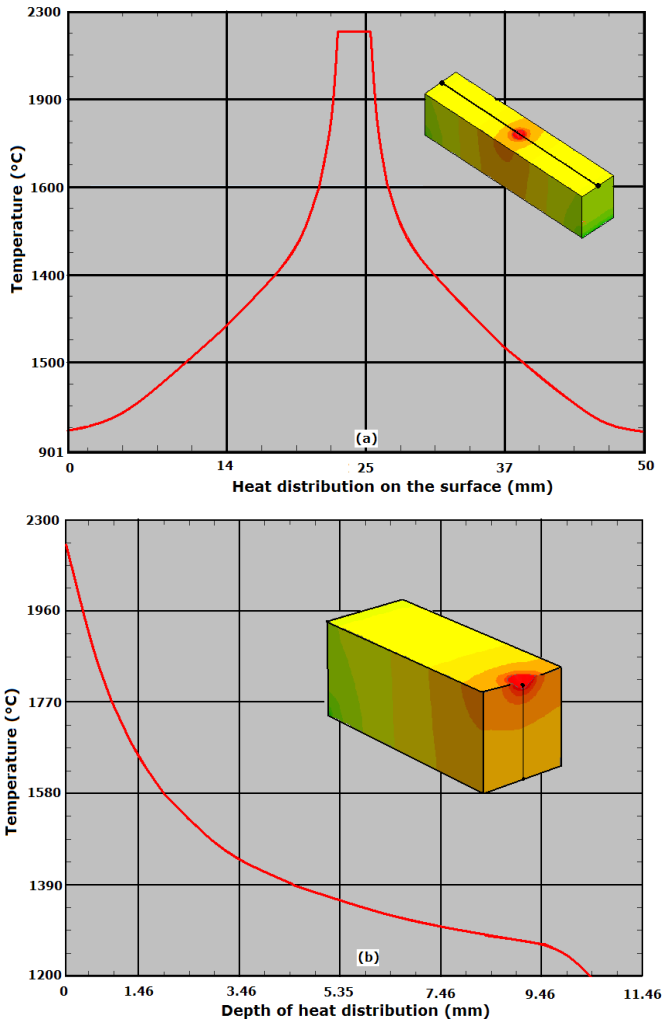

Figure 7.34 Temperature curves from the FEM of the fibre laser irradiation at 25mm from the edge (position 3) of the Si_3N_4 ceramic for (a) the heat distributed over the length of the sample and (b) the heat distribution through the depth of the sample.

7.4.3.3 Comparison of the experimental and the FEM of the fibre laser irradiated surfaces of the Si_3N_4

At the laser-ceramic interface the surface temperature was found to be 2269°C. The temperature readings was again stable throughout one surface plane as up to 36% difference in temperatures between Positions 2 to 3 and 4 to 5 was observed. The difference between the two results may have resulted from the error in reading the temperature resulting from the contact-less IR thermometer device, fluctuation in the laser power during the processing stage (although, stable output powers were recorded prior to the laser surface treatment) and the ceramic being somewhat inhomogeneous.

The average temperatures measured within the bulk of the Si_3N_4 after five readings was 1497°C at 3mm, 972°C at 7mm and 1164°C at 6mm below the surface of the Si_3N_4 engineering ceramic (see Figure 7.27). When compared to the experimental bulk temperatures with that of the FEM, the difference found was 1475°C at 3mm, 1266°C 7mm, and 1342°C at 6mm. In this case, the temperature difference was 1% at 3mm, 29% at 7mm and 15% at 6mm beneath the surface. Despite

the temperatures being within the expectable range more closely to the surface, the FEM however, does, have the tendency to generate higher temperatures in comparison to the experimental values found. These factors have been discussed previously in this Chapter in Section 7.4.1.3.

7.4.3.4 Development of extended parameters from the FEM of the fibre laser surface treatment of the Si_3N_4

Various possibilities can be accrued based on the results obtained from the FEM for parameters such as traverse speed; power density; depth of heat distribution; temperature; and time, in relationship to one another. Based on this, prediction of the input parameters during fibre laser surface treatment of the Si_3N_4 at various input parameters (see Figure 7.35 (a-g)) can be made. As with all laser processes, the results herein show that a lower traverse speed at high power density would generate high processing temperatures. This inherently, would produce deeper distribution of the thermal energy; the effects are opposite when the processing speeds increases or the power density decreases. This is when the surface temperature is also reduced with lower penetration of the thermal energy into the bulk of the ceramic. Consideration of power density would also allow one to gauge the effect of the laser spot size as an additional parameter, since the spot is a function of the power density. Typically, a smaller spot size than 3mm by using the same power input (143.25 W) would produce a much bigger power density and would further compliment the model that are presented in this study.

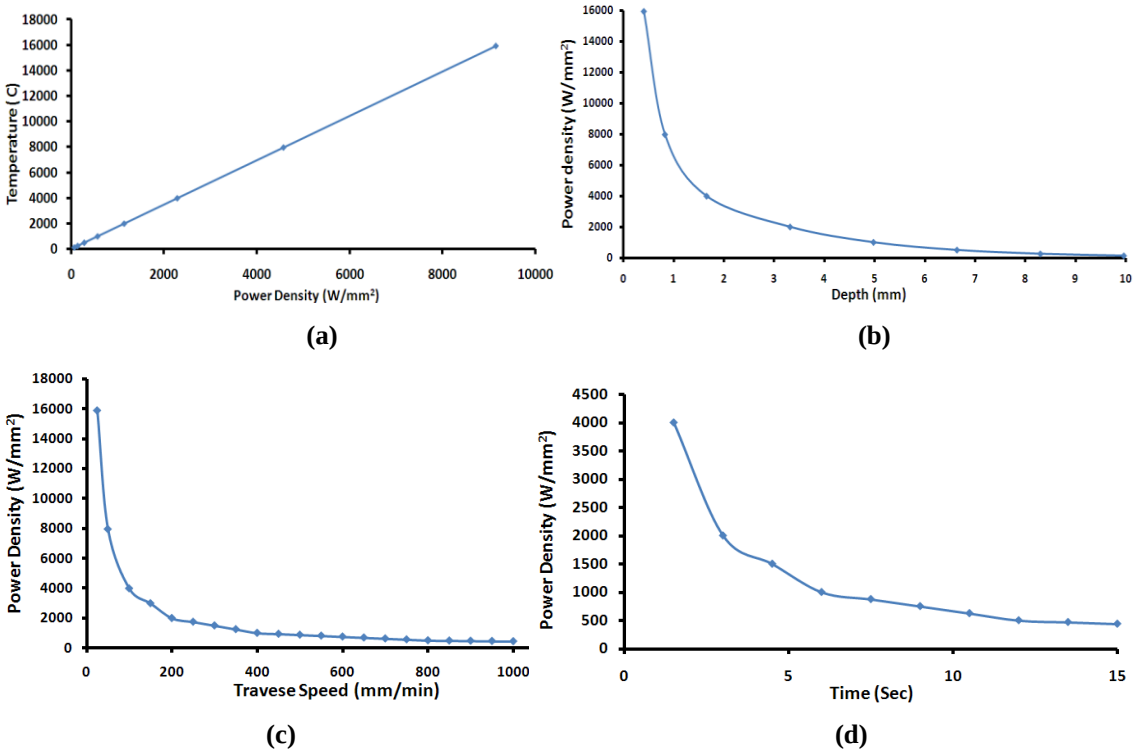

Figure 7.35 Parameters obtained from the FEM showing the coloration of various aspects with one another; (a) power density *versus* temperature; (b) depth *versus* power density; (c) power density *versus* traverse speed and (d) power density *versus* time.

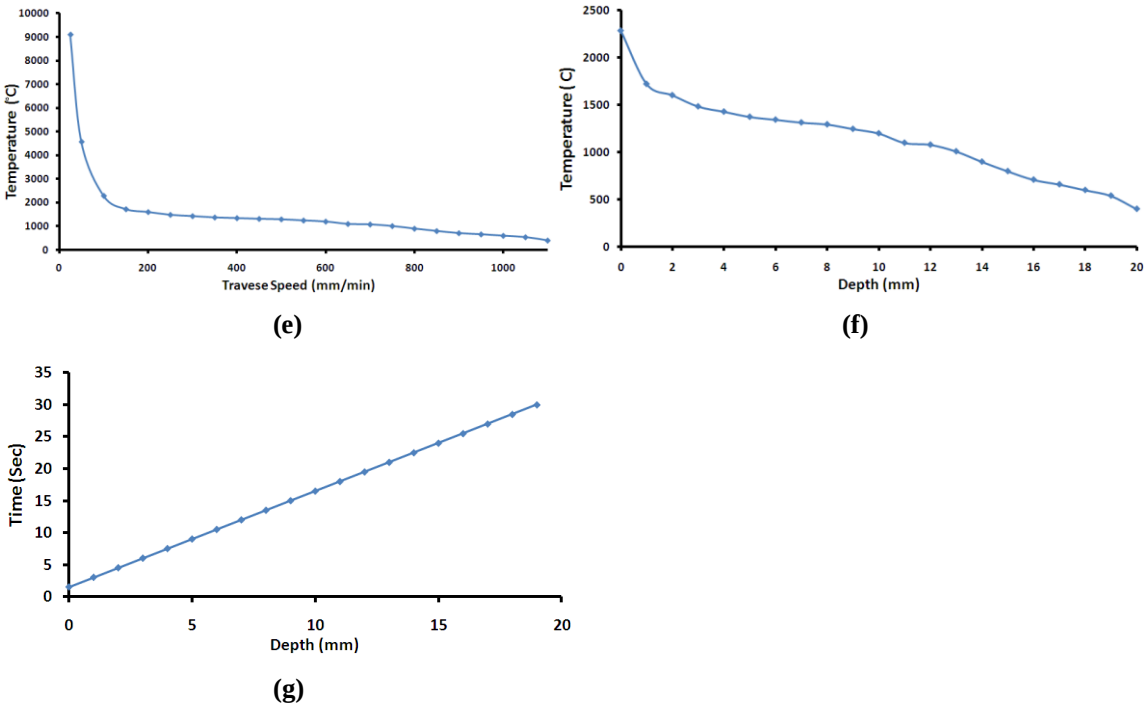

Figure 7.35 Parameters obtained from the FEM showing the coloration of various aspects with one another; (e) traverse speed *versus* temperature; (f) depth *versus* temperature and (g) depth *versus* time for fibre laser surface treatment of the Si_3N_4 engineering ceramic.

7.4.3.5 Phase transformation of Si_3N_4 engineering ceramic

Figure 7.36 and Figure 7.37 show the changes within the Si_3N_4 engineering ceramic after heating to 1500°C and cooling to room temperature during the TG-DSC analysis. Figure 7.36 represents the as-received surface and Figure 7.37 illustrates the fibre laser irradiated surface. As one can see, there is a considerable difference in the events which have occurred for the two samples. The fibre laser irradiated surface in comparison to the as-received surface has allowed much more mass flow to have taken place. The highest mass flow found on the fibre laser irradiated surface was about 270mW when compared to the as-received surface which was about 37mW. A decline in the mass flow from 1450°C to 1500°C was also observed in the as-received sample (see Figure 7.36). This would have occurred from the heat induced by the fibre laser irradiation. This in turn caused some degree of densification of the Si_3N_4 engineering ceramic. This intrinsically allowed more heat to flow through the bulk due to air blocks or cavities within the as-received sample. Therefore, a decline in the mass occurred. On the other hand the fibre laser induced heat would have also affected the composition of the Si_3N_4 engineering ceramic where a formation of an oxide layer would have occurred as shown from the chemical analysis in Chapter 5. This oxide layer would have increased porosity and allowed more mass flow to occur for the fibre laser treated sample in Figure 7.37.

At 50°C, a rapid decline in the heating curve can be seen. This indicated an endothermic reaction as the Si_3N_4 would have begun to absorb the atmospheric gases and had began the process of oxidation. This would last over the full course of heating the sample to high temperatures. Evidence of some

change was also observed from the curve between 1300°C to 1450°C. From this, it can be postulated that the phase transformation of the Si_3N_4 engineering ceramic has started to take place where large percent of the α-phase is present and the β-phase has began to form. At 1400°C the transition between α-phase to β-phase would have occurred where $\alpha+\beta$ would be found. The gradient of the curve begins to increase beyond 1400°C. This showed increase in the mass flow and indicated the end of the phase transformation, where mainly the β-phase is present. Beyond 1450°C, the Si_3N_4 engineering ceramic has fully transformed to β-phase and shows the end of the phase transformation. At 1500°C the cooling cycle begins, where it can be seen that the cooling curve has lower mass flow on average and almost identical events occurring. When the sample was cooled it can be seen that the mass flow was slightly lower and the decline in the curve found at about 1400°C was not to be observed during the cooling stage. This was because the Si_3N_4 engineering ceramic does not usually have the tendency to produce reverse phase transformation as stated by Messier *et al*. [217]. The TG-DSC analysis was only performed from room temperature to 1500°C. This demonstrated the expected changes that have occurred. Although, postulation can be made for the events which would take place after the 1500°C, since the temperature found both in the FEM and the experimental model was up to 2200°C. This indicated that decomposition and melting would occur around 1900°C.

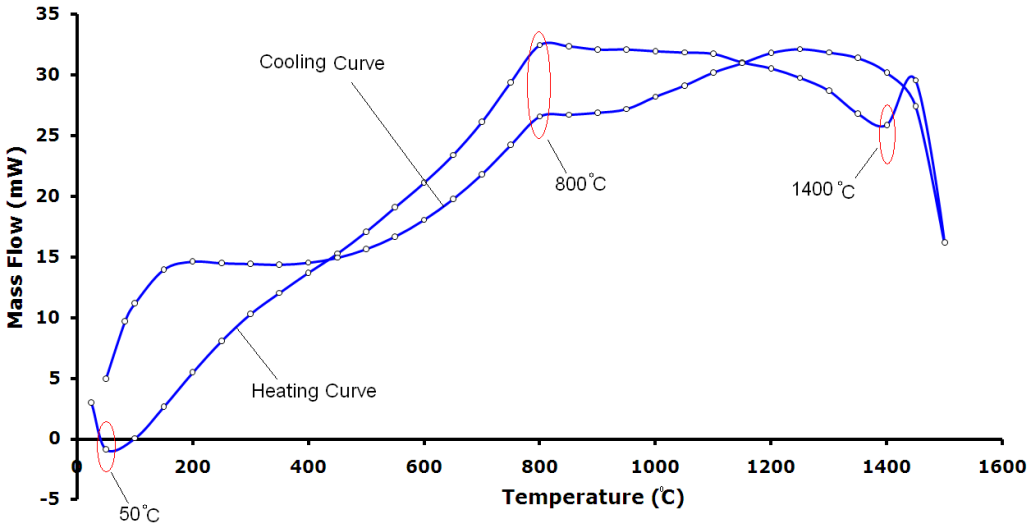

Figure 7.36 Heating and cooling curve from the TG-DSC analysis for the as-received surface of the Si_3N_4 engineering ceramic.

The TG-DSC curve for the fibre laser irradiated surface was somewhat different in comparison to that of the as-received surface as mentioned previously. This was because the fibre laser irradiation has produced a change in composition of the Si_3N_4 which was considerably different to that of the as-received Si_3N_4. This change has been presented Chapter 5 which demonstrated the formation of the SiO_2 layer formed on the Si_3N_4. Therefore, the oxidized surface did not show any evidence of major change during the TG-DSC analysis as there was considerable amount of change which took place already from the fibre laser irradiation.

The TG-DSC curve for the fibre laser irradiated surface was somewhat different in comparison to that of the as-received surface as mentioned previously. This led to the difference in the mass flow in Figure 7.36 and Figure 7.37 which occurred because the Si_3N_4 ceramics in Figure 7.36 is of the as-received sample and Figure 7.37 is of the fibre laser treated sample. In other words, the fibre laser treated sample comprised of the oxidized layer which consequently reflected the mass flow to be different when compared to the as-received surface which was mainly comprised of the α-phase. The α-phase existed in the as-received sample (Figure 7.36), which then began the transformation to $\alpha+\beta$ at around 1450°C during heating. This in comparison to the sample which was heated by the fibre laser irradiation (Figure 7.37) was not in the same form as it is likely that the β-phase was already developed (before the TG-DSC analysis) when the fibre laser surface treatment was being undertaken at temperatures of 1600°C and over. The temperatures were confirmed by the FEM and the experimental models.

From analysing events which has taken place during the TG-DSC analysis of the fibre laser irradiated sample of the Si_3N_4 engineering ceramic; it can be said that the α-phase to β-phase transformation would have already occurred within this during the fibre laser treatment. This was possibly between 1300°C to 1450°C, which then was irreversible during the cooling stage. The presence of the β-phase can be confirmed by comparing the microscopic image of the fibre laser irradiated surface presented in Figure 7.38(b) and comparing it with the as-received surface of the Si_3N_4 in Figure 7.38(a). This is where it is indicated that a change in morphology and the microstructure by elongated rod-like grains in large numbers as well as the formation of the SiO_2 zones is to be seen on the fibre laser irradiated surface as shown in Figure 7.38(b). This type of behaviour was also mentioned by the work of Sarin [216], Messier *et al.* [217], Ziegler and Hasselman [218] and Dai *et al.* [219] who investigated the phase transformation of the Si_3N_4 ceramic during its exposure to high temperature gradients. Also, the microscopic image in Figure 7.38(b) was found to be somewhat similar to previous investigations [226, 227] where formation of elongated β-grains was discussed. Hence, a comparison was made to further confirm that the phase transformation herein was valid.

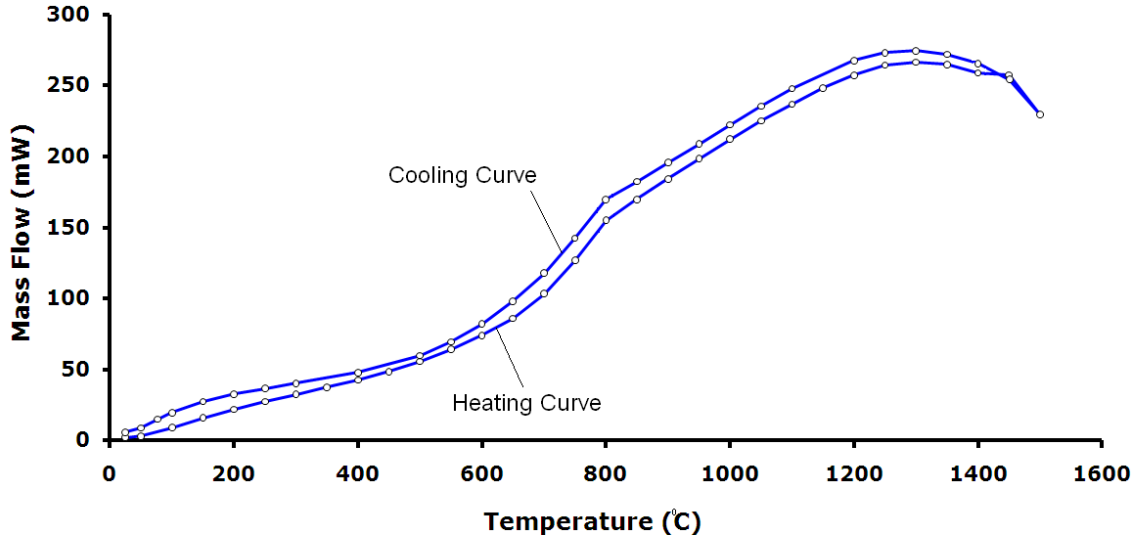

Figure 7.37 Heating and cooling curves from the TG-DSC analysis for the fibre laser irradiated Si_3N_4 engineering ceramic.

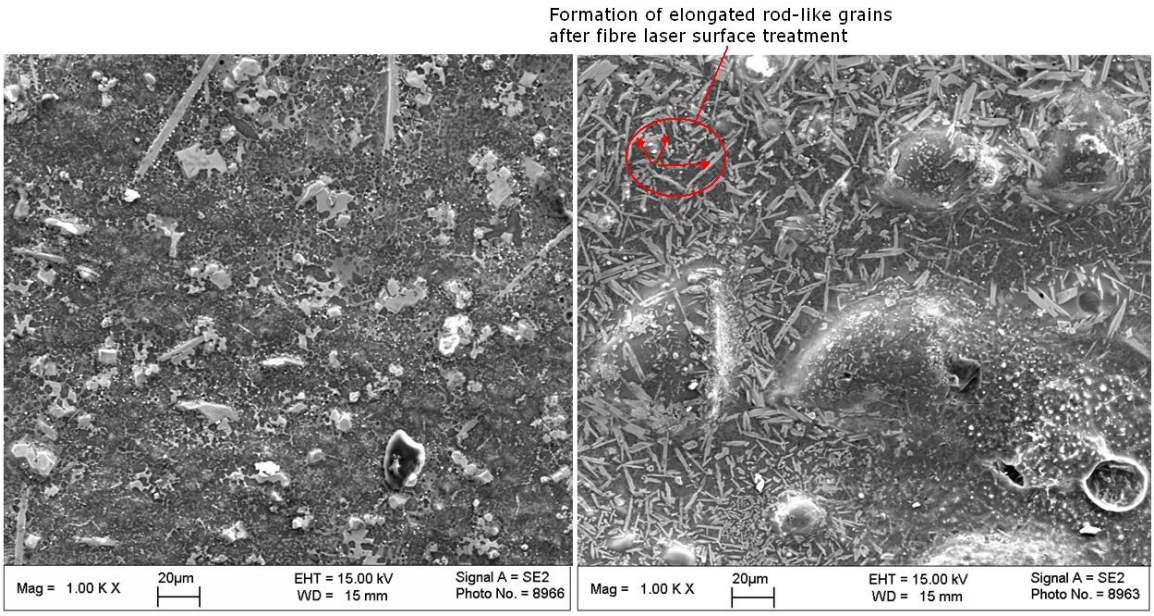

(a) **(b)**

Figure 7.38 SEM images of (a) the as-received surface and (b) the fibre laser irradiated surface of the Si_3N_4 engineering ceramic.

7.4.4 CO_2 Laser Surface Treatment of the Si_3N_4 Engineering Ceramic

7.4.4.1 Experimental temperature reading

Figure 7.39(a) and Figure 7.40(a) presents the experimental model of the Si_3N_4 ceramic irradiated by the CO_2 laser. This demonstrated the temperature distribution over the surface of the sample. The average surface temperature was found to be 1935°C at 25mm from the edge of the sample and was slightly higher than the decomposition temperature of the Si_3N_4 ceramic in general. This meant that the CO_2 laser had also melted the ceramic which further led to decomposition at 1900°C. Compositional analysis of CO_2 laser surface treatment as presented in Chapter 5 for the Si_3N_4

ceramic showed that the Si_3N_4 was being transformed to SiO_2. This is because melting and decomposition had taken place. Surface temperature values showed in Figure 7.39(a) also supports this finding. Like with previous results of the fibre laser irradiated surfaces, the temperature away from the CO_2 laser-material interaction zone was much lower due to the heat being distributed through the bulk. However, the temperatures were again not similar on one surface plane. This was also found with other samples as there was up to 120°C difference found on one surface plane between the highest and the lowest values. In general, at 25mm position the temperature found at the CO_2 laser-Si_3N_4 interaction was 1935°C. At the same time the surface temperature going further away from the beam began to decrease. The bulk temperatures presented in Figure 7.40(b) was used to further demonstrate the temperature distribution through the bulk which is illustrated in Figure 7.40(b). The results showed that the temperature was at its highest (1935°C) at the surface and began to decrease through the bulk and was found to be 254°C at the bottom of the sample as the heat distributed into the bulk of the Si_3N_4 engineering ceramic.

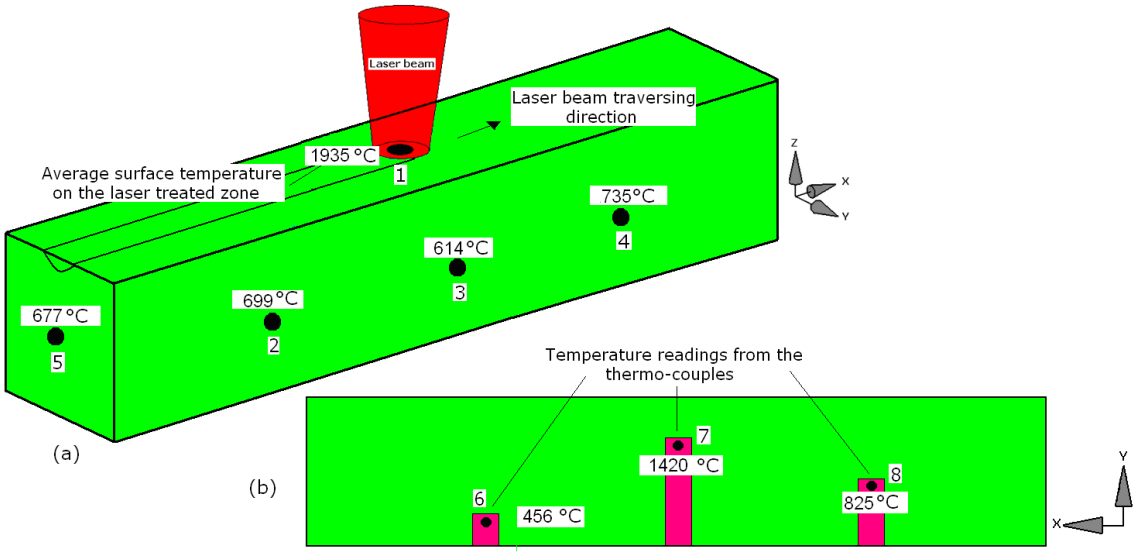

Figure 7.39 Schematic diagrams of the surface temperature reading in (a) and (b) the bulk temperature during CO_2 laser surface treatment of the Si_3N_4 engineering ceramic.

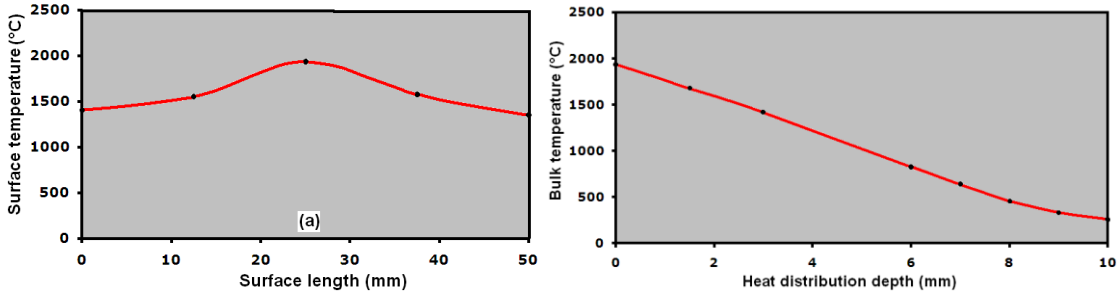

(a) **(b)**

Figure 7.40 Experimental temperature distributions over the surface length in (a) and (b) the temperature distribution through the bulk of the CO_2 laser surface treatment of the Si_3N_4 engineering ceramic.

7.4.4.2 FEM temperature reading

The heat distribution of the CO_2 laser on the surface of the Si_3N_4 in position 1 is presented in the FEM illustrated in Figure 7.41(a) and (b) for the surface and through the cross-section through the bulk. The maximum temperature found on the surface was 2140°C. This is also presented by the graph in Figure 7.42 (a) and (b) where it can be seen that the surface temperature is at maximum, where the interaction of the Si_3N_4 surface with the CO_2 laser was taking place. During this time, the temperature begins to lower by moving away from the CO_2 laser-Si_3N_4 interaction zone. Comparing the FEM with the experimental model, it is found that the FEM was just over 10% higher.

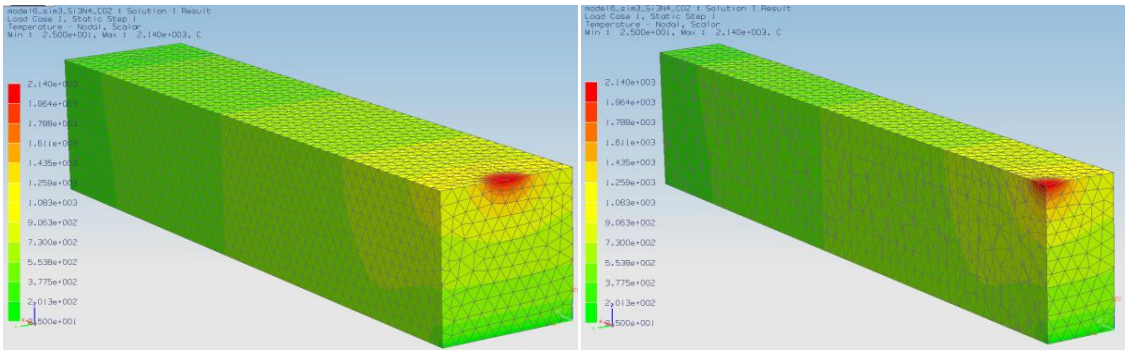

(a) **(b)**

Figure 7.41 FEM of the heat distribution of the CO_2 laser focused at 0mm from the edge (position 1) of the Si_3N_4 ceramic (start of the laser treatment) in (a) and (b); the cross-sectional view.

The graph in Figure 7.42(a) and (b) illustrated the temperature distribution obtained on the surface and the bulk of the Si_3N_4 ceramic. The surface temperature curve for the start of the CO_2 laser treatment showed that the temperature during the CO_2 laser surface interaction near enough to the edge of the sample was about 2140°C whilst, the temperature on other parts of the surface was lower. A regime where the temperature began to decrease further away from the CO_2 laser interaction zone was again as shown in the temperature map in the FEM (see Figure 7.41 and Figure 7.42(b)). Similar results in the bulk of the ceramic were also found, as the temperature was reduced from being the highest at the surface but declined through the bulk.

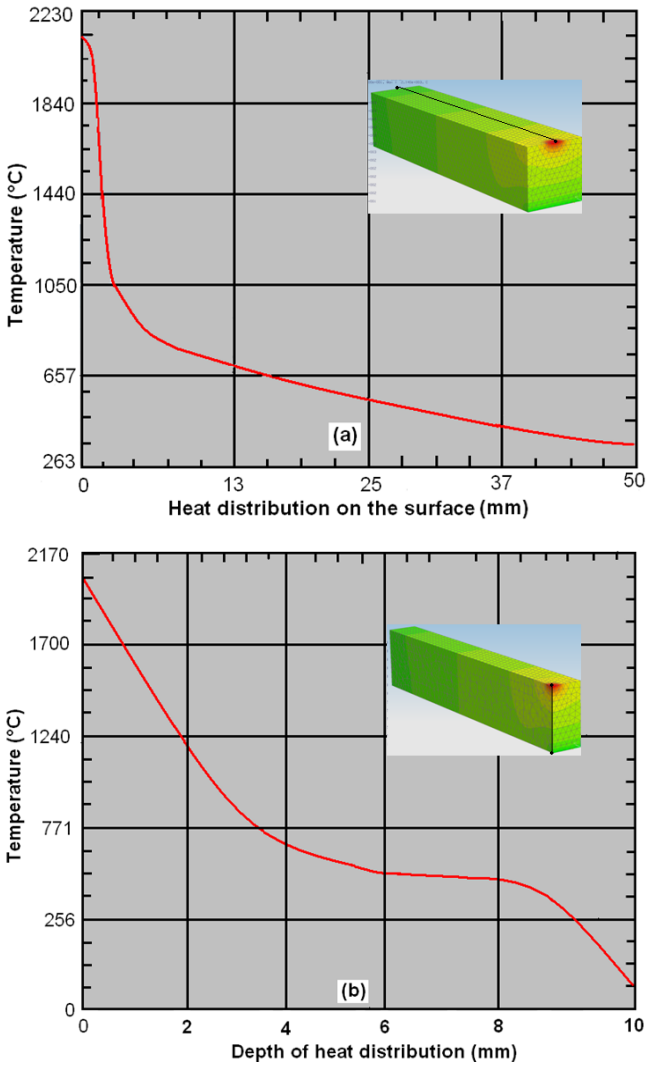

Figure 7.42 Temperature curves from the FEM of the initial stage at 0mm from the edge (position 1) of the CO_2 laser irradiation of the Si_3N_4 ceramic for (a) the heat distributed over the length of the sample and (b) the heat distribution through the depth of the sample.

In position 2 as demonstrated in Figure 7.43(a-c), the temperature illustrated by the model was somewhat higher to that of the FEM of position 1. The temperatures were higher in position 1 as opposed to position 2 due to the fact that more surface area was available in position 2 for the CO_2 laser to distribute the heat more equally. The maximum temperature found on the surface at this position was 2167°C. This in comparison to the experimental model was 12% higher. The bulk temperature within this position is presented in Figure 7.43(b) and (c) and Figure 7.44(b). The temperature was found to be about 2167°C and had gradually decreased to 1410°C at 5mm into the bulk and then reduced to about 1355°C at 10mm at the bottom of the surface.

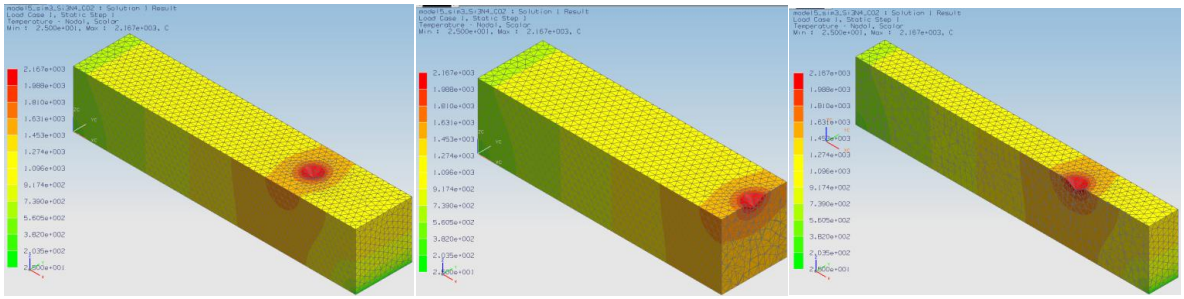

(a) **(b)** **(c)**

Figure 7.43 FEM of the heat distribution of the CO_2 laser focused at 12.5mm from the edge (Position 2) of the Si_3N_4 ceramic in (a) and the cross-sectional view in (b) and (c).

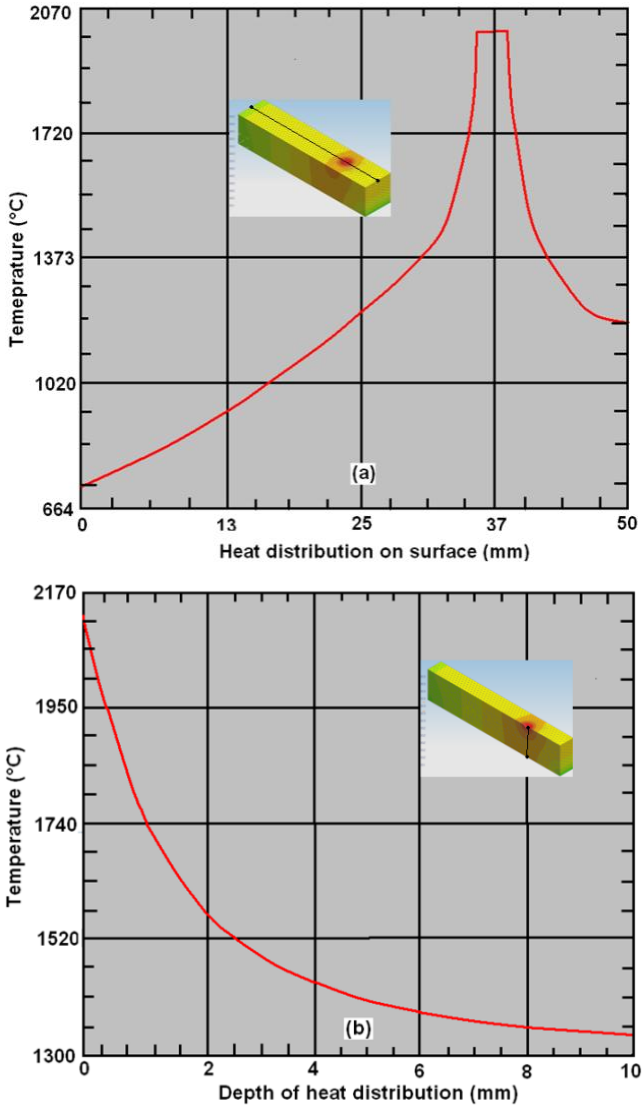

Figure 7.44 Temperature curves from the FEM of the CO_2 laser irradiation at 25mm from the edge (position 3) of the Si_3N_4 ceramic for (a) the heat distributed over the length of the sample and (b) the heat distribution through the depth of the sample.

The FEM for the CO_2 laser surface treatment for position 3 in the centre of the sample at 25mm from the edge is presented in Figure 7.45. The FEM produced a temperature of 2071°C as one can see

from Figure 7.45. As mentioned previously the sample according to its dimensional size is at maximum thermal equilibrium. This means that the heat is equally distributed on all sides of the sample as the CO_2 laser was focused on the centre. Figure 7.45(b) and (c) as well as Figure 7.46(b) illustrated the bulk temperature within the same sample. The temperature within the bulk was found to be 1375°C at 5mm depth and 1307°C at the bottom of the sample at 10mm depth. This was about 7.5% higher than that of the experimental model. The FEM produced for the position 1, 2 and 3 has demonstrated the temperature map of the first half of the samples (at 1.5mm, 12.5mm and 25mm from the edge). The temperature map would be identical on the other half of the sample as the laser beam traverse further to surface of the whole 50mm long ceramic. Figure 7.46(a) showed the balanced distribution in the surface temperature during the CO_2 laser beam exhibiting on the centre of the ZrO_2 as the sample is under thermal equilibrium for a period of 1.66 sec. Figure 7.46(b) illustrated the gradual decline in the temperature as the heat was distributed from the surface to the bulk.

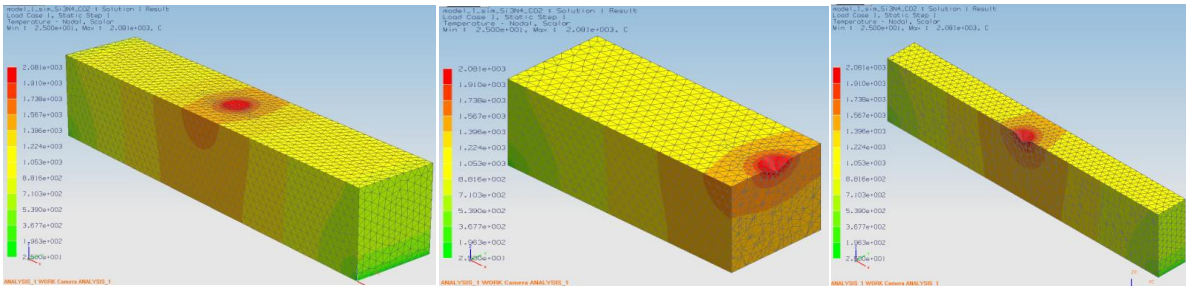

(a) **(b)** **(c)**

Figure 7.45 FEM of the heat distribution of the CO_2 laser beam focused in the centre (position 3) of the Si_3N_4 ceramic in (a) and in the cross-section in (b) and (c).

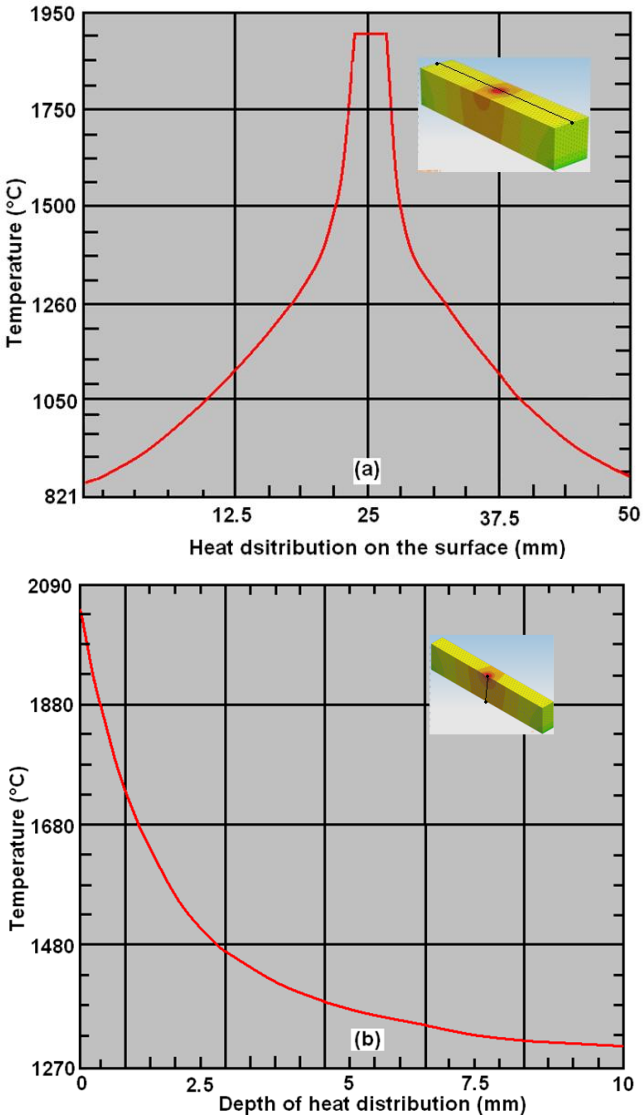

Figure 7.46 Temperature curves from the FEM of the CO_2 laser irradiation at 25mm from the edge (position 3) of the Si_3N_4 ceramic for (a) the heat distributed over the length of the sample and (b) the heat distribution through the depth of the sample.

7.4.4.3 Comparison of the experimental and the FEM

The surface temperature found on the experimental model at the CO_2 laser-Si_3N_4 interface was 1935°C. This in comparison to the FEM was about 7.5% lower which is generally acceptable. The surface temperatures difference between the two models on the outer skin of the sample was about 5% for the in position 1 in Figure 7.7, just under 14% for position 2, and 5.5% for position 4.

The bulk temperatures on the model were found to be +4.5% higher for the FEM at 3mm, but was up to 27.5% for the position at 6mm beneath the surface. At 7mm below the surface the difference in the temperature was over 50%. This indicated that the surface temperatures and bulk temperatures closer to the surface were in good match but deeper into the bulk. Despite the temperatures being within the expectable range more closer to the surface, the FEM however, does, have the tendency to generate higher temperatures found by the experimental values. This indicated that the way in which

the CO_2 laser is induced into the Si_3N_4 ceramic is somewhat different to what is expected by the FEM. Consideration is also given to factors such heat loss through the 3mm holes drilled into the sample, lack of contact of the thermocouples to the material surface and the thermocouple response time. These are not directly considered by the FEM so the results will be higher in most cases. However, the CO_2 laser wavelength is surely having an effect on the Si_3N_4 ceramic which is not in consideration by the FEM.

7.4.4.4 Development of extended parameters

Figure 7.47 shows the multi-factor laser parameters which were determined from the FEM. Parameters such as traverse speed; power density; depth of heat distribution; temperature and time, in relationship to one another.

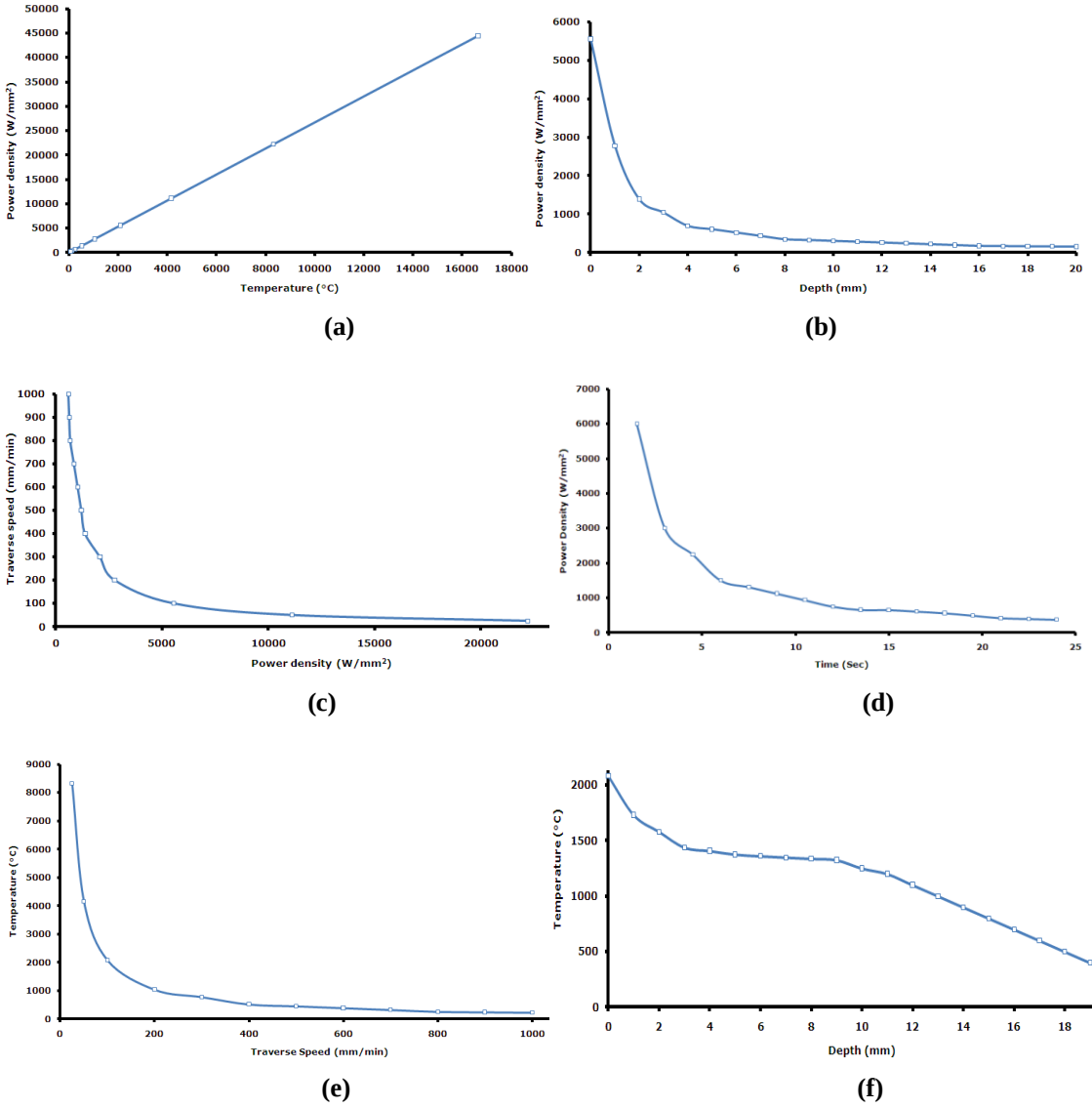

Figure 7.47 Parameters obtained from the FEM showing the coloration of various factors with one another: (a) power density *versus* temperature, (b) depth *versus* power density, (c) power density *versus* traverse speed, (d) power density *versus* time, (e) traverse speed *versus* temperature and (f) depth *versus* temperature.

7.4.5 Comparison of Temperatures between the CO_2 and the Fibre Laser Surface Treatment of the ZrO_2 Engineering Ceramics.

Table 7.2 illustrates the temperatures found by the CO_2 and fibre laser surface treatment of the ZrO_2 engineering ceramics from the FEM and the experimental model. It can be seen that there is a considerable difference in the temperatures obtained by the two lasers on the surface and the bulk of the ZrO_2. The temperature over the surface of the CO_2 laser irradiated sample was 1752°C. This in comparison to the fibre laser was up to 42% lower as the average temperature after 5 passes was found for the fibre laser irradiated sample of the ZrO_2 to be 2472°C. The surface temperatures produced by the FEM for the CO_2 and the fibre laser irradiated sample were 1747°C and 2577°C. A 40% increase in the temperatures generated by the fibre laser irradiated surface.

The bulk temperature by the experimental model was also higher for the fibre laser irradiated surface in comparison to the CO_2 laser irradiated surface and was 50% lower as the average temperature at 5mm below the surface of the CO_2 laser irradiated sample was 700°C and the fibre laser irradiated sample being 1600°C. This was also similar for the bulk temperatures found within the FEM as the readings were measured to be 1230°C for the CO_2 laser and 1951°C for the fibre laser. The bulk temperatures for the FEM were 59% higher for the fibre laser in comparison to the temperatures accrued by the CO_2 laser irradiation.

As one can see that the temperature of the fibre laser irradiation in comparison to that of the CO_2 laser was somewhat higher in both areas (the surface and the bulk) of the ZrO_2 ceramic for both the FEM and the experimental model. This was due to the influence of several factors which caused the difference in the temperatures generated during the laser-ZrO_2 interaction. Those are namely:

- The difference in the threshold for the ZrO_2 whilst processing with the two laser types. As presented in Chapter 4. The power density induced into the ZrO_2 for the CO_2 laser was considerably lower than that of the fibre laser as the ZrO_2 was cracking at considerably lower powers during CO_2 laser-ZrO_2 interaction in comparison to that of the fibre laser irradiation. Moreover, the traverse speed was also increased during the CO_2 laser surface treatment in comparison to the fibre laser surface treatment. This in turn had influenced the surface temperatures. Although, the FEM did not take in consideration of the traverse speed, the experimental model yet reflected this factor which showed considerably low temperatures in comparison.

- Furthermore, the bulk temperature for the CO_2 laser irradiated surface was also lower in comparison to that of the fibre laser. From this it was indicative that the absorption of the CO_2 laser wavelength with the ZrO_2 ceramic was somewhat lower in comparison to that of the fibre laser irradiation. However, the CO_2 laser interaction with the ZrO_2 on the surface was remarkably noticed by the topographical analysis. Though, the influence of the CO_2 laser was

limited to the local surface and the sub-surface only, whereas the fibre laser was absorbed to a sufficient level of depth. In comparison, the NIR of the fibre laser was more absorbent through the ZrO_2. This resulted to recording high processing temperatures. Due to this there was also a significant difference within the hardness of the ZrO_2 as previously discussed in Chapter 6, Section 6.6.9.1.

Table 7.2 Comparison of the surface and the bulk temperature obtained by the experimental investigation and the FEM of the CO_2 and the fibre laser surface treatment of the Si_3N_4 and ZrO_2 engineering ceramics.

Laser Types	Experimental Model				FEM			
	Surface temperature (˚C)		Bulk temperature (˚C) at 5mm below surface		Surface temperature (˚C)		Bulk temperature (˚C) at 5mm below surface	
	Si_3N_4	ZrO_2	Si_3N_4	ZrO_2	Si_3N_4	ZrO_2	Si_3N_4	ZrO_2
CO_2 Laser	1935	1752	1100	700	2071	1747	1375	1230
Fibre Laser	2269	2473	1350	1600	2277	2577	1366	1951

7.4.6 Comparison of CO_2 Laser with the Fibre Laser Surface Treatment of the Si_3N_4 Engineering Ceramic.

Comparison of the temperatures of CO_2 and the fibre laser surface treatment of the Si_3N_4 engineering ceramics are also presented in Table 7.2 for both the FEM and the experimental model. The CO_2 laser irradiated sample produced 1935˚C. This was 17% lower in comparison to the fibre laser irradiated sample as the average temperature after 5 passes was found to be 2269˚C on the fibre laser irradiated surface. The average surface temperature configured by the FEM of the CO_2 laser was 2071˚C and 2277˚C for the fibre laser irradiated sample which was a difference of just over 10 %.

The bulk temperature by the experimental model at 5mm below the surface was 1100˚C for the CO_2 laser irradiated sample of the Si_3N_4. This in comparison to the fibre laser irradiated sample was 1350˚C, which is a difference of 23%. The FEM bulk temperature was 1375˚C for the CO_2 laser and 1366˚C for the fibre laser irradiated sample of the Si_3N_4. Although, in this case, the temperatures were almost identical but the pattern of the fibre laser irradiated temperature being higher still continued as 0.5% difference was found.

Similar differences in the temperature readings were also found with the CO_2 and fibre laser surface treatment of the Si_3N_4 ceramics to that of the CO_2 and fibre laser surface treated ZrO_2 ceramics. This was because the temperatures found by the fibre laser irradiation were considerably higher on the surface and the bulk of the Si_3N_4. This was again due to the fact that the absorption of the NIR wavelength of the fibre laser was better in comparison to that of the MIR wavelength of the CO_2 laser. This intrinsically generated bigger interaction zone at the surface in comparison to the fibre

laser surface treatment, but was not induced further into the bulk as was the case with the fibre laser irradiation. This can be further justified by the fact that the bulk temperatures for the fibre laser surface treatment were higher than that of the CO_2 laser surface treatment. As well as the fact that the thicker SiO_2 layer produced by the CO_2 laser irradiation in comparison to that of the fibre laser (as previously shown in Chapter 5 and also discussed in Chapter 6) produced higher K_{1c} values. This was due to the result of the softer surface being generated on the Si_3N_4 ceramic because of the thicker oxide layer being produced by the CO_2 laser irradiation. However, it can be said that the absorption by both the Si_3N_4 and the ZrO_2 engineering ceramics of the NIR wavelength of the fibre laser is higher in comparison to the absorption of the MIR wavelength of the CO_2 laser. Yet the MIR wavelength of the CO_2 laser is rather suitable for mainly the surface treatment of the oxide ceramics which does not require deep penetration. For the nitride ceramics, the temperature induced are fairly high in comparison to ZrO_2 ceramics. This indicates that the CO_2 laser wavelength is further absorbed into nitride ceramics in comparison to the oxide ceramics but surface interaction of the CO_2 laser wavelength is also considerable.

7.5 Summary

The following conclusions are drawn from conducting an experimental and a thermal FEM of the fibre and the CO_2 laser surface treatment of the ZrO_2 and Si_3N_4 engineering ceramics:

- From both of the surface and the bulk temperature measurements, the distribution of the temperature over the length and the depth of the two engineering ceramics treated by the fibre and the CO_2 laser was also presented and the FEM was verified with an overall error of +10%.

- This is consistent over estimate of temperature by the FEM which may have resulted due to: (a) heat loss through the 3mm holes drilled into the sample; (b) lack of contact of the thermocouples to the material surface and (c) the thermocouple response time. Such aspects were not taken in account by the FEM and so the FEM results will always be higher.

- Furthermore, the FEM expands to demonstrate the relationship between the processing temperatures, time and the depth of the heat distribution, with parameters such as traverse speed and power density. These would correlate with one another to reveal the extended range of parameter window during the fibre and the CO_2 laser surface treatment of the ZrO_2 and the Si_3N_4 engineering ceramics.

- The thermal analysis of the CO_2 and the fibre laser of the ZrO_2 engineering ceramics showed that there was a considerable amount of temperature difference between the CO_2 and the fibre laser surface treatment with the FEM as well as the experimental temperature readings within both engineering ceramics.

- The bulk temperature by the experimental model was also higher for the fibre laser surface treatment in comparison to the CO_2 laser surface treatment and was 50% lower as the average temperature at 5mm below the surface of the CO_2 laser irradiated sample was 800°C and the fibre laser irradiated sample being 1600°C. The bulk temperatures for the FEM were 59% higher for the fibre laser in comparison to the temperatures found by the CO_2 laser irradiation.

- The temperature of the fibre laser irradiation in comparison to that of the CO_2 laser is somewhat higher on the surface and the bulk of the ZrO_2 ceramic for both the FEM and the experimental model. This was due to the difference in the threshold for the ZrO_2 whilst processing with both the lasers.

- The power density induced into the ZrO_2 for the CO_2 laser was considerably lower than that of the fibre laser as the ZrO_2 was cracking at considerably lower powers during the CO_2 laser-interaction in comparison to that of the fibre laser.

- Comparison of the temperatures distributions of the CO_2 and the fibre laser surface treatment of the Si_3N_4 for both the FEM and the experimental model showed that the CO_2 laser irradiated sample was 17% lower in comparison to the fibre laser irradiated sample. The average surface temperature configured by the FEM for the CO_2 laser was 2081°C and 2287°C for the fibre laser irradiated sample, producing a difference of just over 10%.

- The surface temperature reading between the CO_2 and fibre laser irradiation of the Si_3N_4 showed that the fibre laser irradiation was considerably higher on the surface and through the cross-section. This was because of the fact that the NIR wavelength absorption of the fibre laser was better in comparison to that of the MIR wavelength of the CO_2 laser. This generated a bigger interaction zone at the surface in comparison to the fibre laser surface treatment but was not induced further into the bulk as was the case with the fibre laser irradiation.

- Furthermore, the bulk temperatures for the fibre laser surface treatment were higher than that of the CO_2 laser. However, it can be said that the absorption of the NIR wavelength by both the engineering ceramics was higher in comparison to the absorption of the MIR wavelength of the CO_2 laser. Yet the MIR wavelength was rather suitable for mainly surface processing of oxide ceramic which does not require deep penetration as previously stated.

- For the nitride ceramic, the temperatures induced are fairly high in comparison to oxide ceramic. This indicated that the MIR wavelength was further absorbed into nitride ceramic in comparison to the oxide ceramics, but surface interaction of the MIR wavelength (CO_2 laser) was also still considerable.

- Phase transformation of the ZrO_2 from the M state to a mixture of T+C during fibre laser irradiation and from T+C to T followed by the M state during solidification had occurred. The TG-DSC analysis for the fibre laser irradiated Si_3N_4 engineering ceramics showed that the fibre laser surface treatment generally resulted in a phase transformation of the Si_3N_4 from α-phase to β-phase. The transformation began at 1300°C and ended at round 1400°C, where a mixture of α-phase and β-phase ($\alpha \rightarrow \alpha + \beta$) was found. Then transformation of $\alpha+\beta$ occurred at about 1400°C and full transformation from $\alpha+\beta \rightarrow \beta$-phase occurred at 1450°C.

PART 4

NEW PERSPECTIVES ON LASER BEAM-MATERIAL INTERACTION

CHAPTER 8
Influence of Laser-Beam Brightness During Surface Treatment of ZrO_2 Engineering Ceramic

Effects of the laser parameter brightness or radiance of the fibre and the Nd:YAG laser surface treatment of the ZrO_2 engineering ceramic were investigated. This has been done because the distinctive surface modifications, K_{1c} and the differences in processing temperatures that were found in the previous Chapters after fibre laser surface treatment and when compared to the CO_2 laser surface treatment. By applying identical parameters, except for wavelength (which in this case was similar between the Nd:YAG and the fibre laser), the influence of brightness exhibited by the two lasers was investigated in respect to the change in the hardness, dimensional size of the laser irradiated zones and the microstructure of the ZrO_2 engineering ceramic.

8.1 Introduction

Brightness is a very important characteristic of a light source. It is defined as the amount of light delivered from a surface per unit of area [228-229]. The term brightness is mainly used when the visual quality of a light source in relation to contrast and glare is being expressed. However, brightness in turn does not only relate to a light source such as a lamp or a candle as light can be found through reflection and transmission also. For instance, a bright surface will have high reflections and a dull surface will have low reflection [229]. The use of the term brightness in some way or another is a comparison of two light sources which are judged by the human eye as it creates variation in the intensities on the surface of the retina [230].

Brightness in general terms is defined as candles per square meter of light being emitted on a surface and is classified as “luminance” or “radiance”, depending on its application [229, 231]. When the brightness is mentioned as a photometric quantity the term luminance is usually used. However, the term radiance is mentioned when describing radiometric quantity [231]. Luminance can be expressed as the direction of light emission. This means that the brightness of an object is dependent on the direction or the angle which one can look from [228]. Luminance is also the intensity of light that is emitted from the surface whereas the intensity of light that is directed on a surface is classified as illuminance which is the opposite of luminance. In some instance, radiometric term radiance of a light source is used in literatures for the sake of simplicity, particularly, when expressing laser beam brightness, which is the power per unit area per solid angle of divergence [229].

Laser beams in comparison to other light sources comprise of high brightness energy since a laser light exhibits very high power levels in a narrow beam or a spot size [230]. Hence, the spot size which the laser beam can be focused to is very important [232]. Brightness of lasers is an unchangeable property. This means that the brightness is not affected by focusing or defocusing a laser beam. This is made clear by a primary law of optics which states that the brightness of a light source is an unchangeable quantity [229, 233]. The brightness of a Gaussian beam does not change as it propagates because the brightness is inversely proportional to the solid angle. The solid angle produced by a laser beam is proportional to the square of the divergence angle θ. The smaller the divergence the higher the brightness of the laser. High brightness beams, however, has the most idealised beam profile and tend to have a high beam quality factor.

Laser power density and laser brightness has close relationship due to their parameters being somewhat common. The laser power is input power per spot size. This is multiplied by the Gaussian beam configuration value, whereas the brightness is the input power per unit area per solid angle (beam divergence) [233-237]. Brightness is important in laser processing applications since the intensity obtained within a focusing area within a lens is proportional to the brightness of the beam. High brightness laser processing allows fine spot size of the beam and allows longer focusing distance so that flexibility is further achieved with material processing as more distance is covered during laser processing. This is particularly offered by the fibre laser and are both used for the investigation herein as further presented.

High brightness laser sources such as a fibre laser or a HPDL produces high temperature during material interaction [235, 238]. High brightness laser source in particular – a fibre laser also offer a longer depth of field (long focal length), small spot sizes and beam quality as well as stability of the laser beam during execution. The brightness of a laser is more effective in comparison to the laser power intensity. This is because by achieving high brightness would generate high processing temperatures [238]. This is particularly important for ceramic processing in order to achieve surface melting, to cover the surface cracks and to achieve localized modification and phase transformations within the ceramic. The use of high brightness laser for material processing is also advantageous due to its potential of achieving low cost per wattage output [231].

Measuring the brightness of a light source is a difficult practice and requires a complex set-up and procedures to follow. This is specially so for measuring the brightness of an industrial laser due to the complexity of the machines and the experimental set-up required. The correct measuring technique for brightness of a laser beam is strategically documented in the British standards [239-241]. Forbes *et al.* [242] modelled the brightness from a cross porro-prism resonators and showed that the brightness is significantly influenced by the angle between the two prism edges. At higher prism angles the brightness was increased as fewer petals of the beam footprint were to be seen.

With decreasing angles and increasing the number of petals of the beam footprint showed decreasing the prism angles and inherently a reduction in the brightness.

The use of high brightness emitting lasers have made a way forward within the laser aided material processing industry in the recent years by several workers. Wallace [243] described the use of high brightness beam diode lasers which produces high efficiencies and lower operating costs. Wenzel *et al.* [244] modelled features of high brightness semiconductor lasers and showed that high reliability and efficiency can be obtained from applying high brightness laser beam despite having low beam quality. Brown and Frye [245] also showed the use of high brightness cutting and drilling of aerospace materials by using a Nd:YAG laser. The results showed improved cutting and also achieved shallow angle holes. Li *et al.* [246] investigated the reliability and efficiency of high brightness lasers of 940 nm wavelength and demonstrated the maximum power conversion efficiency of 60% at an output power of 72 W with very good beam quality. Treusch *et al.* [247] studied the use of high-brightness semiconductor lasers for material processing and revealed that collimation lenses can be used to increase the brightness of the laser by a factor of two as well as the wavelength and polarization coupling also contributing to the increased brightness. Leibreich and Treusch [248] followed a similar investigation on improving the brightness of a semiconductor diode laser by using stacking laser bars (beams) comprising of different wavelength to increase the output power as well as the brightness. Their results briefly described that the brightness can be enhanced by two without any changes to the beam quality factor (M^2). This in turn would improve and open a new avenue for the laser materials processing sector. Other investigation by Hanna [249, 250] showed that an increase in brightness can be obtained by altering the transverse mode. Variation in the transverse mode leads to a change in the beam divergence and alters the brightness of the laser source [249].

Val *et al.* [251] investigated the effects of laser cladding of flat plates of AISI 304 stainless steel and Co-based super-alloy powder as a coating material by applying a Nd:YAG laser and a Yb: YAG fibre laser. The results from the fibre laser in comparison to that of the Nd:YAG showed more versatility with regard to the parameter window as well as enlarged clad track, and deeper penetration. However, similar hardness was obtained from applying both lasers. Val *et al.* further concluded that this effect had occurred due to the better beam quality and also due to the high brightness on offer by the fibre laser. This is ideal for producing wider clad tracks and a Nd:YAG laser is ideal for producing narrower clad tracks. The work of Val *et al.* closely relates to the work in this study as the effects of brightness between an Nd:YAG laser and a fibre laser are investigated but by using engineering ceramics (in particular ZrO_2).

Although, several investigations have been published in the field of improving the laser brightness, there is still limited work that has been published with the use of a fibre laser to process materials.

This is particularly so for engineering ceramics as to date, no work has been conducted hitherto with employing the fibre laser to surface treat engineering ceramics. This investigation considers the laser-beam brightness as an influential parameter of laser-ceramic and other material processing in general. Also, the physical effect of high laser-beam brightness during the surface interaction with such materials is detailed. Also, brightness is an important parameter of laser material processing rather than the input power. It is the brightness that is the driving force rather than the power intensity and is very much discarded when it come to laser material processing. Hence, the work in this investigation attempts to introduce the likely effects that could occur by the different brightness of laser sources which have the same processing parameters. Physical differences in the effects of the fibre laser and the Nd:YAG laser brightness up on surface treatment of the ZrO_2 engineering ceramic in particular are discussed after the laser-ceramic surface interaction has taken place. The fibre and Nd:YAG lasers were selected as they both have similar operational wavelength. Therefore, would serve to provide a better comparison than the CO_2 laser. Nevertheless, the brightness of the CO_2 laser beam is not disregarded in this Chapter, since the content of this thesis has mainly focused on the effects of the CO_2 and the fibre laser surface treatment.

8.2 Background of Laser-Beam Brightness Calculation

Theoretical brightness is calculated by means of simplified equations described in several literatures [229-233]:

$$\mathbf{Br} = \frac{\mathbf{P_{out}}}{\mathbf{A\Omega}} \tag{8.1}$$

Where P_{out} is the power over the surface area and $A\Omega$ is the solid angle of divergence of the beam. Brightness is inversely equal to the solid angle of divergence. The solid angle of divergence created by a laser beam is equal to the square of the divergence angle θ as shown in Figure 8.1. The solid angle of a Gaussian beam equates to:

$$\mathbf{\Omega = \pi\, \theta^2 = \lambda^2 / \pi\, w^2{}_0} \tag{8.2}$$

and is inversely proportional to ($\pi\, w^2{}_0$). Where λ is the wavelength of the particular laser beam and w_0 is the beam radius at the beam waist or divergence. The solid angle of divergence is usually small for laser beams in comparison to other light sources due to their high directionality. This in turn generates high brightness beams.

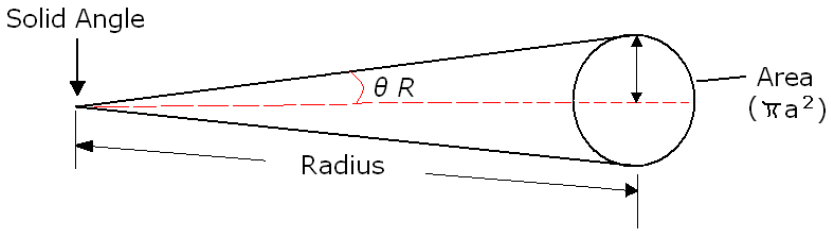

Figure 8.1 A schematic diagram illustrating the solid angle of divergence of a laser beam.

For a circular Gaussian laser beam; the beam propagation ratio is illustrated in Equation 8.3. Where M^2_y and M^2_x are the beam propagation ratio's in the x-and the y-direction. Furthermore, brightness can be derived in Equation 8.4 which comprises of feature in Equation 8.1 to 8.3:

$$\mathbf{M^4 = M^2_y \, . \, M^2_x} \tag{8.3}$$

$$\mathbf{Br} = \frac{\mathbf{P_{out}}}{\mathbf{M^4 \, x \, \lambda^2}} \tag{8.4}$$

The solid angle presented in Figure 8.1 is a unique dimension for all laser beams with different beam profile and Gaussian configuration. This solid angle is the divergence of the beam after being focused by the optics (focusing lens). The angle of beam divergence the calculated brightness values of the fibre, Nd:YAG and the CO_2 lasers are presented in Table 8.1, along with other beam characteristics and properties as a comparison.

Table 8.1 Properties of the fibre, the Nd:YAG and the CO_2 laser used for this investigation.

Laser Type	Beam divergence (m/rad)	Brightness ($W/cm^2 / sr^{-1}$)	Beam quality factor (M^2)	Gaussian beam shape		Gaussian beam mode
				Cross-sectional view	Plan view	
Nd:YAG laser	5.5	609.50	6.7	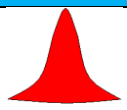		TEM_{00}
Fibre laser	0.2	1755.37	1.2	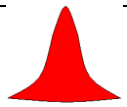		TEM_{00}
CO_2 laser	5	1471.57	1.3	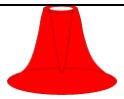		TEM_{01}

7.2 Experimentation and Analysis

8.3.1 Experimental Material

The material used for the experimentation was CIPed ZrO_2 engineering ceramic which was previously described in Chapter 4 (see Section 4.1, Figure 4.1).

8.3.2 Nd:YAG Laser Surface Treatment

A 65 W Nd:YAG laser (HK, SL902; Hahn & Kolb Ltd.) emitting a CW mode beam at a wavelength of 1.064µm was used in this work (see Figure 8.2). The focal position was kept to 210mm above the work-piece to obtain a 2.2mm spot size. The processing gases used was N_2 at a flow rate of 25 l/min. Programming of the laser was conducted by using a Hahn & Kolb, U3 CAD software. This integrated with the laser system as a 50 mm line was programmed by using NC programming as a potential beam path. To obtain an operating window, trials were conducted at the fixed spot size of 2.2mm and 65W by varying the speed between 4 and 100 mm/sec. this was because 65W was the maximum power and a 2.2mm beam was the largest spot size which the Nd:YAG laser could exhibit. From these trials, it was found that 10mm/sec at 65W were the ideal laser parameter to use in terms of achieving a sufficient footprint on the material to conduct further analysis.

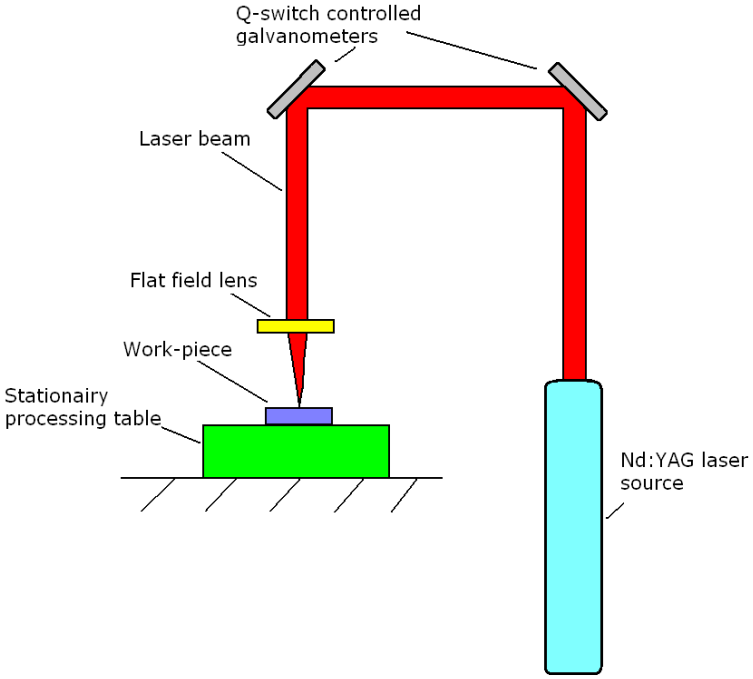

Figure 8.2 A Schematic diagram showing the experimental set-up of the Nd:YAG laser surface treatment of the ZrO_2 engineering ceramic.

8.3.3 Fibre Laser Surface Treatment

A 200W fibre laser (SPI-200c-002; SPI, Ltd.) emitting a CW mode beam at a wavelength of 1.075µm was used in this work as previously shown in the work of earlier Chapters. The focal position was kept to 20mm above the work-piece to obtain a 2.2mm spot size. The processing gases used were N_2 supplied at a flow rate of 25 l/min. Programming of the laser was conducted by using an SPI software which integrated with the laser system. A 50mm line was also programmed by using NC programming as a potential beam path, which was transferred by .dxf file. The nozzle indicated in Figure 4.2 (see Chapter 4, Section 4.3) was removed for all experiments. To obtain an operating window, trials were conducted at the fixed spot size of 2.2mm 65W and at a traverse speed between

10mm/sec so that an equal comparative study of the effects of the Nd:YAG laser and the fibre laser can be performed.

8.3.4 Hardness Measurement

Vickers indentation method was adopted for measuring the hardness of the laser irradiated surfaces of the ZrO_2 engineering ceramics by applying an indentation load of 2.5kg (24.51 N). The methodology has been described in the previous Chapters (see Chapter 5, Section 5.2.3 and Chapter 6, Figure 6.2).

8.3.5 Sample Preparation and Etching

The as-received and the laser irradiated samples were mounted in epoxy resin (Epofix, Struers Ltd.) and were finely polished by using a semi-automatic polishing machine (TegraPol-25, Struers Ltd.) aided by using a successively finer diamond polishing discs. The final polishing procedure was conducted by using a 0.04µm colloidal silica suspension (OP-S; Struers Ltd.). The samples were then removed from the epoxy resin. Furthermore, the samples were etched by using a thermal etching technique in order to expose the grains, to determine the grain size and to investigate the microstructure of the ZrO_2 engineering ceramic. Temperature of 1300°C was applied in a furnace to samples of the as-received, fibre and Nd:YAG laser irradiated ZrO_2 engineering ceramic. The samples were held at 1300°C for 5min with a heating/cooling rate of 10°C /min.

8.3.6 Microscopic Imaging

The Vickers indentation footprint of the as-received, fibre and the Nd:YAG laser irradiated zones were all observed by employing the optical microscopy (Optishot; Nikon Ltd.). Further analysis was conducted by employing a FEGSEM (Ultra-high-resolution, 1530VP; Leo Ltd.). This investigated the microstructure of the laser untreated surface, Nd:YAG and fibre laser irradiated surfaces of the ZrO_2 engineering ceramics.

7.3 Results and Discussion

8.4.1 Change in Hardness

The average hardness was measured for the as-received, fibre and Nd:YAG laser irradiated surfaces of the ZrO_2 engineering ceramic. The average indentation size, hardness readings along with its STDEV and the ranges in the values are presented in Table 8.2. The average indentation size for the as-received surface was 61µm with an average hardness of 1225 HV (12.01 GPa). This in comparison to the Nd:YAG laser irradiated surface was somewhat smaller and indicated that the Nd:YAG laser irradiated surface had become more ductile and softer. The average diamond indentation size of the Nd:YAG laser irradiated surface was 79µm with an average hardness of 747 HV (7.32 GPa). A 36% reduction in the hardness and up to 29.5% increase in the diamond indentation size was obtained by the Nd:YAG laser irradiated surface.

However, when comparing the results of the Nd:YAG laser irradiated surface with that of the fibre laser; it was found that the change in hardness was also sufficiently large but the fibre laser irradiated surface comprised of much higher hardness in comparison to that of the Nd:YAG laser. Sufficiently large surface cracking with the fibre laser surface treatment sample was also found. This indicated that the surface was much harder from the result of reaching high temperature which would have caused a steeper thermal gradient and rapid cooling effect to take place in comparison to the Nd:YAG laser surface treatment. The average size of the diamond indentation was found to be 63µm. This in comparison to the as-received surface was just over 3% larger but 22% smaller in comparison to that of the Nd:YAG laser irradiated surface. The average hardness of the fibre laser irradiated surface was 1179 HV (11.56 GPa). This was just under 4% lower than that of the as-received surface and 32% higher than the Nd:YAG laser irradiated surface. Figure 8.3 to 8.5 illustrates an example of the diamond indentation for the as-received surface (see Figure 8.3). The Nd:YAG laser irradiated surface is shown in Figure 8.4 and the fibre laser irradiated surface is shown in Figure 8.5.

Table 8.2 Hardness values found for the as-received, fibre and Nd:YAG laser irradiated surfaces of the ZrO_2 engineering ceramic.

Type of laser	Average indentation size (µm)	Range (µm)	STDEV (µm)	Hardness (HV)		
				Average	Range	STDEV
As-received surface	61	57- 67	0.0312	1225	1002 - 1414	12.01
Nd:YAG laser irradiated surface	79	71-77	0.0055	747	599 - 920	104
Fibre laser irradiated surface	63	59 - 71	0.0043	1179	920 -1332	149

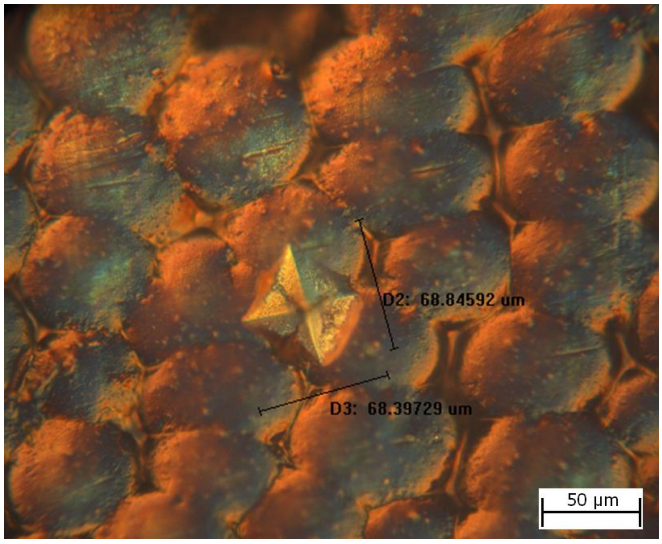

Figure 8.3 Optical image of the diamond indentation produced on the as-received surface indented by a 2.5kg (24.51N) diamond indentation load on the ZrO_2 engineering ceramic.

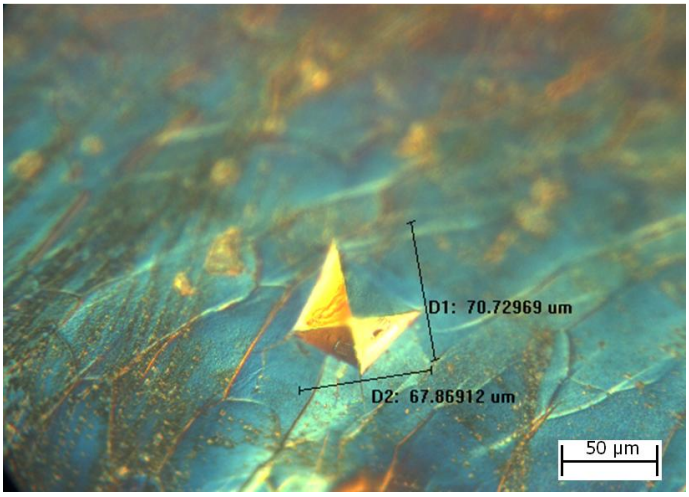

Figure 8.4 Optical images of the diamond indentation produced on the Nd:YAG laser irradiated surface indented by a 2.5kg (24.51N) diamond indentation load on the ZrO_2 engineering ceramic.

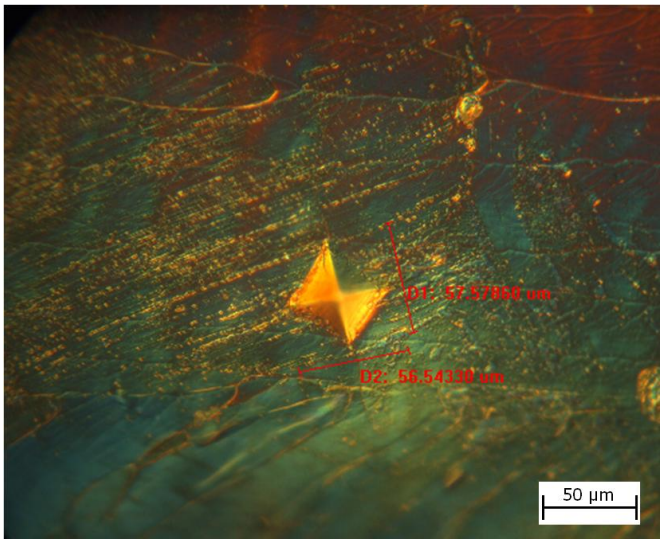

Figure 8.5 Optical images of the diamond indentation produced on the fibre laser irradiated surface indented by a 2.5kg (24.51N) diamond indentation load on the ZrO_2 engineering ceramic.

8.4.2 Change in Size

From the topographical observation of both the Nd:YAG and fibre laser irradiated tracks (footprints); it was found that 32% difference in width was to be seen between the footprint created by the two different lasers. The average width of the Nd:YAG laser irradiated track was 632µm and the average length of the HAZ being 72µm. This in comparison to the track width of the fibre laser was much smaller as presented in the example in Figure 8.6 (a) and (b). The average width of the fibre laser irradiated surface was 737µm. The average width of the HAZ was found to be 79µm. This was 24% higher than that of the Nd:YAG laser irradiated surface.

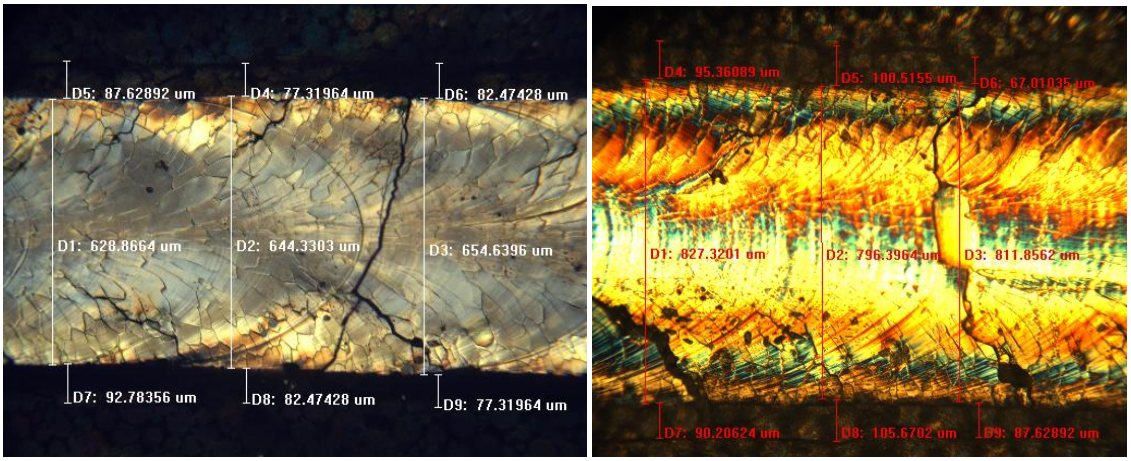

(a) **(b)**

Figure 8.6 Optical images of (a) the width of the Nd:YAG laser irradiated track and (b) the width of the fibre laser irradiated track of the ZrO_2 engineering ceramic.

Furthermore, the optical images in Figure 8.7 presents the cross-sectional view of the ZrO_2 engineering ceramic in (a) the Nd:YAG laser irradiated surface and (b) the of the Nd:YAG laser

irradiated surface with its dimensional sizes, (c) the fibre laser irradiated surface and (d) the dimensional size. It can be seen from the cross-sectional analysis that the fibre laser irradiated surface has produced a larger penetration depth and broader profile in comparison to that of the Nd:YAG laser. In average, the depth of penetration for the fibre laser was 447µm as oppose to the depth of penetration of the Nd:YAG laser being 295µm. This was up to 51.5 % lower. The Nd:YAG laser had produced a partial amorphous glassy zone. This was a mixture of zirconia carbide (see Chapter 5, Section 5.3.2) as can be seen in the image in Figure 8.7(a). This meant that melting did occur with the Nd:YAG laser irradiated surface. However, it was not as remarkable as the fibre laser irradiated surface of the ZrO_2 as the whole cross-section was found to be of the amorphous glassy layer. This intrinsically, indicated that more melting and new formation of the surface layer had occurred with the fibre laser surface treatment despite using the same laser parameters. The increased melting and the glassy layer within the fibre laser irradiated surface had occurred from the difference in temperature between the two lasers as the fibre laser with a higher brightness had created much higher temperature. This characteristically had melted the surface and generated a larger melt pool. The surface and the cross-sectional cracking of the ZrO_2 engineering ceramic particularly after the fibre laser surface treatment compliments the high temperatures generated at the fibre laser-ZrO_2 interaction.

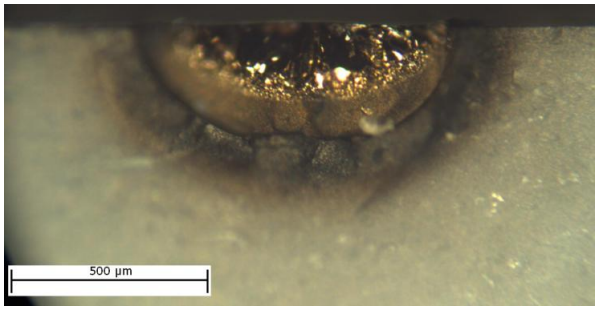

(a)

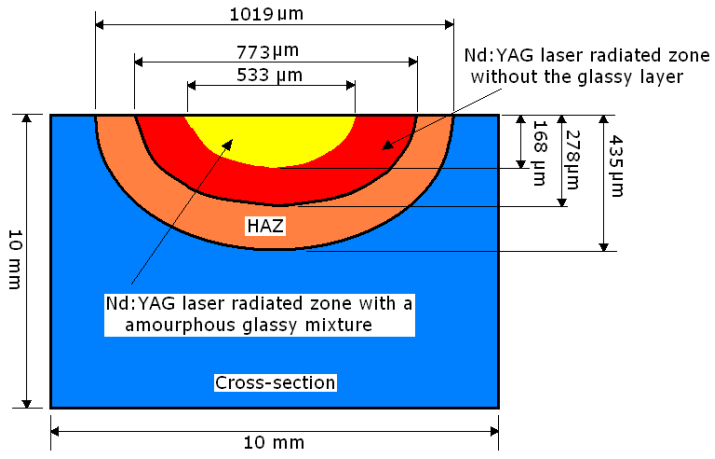

(b)

Figure 8.7 Optical images of the cross-sectional view of (a) the Nd:YAG laser irradiated surface and (b) the schematic diagram the Nd:YAG laser irradiated surface of the ZrO_2 engineering ceramic.

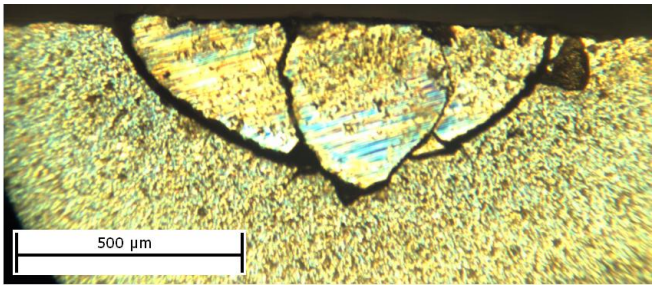

(c)

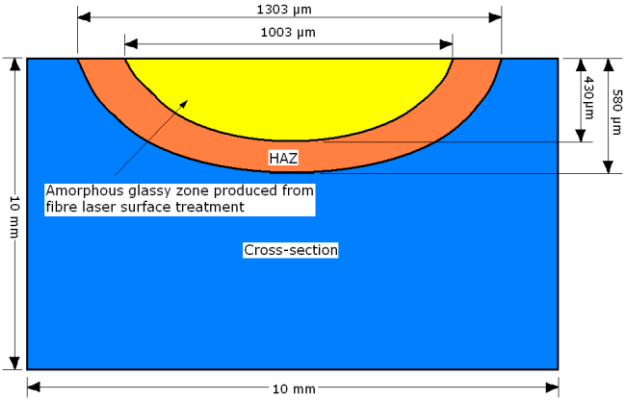

(d)

Figure 8.7 Optical images of the cross-sectional view of (c) the fibre laser irradiated surfaces and (d) a schematic diagram of the fibre laser irradiated surfaces of the ZrO_2 engineering ceramic.

8.4.3 Change in Microstructure

8.4.3.1 As-received surface

The microstructural evaluation by using the FEGSEM of the ground and polished surface of the untreated sample in Figure 8.7 presents the surface morphology. This shows the grain boundaries along with the grain sizes. The grain size ranged between 0.7 to 0.9µm with some porosity also evident. The microstructure presented in Figure 8.7 is somewhat different to that of the one presented in Chapter 5 for the ZrO_2 engineering ceramic. This was due to two reasons: firstly, the surfaces herein were ground and polished and were followed by undergoing a thermal etching process. This helped to enhance the grain exposure and the appearance of the grain boundaries. Thermal etching process was not conducted for the images presented in Chapter 5 for the ZrO_2 engineering ceramics in comparison. Secondly the images in Chapter 5 are also different despite using the ZrO_2 engineering ceramics herein being from the same batch as that of the one in Chapter 5. This is because the images in Chapter 5 comprise of spherical agglomerates which are formed during powder preparation of the ceramic for processing. During this stage the ceramic powder is dispersed in a liquid medium and is sprayed into hot air so that the droplets could dry. This eventually leads to the formation of spherical agglomerates. The spherical agglomerates would improve the flowability of the powder. This increases the processing speed during the preparation of green bodies (ceramic products) by pressing. Then, sintering is conducted to get the final product which is the rectangular ZrO_2 engineering ceramic sample as used in the work. In reality, the agglomerates should crush

during the preparation of the green body when pressed, but it is not always the case. Hence, some agglomerates will only get flattened especially those near the surface of the sample. This is what is to be seen in the microscopic images presented in Chapter 5 for the ZrO_2 engineering ceramic, whereas the images in this Chapter are ground and polished so the agglomerates are not to be seen. Though, by using higher magnification image allows one to see the grain boundaries as further illustrated in this Chapter.

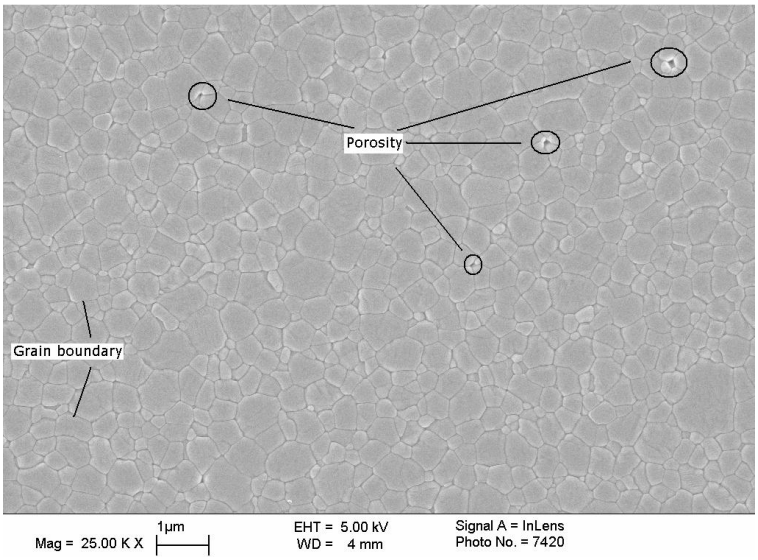

Figure 8.7 FEGSEM image of the as-received surface of the ZrO_2 engineering ceramic.

8.4.3.2 Fibre laser irradiated surface

From observing the fibre laser irradiated surface as shown in Figure 8.9; it can be observed that the grain boundaries have enlarged and elongated in comparison to the ground and polished untreated surface. However, there is also an increase in the porosity and surface flaws in some of the regions of the fibre laser irradiated surface. This would have resulted from escaping of entrapped porosity during the event of the laser interaction with the surface of the ZrO_2. Moreover, the sizes of the grains vary from 3 to 10µm from the top (near) surface layer and through the sub-surface and the bulk of the ceramic. This is because the processing temperature at the top (near) surface layer was much higher than the sub-surface and the bulk. This would have produced the grain growth. Figure 8.10 presents the cross-sectional microstructure showing the increase in the grain size from the bulk of the ZrO_2 to the sub-surface and the top surface layer of the fibre laser irradiated zone. The microstructure at the top surface layer (see Figure 8.11 and Figure 8.12) is somewhat different as significant grain growth has occurred due to the high temperature gradient existing at the laser-ZrO_2 interface.

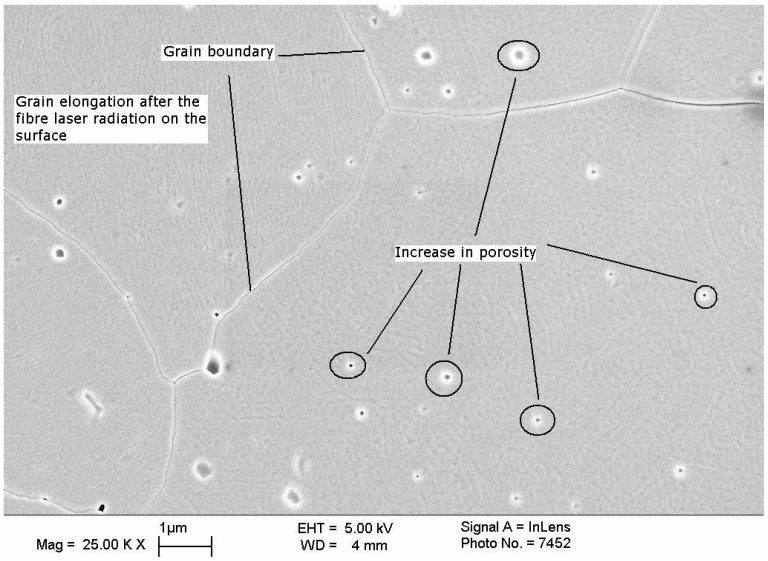

Figure 8.9 FEGSEM image of the cross-section of the sub-surface layer of the fibre laser surface treated ZrO_2 engineering ceramic.

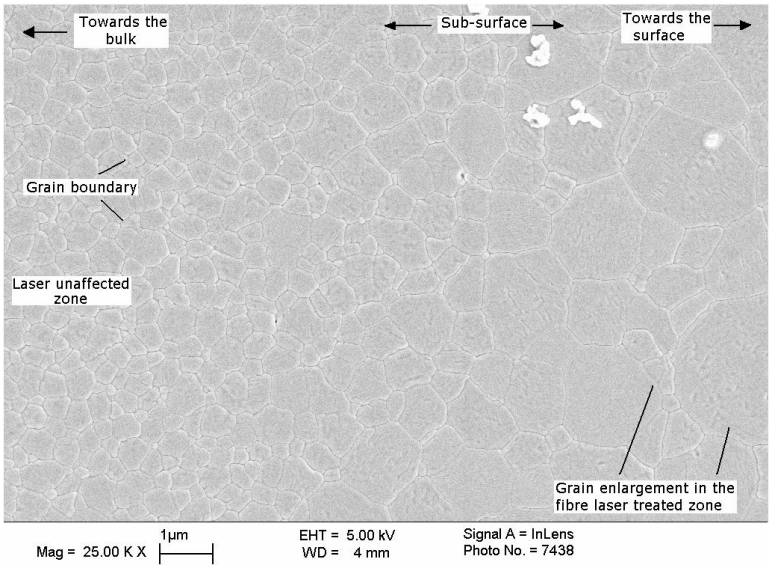

Figure 8.10 FEGSEM image of the cross-section of the fibre laser irradiated surface of the ZrO_2 engineering ceramic showing variation in the grain sizes within the sub-surface, towards the bulk and the top surface layer.

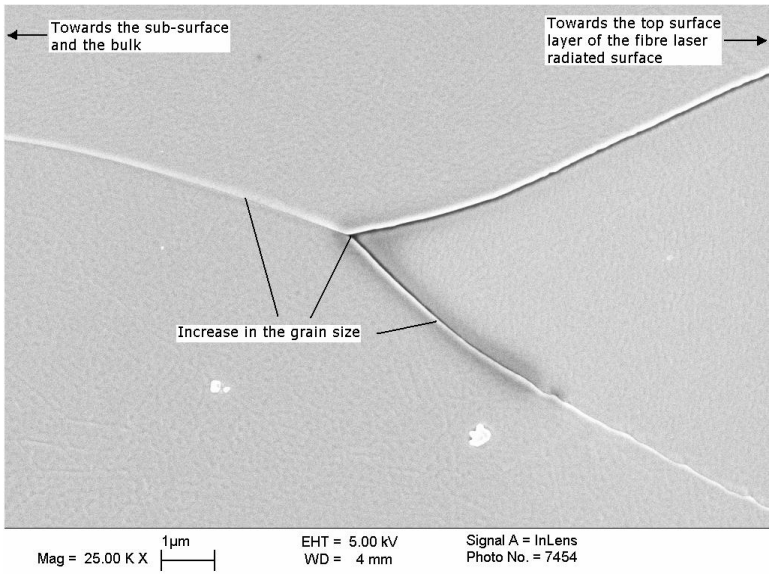

Figure 8.11 FEGSEM image of the cross-section of the top layer of the fibre laser irradiated surface ZrO_2 engineering ceramic at x 25k magnification.

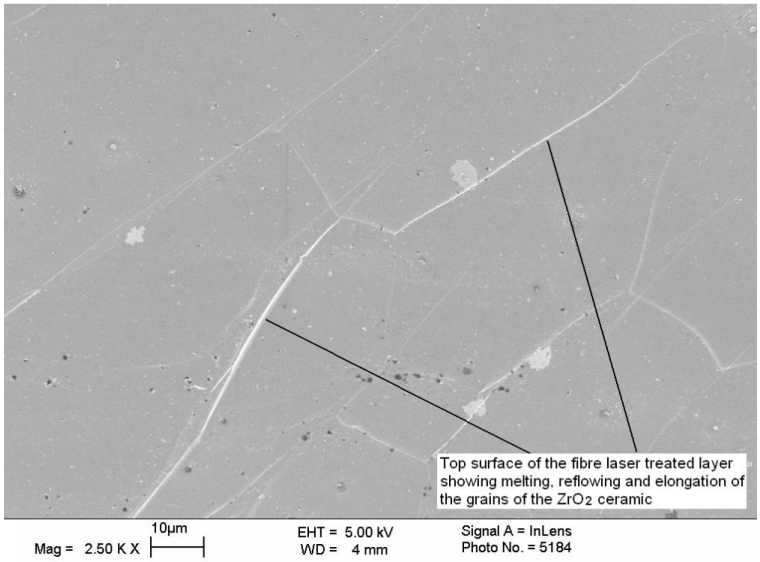

Figure 8.12 FEGSEM image of the cross-section of the fibre laser irradiated ZrO_2 engineering ceramic illustrating the top surface layer at x 2.5k magnification.

8.4.3.3 Nd:YAG laser irradiated surface

The microstructure of the Nd:YAG laser irradiated surface in comparison to that of the as-received surface has been reasonably modified as presented in Figure 8.13 to Figure 8.15. The grain sizes herein range from about 3.5 to 7µm and an average grain size was of about 5µm. This in comparison to the laser untreated surface was considerably large. However, when compared to the fibre laser irradiated surfaces, the grain boundaries were somewhat smaller. Similar effect which occurred with the ZrO_2 samples irradiated by the fibre laser had also occurred with the Nd:YAG laser. But, it was slightly less significant. The sample observed at the cross-section comprised of larger grains at the top near surface layer. This further reduced as it was observed at the sub-surface and the bulk of the

ZrO_2 engineering ceramic as presented in Figure 8.13. However, this type of grain growth was slightly abnormal as elongation of the grains (particularly in Figure 8.15) was seen in few areas. Figure 8.14 showed the very top surface layer of the ZrO_2 which was irradiated by the Nd:YAG laser. The microstructure in this area was reasonably modified in comparison to the microstructure where the laser-ZrO_2 interaction did not occur. Moreover, evidence of surface melting, re-flowing and solidification can be seen particularly in Figure 8.14 where the laser- ZrO_2 interaction had taken place.

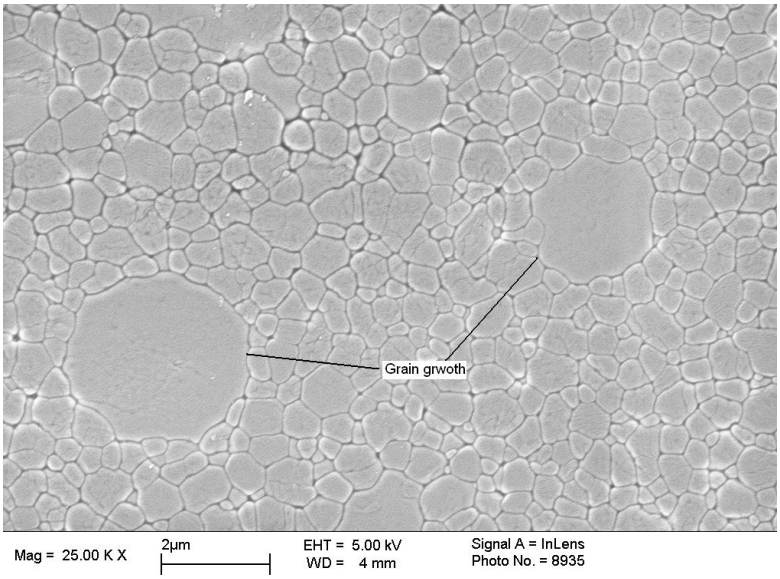

Figure 8.13 FEGSEM image of the Nd:YAG laser irradiated sample of the ZrO_2 engineering ceramic within the sub-surface region.

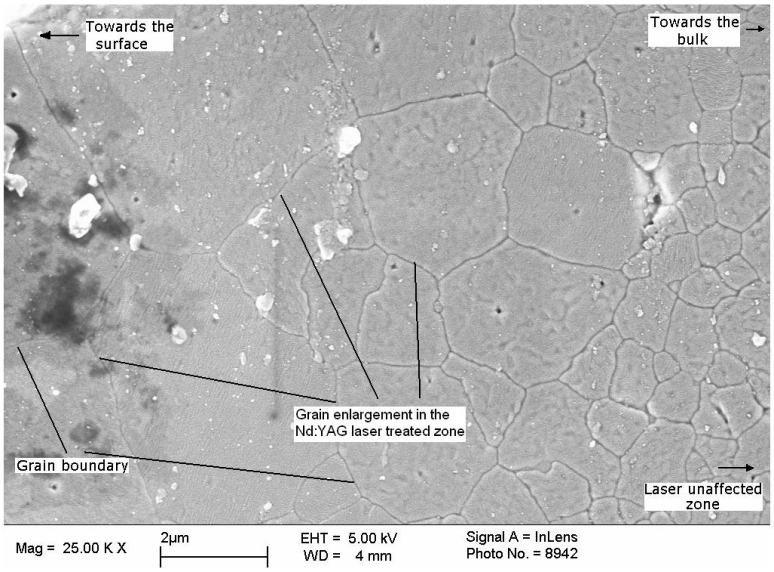

Figure 8.14 FEGSEM image of the Nd:YAG laser irradiated surface of the ZrO_2 engineering ceramic illustrating the surface and the sub-surface layer.

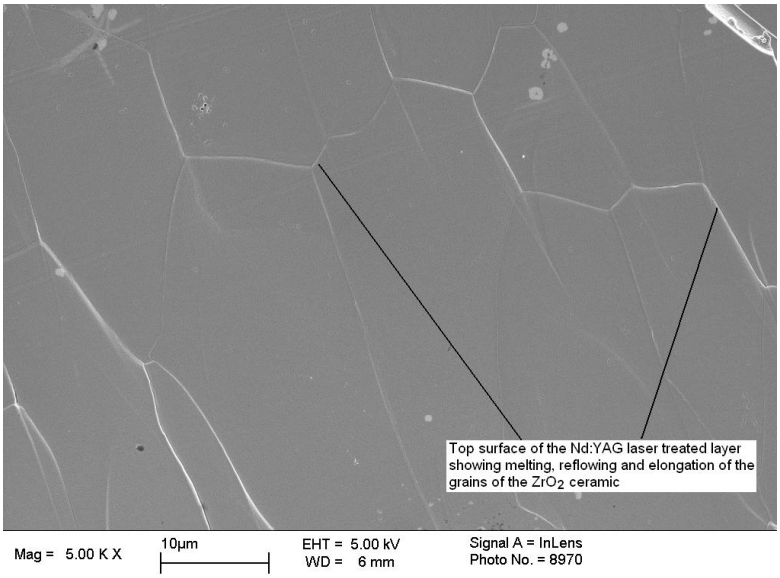

Figure 8.15 FEGSEM image of the cross-section of the Nd:YAG laser irradiated surface of the ZrO_2 engineering ceramic illustrating the top surface layer.

8.4.4 Rationale and the Differences between the Effects Produced by the fibre and Nd:YAG Laser Surface Treatments

From the difference in the hardness values found by the results of the two laser types it can be summarized that the Nd:YAG laser irradiation was producing a much softer and a ductile surface to that of the fibre laser irradiation. From comparing the effects of the fibre laser surface treatment and that of the Nd:YAG laser, it is postulated that the high brightness of the fibre laser would generate high temperature at the surface of the laser-ZrO_2 interface. This was also supported by previous workers [243, 246]. The higher temperature has allowed the fibre laser irradiated ZrO_2 engineering ceramic to generate larger melt-zones in comparison to that of the Nd:YAG laser. This resulted to change in composition as a thicker and a broader glassy layer was produced. This in turn had also shown high hardness in comparison to the Nd:YAG laser irradiated surface. In addition, it is also believed that rapid cooling from the higher temperature gradient of the fibre laser would have contributed to the increased hardness produced as result of the fibre laser surface treatment. It is likely that a high processing temperature of the fibre laser irradiation in comparison to that of the Nd:YAG laser would have caused a phase change from T to L to have occurred. This produced a harder fibre laser treated surface as opposed to the Nd:YAG laser treated surface which did not result to the same phase change. This was due to lower processing temperature exhibited by the Nd:YAG laser.

The change in the dimensional size was produced by the high brightness beam of the fibre laser interacting more with the ZrO_2 engineering ceramic. This in turn had generated higher processing temperatures than that of the Nd:YAG laser, whereas the Nd:YAG laser irradiation only generated lower interaction zone as well as lower depth of penetration of the beam. This is shown by Figure 8.7(a) and (b) and is compared to Figure 8.7 (b) and (c). The difference in size between the footprint

of the fibre and the Nd:YAG laser irradiation (see Figure 8.6(a) and (b)) was also found as well as the cross-sectional images shown in Figure 8.7(a) to (d) of the Nd:YAG and the fibre laser irradiated samples. As well as the depth of penetration being larger for the fibre laser in comparison to the Nd:YAG laser; the high temperature produced by the high brightness of the fibre laser had also created a larger melt zone (see Section 8.4.2) and the amorphous glassy phase. This indicated that the grain refining for both types of lasers were different as the surface of the fibre laser with larger melt-pool was producing bigger grain sizes than that of the Nd:YAG laser. This in turn, generated a harder surface of the fibre laser irradiated sample which was fully melted to the amorphous glassy phase in comparison to the Nd:YAG laser which was a mixture of the amorphous glass and the zirconia carbide through the induction of carbon vacancies. This on the other hand had created a softer surface as the hardness was significantly reduced.

8.4.5 Rationale and the Differences between the Effects Produced by the fibre, Nd:YAG and the CO_2 Laser Surface Treatments

The brightness value for the three lasers used in this research is presented in Table 8.1. The experimental investigation showed that the fibre and the Nd:YAG laser had a considerable influence due to the differences in the beam divergence and the beam quality factor which inherently resulted to the difference in the brightness value, despite having similar wavelength, Gaussian beam mode, power input and the laser beam spot size as well as the traverse speed. The influence of the CO_2 laser beam brightness was not experimentally demonstrated as there was a vast difference in the wavelength of the fibre and the Nd:YAG laser in comparison to the CO_2 laser and also because a like by like study was more comparable in this case. However, the CO_2 and the fibre laser were compared throughout the thesis and it was therefore inevitable to mention the influence of the CO_2 laser beam brightness on the engineering ceramic (ZrO_2 in particular).

The CO_2 laser beam was much lower in brightness in comparison to the fibre laser despite having higher wavelength as shown in Table 8.1. This was because of the lower M^2 value and higher beam divergence of the CO_2 laser which resulted to the lower brightness value by about 26%. It was therefore indicative that the lower brightness value would in turn produce lower surface temperature during laser-ceramic interaction which was already confirmed by the results in Chapter 7 (from the temperature distribution shown by the FEM and the experimental model). Nevertheless, the CO_2 laser with respect to producing the thicker modified laser irradiated layer, broader footprints of the laser irradiated zone was found. This was because of the ZrO_2 engineering ceramic was generally accepting the NIR wavelength of the fibre and the Nd:YAG laser better than the MIR wavelength of the CO_2 laser as previously mentioned in Chapter 7. This resulted to the CO_2 laser interacting more on the surface of the ceramic than the bulk which naturally showed broader footprints and HAZs whereas the fibre and the Nd:YAG laser in comparison had illustrated narrow irradiated footprints

and HAZs, thinner laser irradiated (modified) layers but deeper penetration of heat as the ZrO_2 ceramic was allowing the NIR wavelength to penetrate deeper into the bulk.

8.4.6 Contribution of Laser-Beam Brightness as a Parameter to Effect Laser Processing of Engineering Ceramics.

Brightness is dependent on the output power, the solid angle of divergence and the M^2 factor. These are all parameters of the brightness equation as shown in Section 8.2 in this investigation. However, laser brightness is primarily dependant on the transverse mode as well as the beam quality factor M^2. The better the beam quality of the laser, the higher the brightness exhibited. In this case, despite the transverse mode being in the same region for both the Nd:YAG and the fibre lasers, the beam quality factor was a lot better for the fibre laser as there was over 5 ½ folds of difference between the beam quality factors of the Nd:YAG laser where the M^2 value was 6.7 and M^2 = 1.2 for the fibre laser. This meant that the fibre laser is able to produce a brighter beam. Also, the beam divergence would play a big role in increasing the brightness value as smaller beam divergence produces smaller solid angle of divergence ($\Omega = \pi \theta^2$). The beam quality factor therefore, allows higher brightness to be exhibited. This consequently affected the change in the hardness, dimensional size and the microstructure of the ZrO_2 engineering ceramic.

The difference in the two brightness values for the Nd:YAG and the fibre laser was over 3 folds. The fibre laser comprised of high brightness but did not produce the same difference with the physical effects that took place from the Nd:YAG and fibre laser surface treatment. Moreover, to suggest a consistent relationship between the difference in the brightness value and the effects which take place from of the laser surface treatments as a quantitative value would require further experimental investigation. It is also suggested that the relationship between the brightness value for two lasers and its relative effects are unique for each ceramic. This is because factors such as the material property as well as the absorption of the laser wavelength are taken into consideration.

As shown, the high laser-beam brightness can exhibit longer depth of penetration and bigger footprints by using identical laser power. Furthermore, it is therefore possible to operate the high brightness laser at much lower powers. This in turn, would exhibit a surface treatment with the same dimensional size. This in the long run would help to achieve low cost per wattage laser surface treatment which is just as effective as the surface treatment applied by using a low brightness beam at higher cost per wattage. High brightness laser such as the fibre laser is ideal in terms of laser processing of ceramics where high powers are required for surface modification and microstructural changes as well as phase modification where obtaining elevated processing temperatures are important to create a phase change.

8.5 Summary

Influence of the laser-beam brightness was investigated after the fibre and the Nd:YAG laser surface treatments thereon the ZrO_2 engineering ceramic. The findings revealed:

- The hardness of the ZrO_2 was reduced by 36% for the Nd:YAG laser in comparison to the as-received surface. However, only 4% reduction in the surface hardness was found from employing the fibre laser surface treatment. This was because the diamond footprints were reduced which indicated that the fibre laser irradiated surface had also become somewhat softer, although, it was not significant as much as the results of the Nd:YAG laser.

- The width of the fibre laser irradiated zone was also broader in comparison to the Nd:YAG laser irradiated zone by 32%. The depth of penetration was up to 48.5% higher for the fibre laser surface treatment.

- The microstructural changes also showed that the fibre laser irradiated surface was producing large grains in comparison to the Nd:YAG laser irradiated surface by over 20% difference in size.

- The physical and the microstructural effects differed for the two lasers despite using identical laser processing parameters. This resulted from the high brightness generated from the fibre laser in comparison to that of the Nd:YAG laser. This in turn, produced higher processing temperatures, causing larger thermal gradient. This characteristically produced a bigger melt pool. Hence, a harder surface in comparison to the Nd:YAG laser was produced and caused, an increase in the width and the depth of penetration, as well a change in the microstructure.

- It can be concluded that high brightness lasers require lower powers to penetrate at equivalent dimensions to that of the low brightness lasers. This would be more cost effective since less cost per wattage is utilized. Processing of engineering ceramics is ideal by applying high brightness lasers. This inherently produces remarkable surface modifications in terms of composition, phase changes and K_{1c}.

- Experimental investigation of the effects of the brightness on laser processing is rather limited. This work is first step demonstration of what the effective results of laser brightness has on the engineering ceramics. Further work in this field would be considerably fruitful for better understanding of the possible effects and to conduct an efficient laser surface treatment of the engineering ceramics.

Summary and Conclusions

The work presented in this thesis elucidates several key issues associated with fibre and CO_2 laser interaction with Si_3N_4 and ZrO_2 engineering ceramics during surface treatment. The following conclusions were drawn from the thesis:

- To achieve a surface treatment with minimal defects, fibre laser treatment of the Si_3N_4 used a power density of 5556 W/mm^2 and 3919 W/mm^2 for the ZrO_2. For both the engineering ceramics, a traverse speed of 100 mm/min was used. For the CO_2 laser surface treatment of the Si_3N_4; a power density of 5556 W/mm^2 at a traverse speed of 100 mm/min and 1736 W/mm^2 at 600 mm/min for the ZrO_2 was used.

- A lower traverse speeds or higher power density than above resulted to an increase in surface cracks and considerable melt zones. Higher traverse speed and lower power density had a minimal effect on the surface of the two engineering ceramics.

- A reduction in hardness of both the engineering ceramics was found when employing both lasers. But the reduction in hardness was more significant when employing the CO_2 laser. Softer surfaces were found when using O_2, compressed air, ambient air, followed by N_2 and Ar assist gases.

- Reactive gases generated the highest material removal and the roughest surface finish along with a high level of oxidation and average porosity. Large surface profile of the laser treated and the HAZ were also observed on both engineering ceramics.

- The use of Ar and N_2 assist gases resulted in producing the finest surface finish with a lower material removal in comparison with the sample treated by using other conditions. A compositional change was yet apparent but to a lesser extent despite N_2 and Ar showing less influence of oxidation.

- The compositional study confirmed that the Si_3N_4 was transformed to SiO_2. Likewise, the surface of the ZrO_2 engineering ceramic was also modified to ZrC. Both laser surface treatments produced an interlocking microstructure particularly by using Ar and N_2 assist gases.

- From assessing the fracture toughness property K_{1c} of the as-received, CO_2 and the fibre laser treated engineering ceramics, it was identified that Equation: $K_{1c} = 0.016\ (E/Hv)^{1/2}\ (P/c^{3/2})$ was the most relevant to employ for both engineering ceramics.

- A change in the hardness and the crack length as result of the Vickers indentation was found to be influential parameters. This resulted to a change in the end K_{1c} value (under the applied conditions).

- The K_{1c} of the top surface layer improved with both the CO_2 and the fibre laser treated surfaces when compared to the as-received surfaces. However, the hardness was considerably lower for the CO_2 laser treated surface compared to that of the fibre laser. This resulted to a lower K_{1c} value for the fibre laser surface treatment compared to that of the surface treated by the CO_2 laser under the applied conditions.

- The FEM and the experimental model of the fibre and CO_2 laser surface treatment of both the engineering ceramics was verified with an overall error of +10% over the surface and through the cross-section. The FEM further expands to demonstrate the relationship between various parameters which would correlate with one another to reveal the extended range of parameter window during the fibre and the CO_2 laser surface treatments.

- The surface and the bulk temperature produced by the fibre laser surface treatment of the Si_3N_4 and the ZrO_2 were considerably higher in comparison to the CO_2 laser.

- The difference in processing temperature resulted from high laser-beam brightness and high absorption of the NIR wavelength of the fibre laser in comparison to the MIR wavelength of the CO_2 laser during surface treatment of both engineering ceramics.

- Nevertheless, the CO_2 laser generated a bigger interaction zone on the surface and was not induced further into the bulk as was the case with the fibre laser.

- The MIR wavelength is rather suitable for mainly surface processing of oxide ceramics that do not require deep penetration. For the nitride ceramics, the temperatures induced were fairly high in comparison to the oxide ceramic. This indicated that the CO_2 laser wavelength is further absorbed into the nitride ceramic in comparison to the oxide ceramic. But, the surface interaction of the MIR wavelength was also considerable for surface processing oxide ceramics.

- Thermal mapping of the as-received and fibre laser irradiated ceramics revealed that the fibre laser surface treatment generally produced a phase transformation of the ZrO_2 from the M to a mixture of T+C to T and then a partially L phase (during heating), followed by the M state during solidification. Thermal analysis of the fibre laser irradiated Si_3N_4 showed that a phase transformation from α-phase to β-phase occurred during fibre laser-Si_3N_4 interaction.

- Influence of the laser-beam brightness parameter showed a reduction in the hardness for the Nd:YAG laser surface treatment in comparison to that of the fibre laser and the as-received surface of the ZrO_2. But the width and depth of penetration were higher and the grain sizes were larger for the fibre laser irradiated zones in comparison to that of the Nd:YAG laser.

- The physical and microstructural effects differed when applying the two lasers despite using identical processing parameters. This was because the fibre laser exhibited a high brightness laser

beam which produced high processing temperatures. Consequently, this produced a harder surface compared to the Nd:YAG laser and caused an increase in the width and the depth of penetration.

- It can be concluded that high brightness lasers require lower powers to penetrate at equivalent dimensions compared to a low brightness laser. This would be more cost effective since lower cost per wattage would be utilized.

- Processing of engineering ceramics is more ideal by using high brightness lasers as high power densities are required. This inherently, produces remarkable surface modifications in terms of compositional, topographical, temperature difference, phase changes and K_{1c} values under set conditions.

Future Recommendations

The research presented in this thesis has established several scientific finding. These findings compliment the development of a laser surface treatment process of engineering ceramics. In particular, the effects of the fibre laser are is still new in the market and has several advantages over the more conventional systems previously used for processing engineering ceramics. These are discussed in this thesis and are also compared with the effects of the CO_2 laser. Thereby, suggestions are recommended for future investigations in order to take forward the work detailed in this thesis.

Laser Processing Aspects

Future experiments could apply the dual laser beam processing technique with either a trailing or a leading laser beam. This could be carried out by either leading or by a trailing laser which is selected as an additional heat source for the ceramic rather than a single laser beam. The additional laser beam could be executed at lower power density to that of the main laser source. This will allows either heating the material to a certain temperature or elongating the cooling after the main laser source has been in contact with the ceramic.

As well as CW beam processing it would be valuable to conduct surface treatment by using a pulsed laser beam. This is because the microscopic, multiple shock waves could be induced into the ceramic surface and possibly the sub-surface. This could enhance the possibility of inhibiting residual stresses in form of compression. Very little work has been done in this area but a recent publication has showed some successful results particularly with a Si_3N_4 ceramic. Hence, an in depth future investigation would show some new findings and valuable contributions to knowledge, as well as diversity for application of many ceramic components currently used within the sectors where ceramics are readily used.

Material Characterization and Thermal Analysis Aspects

Although, the TG-DSC analysis was successfully employed to observe the changes within the ceramics during heating and cooling; it would be useful to characterise the ceramics by means of X-Ray diffraction method in order to gauge the existing phases present within the as-received ceramics prior to undertaking the laser surface treatments.

In addition, it would also be interesting for one to investigate the effects at higher temperature than 1500 $^{\circ}$C on the phase transformation of the ceramics. Due to lack of availability of appropriate equipment for thermal testing, the investigation herein was only conducted between the temperatures ranging from 25°C to 1500°C. It would add more insight into the ceramics behaviour at elevated temperatures if this is further investigated. For example confirmation of the cubic phase taking effect at melting temperatures for the ZrO_2 engineering ceramic.

Thermal analysis of the Si_3N_4 and the ZrO_2 engineering ceramics irradiated by the CO_2 laser and the Nd:YAG laser would also be ideal so a comparison of the events which have occurred with the fibre laser irradiated ceramics can be put forward. This would give further understanding of the changes during the heating and cooling cycle.

It is also suggested that temperature measurements of the laser process should be performed for all types of gases. This will allow one to understand exactly how much temperature is raised whilst using more reactive gases in comparison to the non-reactive gases. This will also allow the physical effects on the surface to be compared by the different types of gases with their resulting temperature differences generated. In addition, it is suggested that wear test and tensile strength of laser surface treated engineering ceramics is conducted as it will give further indication of the effects produced as result of the laser-material interaction.

Accuracy with Calculating the Mechanical Property

Grinding and polishing of the ceramics prior to the laser surface treatment would be ideal as this will enhance the surface strength and improve the response by the ceramics during the insertion of the Vickers diamond indentation. This in turn will produce less fluctuation in the hardness values and propagation of the resulting crack lengths and the end K_{1c} values. However, this will have produced a smooth shiny surface which intrinsically will have an adverse effect as the laser beam during the interaction stage will reflected due to the processing surface being somewhat shiny. Therefore, it is suggested that a special absorption tape is used to cover the ceramic surface during laser processing. This will particularly improve the absorption of the ceramics and give better results for the depth of penetration and the wavelength suitability.

Prediction of the residual stress could be conducted by the X-ray diffraction method or by using the Raman Spectroscopy. In addition, the results can then be compared with that of a FEM model by using the current software package (Nx-5.0 Nastrad Unigraphics package) used in this research.

Finite Element Modelling Issues

The FEM constructed for this research is a collection of temperature distributions for various positions. It would be ideal to observe the whole event of the laser-ceramic interaction by taking in consideration of the kinematics associated with the event. In other words FEM of the moving laser is suggested for further study. This demonstrates temperature distributions of a moving beam rather than the FEM of a still laser beam at various positions. This would surely reveal good information of the temperature profiles. However, it can be improved for better understanding of laser-material interaction. In addition, absorption of both laser wavelengths should be measured for the Si_3N_4 and the ZrO_2 engineering ceramics by experimental means. This will produce more accurate temperature readings by the FEM.

Laser-Beam Brightness Measurement

It is also recommended that experimental investigation to measure the laser-beam brightness is conducted by using the method mentioned in the European standards (ISO 11146-1) [252-255]. The experimental brightness values calculated for the work herein are estimation for the laser brightness exhibited by the two lasers but they do not take in account of the losses or the gains of the laser beam during its delivery and during passing through the optics.

Modifications with Ceramic Processing Stage

Laser processing of ceramics is limited due to the effect of the thermal shock and the associated stresses effects which the ceramics tends to undergo. This is purely due to the characteristics of the material as it is hard and brittle and has very low ability to generate plastic deformations when it is exposed to thermal gradients. Therefore, it is suggested that one step should be taken in reverse by considering its processing method where certain additives should be placed within the ceramics so that it has the tendency to withstand the thermal shock. This could be done by laser surface treating the green slurry as opposed to a high strength fully sintered ceramic which is very hard and brittle and prone to the effect of thermal shock, which in the case by using a (semi-heated) ductile slurry could well eliminate the usual problems that are seen with laser processing of the engineering ceramics in general.

Technology Transfer

The scientific finding and methods approached in this research could be used for future studies where the foundation of processing engineering ceramics is essential before it is applied to an industrial problem. Such understanding can now be applied for joining fuel cell tubes which are used within the power generation sector where the current manufacturing process of joining fuel cells are time-consuming and expensive. This is due to the required processes needed to vitrify surface of the fuel cell tubes so that they are sealed together. However, the firing process required for this vitrification could take up to four-days for each tube to be sealed. This in turn would add cost to the manufacturing process when these tubes are combined into bundles, then into strips and ultimately into stacks [6]. This is why industrial lasers such as a fibre laser can be introduced, primarily to investigate if such a seal between the fuel cell tubes can be achieved by laser surface treatment. If this is successful then it would mean that the fuel cell manufacturers in the UK would have access to a technique that allows reduced fuel cell manufacturing times and all other associated benefits as previously mentioned in the introduction.

References

1. Norman, S., Zervas, M., Appleyard, A., Durkin, M., Horley, R., Varnham, M., Nilsson, J., and Jeong, Y. (2004) 'Latest development of high power fibre lasers in SPI'. *Proceedings of SPIE* **5335**, 229 – 237.

2. Salminen, A., Piili, H., and Purtonen, T. (2009) 'Characteristics of high power fibre laser welding'. *Proceedings of IMechE Part C: Journal of mechanical engineering science* **224**, 1019 – 1029.

3. Bachmann, F. (2003) 'Industrial applications of high power diode lasers in materials processing'. *Applied Surface Science* 207- 209, 129 – 136.

4. Lawrence, J. (1999) *The characterization and feasibility of a two-stage ceramic tile grout sealing process using a high power diode laser*, PhD thesis, Institute of Science and technology: University of Manchester.

5. Steen, W. (1997) *Laser Material Processing 2nd Edition*, Springer Publication: London.

6. A personal reference with Mr. Rowland Travis of Rolls Royce Fuel Cell Systems Ltd. in January 2008.

7. Witt, M. (1977) 'Industrial applications of excimer lasers'. *Hyperfine Interactions* **37**, 415 - 422.

8. Yamomoto, J.C. (1977) *Laser machining of Silicon Nitride*, LAMP'77.

9. Solomah, A.G., Mannik, L., and Brown, S.K. (1993) 'Laser Machining of Silicon Nitride Ceramics'. *Proceedings of the international conference on machining of advanced materials.*

10. Lee, Y.C., and Kuo, S.H. (2001) 'Miniature Conical Transducer Realized by Excimer Laser Micro- Machining Technique'. *Sensors & Actuators* **93**, 57 – 62.

11. Tian, Y., and Shin, Y.C. (2006) 'Laser assisted machining of damage free – silicon nitride parts with complex geometric features via in process control of laser power'. *Journal of American Ceramic Society* **79**, 3397 – 3405.

12. Lawrence, J., and Hao, L. (2005) *Laser Surface Treatment of Bio - Implant Materials.* United-Kingdom: John Willey & Sons Ltd. Publications.

13. Shukla, P.P. (2007) *Surface Treatment of Ceramics using Contact –less Energy Beams*, MSc By Research Thesis, Advanced Joining Centre: Coventry University.

14. Sun, L., Malshe, A.P., Jiang, W., and Mccluskey, P.H. (July 2006) 'Effect of CO_2 Laser Surface Processing on Fracture Behaviour of silicon Nitride Ceramic'. *Journal of Engineering Materials and Technology* **127**, 460 – 467.

15. Sun, L., Malshe, A.P., Wen Ping, J., and Mccluskey, P.H. (2006) 'Experimental Investigation of Laser Surface Processing of Flexure Silicon Nitride Ceramics'. *Transaction of Nonferrous Metals Society of China* **16**, 557 – 65.

16. Lawrence, J., and Li, L. (2002) 'On the difference between the beam interactions characteristics of CO_2, Nd: YAG Excimer and high powered diode lasers with a SiO_2/Al_2O_3 ceramic'. *Lasers in Engineering* **12 (2)**, 71 – 93.

17. Petitbon, A., and Guignot, D. (1979) 'Laser Surface treatment of ceramic coatings'. *Material Science and Engineering A***, 121**, 545 – 547.

18. Lawrence, J., Evans, D.W. (2007) 'An analysis of crack and porosity formation in laser surface treated Magnesia partially stabilized Zirconia (MgO-PSZ) and Methods for alleviation'. *Lasers in Engineering* **17**, 255 – 271.

19. Lawrence, J. L., Li, J., and Spencer, T. (1999) 'Diode modification of ceramic material surface properties for improved wettability and adhesion'. *Applied Surface Science* **137 – 139**, 377 – 393.

20. Morita, N., Watanabe, T., and Yoshida, Y. (1991) 'Crack Free Processing of Hot – Pressed Silicon Nitride Ceramics using Pulsed YAG Laser'. *JSME International Journal Series III*, **34 (1)**, 149 – 153.

21. Mendes, M., Ohveira, V., Vilar, R., Bemhorn, F., Ihlemann J., and Conde, O. (1999) 'Femtosecond Ultraviolet laser Micromachining of Al2O3 – TiC Ceramics'. *Journal of Laser Applications* **11**, 211 – 215.

22. Lawrence, J. (2002) 'An analysis of the bonding mechanism active in a high powered diode laser generated two stage ceramic tile grout'. *Lasers in Engineering* **12(4)**, 279 – 309.

23. Tonshoff, H.K. and Emmelmann, C. (1979) 'Laser cutting of advanced ceramics'. *Laser Zentrum Hannover, Annals of the CIRP* **37**, 219- 222.

24. Lei, H., and Lijun, L. (1999) 'A study of laser cutting engineering ceramics'. *Optics & Laser Technology* **31**, 531 – 537.

25. Lingfi, J., and Yan, Y. (2007) 'Crack free cutting of thick and dense ceramics with CO_2 laser by single – pass process'. *Optics and Lasers in Engineering* **46**, 775 – 790.

26. Naeem, M., Preston, M. E., and Tyrer, J.R. (1979) 'Processing of Engineering Ceramics with High Powered CO_2 Lasers, *Material & Design* **10**, 271- 375.

27. Kaur, A.S., Doloi, B., Bhattacharyya, B. (2005), 'Experimental investigations on Nd:YAG laser cutting of silicon nitride', *International Journal of Manufacturing Technology and Management*, **7 (No. 2/3/4)**, 171 – 191.

28. Voisey, K. (2003) 'Laser Processing of Ceramics'. *Industrial Laser User* **33**, 23 -25.

29. Cappelli, E., Orlando, S., Mattel, G., Montozzi, M., Pinzari, F., and Seith, D. (1999) 'Surface Modification of Carbide Ceramics Induced by Pulsed Laser Treatment', *Applied Physics A* **69S**, S515-S519.

30. Solomah, A.G., Mannik, L., and Brown, S.K. (1993) 'Laser Machining of Silicon Nitride Ceramics', Proceedings of the international conference on machining of advanced materials, Gaithersburg: USA **747**, 543-547.

31. Mendes, M., Ohveira, V., Vilar, R., Bemhorn, F., Ihlemann, J., and Conde, O. (1999) 'Femtosecond Ultraviolet laser Micromachining of Al2O3 – TiC Ceramics'. *Journal of Laser Applications* **11**, 211 – 215.

32. Lee Y.C., and Kuo, S.H. (2001) 'Miniature Conical Transducer Realized by Excimer Laser Micro- Machining Technique'. *Sensors & Actuators* **93**, 57 – 62.

33. Geiger, M., Becker, W., Rebhan, T., Huttles J., and Luts, N. (1996) 'Increase of Efficiency for the XeCl Excimer Laser Ablation of Ceramics'. *Applied Surface Science* **96 – 97**, 309 – 315.

34. Murray, A.J., and Tyrer, J.R (1997) 'Nd:YAG Laser cutting and drilling of PSTZ- influence of substrate heating temperature on recast layer microcracking'. *Journal of Laser Applications* **11 (3)**, 127-135.

35. Murray, A.J., and Tyrer, J.R (1997) 'Pulsed CO_2 and Nd: YAG laser drilling of PSTZ – A study into the wavelength, effects on Recast layer micro-cracking'. *Lasers in Engineering* **9**, 23 -37.

36. Murray, A.J., and Tyrer, J.R. (1997) 'Nd: YAG laser drilling of 7.3 mm thick partially stabilized tetragonal Zirconia- control of recast layer micro-cracking using localized heating techniques'. *Journal of Laser Applications* **11 (4)**, 179 – 174.

37. A.J Murray (2001) *'The reduction of micro-structural damage during the drilling of ceramics by high power laser'*, PhD Thesis, Loughborough University.

38. Richardson, D. W. (2006) *Modern Ceramic Engineering, Third Edition.* Published by CRC Press, Taylor & Francis Group.

39. Kawamura, H. (1999) 'New Perspectives in Engine Applications of Engineering Ceramics'. *Science of Engineering Ceramics II, International Symposium* **161**, 9-16.

40. Mikijelj, B., and Mangels, J. (2000) 'SRBSN Material Development for Automotive Applications'. 7th International Symposium of Ceramic Materials and Components for Engines. n. pp.

41. Mikijelj B., Mangels, J., and Belfield, E. (2003) 'High Contact Stress Applications of Silicon Nitride in Modern Diesel Engines'. Institution of Mechanical Engineers, Fuel Injection System Conference, London. (www.ceradyne.com). n. pp.

42. Granta Design Ltd. CES selector, version 5.1. Cambridge, UK, 2007. www.granta.co.uk.

43. Mangels, J. (2006) 'A proven Ceramic Material for Engine Applications'. Institution of Mechanical Engineers, Fuel Injection System Conference, London. n. pp.

44. Reed, J.S. (1995) *Principles of Ceramics Processing Second Edition*. Canada: John Wiley & Sons.

45. Kawamura, H. (1999) 'New Perspectives in Engine Applications of Engineering Ceramics'. Science of Engineering Ceramics II, International Symposium **161**, 9-16.

46. Onoda, G.Y., and Hench, L.L. (1979) *Ceramic Processing Before Firing*. New York: Wiley & Sons.

47. Kalpakjian S., and Schmid S.R, (2001) *Manufacturing Engineering and Technology 4th Edition*. New Jersey: Prentice Hall.

48. Peng, H. (2004) *Spark Plasma Sintering of Si_3N_4 based Ceramic:* Doctoral Dissertation, Department of Inorganic Chemistry: Stockholm University, S- 10691 Stockhom, Sweden.

49. Mikijelj, B. and Mangles, J. (2006) 'Advanced Technical Ceramics Improve Performance and Reduce Life Cycle Cost'. *Ceradyne Ceramics Internal Article*. (www.ceradyne.com)

50. Mikijelj, B. and Mangles, J. (2006) Automotive Application, Ceradyne ceramics Internal Technical Article, (www.ceradyne.com).

51. Lawrence, J., and Hao, L. (2005) *Laser Surface Treatment of Bio – Implant Materials*. United Kingdom: John Willey & Sons Ltd. Publications.

52. Guedes Silva, C.C., König Jr, B., Carbonari, M.J., Yoshimoto, M., Allegrini Jr, S., and Bressiani, J.C. (2007) 'Bone growth around silicon nitride implants - An evaluation by scanning electron microscopy', *Material Characterization* **59**, 1339 – 1341.

53. Sands J.M, Fontzoulas C.G., Gilde G.A., Patel P.J., (2009) 'Modelling transparent ceramics to improve military armour'. *Journal of European Ceramic Society* **29**, 261 – 266.

54. Silfvast, W.T. (2004) *Laser Fundamentals 2nd Edition*, Cambridge: Cambridge University Press.

55. William T. Silfvast, (2007), *Laser Fundamentals*, Updated 2nd Edition, Cambridge University Press, Cambridge.

56. Hecht, J. (1992) *The Laser Guidebook 2nd Edition*. USA: McGraw - Hill Publication.

57. Shimoda, K. (1973) *Introduction to Laser Physics 2nd Edition*. New York: Sringer Verlag Berlin Publication

58. Svelto, O. (1997) *Principles of Lasers 4th Edition*. New York: Plenum Publication

59. Siegman, A.E. (1976) *Lasers*. Oxford: Oxford University Press

60. Charschan, S.S. (1972) *Lasers in Industry*. New York: Van Nostrand Reinhold Company

61. Maitland, Dunn, M.H. (1969) *Laser Physics*. Amsterdam: North Holland Publishing Company

62. Demmer, A. Bausch, S. and Groll, K. (2005) 'Perspectives for Laser Assisted Machining'. *Industrial Laser User*, Issue **39**, 37-41

63. Page, C.J., Devermann, T. Biffin, J. and Blundell, N. (2002) 'Plasma Augmented Welding and its Applications', *Science and Technology of Welding and Joining* **7(1)**, 1-10.

64. Blundell, B., Biffin, J., Johnson, T. A., and Page, C. (1997) 'High Speed Augmented –Laser welding of thin sheet metals'. *5th Internal conference on trends in welding research AWS ASM interotrad*, Georgia, 473-477.

65. AETC Turbines Ltd. (PCC Group of Companies) (2007) Industrial and Aerospace turbine Manufacturing, Leeds, United Kingdom.

66. Hackle, L. (2005) 'Shaping the future-laser peening technology has come of age'. *Metal Improvement Company, TSP*, **19(3)**, n.pp

67. Wright, C. (2005) 'Shot Peening Applications Ninth Edition'. *Metal Improvement Company: a subsidiary of Curtis-Write Corporation,* 1-60 (www.metalimprovement.com).

68. Hill, M. R., De Wald, A. T., Demma A. G. (2003) *Laser Peening Technology.* City: ASM International publications **161(7)** or www.asminternational.org/AMP.

69. Rofin Sinar Ltd. (2005) *Operating Technical Manual*; Daventry: united Kingdom

70. The Royal college of Ophthalmologists (2006) *A patients guide to Excimer Laser Refractive Surgery*, 17 Cornwall Terrace, London,

71. Kubacki, E., and Abbot, L. (2005) *Optics for Fibre Laser Applications,* CVI Laser, LLC, Optical Component & Assemblies (www.cvilaser.com).

72. Kell, J., Tyrer, J., Higginson, R., Thomson, R., Jones, J., and Noden, S. (2006) 'Holographic Diffractive Optical Elements Allow Improvements in Conduction Laser Welding of Steels'. *Proceedings of the 25th International Conference on Applications of Lasers and Electro-Optics* **99**, 7-17.

73. Shukla, P.P., Wu, H. and Johnson, T. A. (2007) 'Effects of High Speed Laser Welding on Thin Sheet Steels as Applicable to Manufacture Three Piece Packaging Cans'. *National Conference of Futuristic Trends in Mechanical Engineering (NCME)2007*, Shree Ram Collage of Engineering and Management (SRCEM), Banmore (Gwalior), India, 49-55.

74. Wang, X., Takacs, J., Krallics, G., Szilagyi, A., and Markovits, T. (2000) 'Experimental Research on Laser-Material Interaction'. *Periodica Polytechnica Ser. Transp. Eng.* **27, No. 1–2**, 143-152.

75. Prat, C., Autric, M., and Inflesakis, G. (1992) 'Pulsed CO_2 laser materials interaction: Thermomechanical effects, gas flow and chemical lasers'. *SPIE*. **1710**, 590-593.

76. Prat, C., Autric, M., Inglesakis, G. And Astic, D. (1991) 'Pulsed CO_2 laser material interaction: Mechanical coupling- Reflection and scatter radiation'. *Eight International Symposium on gas flow and chemical lasers*, SPIE **1397**, 701 – 704.

77. Lim, S.Y., and Chatwin, C.R. (1994) 'Special Chaos Aspects of Laser – Material Interaction', *Optics and Lasers in Engineering* **20**, 341- 356.

78. Illyefalvi Z, – Vitez. (1979) 'Thermal Processing of laser – Material Interaction'. *Acta Polytechnica – Prace.* CVUT v Praze, 7 (III, 2), 13 – 17.

79. Zhao, X., Ang, W., Li-jun, J., Xie, Y., YI Ai-ping, W., Ang, Lh., Liu. J.Y., Uan, X., Liu, Jr. (2001) 'Experimental Study on 307nm Laser Interaction with Materials'. *Plasma Science & Technology* **3(3)**, 727-734.

80. Wong, K.H., Hau, S. K., Chan, P. W., Leung, L. K., Choy, C. L., and Wong, H. K. (1991) 'XeCI excimer laser interaction with partially stabilized zirconia target'. *Journal of Materials science, Letters* **10**, 701-703.

81. Vlasova, M., Ma´rquezAguilar, P.A., Rese´ndiz-Gonza´lez, M.C., Kakazey, M., Gonza´lez, I., Stetsenko, V., Tomila, T., and Ragulya, A. (2010) 'Laser treatmentofSi–Al_2O_3 two-layer target'. *Optics & Laser Technology* **42**, 7-17.

82. Riviere, C., Robin, M., and Fantozzi, G. (1994) 'Comparison between two techniques in laser welding of ceramics'. *Journal de Physique IV 4*, C4-135 - C4-137.

83. Hirsch, J. W**.,** Olson L. G., Nazir, Z., and Alexander D. R. **(1997**) 'Axisymmetric laser welding of ceramics: comparison of experimental and finite element results'. *Optics and Lasers in Engineering* **29(6)**, 465-474.

84. Mikhailova, G.N., Mikhailov, B.P., and Troitskii, A.V. (2004) 'Laser welding of HTSC ceramics'. *Laser Physics Letters* **1 (10)**, 525–527.

85. Peyre, P., Merrien, P., Lieurade H.P., Fabbro R. (1995) Laser induced shock wave surface treatment for 7075-T7351 aluminium alloys, *Surface Engineering* **11(1)**, 47 - 52.

86. Vollertsen, F., Partes, K., and Meijer, J. (2005) 'State of the art in laser hardening cladding'. *Proceedings of the third international WLT-conference on lasers in manufacturing*, Munich: Germany 1-25

87. Kazuma, T., Koichi, A., Shin'ichi, O., Yuji, S., Hideki, N., Masugu, S., and Kentaro, K. (2006) 'Strengthening of Silicon Nitride Ceramics by Laser Peening'. *Proceedings of the Symposium on X-Ray Studies on Mechanical Behaviour of Materials* **41**, 109-113.

88. Bauerle, D. (1996) *Laser Processing and Chemistry*, Berlin: Springer.

89. Dyer, P.E., Jenkins, S.D., and Sindhu, J. (1976) 'Development and origin of conical structures on xecl laser ablated polyimide'. *Applied Physics Letters* **49**, 453 – 455.

90. Dyer, P.E., and Shindu, J. (1975) 'Excimer Laser Ablation and Thermal Coupling Efficiency to Polymer Films' *Journal of Applied Physics* **57(4)**, 1420-1422.

91. Lawrence, J., and Li, L. (2002) 'On The difference between the beam interactions characteristics of CO_2, Nd: YAG Excimer and high powered diode lasers with a SiO_2/Al_2O_3 ceramic'. *Lasers in Engineering* **12(2)**, 71 – 93.

92. Lawrence, J., and Hao, L. (2005) *Laser Surface Treatment of Bio – Implant Materials*, United Kingdom: John Willey & Sons Ltd Publications.

93. Lawrence, J., Li, L., and Spencer, J. T. (1999) 'Diode modification of ceramic material surface properties for improved wettability and adhesion'. *Applied Surface Science* **137-139**, 377 – 393.

94. Coherent Ltd, (2007) *Internal Technical Paper*, [online] available from http://www.coherent.com/ [c. 2007]

95. Ester, F.J., Merino, R. I., Pastor, J. Y., Martin, A., and Llorca, J. (2007) 'Surface Modification of Al_2O_3-$ZrO_2(Y_2O_3)$ eutectic oxides by laser melting: Processing and wear resistance'. *Journal of the American Ceramic Society* **91(11)**, 2552-3559.

96. Triantafyllidis D., Li, L. and Stott F. H. (2002) 'Surface treatment of alumina-based ceramics using combined laser sources'. *Applied Surface Science* **176**, 140–144.

97. Triantafyllidis, D., Bernstein, J. R., and Stott, F.H. (2003) 'Dual Laser beam modification of high alumina ceramics'. *Journal of Laser Applications* **15(1)**, 49-54.

98. Triantafyllidis D., Li, L., and Stott, F. H. (2004) 'Surface properties of laser-treated ceramic materials'. EMRS Spring Conference. Strasbourg: France, *Thin solid Films* **453**, 76 – 79.

99. Triantafyllidis, D., Li, L., and Stott F. H. (2005) 'The effect of laser-induced modification of surface roughness of Al_2O_3-based ceramics on fluid contact angle'. *Material science and Engineering A-structural Material Properties Microstructure and Processing* **390 (1-2)**, 271-277.

100. Triantafyllidis D., Li L., and Stott F. H. (2006) 'Crack-free densification of ceramics by laser surface treatment'. *Surface and Coating Technology* **210**, 3163 – 3173.

101. Clauer H. A. (1996) 'Laser shock peening for fatigue resistance in surface treatment of titanium alloys'. *The Metal Society of AIME Conference*, 217-230.

102. Maynard C. D. (1970) *Ceramic Glazes*. London: The Gresham Press.

103. Ion J. C. (2005) *Laser Processing of Engineering Materials: Principals, Procedures and Industrial Applications*. Cambridge: Elsevier Butterworth–Heinemann.

104. Wang, H. A., Wang, W. Y., Xie, C. S., Song, W. L., and Zeng, D. W. (2003) 'Microstructural characteristics of Al_2O_3-based refractory containing ZrO_2 induced by CO_2 laser melting'. *Applied Surface Science* **221**, 291–301.

105. Wang, H. A. Wang, W. Y. Xie, C. S., Song, W. L., and Zeng, D. W. (2003) 'CO_2 laser-induced structure changes on a zircon refractory'. *Applied Surface Science* **223**, 104–113.

106. Wang, H. A., Wang, W. Y., Xie, C. S., Song, W. L., and Zeng, D. W. (2004) 'CO_2 laser-induced structure changes on an alumina–mullite–zirconia refractory'. *Applied Surface Science* **223**, 244–251.

107. Wang, H. A., Wang, W. Y., Xie, C. S., Song, W. L., and Zeng, D. W. (2005) 'Nd:YAG laser surface densification of a zircon refractory by adding AlN nano-particles: Material characterization'. *Applied Surface Science* **256**, 227–231.

108. Triantafyllidis, D., Li, L., and Stott, F. H. (2004) 'Laser cladding of high performance ceramic sheets on a low quality ceramic substrate'. *Thin Solid Films* **453-454**, 70–73.

109. Faerber, M. (1995) 'Gases of increased productivity of laser processing'. *Optical and Quantum Electronics* **27**, 1449–1455.

110. Jxe, J., and Kar, A. (1999) 'Laser welding of thin sheet steel with surface oxidation'. *Journal of Welding Research Supplement* 343s–347s.

111. Abbott, D.H., and Albright, C.E. (1994) 'CO_2 shielding gas effects in laser-welding mild-steel'. *Journal of Laser Applications* **6(2)**, 69–70.

112. Bagger, C., Broden, E., Beske, E., and Olsen, F. (1994) 'The influence of shielding gas type in high power Nd:YAG laser welding'. *International Joining* **6**, 67–72.

113. Low, D.K.Y., Li, L., and Corfe, A.G. (2000) 'The influence of assist gas on the mechanism of material ejection and removal during laser percussion drilling'. *Proceedings of the Institution of Mechanical Engineers Part B: Journal of Engineering Manufacture* **214(7)**, 521–527.

114. Minami, K., Lawrence, J., Li, L., Edwards, R. E., and Gale, A. W. (2002) 'Effects of gases on high powered laser ablation of tile grout'. *Applied Surface Science* **176(1-4)**, 264–270.

115. Minami, K., Lawrence, J., Li, L., Edwards, R.E., and Gale, A. W. (2002) 'The removal of epoxy grout using high powered diode laser'. *Optics and Lasers in Engineering* **37(6)**, 475–497.

116. Lawrence, J., and Li, L. (2000) 'The influence of shield gases on the surface condition of laser treated concrete. *Applied Surface Science* **167(1-4)**, 25–27.

117. Zum Gahr, H. K., Bogdanow, C. H., and Schneider, D. (1994) 'Friction and wear reduction of Al_2O_3 ceramics by laser induced surface alloying'. *Wear* **171-173**, 117–127.

118. McColm, I. J. *Ceramic Hardness*. New York: Platinum Press. 1990.

119. British Standards (2005) Vickers Hardness Test- Part 2- Verification and Calibration of testing Machines. *Metallic Materials - ISO 6507-1*.

120. Cengel, Y.A., Turner, R.H. (2001). *Fundamentals of Thermal-Fluid Sciences*. Singapore: McGrae Hill international Edition.

121. Bass M. *Laser Material Processing*. (1997) New York: North-Holland Publishing Company.

122. Lysenko, V. S., Nazarov, A. N., Lokshin, M. M., and Kaschieva, S. B. (1977) 'Effects of laser irradiation on the structure of silicon dioxide film with implanted phosphorus ions'. *Fiz. Tekh. Poluprovodn* **1(11)**, 2254–2257.

123. Sakuma, T., Zhou, Y., Ge, Q. L. and Lei, T.C. (1990) 'Microstructure and mechanical properties of ZrO_2-2 mol% Y_2O_3 ceramics'. *Ceramics International* **16**, 349 - 354.

124. Hoffman, J., Moscicki, T., Szymanski, Z. (2006) 'Modelling of time dependant plasma plume induced laser welding'. *Journal of Physics* **56(1)**, B937 - B943.

125. Raciukaitis, G., Brikas, M., Kazlauskiene, V., and Miskinis, J. (2006) 'Applied physics'. *A Material Science & Processing* **75**, 445 – 450.

126. Rozman, R., Grabec, I., and Govekar, E. (2007) 'Influence of absorption mechanisms on laser-induced plasma plume'. *Applied Surface Science* **254**, 3295 – 3305.

127. Boulmer, J., Guedj, C., and Debarre, D. (1997) 'Incorporation of substitutional carbon in Si and SiGe by laser processing in methane and propylene '. *Thin Solid Films*. **294**, 137 - 140.

128. Ponton, C. B., and Rawlings, R.D. (1979) 'Vickers indentation fracture toughness test, Part 1 - Review of literature and formulation of standardised indentation toughness equations'. *Materials Science and Technology* **5**, 765- 772

129. Ponton, C.B. Rawlings, R.D. (1979) 'Vickers indentation fracture toughness test, Part 2 - Review of literature and formulation of standardised indentation toughness equations'. *Materials Science and Technology* **5**, 961- 976.

130. Mitchell, T.E. (1975) 'Dislocations in Ceramics'. *Materials Science and Technology* **1**, 994 – 949.

131. Castaing, J., and Veyssiere, P. (1975) *Core Structure Dislocations in Ceramics*. U.K: Gordon and Breach Science Publishers Inc and OPA Ltd. **12**, 213 -227.

132. Castaing, J. (1995) *Plastic Deformation and dislocations in ceramic materials. Radiation Effects and Defects in Solids.* U.S.A.: Gordon and Breach Science Publishers Inc and OPA Ltd, S.A **137**, 205 – 212.

133. Segall, A.E., Cai, G., Akarapu, R., and Ramasco, A. (2005) 'Fracture control of unsupported ceramics during laser machining using a simultaneous prescore'. *Journal of Laser Applications* **17 (Issue 1)**, 57-62

134. Samant, A.N., and Dahotre, N.B. (2009) 'Differences in physical phenomena governing laser machining of structural ceramics'. *Ceramics International* **35**, 2093–2097.

135. Hao, L., and Lawrence, J. (2006) 'Effects of Nd:YAG laser treatment on the wettability characteristics of a zirconia-based bio-ceramic'. *Optics and Lasers in Engineering* **44**, 703-714.

136. Hoe, L., Lawrence, J., and Chian, K. S. (2005) 'Osteoblast cell adhesion on a laser modified zirconia based bio-ceramic'. *Journal of Material Science: Materials in Medicine* **16**, 719–726

137. Hao, L., and Lawrence, J. (2006) 'Numerical modelling of the laser surface processing of magnesia partially stabilized zirconia by the means of three-dimensional transient finite element analysis'. *Proceedings of the Royal Society A* **462 (2065)**, 43-57

138. Lawrence, J., and Li, L. (2003) 'Augmentation of the mechanical and chemical resistance characteristics of an Al_2O_3-based refractory by means of high power diode laser surface treatment'. *Journal of Materials Processing Technology* **142**, 461 – 465

139. Lawrence, J., and Li, L. (2003) 'The enamelling of concrete for improved performance characteristics by means of high power diode laser interaction'. *Journal of Materials Processing Technology* **137**, 551–559

140. Liang, K.M., Orange, G., and Fantozzi, G. (1990)' Evaluation by indentation of fracture toughness of ceramics'. *Journal of material Science* **25**, 207 – 214

141. Matsumoto, R.K.L (1977) 'Evaluation of fracture toughness determination method as applied to ceria – stabilized tetragonal Zirconia poly-crystal'. *Journal of American Ceramic Society* **70**, 366 – 367.

142. Chicot, D. (2004) 'New Development for fracture toughness determination by Vickers indentation'. *Materials Science and Technology* **20**, 777- 774.

143. Liang, K.M., Orange, G., and Fantozzi, G. (1977) 'Crack resistance and fracture toughness of Alumina and Zirconia ceramics: *Comparison of notched- beam and indentation technique'. Science Ceramics 14th International Conference*. **14**, 709- 714.

144. Exner, H.E. (1979) 'The Influence of Sample Preparation on Palmqvist's Method for Toughness Testing of Cemented Carbides'. *Transactions of the Metallurgical Society of AIME* **245 (4)**, 677 – 673

145. Marion, R.H. (1979) In fracture mechanics applied to brittle materials. STP 677 (Ed S. W Freiman), PA, ASTM: 103 – 111, Philadelphia.

146. Miannay, D. (1997) *Fracture Mechanics*. New York: Springer-Verlag.

147. Evans, A.G. (1976) 'Wilshaw TR Quasi static particle damage in brittle solids'. *Acta Metal* **24**, 939 – 956

148. Evans, A.G., and Charles, E.A. (1976) Fracture Toughness Determinations by Indentation. *Journal of American Society* **59(7 – 7)**, 371 – 372

149. Lawn, B.R., and Evans, A.G., and Marshall, D.B. (1970) 'Elastic/ Plastic Indentation Damage in ceramic: The Meadian/ Radial Crack System'. *Journal of American Ceramic Society* **63(9–10)**, 574 – 571

150. Marshall, D.B. (1973) 'Failure from contact induced surface flaws'. *Journal of American Ceramic Society* **66**, 127 – 131

151. Anstis, G.R., Chantikul, P., Lawn, B.R., and Marshall, D.B. (1971). *Journal of American Ceramic Society* **64**, 533 – 537

152. Niihara, K., Morena, R., and Hasselman, D.P.H. (1972) 'Evaluation of K_{1c} of brittle solids by the indentation method with low crack-to-indent ratios'. *Journal of material Science Literature* **1**, 13 – 16.

153. Tani, T., Miyamoto, Y., and Koizumi, M. (1976) 'Grain Size Dependences of Vickers micro hardness and fracture toughness in Al_2O_3 and Y_2O_3 ceramics'. *Ceramics International.* **12(P1)**, 33 – 37.

154. Hoshide, T. (1993) 'Grain fracture model and its application to strength evaluation in engineering ceramics'. *Engineering Fracture Mechanics* **44(3)**, 403 – 407.

155. Kelly, J.R., Cohen, M.E., and Tesk, J.A. (1993) 'Error Biases in the Calculation of Indentation fracture Toughness for Ceramics'. *Journal of American Ceramic Society* **76(10)**, 2665 – 2667.

156. Gong, J. (1997) 'Determining indentation toughness by incorporating true hardness into fracture mechanics equations'. *Journal of European Ceramic Society* **19**, 1575 – 1592.

157. Orange, O., Liang, K.M., and Fantozzi, G. (1977) 'Crack Resistance and fracture toughness of alumina and Zirconia ceramics: comparison of notched beam and indentation technique'. *Science of Ceramics* **14(PT 7 – 9)**, 709 – 14.

158. Glandous, J.C., Rouxl, T., and Qiu, T. (1991) 'Study of the Y- TZP toughness by an indentation method'. *Ceramic International* **17**, 129 -135

159. Fischer, H., Waindich, A., and Telle, R. (2006) 'Influence of preparation of ceramic SEVNB specimens on fracture toughness testing results'. *Academy of Dental Material, Science Direct* **24**, 617 – 622

160. Salem, J.A., Shannon Jr. J.L., and Jenkins, M.G. (1992) 'Some observations in fracture toughness and fatigue testing with Chevron Notched Specimens', *ASTM International Special Technical Publications* **1172**, 579 -590.

161. Anstis, G.R., Chantikul, P., Lawn, B.R., and Marshall, D.B. (1970) 'A critical evaluation of indentation technique for measuring fracture toughness, I, direct measurement'. *Journal of American Ceramic Society* **64**, 533 – 537.

162. Lawn, B.R., and Swain, M.V. (1975) 'Microfracture: Beneath Point In- dentations in Brittle Solids'. *Journal of Material Science* **10**, 113 – 122.

163. Li, Z., Gosh, A., Kobayashi, A.S., and Bradt, R.C. (1979) 'Indentation fracture toughness of sintered silicon nitride in the Palmqvist crack regime'. *Journal of American Ceramic Society* **72**, 904 – 911

164. Strakna, T.J., and Jahanmir, S. (1995) 'Influence of grinding direction on Fracture strength of silicon nitride'. *Machining of Advanced Materials* **207**, 53 – 64

165. Lawn, B.R., and Wilshaw, T.R. (1975) 'Indentation fracture: principles and application'. *Journal of Material Science* **10**, 1049 – 1071

166. Lawn, B.R. and Fuller, E.R. (1975) 'Equilibrium penny-like cracks in indentation fracture'. *Journal of Material Science* **10**, 2016 – 2024.

167. Lankford, J. (1972) 'Indentation micro-fracture in the Palmqvist crack regime: implication for fracture toughness evaluation by the indentation method'. *Journal of Material Science Letters* **1**, 493-495

168. Laugier, M.T. (1975) 'The elastic/plastic indentation of ceramics'. *Journal of Material Science Letters* **4**, 1539 – 1541

169. Tanaka, K. (1977) 'Elastic/plastic indentation hardness and indentation fracture toughness: The inclusion core model'. *Journal of Material Science* **22**, 1501 – 1507.

170. Miranzo, P., and Moya, J.S. (1974) 'Elastic/plastic indentation in ceramics: a fracture toughness determination'. *Ceramic International* **10(4)**, 147 – 152.

171. Jiang, J.Z. Kragh, F. Frost, D.J. Stahl, K. and Lindelov, H. (2001) 'Hardness and thermal stability of cubic silicon nitride'. *Journal of Physics Condensed Matter* **13(22)**, L515-L520.

172. Moon, W. Ito, T. Uchimura, S. and Saka, H. (2004) 'Toughening of ceramics by dislocation sub-boundaries'. *Material Science and Engineering A* **377 – 379**, 737 – 739

173. Pfeiffer, Frey, W (2002) 'Shaping the future – damage or benefits'. *Fraunhofer Institute for Mechanics of Materials ICSP – 7.* Germany, 175-190.

174. Tensky International Co. Ltd. (2009) *Tensky International Technical Specification.* (See appendix A)

175. White, R.M., Kunkle, J.M., Polotai, A.V., and Dickey, E.C. (2010) 'Microstructure and hardness scaling in laser-processed B4C–TiB_2 eutectic ceramics'. *Journal of the European Ceramic Society* (in press).

176. Ahn, Y., Chandrasekar, S., Farris, T.N. (1996) 'Determination of Surface residual stress in machined ceramics using indentation Fracture'. *Journal of Manufacturing Science and Engineering* **117**, 473 – 479.

177. Cline, H. E., and Anthony, T. R. (1997) 'Heat treating and melting materials with a scanning laser beam'. *Journal of Applied Physics* **48**, 3895 – 3900.

178. Lax, M. (1977) 'Temperature rise induced by a laser beam'. *Journal of Applied Physics* **47**, 3919 - 3924.

179. Lax, M. (1977) 'Temperature rise induced by a laser beam II. The nonlinear case'. *Journal of Applied Physics* **33**, 1127-1129.

180. Nissim, Y. I., Lietoila, A., Gold, R. B., and Gibons, J. F. R. (1970) 'Temperature distributions produced in semiconductors by a scanning elliptical or circular CW laser beam'. *Journal Applied Physics* **51**, 274-279.

181. Moody, J.E., and Hendel, R. H. (1972) 'Temperature profiles found by a scanning laser beam'. *Journal Applied Physics* **53**, 4364 – 4371.

182. Sanders, D. J. (1974) 'Temperature distribution produced by a scanning Gaussian laser beam'. *Journal of Applied Optics* **23**, 30- 35.

183. Kar, A., and Mazumber, J. (1979) 'Three-dimensional transient thermal analysis for laser chemical vapour deposition on uniformly moving finite slabs'. *Journal of Applied Physics* **65**, 2923 – 2934.

184. Kar, A. (1996) 'Effects of mode structure on three-dimensional laser heating due to single or multiple rectangular laser beams'. *Journal Applied Physics* **70**, 667 – 674.

185. Cheng, J., and Kar, A. (1997) 'Mathematical model for laser densification of ceramic coating'. *Journal of Material Science* **32**, 6269 – 6277.

186. Zhang, Z., and Modest, M. F. (1997) 'Temperature dependent Absorptances of ceramics for Nd:YAG and CO_2 laser processing Applications'. *Journal of Heat Transfer* **120**, 322 -327.

187. Hao, L., and Lawrence, J. (2006) 'Numerical modelling of the laser surface processing of magnesia partially stabilized Zirconia by the means of three-dimensional transient finite element analysis'. *Proceedings of the Royal Society A* **462(2065)**, 43-57.

188. Ignatiev, M. B., Smurov, Yu. I., Flamant, G., and Senchenko, V. N. (1996) 'Surface temperature measurement during pulsed laser action on metallic and ceramic materials'. *Journal of Applied Surface Science* **96-97**, 505 -512.

189. Braisted, W., and Brockman, R. (1997) 'Finite Element Simulation of laser shock peening'. *Internationa*l *Journal of Fatigue* **21**, 719 – 724.

190. Yongxiang, Hu., Zhenqiang, Yao., and Jun, H. (2006) '3-D FEM Simulation of laser Shock Processing'. *Surface and Coating Technology* **21(3-4)**, 1426 – 1435.

191. Ocana, J. L., Morales, M., Molpeceres, C., and Torres, J. (2004) 'Numerical simulation of surface deformation and residual stresses fields in laser shock processing experiments'. *Journal of Applied Surface Science* **237**, 224 – 247.

192. Chen, H., Kysar, J. W., and Lawrence, Y.Y. (2004) 'Characterization of plastic deformation induced by micro-scale laser shock peening'. *Journal of Applied Mechanics (ASME)* **71**, 713-723.

193. Kim, M. J. (2005) '3-D Finite element analysis of evaporative Laser cutting'. *Applied Mathematical Modelling* **29**, 937 – 954.

194. Shiomi, M., Yoshidome, A., Abe, F., and Osakada, K. (1997) 'Finite element analysis of melting and solidifying processes in laser rapid prototyping of metallic powders'. *International Journal of Machine Tools and Manufactures* **39**, 237 – 252.

195. Carmingnani, C., Meres, R., and Toselli, G. (1999) 'Transient finite element analysis of deep penetration laser welding process in single pass butt-welded, thick steel plate'. *Computer Methods in Applied Mechanics and Engineering* **179**, 197- 214.

196. Spina, R., Tricarico, L., Basile, G., and Sibilano, T. (2007) 'Thermo- mechanical modelling of laser welding of AA5073 sheets'. *Journal of Material Process Technology* **191**, 215 – 219.

197. Yilbas, B. S., Arif, A. F. M., and Abdul Aleem, B. J. (2009) 'Laser welding of low carbon steel and thermal stress analysis'. *Optics & Laser Technology* **42**, 760 – 767.

198. Zain-Ul-Abdein, M., Nélias, D., Jullien, J. F., and Deloison, D. (2007) 'Thermo-mechanical Analysis of Laser Beam Welding of Thin Plate with Complex Boundary Conditions'. *International Journal of Material Forming* **1**, 1063- 1066.

199. Naeem, Ullah. Dar., Qureshi, M. E., and Hammouda, M. (2009) 'Analysis of weld-induced residual stresses and distortions in thin-walled cylinders'. *Journal of Mechanical Science and Technology* **23**, 113-117.

200. Zakurdaev, A., and Huang, X. (2009) 'Experimental study of phase transformation and specific heat of ternary Zirconia-based oxides using differential scanning calorimetry'. *Journal of Alloys and Compounds* **477**, 469 - 477.

201. Luping, Li., Peigen, Zhang., Jiandong, Liang., and Guo, S. M. (2009) 'Phase transformation and morphological evolution of electrospun Zirconia nanofibers during thermal annealing'. *Ceramics International* **36**, 579–594.

202. Holand, W., and Beall, G. (2002) *Glass- ceramic Technology*. USA: The American ceramic society.

203. Garvie, R. C., Hannink, R. H., and Pascoe, R. T. (1965) 'The occurrence of metastable tetragonal Zirconia as a crystallite size effect'. *Journal of Physics and Chemistry* **69(4)**, 1237–1243.

204. Porter, D. L., and Heuer, A. H. (1977) 'Mechanisms of Toughening Partially Stabilized Zirconia (PSZ)'. *Journal of American Ceramic Society* **60**, 173.

205. Sergio, M. (1972) 'Thermal evaluation of ciria Zirconia metallorganic precursors'. *Thermo-chemica Acta (Elsevier Scientific Publishing Company)* **57**, 253-259.

206. Zhou, Y., Ge, Q. L., and Lei, T.C. (1990) 'Microstructural and Mechanical Properties of ZrO_2 – 2, mol % Y_2O_3 ceramics'. *Ceramics International* **16**, 349 – 354.

207. Sato, T., and Shimada, T. (1975) 'Control of the tetragonal-to-monoclinic phase transformation of yttria partially stabilized Zirconia in hot water'. *Journal of Material of Science* **20**, 3977 - 3992.

208. Haraguchi, K., Sugano, N., Nishi, T., Miki, H., Oka, K., and Yoshikawa, H. (2001) 'Phase transformation of a Zirconia ceramic head after total hip arthroplasty'. *The journal of Bone & Joint Surgery (Br)* **73-B, No.7**, 996- 1000.

209. Shackelford, J. F., and Doremus, H. R. (2007) *Ceramic and glass materials (Structure properties and processing)'*. New York: Springer Science and Business media.

210. Huang, X., Zakurdaev., and Wang, D. A. (2007) 'Microstructure and phase transformation of Zirconia- based ternary oxides from thermal barrier coating applications'. *Journal of Material Science* **43**, 2631 – 2641.

211. Lee, W. L., and Rainforth, W. M. (1994) *Ceramic Microstructures*. London: Chapman & Hall.

212. Xigeng, M., Dan, S., Pui, H., Liu, W., Hu, J., Yifei, and Yanming, C. (2004) 'Effect of Titania addition on yttria-stabilised tetragonal Zirconia ceramics sintered at high temperatures'. *Ceramics International* **30(6)**, 1041-1047.

213. Nayak, Y., Rana, R., Pratihar, S., and Bhattacharyya, S. (2007) 'Low-Temperature Processing of Dense Hydroxyapatite– Zirconia Composites'. *International Journal of Applied Ceramic Technology* **5(1)**, 29- 36.

214. Sato, T., Ohtaki S., and Shimada, M. (1975) 'Transformation of yttria partially stabilized Zirconia by low temperature annealing in air'. *Journal of Material Science* **20**, 1466 – 1470.

215. Zhu, W. Z. (1996) 'Grain size dependence of the transformation temperature of tetragonal to monoclinic phase in ZrO_2 (Y_2O_3) ceramics'. *Ceramics International* **22(5)**, 379- 395.

216. Sarin, V.K. (1971) 'On the *α*-to-*β* Phase Transformation in Silicon nitride'. *Material Science and Engineering A* **105-106**, 151-159.

217. Messier, D. R., Riley, F. L., and Brook, R. J. (1977) 'The *α/β* silicon nitride phase Transformation'. *Journal of Material Science* **13**, 1199 – 1205.

218. Ziegler G., and Hasselman, D.P.H. (1971) 'Effect of phase composition and microstructure on the thermal diffusivity of Silicon Nitride'. *Journal Material Science* **16**, 495 – 503.

219. Sajgalik, P., and Galisek, D. (1993) '*α/β* Phase transformation of silicon nitride: homogeneous and heterogeneous nucleation'. *Journal of Material Science Letters* **12**, 1937-1929.

220. Rouxel, T., Rossignol, F., Besson, J.L., and Goursat, P. (1996) 'Superplastic forming of α-phase rich silicon nitride'. *Journal of Material Research* **12(2)**, 470-492.

221. Yang, H., Yang, G., and Yuan, R. (1997) 'Densification and α-β phase transformation of Si_3N_4 containing MgO and CeO_2 during sintering'. *Materials Chemistry and Physics* **55**, 164 – 166.

222. Dai, J., Li, J., and Chen, Y. (2003) 'The phase transformation behaviour of Si_3N_4 with Re_2O_3 (Re=Ce, Nd, Sm, Eu, Gd, Dy, Er, Yb) additives'. *Material Chemistry and Physics* **70**, 256 – 359.

223. Jiang, J. Z., Kragh, F., Frost, D.J., Ståhl, K., and Lindelov, H. (2001) 'Hardness and thermal stability of cubic silicon nitride'. *Journal of Physics Condensed Matter* **13(22)**, L515 – L520.

224. Sham, T. (2007) *NX 5.0 for designers*. Purdue University Calumet. USA : CADCIM Technologies.

225. Rolph, W. D., and Bathe, K. J. (1972) **'**An efficient algorithm for analysis of non-linear heat transfer with phase changes'. *International Journal of Numerical Methods in Engineering* **17**, 119–134.

226. Rhee, S. H., Lee, J. D., Kim, D. Y. (2000) 'Effect of a-Si_3N_4 initial powder size on the microstructural evolution and phase transformation during sintering of Si_3N_4 ceramics'. *Journal of the European Ceramic Society* **20**, 1787 – 1794.

227. Leea, J. S., Muna, J. H., Hanb, B. D., Kimb, H. D. (2003) 'Effect of b-Si_3N_4 seed particles on the property of sintered reaction-bonded silicon nitride'. *Ceramics International*' **29**, 897–905.

228. Robieux, J. (2000) *High power Laser Interactions*. Paris: Lavoisier Publishing.

229. Milonni, P.W., Eberly, J.H. (1977) *Lasers*. Canda: John Wiley & Sons, Inc.

230. Breck Hitz, C. (1991) *Understanding Laser technology* (2nd Edition). Oklohoma (USA): Penn Well Publishing Company.

231. Rudiger, P. (2007) *Encyclopedia of Laser Physics and Technology*. Berlin: Wiley – VCH.

232. Wilson, J., and Hawkes, J.F.B (1977) *Lasers Principles and Applications.* United Kingdom: Prentice Hall International Ltd.

233. Ready, J.F. (1977) *Industrial Applications of Lasers*. New York: Academic Press Inc.

234. Ion, J. C. (2005) *Laser Processing of Engineering Materials*. Oxford (United Kingdom): Elsevier Butterworth Heinemann.

235. Diehl, R. (2000) *High Powered Diode laser fundamentals, technology, applications*. Berlin (Germany): Springer Verlag.

236. Shepelev, A.V. (2009) 'About transforming of radiation brightness in optical processes'. *American Association of Physics Teachers* **77(2)**, 157- 159.

237. Koechner, W. (1999) *Solid- State laser engineering, 5th revised and updated edition*. Berlin (Germany): Springer – Verlag.

238. Das, P. (1991) *Lasers and Optical Engineering.* New York: Springer Verlag.

239. British Standards Institution (2000) *Laser and laser-related equipment -Test methods for laser beam parameters- Beam width, divergence angle and beam*. BS EN ISO 11146:2000. London: British Standard Institution.

240. British Standards Institution (2005) *Lasers and laser-related equipment - Test methods for laser beam widths, divergence angles and beam propagation ratios - Part 1: Stigmatic and simple astigmatic beams.* BS EN ISO 11146-1:2005. London: British Standard Institution.

241. British Standards Institution (2005) *Lasers and laser-related equipment - Test methods for laser beam widths, divergence angles and beam propagation ratios - Part 2: General astigmatic beams.* BS EN ISO 11146-2:2005. London: British Standard Institution.

242. Forbes, A., Burger, L., and Litvin, I.A. (2006) 'Modelling laser brightness from cross Porro-prism resonators'. Laser Beam Shaping VII'. *Proceedings of SPIE* 6290, M-1-M-7.

243. Wallace, J. (2009) 'Direct-diode lasers combine to form powerful, high- brightness beam'. *Laser Focus Word*, June, 24 - 25.

244. Wenzel, H., Sumf, B., and Erbert, G. (2003) 'High brightness diode lasers'. *Computers Rendus Physique* 4, 649 – 661.

245. Brown R. T., and Frye, R. W. (1996) 'High-brightness laser cutting & drilling of aerospace materials'. *Proceedings of ICALEO*-1996, Section C, 77-75.

246. Li, H., Truchan, T., Brown, D., Pryor, R., Pandey, R., Reinhardt, F., Mott, J., Treusch, G., and Macomber, S. (2004) 'Reliable high-efficiency high-brightness laser diode bars at 940 nm'. *Optics & Laser Technology* **36**, 327 – 329.

247. Treusch, H.G., Ovtchinnikov, A., He, X., Kanskar, M., Mott, J., and Yang, S. (2000) 'High-Brightness Semiconductor Laser Sources for Materials Processing: Stacking, Beam Shaping, and Bars'. *IEEE Journal of Selected Topics In Quantum Electronics* **6(4)**, 601 – 614.

248. Leibreich F., and Treusch, H.G. (2001) 'Innovative stacking techniques increase the output power and brightness of diode laser bars for materials-processing applications. Micro/Nano Lithography & Fabrication'. *SPIE Newsroom*. DOI: 10.1117/2.5200109.0004.

249. Hanna, D.C (1970) 'Increasing laser brightness by transverse mode selection -1, Laser Techniques Series -1'. *Journal of Optics and Laser Technology*, 122 – 125.

250. Hanna, D.C (1970) 'Increasing laser brightness by transverse mode selection -2, Laser Techniques Series -1'. *Journal of Optics and Laser Technology*, 175 – 177.

251. Val, Comesaña, J. R., Lusquiños, F., Boutinguiza, M., Riveiro, A., Quintero, F., and Pou, J. (2010) 'Laser cladding of Co-based superalloy coatings: Comparative study between Nd:YAG laser and fibre laser'. *Journal of Surface & Coatings Technology* **204**, 1957–1961.

Appendix

Appendix A

Table 11.1 Technical Specification of the As-received Si_3N_4 and the ZrO_2 engineering ceramics used for experimentation in this work.

Item	Unit	Si_3N_4	ZrO_2
Density	g/cm^3	3.20~3.30	6.05
Thermal expansion coefficient	10-6/k	3.2	10.5
Modulus of elasticity	GPa	300~320	210
Poisson's ratio		0.26	0.30
Hardness	(HV)	1500~1700	1200
	(HRC)	75~70	70
Flexural strength (700℃)	MPa	200	300
Compressive strength (700℃)	MPa	1400	2100
Fracture toughness	MPa $m^{1/2}$	2.5	10.0
Thermal conductivity (500℃)	W/mk	17	2
Specific resistance (600℃)	$\Omega mm^2/m$	10^{17}	10^{15}
Maximum operation temperature	℃	700~1300	550
Anti-chemical corrosion		strong	strong
Stress cycle (50% damage probability)	Times	10^7~10^9	10^5
Size stability (temperature)		--	--
Operating centrifugal force		low	highest
Unlubricated friction		low	low
Magnetism		no	no
Rolling contact fatigue failure mode		Peel off	fragments